Metallic Glasses
Formation and Properties

Edited by Behrooz Movahedi

METALLIC GLASSES - FORMATION AND PROPERTIES

Edited by **Behrooz Movahedi**

Metallic Glasses - Formation and Properties
http://dx.doi.org/10.5772/61764
Edited by Behrooz Movahedi

Contributors

Hui Li, Weikang Wu, Kun Zhang, Aras Kartouzian, Jerzy Antonowicz, Celal Kurşun, Musa Gogebakan, Shanlin Wang, Chang Haijun, Vladimir Voitsenya, Devinder Singh, O.N. Srivastava, R.S. Tiwari, Rajiv Kumar Mandal

Notice

Statements and opinions expressed in the chapters are these of the individual contributors and not necessarily those of the editors or publisher. No responsibility is accepted for the accuracy of information contained in the published chapters. The publisher assumes no responsibility for any damage or injury to persons or property arising out of the use of any materials, instructions, methods or ideas contained in the book.

We are IntechOpen,
the world's leading publisher of Open Access books
Built by scientists, for scientists

3,700+
Open access books available

116,000+
International authors and editors

119M+
Downloads

151
Countries delivered to

Our authors are among the

Top 1%
most cited scientists

12.2%
Contributors from top 500 universities

BOOK CITATION INDEX
CLARIVATE ANALYTICS
INDEXED

WEB OF SCIENCE™

Selection of our books indexed in the Book Citation Index
in Web of Science™ Core Collection (BKCI)

Interested in publishing with us?
Contact book.department@intechopen.com

Numbers displayed above are based on latest data collected.
For more information visit www.intechopen.com

Meet the editor

Dr. Behrooz Movahedi obtained his PhD degree in Materials Engineering at Isfahan University of Technology (IUT) in Iran in 2010. During this period, he visited as a sabbatical leave at the School of Materials Science and Engineering in Nanyang Technological University (NTU) in Singapore. Then he joined the Department of Nanotechnology Engineering in the University of Isfahan (UI) as an assistant professor. Recently, he is the head of the Nanotechnology Engineering Department in Faculty of Advanced Sciences and Technologies. Dr. Behrooz Movahedi has over 10 years of experience in the nanotechnology, amorphous materials, optical ceramics, and advanced thermal spray coatings for environmental and industrial applications. He was invited as a reviewer in some potential ISI journals such as *Materials & Design*, *Journal of Alloys and Compounds*, *Surface and Coatings Technology*, *Applied Surface Science*, and *Materials Science & Engineering B*.

Contents

Preface

Metallic glasses and amorphous materials have attracted much more attention in the last two decades. The first claim is their potential industrial applications as appropriate materials for fabricating devices, and the second claim is the lack of understanding of many properties of these materials, which are very different from those of crystalline counterparts. A noncrystalline solid produced by continuous cooling from the liquid state is known as a " *glass* ". From the other point of view, a noncrystalline material, obtained by any other process, for example, vapor deposition or solid-state processing methods such as mechanical alloying, but not directly from the liquid state, is referred to as an "amorphous" material. But, it should be remembered that both glasses and amorphous solids are noncrystalline in nature. These could be extensively grouped into metal–metalloid or metal–metal type. In a typical metal–metalloid-type glass, the metal atoms constitute about 80% and the metalloid atoms (typically B, C, P, and Si) about 20%. The metal atoms may be of one type or a combination of different metals, but the total amount of the metal atoms is about 80%. Correspondingly, the metalloid atoms may be of one type or a combination of different metalloid atoms, and also the total amount of the metalloid atoms is about 20%. At this moment, bulk metallic glasses (BMG) are appearing as a new class of metallic materials with unique physical and mechanical properties for structural and functional usage. Extreme values of strength, fracture toughness, magnetic properties, corrosion resistance, and other properties have been registered in BMG materials.

The overall purpose of this book titled *"Metallic Glasses: Formation and Properties"* is to provide opportune and fully developed coverage of selected advanced topics in metallic glasses as well as amorphous materials. The articles for this book have been contributed by the most respected researchers in this area. This book is divided into three sections including I. formation and characterizations, II. structural features, and III. applications. InTech Publisher and myself as the editor hope that this book will be supportive for the current researches and prove to be very useful for the scientific community. If so, this will be the nicest reward for us. Ultimately, I wish to thank all the authors for their contributions, and I should like here to acknowledge the sustained helpfulness and dedication of the publisher's staff, in particular of Ms. Andrea Koric, for her persistance in concluding this interesting project.

Dr. Behrooz Movahedi
Department of Nanotechnology Engineering,
Faculty of Advanced Sciences and Technologies,
University of Isfahan,
Isfahan, Iran

Formation and Characteristics

Metallic Glasses from the Bottom-up

Aras Kartouzian and Jerzy Antonowicz

Additional information is available at the end of the chapter

Abstract

The main challenge in understanding the relation between the structure and properties of metallic glasses is describing their structure at the atomic level. Currently, their structures are considered simply *disordered* and indeed our understanding of their structure is as undefined as this term. Following the most advanced structural models of metallic glasses that are based on metal clusters, a bottom-up approach to fabrication of metallic glasses using cluster beam technology is introduced. Using metal clusters to fabricate metallic glasses from the bottom-up, that is, formation of cluster-assembled metallic glasses, provides us with the possibility of varying their structure at the atomic level while keeping their composition unchanged. A unique feature working with cluster-assembled metallic glasses is the *independent* control of their structure and composition. The advantages of this approach are presented, and its potential toward the resolution of structure–property puzzle in metallic glasses is demonstrated along with the main challenges.

Keywords: Cluster-assembled metallic glasses, metal clusters, structure–property relation, cluster deposition, cluster-based structural models

1. Introduction

First discovered in 1959 by rapidly quenching (>106 Ks^{-1}) an alloy of $Au_{75}Si_{25}$ (at.%) [1], metallic glasses (MGs) are among the most studied metallic materials. The non-periodic character of MGs underlies their unique properties which are often superior to conventional crystalline materials. Due to their reduced eddy current losses, as compared to the crystalline alloys of identical compositions, for instance, ferromagnetic MGs are commonly used as magnetic core materials [2]. Also, the corrosion resistance of iron-based metallic glasses was shown to be

much higher than that of crystalline stainless steel [3]. As another example, the $Ti_{40}Cu_{36}Pd_{14}Zr_{10}$ metallic glass is a biocompatible material that is about three times stronger than titanium, has an elastic modulus that matches that of bone, and does not produce abrasion powder [4]. Further, the combination of high toughness and high strength in Pd-based MGs puts them among the strongest and most damage-tolerant materials ever known [5].

As of now, the main challenge in investigating these materials is to describe their structure at an atomic level. In absence of an atomic description, no systematic design of MGs has been possible, and the progress in the field is merely based on the costly and inefficient procedure of trial and error. The pioneering work by Bernal [6, 7] on the structure of metallic liquids, who suggested "dense random packing of hard spheres" as the structural model, was the first step in this direction. Further research in the field has led to the discovery of many other metallic alloys that could be solidified into the amorphous state with moderate cooling rates ($10^2–10^0$ Ks^{-1}) such as $Pd_{40}Ni_{40}P_{20}$ glass for which bulk sections of 10 mm across were produced at a cooling rate of 1 Ks^{-1} [8]. Based on the observations across the compositions of the MGs, Inoue put forward a set of empirical criteria for their formation and stability [9]. This highly valuable classification accelerated the discovery of new glass forming alloys. As a result, very soon a revision of the criteria was required [10]. Such criteria that have been proven very helpful in designing new glasses, however, naturally suffer from numerous exceptions. For instance, based on the binary phase diagram of Au–Al alloy and the relative atomic radii of gold and aluminum, it is expected to be possible to produce an Al_xAu_{1-x} MG. However, to date, no one has succeeded in the production of MGs in this alloy system regardless of the employed techniques [11].

Despite the intensive research in the field of MGs, the understanding of the fundamental link between their structure and properties is still missing [12–15]. Theoretical computations have made a large contribution toward our understanding of the structure of MGs but are damned to be inaccurate due to their restricted timescale, which imposes cooling rates that are many orders of magnitude higher than what is experimentally achievable (beside the ultrafast liquid quenching reported by Mao et al. [16] with a cooling rate of $\sim 10^{15}$ Ks^{-1}). Currently, there exists no perspective to solving this issue without external help from other disciplines. Currently, the structure of MGs is addressed as *disordered* and our understanding of it is in fact as diffuse and undefined as this term. Of course, considerable progress has been made in the past toward describing the structure of MGs at the atomic level, but we are still far from having a coherent and consistent model.

Assuming we have the correct model to describe the structure of MGs, the next step would be to figure out the structure–property relation. Obviously in the absence of periodicity, it will still be much more complicated to develop this relation in MGs compared to oxide glasses considering that bond angles and lengths are much more flexible and distortable in MGs.

In this chapter, we introduce some of the most advanced experimental approaches to tackle these issues using cluster beam technology. Accordingly, this chapter aims to put forward an interdisciplinary approach and familiarize the material scientists working on MGs with cluster beam technology and how it can be used.

2. Cluster-based structural models for MGs

Although amorphous alloys lack long range order, they possess well defined nearest neighbor shells. The resulting short and medium range order is experimentally observed in MGs. The latest structural models for MGs [17–22] take this observation into account and use atomic clusters[1] to describe the structure of amorphous alloys. A structure model based on efficiently packed solute-centered atomic clusters was introduced by Miracle. In this model, atomic clusters are idealized as spherical particles, which similar to atoms, fill the space in face-centered cubic (fcc) or hexagonal close-packed (hcp) arrangements [22]. However, unlike atoms, atomic clusters can overlap and share atoms with each other. This model has gained some credit because firstly it is consistent with a broad range of previously established guidelines for metallic glasses, and secondly, it has a predictive capability for the experimentally observed medium-range order in MGs. Shortly after the presentation of Miracle's model, a revised version was suggested by Fan et al. [20] where the building blocks are again atomic clusters, but are arranged randomly instead. Later, the same group refined their model based on reverse Monte Carlo simulations and introduced the "tight-bond cluster model", which includes the clusters, the free volume between the clusters, and the interconnecting zones among clusters [19]. In a closely related approach, Dong et al. [18] introduced the "cluster-plus-glue-atom model", where the structure of the MG is described by specific metal clusters that are glued together by additional glue atoms. The recent review by Liu and Zhang [23] provides a concise summary of structural models for MGs. **Figure 1** presents a graphical summary of the cluster-based models.
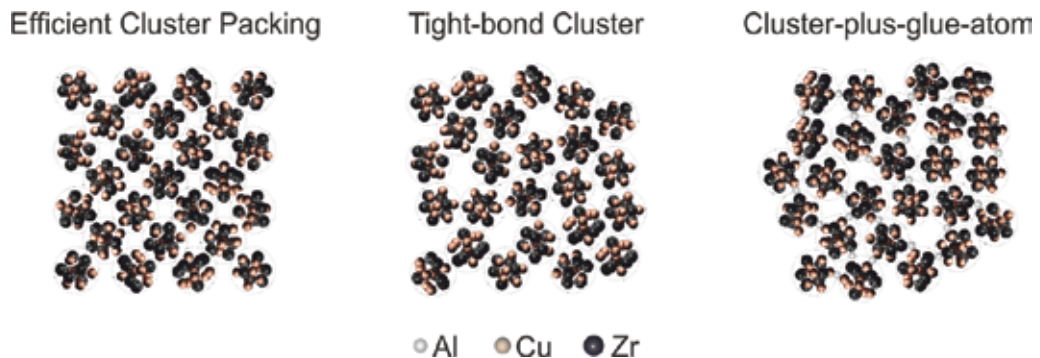
Figure 1. Planar representations of cluster-based structure models for metallic glasses. Left—A $Zr_{46}Cu_{54}$ glass consisting of Zr_7Cu_6 clusters[2] arranged in fcc structure [100]. Middle—A $Zr_{46}Cu_{54}$ glass consisting of randomly arranged tightly bonded Zr_7Cu_6 clusters. Right—A $Zr_{43}Cu_{50}Al_7$ glass consisting of randomly arranged Zr_7Cu_6 clusters glued together by Al atoms.

---

[1] In this context atomic clusters are small particles consisting of up to 200 atoms.

[2] Notation of clusters: Ag_m indicates a clusters consisting of m Ag atoms; Ag_5 indicates a cluster made out of 5 Ag atoms. In the same way, Zr_7Cu_6 indicates a cluster made out of 7 Zr and 6 Cu atoms.

All these cluster-based models allow short- and medium-range order (up to distances of few cluster sizes), while the disordered nature of MGs on the long-range is retained due to local atomic stresses and topological frustration.

Cluster-based models have been employed by various groups for the interpretation of their experimental and theoretical results. Probably, the best example was delivered by Hirata et al. [24] through nanobeam electron diffraction experiments performed on rapidly quenched $Zr_{66.7}Ni_{33.3}$ MGs in combination with ab initio molecular dynamics simulations. They have shown that sub-nanoscale-ordered regions can produce distinctly symmetric electron diffraction patterns that originate from individual and interconnected atomic clusters as building blocks of MGs.

Cluster-based structural models have improved our understanding of MGs to a great extent; the positive observations are exclusively limited to searching for and finding of cluster units in MGs and occasionally relating the overall composition of MGs to the composition of observed clusters. One definite knowledge that has emerged as the result of cluster-based structural models is, however, that MGs indeed belong to the category of cluster-assembled materials (CAMs)[3]. As such, it should be possible to fabricate metallic glasses by putting appropriate clusters together. This approach, which has been neglected till quiet recently for practical reasons as it will be outlined below, is the subject matter of this chapter.

3. The bottom-up approach to MGs

In order to verify the appositeness of cluster-based structural models for MGs, which suggest that metal clusters are the building blocks of MGs, their fabrication by deposition of select-ed[4] metal clusters to form cluster-assembled metallic glasses (CAMGs) was recently proposed [25]. In the following sections, we will go into some details about what metal clusters are, and how are they synthesized. Despite the fact that CAMGs are still at a very early stage of their development, they make up the core of this chapter, because they are expected to contribute largely to our understanding of amorphous structure of MGs at the atomic level and also help to decipher the structure–property enigma.

Generation, selection, and deposition of metal clusters are all among the most advanced disciplines of material science. The current state-of-the-art only allows for the fabrication of CAMG samples in form of thin films. This temporary technical limitation, which will probably accompany us for another decade, brings CAMGs very close to thin-film metallic glasses (TFMGs) that also have attracted interest [26].

TFMGs are also fabricated in a bottom-up approach and thus are included in this chapter. However, they will not be at the spot light here, mainly due to the following two reasons: Firstly, in TFMGs, the building blocks cannot be actively altered and controlled as they are always atoms or an undefined distribution of clusters. Consequently, it is not possible to

---

[3] CAMs are materials that are fabricated by assembling atomic clusters i.e. have atomic clusters as their building blocks.

[4] In this context and throughout the text, selection refers to mass-selection; separation of clusters based on their mass.

actively influence the structure of TFMGs at the atomic level. Secondly, the composition and the building blocks of the films cannot be modified *independently*, so that a correlation between the building blocks and the film properties cannot be established.

Nanoglasses are another class of metallic glasses that are closely related to CAMGs. Introduced by Gleiter et al. [21, 27–29], nanoglasses are generated by sputtering or evaporating the material of choice, and subsequently consolidating the formed glassy droplets into a pellet-shaped sample. Here, only a very vague control on the structure and composition of the droplets may be achieved. There are number of published works on nanoglasses, which deal with them in appropriate details [21, 29, 30].

3.1. Cluster-assembled metallic glasses, CAMGs

Building blocks of CAMGs are metal clusters. In this section, we address generation, selection, and deposition of metal clusters to form CAMGs. Metallic clusters can be generated in metal cluster sources, which will be described briefly in Section 3.1.1. The output of a cluster source is a distribution of neutral and charged clusters, and thus, a selection step (Section 3.1.2) is required to pick out the desired clusters before deposition. Finally, the selected clusters should be deposited on to a support material in order to fabricate CAMG, as will be explained in Section 3.1.3. The three main steps of CAMG fabrication are schematically summarized in **Figure 2**.
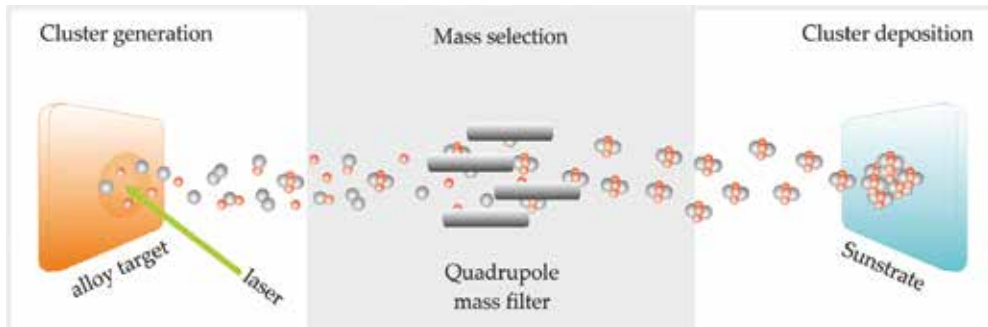
Figure 2. Bottom-up approach to nanofabrication of metallic glasses. Left—mixed metal clusters are generated by laser vaporization of a metal alloy target. Middle—using mass selection, a specific cluster is picked out of the cluster beam. Right—mass-selected clusters are deposited on a support material to form a metallic film.

3.1.1. Generation of metal clusters

The development of cluster sources and subsequently the investigation of clusters, started back in the 1960s with the idea of utilizing the non-equilibrium conditions of an adiabatically expanding vapor, for example, by supersonic expansion[5] of a gas into vacuum [31, 32]. Cluster

---

[5] Supersonic expansion is achieved when a gas expands into vacuum with a Mach number larger than unity.

formation is believed to be due to the supersaturation of rapidly cooled vapor which stimulates homogenous nucleation in the beam [32].

There are various possibilities to produce atomic clusters from bulk materials. Common to almost all these methods is that atoms are firstly ejected from the bulk material and then are brought together to form clusters in the gas phase. A review of all types of cluster sources is beyond the scope of this chapter. Only the laser vaporization cluster source will be introduced here in more detail as this is the only source that has ever been employed for fabrication of CAMGs [33].

The first generation of a laser vaporization cluster source was reported in the early 1980s, at Rice University by Smalley et al. [34]. Many variants of this cluster source have emerged since then. The use of lasers for ablation of material is a very important feature of this kind of cluster source, since it allows for the production of metal vapors of even the most refractory metals such as W and Mo without overheating any part of the apparatus. The supersonic expansion of the cluster beam is the other important feature of this source (also common among other cluster sources). A schematic view of a laser vaporization cluster source is shown in **Figure 3**.
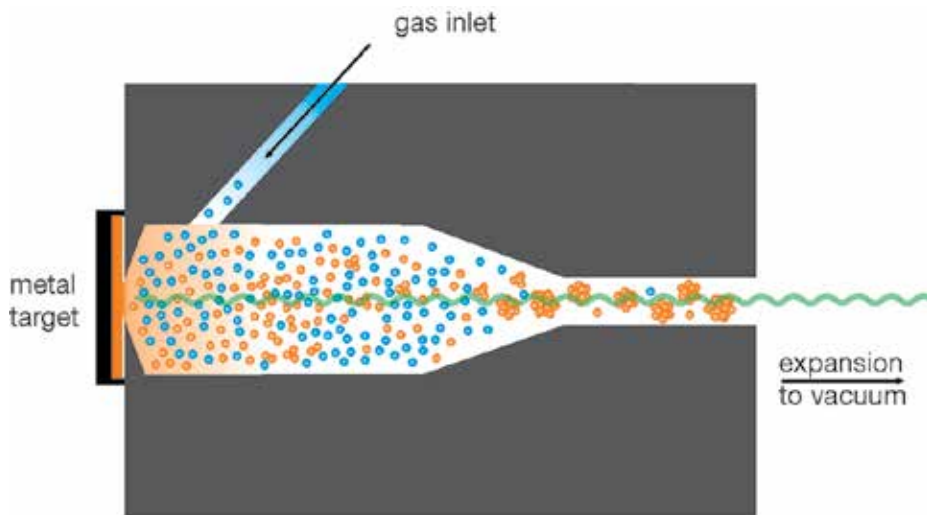
Figure 3. A schematic view of the laser vaporization cluster source is illustrated. A laser beam is focused on to a metal target (either pure metal, or an alloy) in the presence of high pressure of a buffer inert gas. The plume is mixed with the gas and undergoes multiple collisions prior to expansion into vacuum.

The laser vaporization cluster sources produce clusters in the size range from two to several hundreds of atoms per clusters. The vaporized material is cooled by collisions with inert gas atoms which greatly outnumber the ablated metal atoms. The formation of clusters requires three-body collisions between two metal atoms and a rare gas atom (in the case of dimer formation), such that the rare gas atom can take the collision energy away in the form of its kinetic energy and thus make it possible for the metal atoms to stick together without violating the conservation of momentum. This process then needs to be repeated many times to form

larger clusters and that is why higher pressures of the rare gas are required for the generation of larger clusters. The formation of larger clusters can then proceed by either the addition of single atoms to smaller clusters or by merging smaller clusters together.

In most cluster beam facilities, clusters traverse a skimmer after leaving the nozzle. The main function of a skimmer is to collimate the expanded gas mixture that contains the clusters, into a directed cluster beam [35–37]. The cluster beam is then guided further to the mass selection unit before it is deposited.

3.1.2. Cluster selection

The cluster beam that leaves the source contains neutral clusters as well as negatively and positively charged ones. The ion optics used to guide the cluster beam is set to guide either the positive or the negative ions, but it cannot influence the neutral particles. For instance, if negatively charged ions are excluded from the cluster beam through the ion optics, the cluster beam will consist of positively charge ions that are actively guided and neutral clusters that fly in the same direction. In order to exclude the neutrals from the beam, it is common practice to include an electrostatic bender to deflect the charged cluster beam while the neutral beam will not be affected. This separation step is a crucial prerequisite for cluster selection as electrical and magnetic mass filters cannot interact with neutral particles and thus are not able to distinguish among different neutral clusters.

After exiting the deflector, the beam of positively charged clusters is further guided to a mass filter, commonly a quadruple mass spectrometer, which combines DC and radio frequency AC voltages to select a specific cluster mass from the cluster beam. This is the selection step where a single cluster mass or a collection of masses are selected for deposition. The selection criterion of a quadruple mass spectrometer is the mass-to-charge ratio of the clusters; the voltages can be set to make the trajectories of clusters that are heavier or lighter than a set mass instable and thus exclude them from the cluster beam. This selects only those clusters that have a mass within the set mass window while discarding all the others. The width of the mass window can be controlled, and thus, the mass resolution of the device can be adjusted. In general, the mass resolution is set to be just high enough to separate adjacent masses since the transmission of mass filters decreases with increased mass resolution.

The intensity of a cluster beam is commonly evaluated by measuring the current that is caused by charged clusters in the beam. To this end, a Faraday cup[6] or alternatively a metal plate is used to collect the clusters and the current flowing from the collector to ground upon arrival of clusters is measured over time. The performance of a cluster source can be determined from its cluster distribution by recording a mass spectrum. **Figure 4** presents mass spectra for pure Ag and CuZr alloy clusters generated by a laser vaporization cluster source. The number of clusters in the cluster beam can be deduced from the measured current, dividing the cluster beam current by the elementary charge will give the number of singly charged clusters that have been detected over 1s. For instance, a cluster current of 160 pA translates into $\sim 10^9$ clusters

---

[6] Named after Michael Faraday, a Faraday cup is an electrically conductive cup-shaped plate , which is used to collect charged particles under vacuum conditions.

in 1s. For a laser vaporization source with a repetition rate of 100 Hz (100 laser pulses in a second), this means 10 million clusters in each single laser pulse. Although these numbers may sound large, much higher cluster currents are required for deposition purposes, as will be explained in the next section.
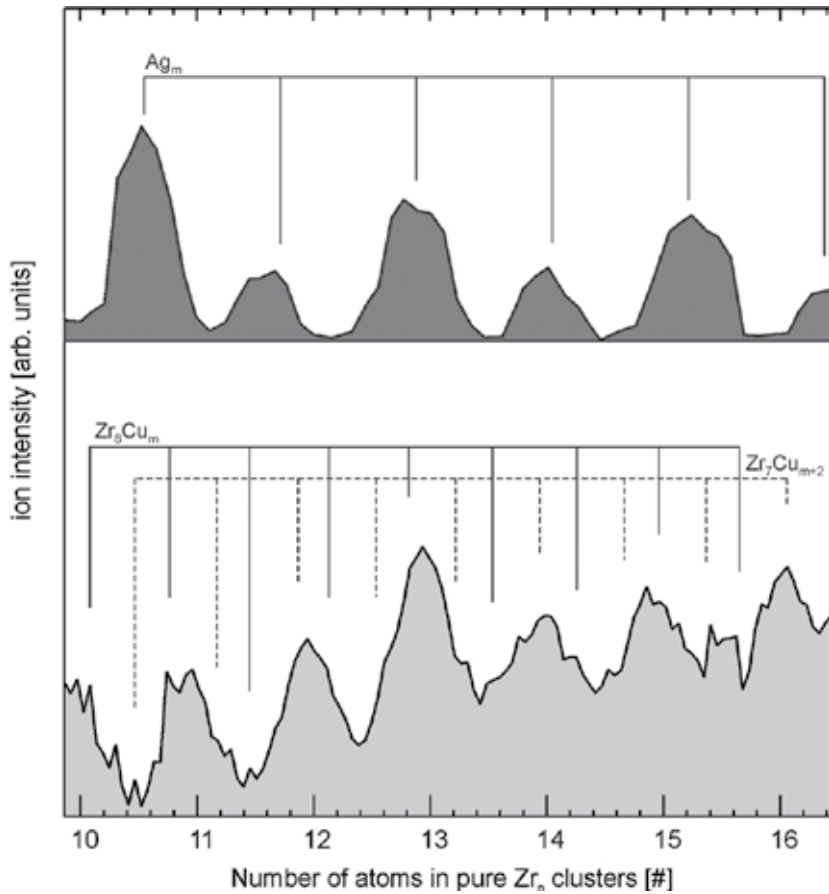
Figure 4. Mass spectra of pure silver clusters (top) and mixed CuZr cluster (bottom) generated by a laser vaporization cluster source are shown. The mass resolution of the quadrupole mass filter is identical for both cases. While in case of silver clusters, the ion peaks are clearly separated, for CuZr clusters peaks cannot be resolved due to the overlap between the masses of mixed clusters plus the fact that Zr with four and Cu with two naturally stable isotopes further broaden the spectrum. In the top, Ag_m^+ clusters[7] with m = 9–14 are observed. The higher intensity of clusters with odd number of atoms is due to their higher stability based on their electronic structure. Such odd-even stability oscillation is common to 1s metals. In the bottom, mixed $Zr_nCu_m^+$ clusters of various compositions are observed while the spectrum is dominated by pure Zr clusters. Two series of $Zr_nCu_m^+$, (m = 3–11) clusters are assigned. The Zr_{13}^+ cluster peak is clearly more intense than other clusters in the mass spectrum. Here, the geometry of the icosahedral clusters with 13 atoms is the stabilizing factor.

---

[7] Notation of clusters: Ag_m indicates a clusters consisting of m Ag atoms; Ag_5 indicates a cluster made out of 5 Ag atoms. In the same way, Zr_7Cu_6 indicates a cluster made out of 7 Zr and 6 Cu atoms.
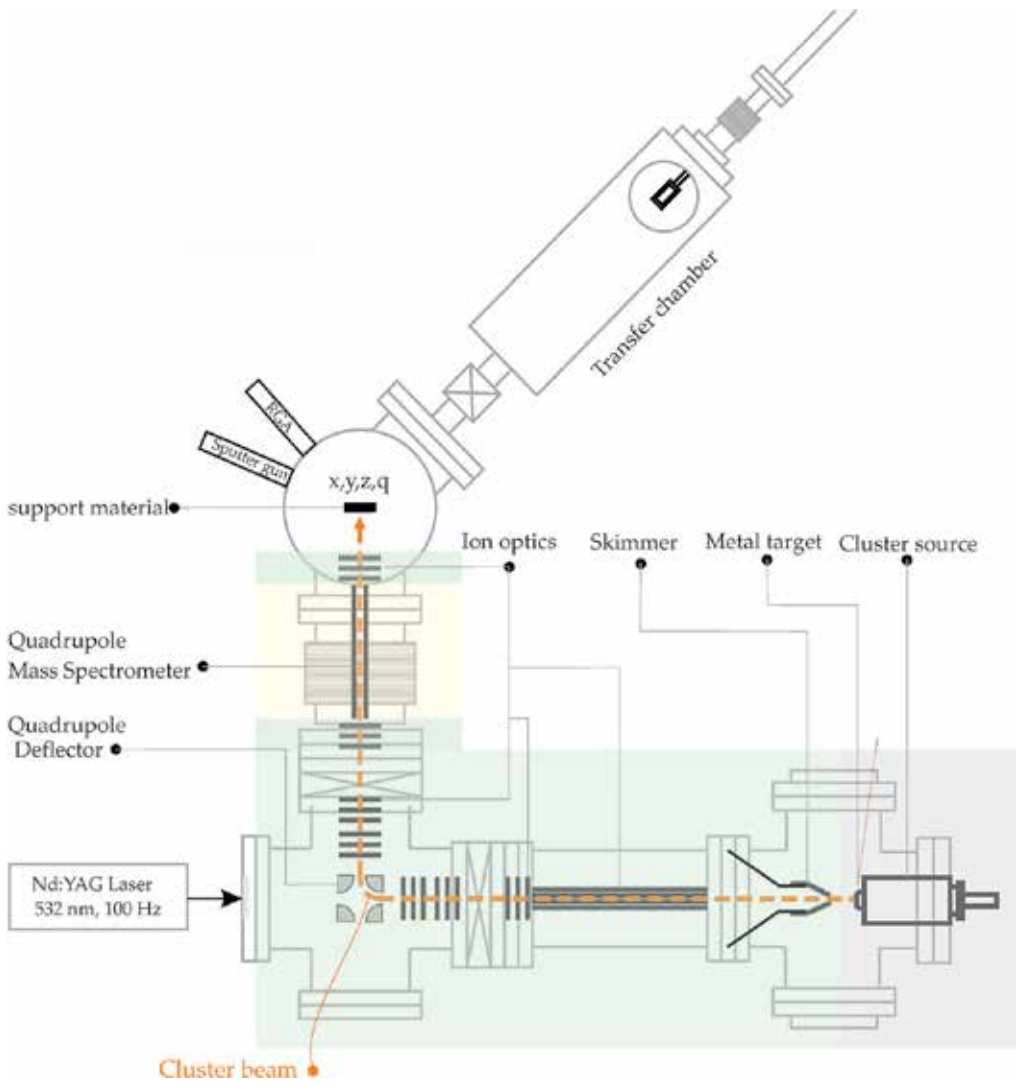
3.1.3. Cluster deposition

After cluster selection, the selected clusters should be deposited onto a support material. Collision with surface may lead to fragmentation of the clusters and render the selection step obsolete. Accordingly, special care should be taken to achieve *soft-landing* conditions when depositing clusters. The material used as support is, therefore, very important. If a conductive support material is used, soft-landing can be easily achieved by applying a voltage to the support to slow down the arriving ions to kinetic energies lower than 0.5 eV per atom (lower than 2 eV for a cluster consisting of 4 atoms or lower than 5 eV for a cluster consisting of 10 atoms and so on). If on the other hand a non-conductive material is used, no adjusting voltage can be applied and the energy of the ion beam should be adjusted by tweaking the ion optics so that the kinetic energies of the ions are low enough to guarantee soft-landing.

Another issue regarding the conductivity of the support material is related to the charge of the clusters. As discussed in Section 3.1.2, clusters are selected based on their mass to charge ratio and thus only charged clusters are suited for mass selection. While the ions will lose their charge once deposited onto a conductive surface, they will keep or only partially lose their charge while in contact with an insulator surface. Consequently, a neutralization mechanism is required to avoid interruption in deposition due to electrostatic repulsion. Due to this effect, almost exclusively positively charged clusters are used for deposition purposes, since they can be neutralized by an electron beam, whereas a proton beam would be required for neutralization of negatively charged clusters.

The other aspect regarding the choice of the support material is its atomic structure, that is, whether it is crystalline or amorphous. Amorphous supports are preferred because they will not provide periodic nucleation cites and thus will not promote the rearrangement of clusters and crystallization of the film. However, as it will be shown in Section 4.1., having an amorphous substrate complicates the structural characterization of CAMGs. The Support material may also be cooled down in order to suppress diffusion of clusters and to enhance the glass forming probability by stopping the clusters from undergoing large geometrical deformations.

As already mentioned in the previous section, high cluster currents are required for deposition of CAMGs. To further illuminate this issue, we may use the following example: A cluster beam can be focused down to a round spot with a diameter of 0.2 cm. Using such a beam to deposit clusters on to a support will result in a coated area of $\sim$0.125 cm^2, the so-called cluster spot. An icosahedral cluster of 55 atoms (one of the largest clusters relevant for MGs) will have a diameter of $\sim$2 nm and thus cover an area of $\sim$12.5 nm^2. Filling a single layer (2-nm-thick film) of the cluster spot with the total area of 0.125 cm^2, with such clusters will demand $\sim$1 $\times$ 10^{12} clusters (for this estimation, the free space between touching spherical clusters was neglected which leads to $\sim$10% overestimation of the number of clusters). In order to get a 1-μm-thick film, at least 500 times more clusters should be deposited. Now assuming a cluster beam current of 160 pA, about 139 h of deposition will be required. Obviously, an enhancement of at least an order of magnitude in cluster beam current is necessary to have a feasible deposition time. Such high cluster beam currents are above what can currently be achieved using state-of-the-art laser vaporization cluster sources, and consequently, the only reported CAMGs to date have used a relatively broad collection of clusters and not an absolutely selected beam of

a single cluster mass. **Figure 5** depicts a cluster deposition facility incorporating all its components.

Figure 5. A schematic view of a cluster deposition facility is depicted. The facility is composed of a laser vaporization cluster source (grey shade), set of ion optics before and after mass selection (green shade), mass selector (yellow shade), and a deposition chamber (unshaded). The deposition chamber is further equipped with a sputter gun for cleaning the surface of the support material prior to deposition, a rest gas analyzer (RGA) for monitoring the quality of the vacuum in this chamber, and a transfer chamber for sample handling purposes such as removing the sample from this facility for transport to other facilities for analysis and characterization. The dashed orange line shows the path of the cluster beam from the cluster source through the ion optics and the mass filter down to the deposition chamber where clusters are soft-landed onto the support material.

3.2. Thin-film metallic glasses TFMGs

Driven to examine the relation between the heat of hole formation and crystallization temperature in amorphous alloys, Nastasi et al. [38] fabricated probably the first thin-film metallic glass in binary systems of Cu–W and Cu–Ta just couple of years after the very first TFMG in La–Au system achieved by solid-state amorphization, where it was also showed that deep eutectics are not a necessary criterion for glass formation in metallic alloys [39]. Currently, TFMGs are commonly fabricated by co-deposition of multiple metals either from an alloy target or multiple targets where the flux of each component can be controlled separately. Zr-based alloys are the most studied systems to date.

Interest in TFMGs is fueled by their distinct properties even compared to counterpart MGs, such as broader glass forming range and higher strength [26, 40–42]. Their broad and continuous glass forming range leads to tunability of their properties by simply adjusting their composition [26]. Their potential application as bio-coatings further increases their relevance. Recently, the corrosion resistance of binary Zr–Ni and Zr–Co TFMGs was investigated [43]. Although TFMG enjoys a great technical significance, they will not play a momentous role in unraveling the structure–property puzzle in MGs.

In the case of TFMGs, the gas phase entities used for fabrication of metallic films are mainly atoms and not atomic clusters. Even if some clusters are available in the deposition beam, up to now no control on the structure and composition of the building blocks could be achieved. Moreover, beside the case of atomic deposition, no information on the properties of the structural units that build up the films has been accessible. In contrast, in the case of CAMGs, atoms are very often deliberately excluded from the deposition beam and only clusters are used to build up a metallic film. The main advantage of CAMGs over TFMGs is that the building blocks can be altered while keeping the composition of the resultant metallic film unchanged.

4. Structure–property relation in CAMGs

In previous sections, CAMGs were introduced and their fabrication using cluster beam technology was described. Here, we will have a closer look on how the study of CAMGs serves to explore the structure–property relation in MGs. Using the example of $Zr_{50}Cu_{50}$ alloy, we will demonstrate this capability. Employing the aforementioned cluster beam technology, a $Zr_{50}Cu_{50}$ film can be fabricated using many different combinations of various clusters as building blocks. The possibility of having the same composition composed of different building blocks is a unique feature of CAMGs. Investigating the properties of these films in comparison with a rapidly quenched MG of the same composition will be a key step in understanding the structure of amorphous alloys and thus the structure–property relation in amorphous metals. On the other hand, comparing the properties of CAMGs with the properties of metal clusters used for their fabrication will reveal the nature of interactions among metal clusters when forming an extended material. Furthermore, looking at the local structure

of CAMGs will unravel the extent of structural deformation that metal cluster undergo as building blocks of CAMGs. **Figure 6** summarizes the different aspects of this approach.
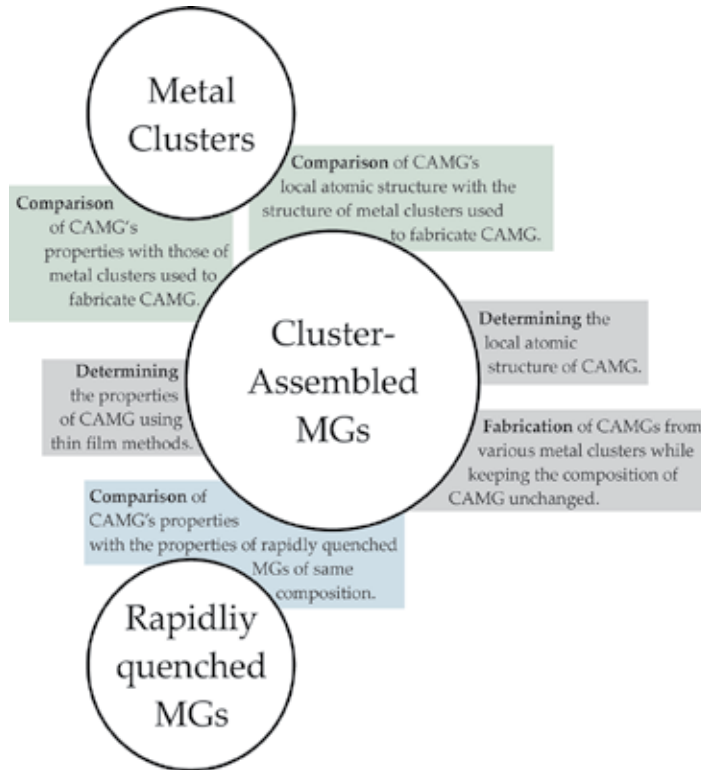
Figure 6. The scientific approach of utilizing CAMGs is presented. After fabrication of CAMGs from specific metal clusters as building blocks, their structure and properties should be determined. On the one hand comparing the properties of CAMGs with the properties of rapidly quenched MGs with identical composition will provide us with information on the structure of rapidly quenched MGs in relation to the metal clusters: the closer the properties of CAMGs and MGs, the closer their structures are! On the other hand, comparing the properties of CAMGs with the properties of their constituent metal clusters will reveal the nature of inter-cluster interactions. Further, by comparing the local atomic structure of CAMGs with the structure of their constituent metal clusters, the degree of deformation and stability of metal clusters while performing as building blocks of MGs can be deduced.

It will not be practicable to consider all the possible combinations. Instead, let us choose some representative combinations to provide a more clear idea about the benefits of CAMGs. Consider the following four scenarios:

1.   the film is fabricated by deposition of equal number of Zr_{13} and Cu_{13} clusters.

2.   the film is fabricated by deposition of equal number of Zr_7Cu_6 and Zr_6Cu_7 clusters.

3.   the film is fabricated by deposition of a set of clusters in the mass range between 400 and 2000 amu, including pure Zr and Cu clusters with more than 4 and 7 atoms, respectively,

and all the mixed clusters with a mass within that range, so that the overall stoichiometry of the film remains is not violated (Atoms and smaller clusters are deliberately excluded).

4. the film is fabricated by deposition of $Zr_{10}Cu_{10}$ clusters.

For all of the above-mentioned hypothetical films, the composition is the same; however, they will possess different atomic structures unless the building blocks are strongly deformed and are highly flexible in sharing atoms among each other. Considering the four different scenarios introduced earlier, only the third scenario (using a set of cluster within a mass range) has been realized experimentally [33] and will be presented in the next section as a proof of principle.

### 4.1. Zr–Cu CAMGs: the first steps

The first attempt to apply cluster beam technology for fabrication of metallic glasses was undertaken recently using binary Zr–Cu alloys [33]. The justification for this choice is threefold. Firstly, Zr–Cu binary system shows high glass forming abilities (GFA) in a wide range of compositions [44–46]. Secondly, a large body of literature on Zr–Cu MGs and TFMGs exists, which proved to be essential in interpretation of the experimental observations [44–59]. And thirdly, cluster generation and cluster selection of mixed metal clusters become more difficult with increasing the number of elements in the cluster, and thus, a binary system is the logical starting point.

Metallic $Zr_{50}Cu_{50}$ films were fabricated by deposition of a set of clusters having masses between 350 and 2000 amu (scenario Nr. 3) on silicate glass substrates, under ultrahigh vacuum, and soft-landing conditions. Films of various thicknesses ranging from 33 to 600 nm were produced. At this stage, the structure and properties of the clusters used to assemble the metallic film are not available. However, all properties of metal clusters can be obtained in state-of-the-art cluster laboratories including their optical, magnetic, chemical, catalytic, electronic, and structural properties. The first question to be answered while fabricating CAMGs for the first time is, however, whether the synthesized film is in an amorphous state at all. Surface X-ray diffraction at the European Synchrotron Radiation Facility (ESRF) was used to answer this question. The details of the experiments and sample preparation are available elsewhere [33]. Here, the most important findings underpinning this bottom-up approach are briefly summarized.

Figure 7 depicts the diffraction pattern of the first cluster-assembled Zr–Cu MG. Despite the interference caused by the broad diffraction band of the silicate glass support, a clear halo peak, which corresponds to a scattering vector of 27.43 nm^{-1}, is observed in excellent agreement with literature values for $Zr_{50}Cu_{50}$ MGs determined from high energy XRD, neutron diffraction, and extended X-ray absorption fine structure (EXAFS) spectroscopy [60]. Accordingly, it could be unambiguously concluded that the fabricated cluster-assembled metallic film is in a glassy state. This observation alone is sufficient to prove the practical feasibility of employing cluster beam technology to form CAMGs.

The good agreement between the observed scattering vector and the literature value may suggest that the structure of the Zr–Cu CAMG is very close to that of rapidly quenched samples. However, it should be noted that the position of the first XRD halo is not very sensitive

to the atomic structure of amorphous metals [61]. In fact, there is almost no difference in peak position for amorphous solids and their corresponding liquids.
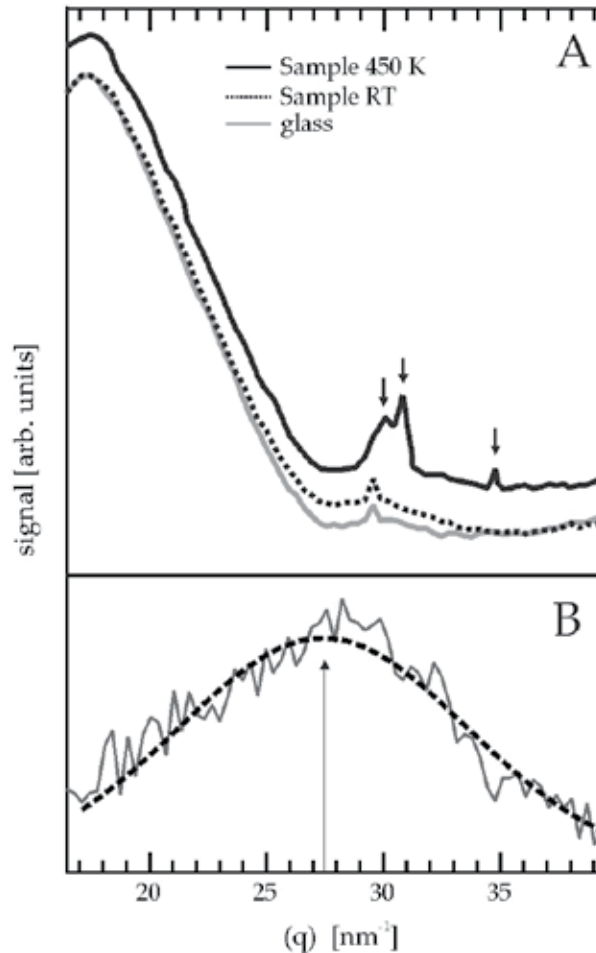
Figure 7. (A) Diffraction patterns of borosilicate glass (solid grey line), cluster-assembled film at room temperature (dashed line), and cluster-assembled film after annealing at 450 K (solid black line) are shown. The arrows indicate the position of the peaks that emerge as a result of annealing. (B) By subtracting the glass signal from the signal recorded for cluster-assembled film, a halo peak is observed that can be fitted by a Gaussian (dashed line). The position of the peak in scattering vector is in excellent agreement with literature values for Zr–Cu MGs of the same composition.

Crystallization temperature, T_x, is a more sensitive probe for the structure. As shown in **Figure 7**, annealing the Zr–Cu CAMG at 450 K for 580 s leads to emergence of sharp crystalline peaks in the diffraction pattern that were not there prior to heat treatment. These diffraction peaks belong to fcc Cu and bcc CuZr phases [33]. The crystallization temperature of Zr–Cu MGs is much higher than 450 K (about 200–300 K higher), which points to the structural

difference between rapidly quenched samples and the glassy film fabricated from metal clusters. A reasonable explanation for the lower T_x of Zr–Cu CAMG under discussion could be based on an increased degree of structural disorder caused by the diversity of metal clusters used to fabricate the film. In Fact, lowering the degree of short-range order is known to lead to the decrease of T_x in glasses [62].

Although the existence of an amorphous $Zr_{50}Cu_{50}$ phase in the fabricated CAMG could be confirmed, the broad range of metal clusters used to produce the amorphous film detains any detailed analysis of the relation between the structure of the film and its constituent building blocks. The example provides a very promising first step in a rather long journey of mostly unforeseeable challenges. Some of the upcoming challenges, however, can be expected, and a number of research groups are working on solving them. The most immediate next steps that have to be (are being) taken in this road are briefly listed in the next section.

4.2. The next steps

Having demonstrated the feasibility of CAMG fabrication using a diverse set of clusters in the Zr–Cu binary system, and the next steps can be taken in three directions of different nature. The first and probably the most important technical issue is the improvement of cluster sources. As described in Section 3.1.3, much higher cluster currents are needed if specific single clusters should be picked out for the deposition of designed CAMGs. Since the cluster science community is continuously engaged in enhancing the performance of the cluster sources, we strongly anticipate that this and other technical issues will be resolved in the near future.

The second communicational issue is the lack of information on clusters relevant for MGs. Scientists working on MGs and metal clusters have not been in any close contact and the information flow between these two fields has been suffering. Yet there is more than enough motivation from both fronts to come together and hopefully put an immediate end to this disconnection. On the one hand, cluster science community is highly interested in understanding cluster–cluster interactions and expanding the borders of the cluster science to more complex clusters. Further, departure from mainly purely fundamental science and moving toward real application by developing cluster-assembled materials (CAMs) has been a long-term goal of cluster scientists. On the other hand, the vision of getting to an atomic structural model which can be verified through CAMGs, and eventually solving the long standing structure–property puzzle has already triggered enthusiastic activities among material scientists. Although not many individuals have been active across the borders of the two fields, an enthusiastic collective interest that has been missing in the past is currently emerging.

The third issue is related to the handling of CAMGs and their characterization. Currently, none of the cluster deposition facilities around the world and the equipment for thin film and MG characterizations are in the vicinity of each other. This requires complicated sample handling endeavors, which are not always compatible with the metastable state of CAMGs. For instance, in the case of the CAMG treated in Section 4.1, the sample transfer from the cluster deposition facility to the apparatus where its structure was studied has been a challenge, which could have been fully avoided by having a cluster deposition facility present at ESRF. We consider this issue less critical because we believe as soon as the other two issues are resolved (even

partly), the interdisciplinary collaborations will naturally lead to emergence of (many) such laboratories.

Author details

Aras Kartouzian[1*] and Jerzy Antonowicz[2]

*Address all correspondence to: aras.kartouzian@mytum.de

1 Department of Physical Chemistry, Technical University of Munich, Garching, Germany

2 Faculty of Physics, Warsaw University of Technology, Warsaw, Poland

References

[1] W. Klement, R. H. Willens and P. Duwez, Non-crystalline structure in solidified gold–silicon alloys, *Nature*, 1960;187:869–870. doi:10.1038/187869b0

[2] T. R. Anantharaman, *Metallic glasses: Production, properties and applications*. Trans Tech Publication, 1984

[3] Y. Waseda and K. T. Aust, Corrosion behaviour of metallic glasses, *Journal of Materials Science*, 1981;16:2337–2359. doi:10.1007/BF01113569

[4] X. Guogiang, Q. Fengxiang and Z. Shengli, Recent progress in Ti-based metallic glasses for application as biomaterials, *Materials Transactions*, 2013;54:1314–23. doi:10.2320/matertrans.MF201315

[5] M. D. Demetriou, M. E. Launey, G. Garrett, et al., A damage-tolerant glass, *Nature Materials*, 2011;10:123–128. doi:10.1038/nmat2930

[6] J. D. Bernal, Geometry of the structure of monatomic liquids, *Nature*, 1960;185:68–70. doi:10.1038/185068a0

[7] J. D. Bernal and J. Mason, Co-ordination of randomly packed spheres, *Nature*, 1960;188:910–911. doi:10.1038/188910a0

[8] A. J. Drehman and A. L. Greer, Kinetics of crystal nucleation and growth in pd40ni40p20 glass, *Acta Metallurgica*, 1984;32:323–332. doi:10.1016/0001-6160(84)90105-6

[9] A. Inoue, Stabilization of metallic supercooled liquid and bulk amorphous alloys, *Acta Materialia*, 2000;48:279–306. doi:10.1016/s1359-6454(99)00300-6

[10] A. Takeuchi and A. Inoue, Classification of bulk metallic glasses by atomic size difference, heat of mixing and period of constituent elements and its application to

characterization of the main alloying element, *Materials Transactions*, 2005;46:2817–2829. doi:10.2320/matertrans.46.2817

[11]   T. Egami, M. Ojha, D. M. Nicholson, et al., Glass formability and the Al–Au system, *Philosophical Magazine*, 2012;92:655–665. doi:10.1080/14786435.2011.630692

[12]   M. Chen, A brief overview of bulk metallic glasses, *NPG Asia Materials*, 2011;3:82–90. doi:10.1038/asiamat.2011.30

[13]   Y. Q. Cheng and E. Ma, Atomic-level structure and structure-property relationship in metallic glasses, *Progress in Materials Science*, 2011;56:379–473. doi:10.1016/j.pmatsci.2010.12.002

[14]   T. Egami, Understanding the properties and structure of metallic glasses at the atomic level, *JOM*, 2010;62:70–75.

[15]   Z. H. Stachurski, On structure and properties of amorphous materials, *Materials*, 2011;4:1564–1598. doi:10.3390/ma4091564

[16]   L. Zhong, J. Wang, H. Sheng, et al., Formation of monatomic metallic glasses through ultrafast liquid quenching, *Nature*, 2014;512:177–180. doi:10.1038/nature13617

[17]   Y. Q. Cheng, E. Ma and H. W. Sheng, Atomic level structure in multicomponent bulk metallic glass, *Physical Review Letters*, 2009;102. doi:10.1103/PhysRevLett.102.245501

[18]   C. Dong, Q. Wang, J. B. Qiang, et al., From clusters to phase diagrams: Composition rules of quasicrystals and bulk metallic glasses, *Journal of Physics D: Applied Physics*, 2007;40:R273–R291. doi:10.1088/0022-3727/40/15/r01

[19]   C. Fan, P. K. Liaw and C. T. Liu, Atomistic model of amorphous materials, *Intermetallics*, 2009;17:86–87. doi:10.1016/j.intermet.2008.09.007

[20]   C. Fan, P. K. Liaw, T. W. Wilson, et al., Structural model for bulk amorphous alloys, *Applied Physics Letters*, 2006;89. doi:10.1063/1.2345276

[21]   H. Gleiter, Nanoglasses: a new kind of noncrystalline materials, *Beilstein Journal of Nanotechnology*, 2013;4:517–533. doi:10.3762/bjnano.4.61

[22]   D. B. Miracle, A structural model for metallic glasses, *Nature Materials*, 2004;3:697–702. doi:10.1038/nmat1219

[23]   W. D. Liu and L. C. Zhang, On the nano/micro-mechanics of metallic glass, *Critical Reviews in Solid State and Materials Sciences*, 2015;40:137–163. doi:10.1080/10408436.2014.973933

[24]   A. Hirata, P. F. Guan, T. Fujita, et al., Direct observation of local atomic order in a metallic glass, *Nature Materials*, 2011;10:28–33. doi:10.1038/nmat2897

[25]   A. Kartouzian, Cluster-assembled metallic glasses, *Nanoscale Research Letters*, 2013;8:339. doi:10.1186/1556-276x-8-339

[26] J. P. Chu, J. S. C. Jang, J. C. Huang, et al., Thin film metallic glasses: Unique properties and potential applications, *Thin Solid Films*, 2012;520:5097–5122. doi:10.1016/j.tsf.2012.03.092

[27] H. Gleiter, Nanocrystalline solids, *Journal of Applied Crystallography*, 1991;24:79–90. doi:10.1107/s0021889890011013

[28] H. Gleiter, Nanostructured materials: state of the art and perspectives, *Nanostructured Materials*, 1995;6:3–14. doi:10.1016/0965-9773(95)00025-9

[29] H. Gleiter, Are there ways to synthesize materials beyond the limits of today?, *Metallurgical and Materials Transactions a-Physical Metallurgy and Materials Science*, 2009;40A:1499–1509. doi:10.1007/s11661-009-9848-7

[30] H. Gleiter, Nanoglasses: a new kind of noncrystalline material and the way to an age of new technologies? *Small*, 2016; n/a–n/a. doi:10.1002/smll.201500899

[31] W. Henkes, Ionisierung und beschleunigung kondensierter molekularstrahlen, *Zeitschrift Fur Naturforschung Part a-Astrophysik Physik Und Physikalische Chemie*, 1961;16:842–842.

[32] E. J. Robbins, R. E. Leckenby and P. Willis, Ionization potentials of clustered sodium atoms, *Advances in Physics*, 1967;16:739–744. doi:10.1080/00018736700101865

[33] A. Kartouzian, J. Antonowicz, T. Lünskens, et al., Toward cluster-assemble metallic glasses, *Materials Express*, 2014; "accepted",

[34] T. G. Dietz, M. A. Duncan, D. E. Powers, et al., Laser production of supersonic metal cluster beams, *Journal of Chemical Physics*, 1981;74:6511–6512. doi:10.1063/1.440991

[35] A. W. Castleman and R. G. Keesee, Metallic-ions and clusters—formation, energetics, and reaction, *Zeitschrift Fur Physik D-Atoms Molecules and Clusters*, 1986;3:167–176.

[36] A. Kartouzian, M. Thaemer, T. Soini, et al., Cavity ring-down spectrometer for measuring the optical response of supported size-selected clusters and surface defects in ultrahigh vacuum, *Journal of Applied Physics*, 2008;104. doi:10.1063/1.3053179

[37] U. Heiz, A. Vayloyan and E. Schumacher, A new cluster source for the generation of binary metal clusters, *Review of Scientific Instruments*, 1997;68:3718–3722. doi:10.1063/1.1148015

[38] M. Nastasi, F. W. Saris, L. S. Hung, et al., Stability of amorphous Cu/Ta and Cu/W alloys, *Journal of Applied Physics*, 1985;58:3052–3058. doi:10.1063/1.335855

[39] R. B. Schwarz and W. L. Johnson, Formation of an amorphous alloy by solid-state reaction of the pure polycrystalline metals, *Physical Review Letters*, 1983;51:415–418.

[40] C. L. Chiang, J. P. Chu, F. X. Liu, et al., A 200 nm thick glass-forming metallic film for fatigue-property enhancements, *Applied Physics Letters*, 2006;88. doi:10.1063/1.2189917

[41] J. P. Chu, C. M. Lee, R. T. Huang, et al., Zr-based glass-forming film for fatigue-property improvements of 316l stainless steel: annealing effects, *Surface & Coatings Technology*, 2011;205:4030–4034. doi:10.1016/j.surfcoat.2011.02.040

[42] F. X. Liu, P. K. Liaw, W. H. Jiang, et al., Fatigue-resistance enhancements by glass-forming metallic films, *Materials Science and Engineering a-Structural Materials Properties Microstructure and Processing*, 2007;468:246–252. doi:10.1016/j.msea.2006.09.099

[43] M. Apreutesei, C. Boissy, N. Mary, et al., Binary Zr–Ni/Co metallic glass films: role of the structural state on their durability, *Acta Materialia*, 2015;89:305–314. doi:10.1016/j.actamat.2015.01.056

[44] M. B. Tang, D. Q. Zhao, M. X. Pan, et al., Binary Cu–Zr bulk metallic glasses, *Chinese Physics Letters*, 2004;21:901–903.

[45] D. Wang, Y. Li, B. B. Sun, et al., Bulk metallic glass formation in the binary Cu–Zr system, *Applied Physics Letters*, 2004;84:4029–4031. doi:10.1063/1.1751219

[46] O. J. Kwon, Y. C. Kim, K. B. Kim, et al., Formation of amorphous phase in the binary Cu–Zr alloy system, *Metals and Materials International*, 2006;12:207–212.

[47] J. Antonowicz, A. Pietnoczka, T. Drobiazg, et al., Icosahedral order in Cu–Zr amorphous alloys studied by means of X-ray absorption fine structure and molecular dynamics simulations, *Philosophical Magazine*, 2012;92:1865–1875. doi:10.1080/14786435.2012.659008

[48] J. Antonowicz, A. Pietnoczka, W. Zalewski, et al., Local atomic structure of Zr–Cu and Zr–Cu–Al amorphous alloys investigated by exafs method, *Journal of Alloys and Compounds*, 2011;509:S34–S37. doi:10.1016/j.jallcom.2010.10.105

[49] K. Georgarakis, A. R. Yavari, D. V. Louzguine-Luzgin, et al., Atomic structure of Zr–Cu glassy alloys and detection of deviations from ideal solution behavior with al addition by X-ray diffraction using synchrotron light in transmission, *Applied Physics Letters*, 2009;94. doi:10.1063/1.3136428

[50] G. A. Almyras, C. E. Lekka, N. Mattern, et al., On the microstructure of the Cu(65)Zr(35) and Cu(35)Zr(65) metallic glasses, *Scripta Materialia*, 2010;62:33–36. doi:10.1016/j.scriptamat.2009.09.019

[51] A. E. Lagogianni, G. Almyras, C. E. Lekka, et al., Structural characteristics of Cu(x)Zr(100?x) metallic glasses by molecular dynamics simulations, *Journal of Alloys and Compounds*, 2009;483:658–661. doi:10.1016/j.jallcom.2008.07.211

[52] A. E. Lagogianni, D. G. Papageorgiou and G. A. Evangelakis, Surface properties of the Cu50Zr50 metallic glass decorated with icosahedral CuxZr100–x (0 < x < 100) clusters by molecular dynamics simulations, *Computational Materials Science*, 2012;54:145–149. doi:10.1016/j.commatsci.2011.10.004

[53] C. E. Lekka, Cu–Zr and Cu–Zr–Al clusters: bonding characteristics and mechanical properties, *Journal of Alloys and Compounds*, 2010;504:Supplement 1:S190–S193. doi: 10.1016/j.jallcom.2010.02.067

[54] M. Li, C. Z. Wang, S. G. Hao, et al., Structural heterogeneity and medium-range order in Zr(x)Cu(100–x) metallic glasses, *Physical Review B*, 2009;80. doi:10.1103/PhysRevB. 80.184201

[55] X. D. Wang, S. Yin, Q. P. Cao, et al., Atomic structure of binary Cu(64.5)Zr(35.5) bulk metallic glass, *Applied Physics Letters*, 2008;92. doi:10.1063/1.2828694

[56] D. H. Xu, B. Lohwongwatana, G. Duan, et al., Bulk metallic glass formation in binary Cu-rich alloy series—Cu100–x Zr x (x = 34, 36, 38.2, 40 at.%) and mechanical properties of bulk Cu64Zr36 glass, *Acta Materialia*, 2004;52:2621–2624. doi:10.1016/j.actamat. 2004.02.009

[57] L. Yang, S. Yin, X. D. Wang, et al., Atomic structure in Zr70Ni30 metallic glass, *Journal of Applied Physics*, 2007;102. doi:10.1063/1.2798386

[58] Y. Zhang, N. Mattern and J. Eckert, Atomic structure and transport properties of Cu(50)Zr(45)Al(5) metallic liquids and glasses: molecular dynamics simulations, *Journal of Applied Physics*, 2011;110. doi:10.1063/1.3658252

[59] Y. Zhang, N. Mattern and J. Eckert, Understanding the relationship between atomic structures and transport properties in (Cu0.5Zr0.5)(100–x)Al–x (≤10) glass forming liquids: molecular dynamics simulations, *Journal of Alloys and Compounds*, 2012;514:141–149. doi:10.1016/j.jallcom.2011.11.034

[60] N. Mattern, P. Jovari, I. Kaban, et al., Short-range order of Cu–Zr metallic glasses, *Journal of Alloys and Compounds*, 2009;485:163–169. doi:10.1016/j.jallcom.2009.05.111

[61] Y. Waseda, H. Okazaki and T. Masumoto, Current views on structure and crystallization of metallic glasses, *Journal of Materials Science*, 1977;12:1927–1949. doi:10.1007/ bf00561964

[62] T. Minemura, J. J. Vandenbroek and J. L. C. Daams, Formation and thermal-stability of amorphous Cu–Zr thin-films deposited by coevaporation, *Journal of Applied Physics*, 1988;63:4426–4430. doi:10.1063/1.340188

Structural Features and Properties

Structural and Dynamical Properties of Metallic Glassy Films

Hui Li, Weikang Wu and Kun Zhang

Additional information is available at the end of the chapter

Abstract

In this chapter, a series of molecular dynamics simulations have been carried out to explore structural and dynamical features of monatomic liquid metallic films during rapid cooling. Results show a semi-ordered inhomogeneous morphology containing crystal-like and disordered regions. The icosahedron contributes to nucleation through the synergy with other short-range ordered structures and participates in crystal growth via assimilation, but the pinning effect should be overcome. The second-peak splitting in pair correlation functions is found as the result of a statistical average of crystal-like and disordered structural regions, not just the amorphous structure. The splitting can be viewed as a prototype of crystal-like peaks exhibiting distorted and vestigial features. Besides, we use the parameter $P(a, \tau, \nu)$ for predicting both local structural order and motion propensity. The fraction of crystalline clusters follows a negative power-law scaling with the cooling rate increasing, which is the inverse of $P(a, \tau, \nu)$.

Keywords: molecular dynamics simulation, metallic glass film, structural evolution, dynamical feature, pair correlation function, local icosahedral order

1. Introduction

Ultrathin metallic glassy films with a thickness of one or a few monolayers attract much attention, since they are now available as epitaxial films on insulating substrates and are, therefore, the best model systems for two-dimensional (2D) conduction in metal systems [1]. Disorder is known to play an important role in the phase diagram of the superconductor material at low temperatures and high magnetic fields [2]. Significant effort is currently being invested in attempting to understand theoretically the interplay between disorder and the conductivity in 2D sys-

tems [3–5]. Specifically, in semiconductor field, thinner and thinner disordered films are needed, since the restriction to a thickness of a few monolayers may lead to novel atomic structures and modify the physical and chemical properties dramatically [6–8]. Huang et al. [9] reported the accidental discovery of 2D amorphous silica supported on grapheme. They found that the images of 2D amorphous silica contain both the crystalline and amorphous regions. Lichtenstein et al. [10] studied the interface between a crystalline and amorphous phase of silica film supported by the Ru(0001) substrate. The atomic structure of the topological transition from a crystalline to an amorphous phase in the thin silica film can lead to a better description of the crystal-to-glass and the liquid-to-glass transitions. Although there has been much progress in the understanding of the properties of amorphous materials in three-dimension [11–13], some important questions on the microstructural feature and its forming mechanism of the metallic glassy films have remained unanswered. Therefore, further studies on the atomic structures of the 2D disordered systems and their physical proprieties are necessary [14–16].

This chapter is organized as follows. In Section 2, we describe the modeling and simulation methods. In Section 3, we discuss the structural evolution of liquid metallic nano-film during rapid solidification as well as the effect of cooling rates [17, 18]. In Section 4, we consider the motion propensity distribution to predict both local structural distribution and dynamical signature in metallic nano-films [18]. In Section 5, we study the synergy and pinning effects of the local icosahedral order during freezing [17]. In Section 6, we clarify the origin of the splitting of the second peak in PCFs based on a statistical explanation [19]. Conclusions are provided in Section 7.

2. Models and theoretical methods

Molecular dynamics (MD) simulations were performed using the embedded atom method (EAM) potential [20] supplied in LAMMPS [21]. The pure copper film and the pure cobalt film are studied respectively. For the copper film, 6400 copper atoms were distributed in a $20 \times 20 \times 1$ lattice unit box based on the structure of FCC crystal and the initial box lattice was set to be 3.61 Å. For the cobalt film, the initial configuration consisting of 8640 cobalt atoms was distributed in a $60 \times 36 \times 1$ lattice unit box, in which atoms were arranged in the light of the HCP crystal structure and the box lattice was set to 2.507 Å. Periodic control was exerted on the x- and y-directions of the box, and the z-direction was nonperiodic. Specially, the lower boundary of the simulation box along the z-direction (not refer to atoms) was fixed, while the upper boundary was free. That was to say, a virtual wall was set at the lower edge of the simulation box in the z-direction, which is similar to the substrate in experiment.

The Velocity-Verlet algorithm was used with an MD time step of 1 fs while the temperature was controlled by a Nosé-Hoover thermostat [22]. A well-equilibrated initial system was prepared by gradually heating perfect crystals to melt at a low heating rate and then relaxing the system at 2000 K for 500 ps. Then, the liquid system was quenched to 300 K at different cooling rates. At each cooling rate, the atomic configuration during the quenching process were recorded for further analysis.

## 3. Structural features in liquid metallic nano-films during rapid cooling

Figure 1 shows the potential energy landscape of the liquid copper nano-film at the temperature of 2000 K, which is composed of single-string structures and partial ring structures (we find the ring structure is the icosahedron). We call the icosahedron in our simulations the quasi-two-dimensional icosahedron (Q2D-I) because of one missing vertex atom due to the dimensional limit. Atoms in single-string structures show high potential energy and motion propensity, while Q2D-Is have a high dense packing [23]. Actually, in the melt film, both structures disintegrate and reunite frequently owing to the random collision and energy transfer of high-energy atoms. Besides, ensembles of atoms in different regions of this liquid film exhibit temporarily enhanced or diminished mobility in comparison with the average. Notably, the cooperative motion of single-string structures is dominant in the metallic liquid film, in accordance with that in three-dimensional liquids [23–25].
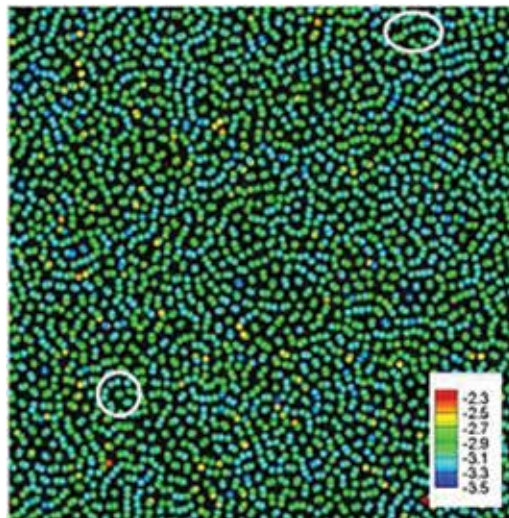
Figure 1. The potential energy landscape of the copper nano-film at 2000 K. The denoted circular region represent the quasi-two-dimensional icosahedron (Q2D-I) and the elliptical one represents the single-string structure.

As the temperature decreases, atoms in the 2D liquid copper tend to gather into clusters. To clarify the liquid-solid transition mechanism in metallic films during the cooling process in the view of an atomic level, the structural evolutions at different cooling rates are investigated as shown in **Figure 2**. At high cooling rates (250 and 500 K/ps), a semi-ordered morphology exhibiting maze-like nano-patterns gradually forms at 300 K. To be specific, at 500 K/ps, compared with the atomic configuration at 2000 K (**Figure 1**), Q2D-Is increases obviously accompanying with the decrease of single-string structures at 1200 K. When the temperature decreases into 900 K, Q2D-Is show continuous increase while the single-string structures begin to arrange side by side, forming crystalline zones. The size scale of crystalline zones in the

simulation is beyond 10–20 Å, meeting the size requirement of MRO (5–20 Å [26]). Thus, the crystalline zone can be considered as the MRO. Notably, these MRO structures are the precursor for nucleuses, whereas Q2D-Is would have barrier effects on nucleation. During the rapid cooling process, Q2D-Is and crystalline zones competite against each other and finally determine the solid structure at 300 K. For example, at 500 K/ps, Q2D-Is play the leading role since crystalline zones are limited due to the high cooling rate, and the system exhibits the most disorder at 300 K. However, when the lower cooling rate (250 K/ps) is performed, crystalline zones tend to be dominant, and finally the film system shows more crystalline MRO characteristics. Although the crystalline MRO gradually forms and develops during rapid cooling, the transition time is so transient that crystalline zones cannot be converted into the crystalline long-range order (CLRO). In contrast, in the case of 10 K/ps (as shown in **Figures 2g–i**), owing to the absence of the icosahedral frustration effect, atoms are mainly arranged in an crystalline order.
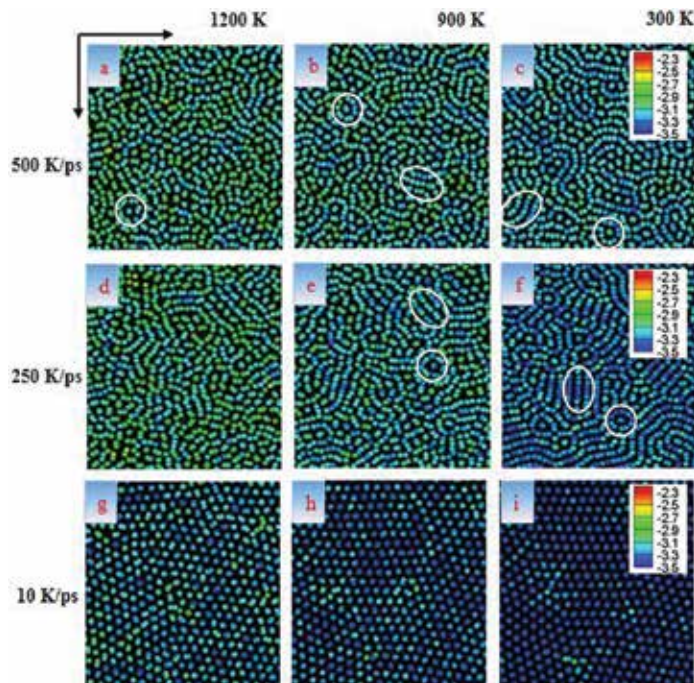

Figure 2. Quenching processes at different temperatures with three different cooling rates. The denoted circular region represent the Q2D-I and the elliptical one represents the crystalline zone.

To further investigate the influence of the cooling rate on the phase transition of metallic films, both the pair correlation functions (PCFs) and the proportion of crystalline zones at different cooling rates are plotted. The crystallization moments can be charaterized by the pressure drops [27], indicating a linear relation between the crystallization moment and the supercooled melt lifetime. However, the faction of crystalline zones in this simulation is determined

through the statistical average of the recorded structural information [28, 29], which is different from Morozov et al.'s method [27]. As shown in **Figure 3a**, the highest cooling rate (500 K/ps) leads to a slight splitting second peak in the PCF curve, while at 250 K/ps, the second peak exhibits obvious splitting and a small shoulder peak appears between the first peak and the second peak. Although the second peak splitting of the PCF curve is usually considered as an important signature of amorphous solids [30], we would rather regard it as the formation of crystalline zones which can be seen as a precursor to the CLRO [31]. At a low cooling rate, such as 10 K/ps, the PCF curve presents typical crystalline features: the splitting characteristic of the PCF second peak becomes more obvious; the small shoulder peak changes into a sharper peak. During the slow cooling process, Q2D-Is disappear while the crystalline MRO integrates together, leading to the CLRO characteristic of the metallic film. **Figure 3b** shows the crystalline fraction change of the above three quehing processes. At the high cooling rate (500 and 250 K/ps), the FCC and HCP structures exhibits a similar amount and shows little changes during the cooling process. However, at 10 K/ps, both the FCC structure and the HCP structure grow fast between 800 and 500 K, and finally FCC structures become the dominant with the faction of more than 50% at 300 K. Such results strongly indicate a non-linear relation between the crystallization fraction and the freezing time, quite different from the Morozov's result in bulk liquid metals [27].
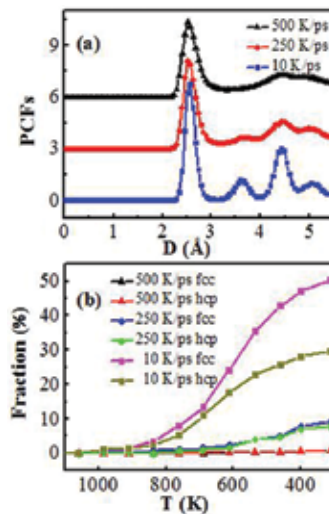
Figure 3. (a) Pair correlation functions (PCFs) at 300 K; (d) the fraction of crystalline zones during the cooling process-es.

4. Power-law scaling of dynamical signatures

In this section, the motion propensity distribution is considered to predict the structural and dynamical features of the liquid copper nano-film. First, the Common Neighbor Analysis

(CNA) and motion propensity are introduced to reveal the relation between crystalline MRO and the subsequent crystallization. The CNA can be used to measure the local crystalline structure around an atom [28, 29, 32], based on the Honeycutt and Andersen bond analysis [33]. Generally, there are five kinds of CNA patterns that LAMMPS recognizes, which are defined as follows: FCC = 1, HCP = 2, BCC = 3, icosahedral = 4, and unknown = 5. The first three indices are all "crystalline". Also note that the CNA calculation in LAMMPS uses the neighbors of an owned atom to find the nearest neighbors of a ghost atom. The local motion propensity of a particle [34, 35] is directly associated with the probability of a particle undergoing a substantial displacement within a short time interval. The motion propensity of a particle p is defined as follows:

$$Q_t(a,\tau,\upsilon)=\frac{1}{N}\sum_P \exp\left(-\frac{\left\|\Delta\vec{r_p}\left(t,t+\tau\right)\right\|^2}{2a^2}\right),$$ (1)

where $\|\Delta\vec{r_p}(t,t+\tau)\|$ is the displacement of the particle p obtained from the quenched configuration between t and $t + \tau$ and a is the length scale over which the motion is probed. Here $a =$ 029, and $\tau = 1000$ fs [36].

Figure 4 shows the CNA pattern and the motion propensity distribution of quecked films at different cooling rates. When the cooling rate is high (500 K/ps), although the barrier effect of Q2D-Is is prominent, several ordered crystalline clusters, such as FCC and HCP structures, still exist at 300 K, indicating that the so-called "full amorphous state" may contain few crystalline SRO structures, namely the crystallite. However, due to the limitation of experimental methods, it is hard to measure the real atomic arrangement within the SRO range. Actually, these crystallites are quite stable, which can be seen from their motion propensity distribution as shown in **Figure 4a**. As the cooling rate reduce, it can be clearly seen that crystallites are rare and discrete initially, but appear at random positions, exhibiting a large structural heterogeneity of the metallic glassy film [37]. At 250 K/ps, more crystallites appear and grow in size at 300 K as shown in **Figure 4b**. A two-step crystallization process is proposed [38]: first, the fluctuations of structure and energy cause the formation of several SRO crystallites which can precursors for the nucleus of crystalline zones; Then, the crystallites expand into surrounding and form crystalline zones. Notably, the FCC or HCP structures do not emerge alone. Instead, the crystalline zone is made up of alternant FCC and HCP structures as presented in the CNA patterns. When the cooling rate is quite low, there would be enough relaxation time for the evolution from HCP structures to FCC structures, similar to Wolde et al.'s viewpoint [39]. For example, at 10 K/ps, the weakening barrier effect of Q2D-Is would result in the ordered atomic arrangement and the formation of nano-polycrystalline structures dominated by FCC structures at 300 K. The appearance of HCP structures is actually just an intermediate state during the crystallization. Besides, it is worth noting that, the complete-disorder region is characterized by high motion propensity, whereas the low motion propensity is related to the crystalline zones. Generally, the basic principle of local propensity $Q_t(a, \tau,$

v) is that the configurational order does not determine the motion of a neighborhood directly but affects the probability of the undergoing motion. Therefore, a theoretical discussion is necessary to verify the possible relation between the structure and dynamics.
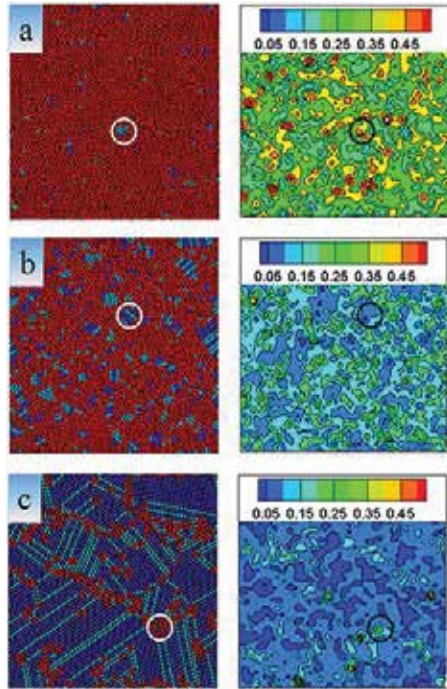
Figure 4. Local atomic ordering (left) and motion propensity (right) of the quenched structures at 300 K with different cooling rates: (a) 500 K/ps; (b) 250 K/ps; (c) 10 K/ps. In the left column, local structures are colored based on the CNA method: blue, FCC; green, HCP; red, disordered structures. In the right column, coloring denotes the motion propensity.

Next, we emphatically studied the relation between the total motion propensity and the crystalline-like structure in the copper film at different cooling rates. Q_{sd} is the standard deviation of the total motion propensity obtained from the quenched configuration at 300 K during a short relaxation time, which may reflect the total fluctuation of the 2D system with respect to time clearly. **Figure 5a** shows the Q_{sd} change as a function of time during a short period $\phi = 1000$ fs, at different cooling rates. For the quenched structure under the highest cooling rates, its Q_{sd} shows the highest dynamical fluctuation during the relaxation, indicating that the system is in the metastable state. In contrast, the dynamical fluctuation at a lower cooling rate exhibits less obvious features, in good accordance with **Figure 4**. This means that the total motion propensity is reliable to measure the system stability. For further exploration, a global measure of the propensity $P(a, \tau, v)$ is calculated by the correlation function $Q_t(a, \tau, v)$:

$$P(a,\tau,v)=N\sum_{p}\left[Q_t(a,\tau,v)-1\right]^2. \tag{2}$$
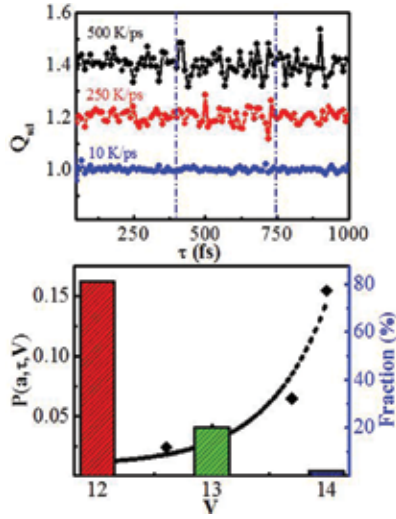
Figure 5. (a) The standard deviation (Q_{sd}) of the total motion propensity and (b) the relationship between the total motion propensity (left) and the fraction of crystalline zones (right) at different cooling rates.

where $v = \log V$, V is the cooling rate. Q_t (a, τ, v) is the motion propensity of a single particle.

Figure 5b shows the relationship between $P(a, \tau, v)$ and the crystalline fraction at 300 K, with respect to the cooling rate. As the cooling rate increases, the fraction of crystalline zones increases and shows an index relationship with the cooling rate. For a low cooling rate ($v <$ 12.5), the copper film exhibits a dominant crystalline characteristic with a relatively low $P(a, \tau, v)$ ($P < 0.025$). However, when the cooling rate increases ($v > 13.8$), Q2D-Is in the metallic film become dominant leading to a high value of $P(a, \tau, v)$ ($P > 0.075$). At a moderate cooling rate, such as $v = 13.8$, a complicated amorphous-crystalline composite forms, with the FCC and HCP structures distributing randomly and exhibiting the crystalline MRO characteristic. Obviously, the fraction of crystalline zones exhibits a negative power-law scaling with the cooling rate, which is the inverse of $P(a, \tau, v)$. This indicates a close relationship between $P(a, \tau, v)$ and the crystalline structure as the cooling rate increases. Such phenomena have not been reported in experimental research, due to some factors associated with multiple scattering and the atomic cluster distortion. To conclude, as a new parameter, $P(a, \tau, v)$ may be a direct consequence of the local structural ordering and the dynamic signature may also result from the local structural ordering.

5. Synergy and pinning effects of local icosahedral order

The above results show that, Q2D-Is appear earlier than crystalline zones during the cooling and can be preserved under the higher cooling rate since the local icosahedral order (LIO) grows with severe undercooling [40]. When crystalline zones emerge, the quantity of Q2D-Is decreases, indicating that Q2D-Is influence the formation of the CMRO.

Figure 6a shows how crystalline zones nucleate through the synergy effect of Q2D-Is. It should be pointed out that, the single-string structure is the basic unit of crystalline zones since it can extend to form the close-packed plane (CPP), similar to the expansion of a graphene piece into a graphite layer. **Figure 6d** reveals the similar topological unit between Q2D-Is and CCPs, which is the structural basis for the assimilation of Q2D-Is. Initially, in the supercooled melt, owing to the strong atomic activity, the SRO structures including the single-string structure and Q2D-Is disintegrate and reunite frequently. During the nucleation, several Q2D-Is are decomposed and integrate into the nucleus with the help of single-string structures, indicating that the LIO should be the raw component of the crystal nucleus. **Figures 6b**, c show the growth of crystalline zones with the assistance of Q2D-Is in the parallel and perpendicular direction to CPPs, respectively. In the parallel growth, when Q2D-Is are contacted by the front of crystalline zones, Q2D-Is would be touched by the CPPs naturally due to their similar topological unit, leading to the gradual assimilation (see **Figure 7** in detail). On the other hand, when the crystalline zones grow in the perpendicular direction and contact a Q2D-I, a suitable connection to the Q2D-I by the surrounding single-string structures or CPPs would assimilate the Q2D-I into the crystalline structures, leading to the perpendicular growth of crystalline zones. Thus, Q2D-Is show the synergy effect during the whole crystallization process. Notably, icosahedra are usually seen as a barrier to crystallization [40], but these results demonstrate that icosahedra can participate the crystal growth through the synergy effect in the 2D system, providing a new view of the correlation between the LIO and crystallization.
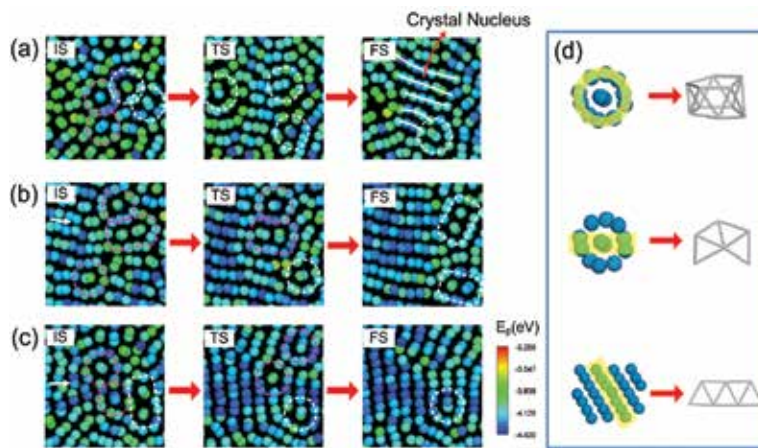

Figure 6. (a) A crystal nucleus forms through the synergy between Q2D-Is and single-string structures. The crystal nucleus is characterized by white solid lines. (b, c) crystalline zones grow through through the assimilation of Q2D-Is in the direction parallel and perpendicular to the close-packed planes (CPPs), respectively. The Q2D-Is are characterized by dotted circles and rounded rectangles. The IS, TS and FS represent the initial state, transition state and final state, respectively. (d) Q2D-Is and CPPs have the similar topological unit. From top to bottom: the side structure of Q2D-Is, longitudinal section of Q2D-Is and CPP.

Next, the detailed assimilation of Q2D-Is by crystalline zones is investigated to explore the mechanism of the synergy effect. **Figure 7a** shows the assimilation process of a Q2D-I by
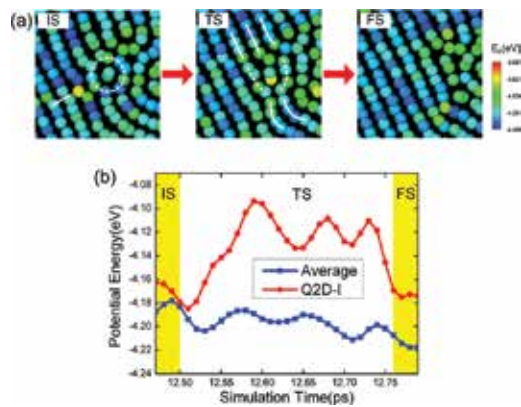
crystalline zones in the direction parallel to CPPs. The contaction between CPPs of crystalline zones and a Q2D-I would result in a half-icosahedral and half-crystalline geometrical frustration, as illustrated in **Figure 7b**. Then, the Q2D-I is gradually assimilated as the geometrical frustration evolves into the crystalline order. According to **Figure 7c**, during the assimilation, the Q2D-I experiences an energy fluctuation accompanying with an obvious oscillation for the average potential energy. In order to measure the energy fluctuation, the root mean squared deviations (RMSDs) [41] are calculated based on the mean value of energy fluctuations in the whole system: $\text{RMSD} = \sqrt{\frac{1}{N} \sum_{i=1}^{N} |\Delta E_i - \overline{\Delta E}|^2}$, where N is the atomic number, ΔE_i is the potential energy fluctuation per atom, $\overline{\Delta E}$ is the average of ΔE_i. The average fluctuation of the system during the process in **Figure 7** is $0.04347915 \pm 0.02080011$ eV (where, $\overline{\Delta E} = 0.04347915$ eV and RMSD = 0.02080011 eV). The fluctuation of Q2D-I just in the range indicates that energy fluctuations lead to the assimilation during the parallel growth. Thus, the Q2D-I can be actually seen as a pin during the assimilation, which needs to be drawn out for the growth of crystalline zones. In another word, Q2D-Is have pinning effects on the crystal growth due to the energy fluctuation. If the pinning effect can be overcome, the assimilation of Q2D-Is would assist the growth of crystalline zones, presenting the synergy effect of the LIO.
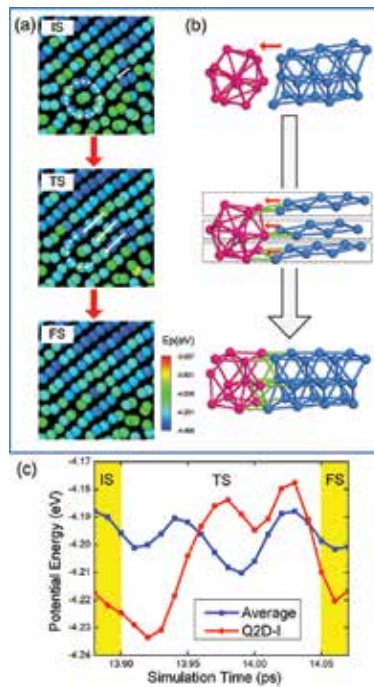

Figure 7. (a) A Q2D-I is assimilated by crystalline zones in the direction parallel to CPPs. White solid arrows show the crystal growth direction. (b) Detailed structural evolution during the assimilation. Three adjacent CPPs naturally connect to the Q2D-I with red solid arrows showing the direction. (c) Potential energy change during the assimilation. The curve of the Q2D-I shows potential energy fluctuations during the assimilation.

Figure 8 shows that the crystalline zone assimilates a Q2D-I in the direction perpendicular to CPPs, which presents more complicated features than that in the parallel growth. However, under closer observation, the assimilation process is very similar to that during a parallel growth. When crystalline zones touch a Q2D-I, the Q2D-I would be gradually connected by the surrounding CPPs, revealing that the crystal growth in the direction perpendicular to CPPs originate from the connection between CPPs and Q2D-Is in the parallel direction. **Figure 8b** presents that the Q2D-I also undergoes a potential energy fluctuation and the average energy oscillates during the assimilation. The potential energy fluctuations during the perpendicular growth indicate the pinning effect of Q2D-Is. The average fluctuation of system is $0.04774295 \pm 0.01739893$ eV (where, $\overline{\Delta E} = 0.04774295$ eV and RMSD $= 0.01739893$ eV), and the Q2D-I's energy fluctuation leads to the leap over the pinning effect during the perpendicular growth. Once the pinning effect succeeds, Q2D-Is might survive as shown in **Figure 9**. In this case, the surrounding CPPs have to bend to cater to the Q2D-I due to the incompatibility between Q2D-Is and the crystals, exhibiting the geometrical frustration. In another word, the Q2D-I is actually a pin, causing the geometrical frustration of the surrounding crystalline order.


Figure 8. (a) A Q2D-Is is assimilated by crystalline zones in the direction perpendicular to CPPs. White solid arrows show the crystal growth direction. The assimilation in (a) is very similar to that in the parallel growth. (b) Potential energy change during the assimilation. The curve of the Q2D-I shows potential energy fluctuations during the assimilation.
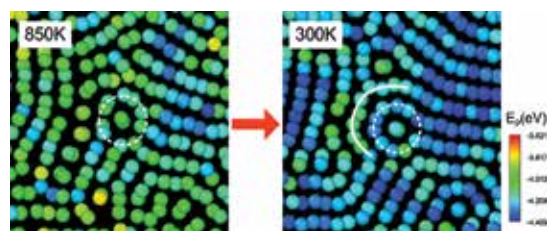
Figure 9. Preservation of a Q2D-I due to the pinning effect. The solid arc line shows the frustrated CPP catering to the Q2D-I.

6. Origin of the second peak splitting in pair correlation functions

A splitting of the second peak in the PCF curve in three-dimensional materials is usually regarded as a characteristic indication of disordered structure forming [42, 43]. However, owing to the lack of one dimensionality as well as the difference of atomic arrangement, the explanation on the second peak of the PCF in 2D systems should be clarified. In addition, previous studies are usually based on the viewpoint of how the clusters connect to each other to form a large supercluster with a specific geometric structure. Due to the fact that the PCF is the statistical average of the atomic configuration, it seems more appropriate to use the statistical methods to interpret the nature of the second peak splitting of the PCF in 2D system. Actually, fewer efforts have focused on the relation between the splitting of the second peak and the crystalline or glass formation of 2D disordered films by statistical average analysis. In order to understand these questions well, this section would provide a statistical explanation on the nature of the splitting of the PCF in the 2D copper system.
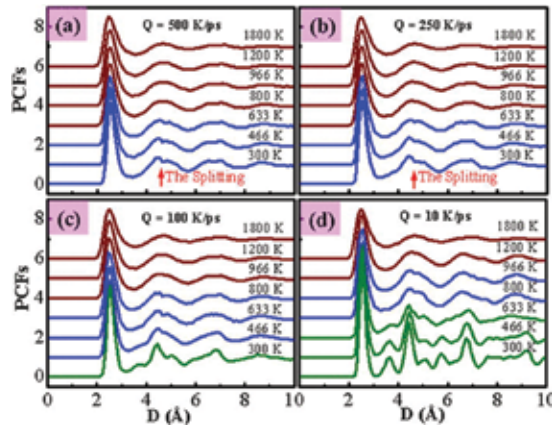

Figure 10. PCF evolutions of the 2D copper at different cooling rates: (a) 500 K/ps; (b) 250 K/ps; (c) 100 K/ps; (d) 10 K/ps. Brown curves represent the PCF without the second peak splitting; Blue curves show the second peak splitting; Green curves show typical crystal peaks.

The PCFs of the 2D copper are shown in **Figure 10**. It is worth noting that the main peak height of the PCFs, which represents the nearest-neighbor shell, increases significantly with the decreasing temperature, and the second peak begins to split. As shown in **Figures 10a, b**, at the cooling rates of $Q1 = 100$ K/ps and $Q2 = 250$ K/ps, the second peak begins to split into two subpeaks at 633 K. Interestingly, a small shoulder peak appears between the first and second peaks at 300 K in **Figure 10b**, which means the short- or medium-range ordered structures form. With the cooling rate decreasing to $Q3 = 100$ K/ps, the splitting emerges at 800 K; moreover, the small shoulder peak between the first and second peaks arises on the left at 300 K with significant height, which indicates that the length of the ordered structure is further extended to a large scale. At the cooling rate of $Q4 = 10$ K/ps, the left shoulder peak arises at 633 K and becomes more prominent than the right subpeak as the temperature decreases,

suggesting that the orientation of the crystalline structure becomes more consistent. It is widely known that the atomic structure of amorphous materials is similar to that of liquid metals, and the fact that the second peak of the PCFs splits into two subpeaks is regarded as a characteristic indication of disordered structures. However, this is not the true case in 2D systems. As shown in **Figures 10c**, **d**, the evolution of the PCFs clearly indicates how the second-peak splitting converts into crystal peaks. For example, as shown in **Figure 10d**, at 800 K, the splitting of the second peak of the PCF appears, but at 633 K, the splitting of the second peak becomes three peaks, and finally these three peaks evolve into three typical crystal peaks at 466 K. Based on this evolution trend, it can be seen that the splitting second-peak has a close relationship with crystal peak, and that the splitting second-peak is the rudiment of the crystal peaks. Our simulations do not support other hypothesis which states that the splitting of the second peak occurs as a result of the connection of some small clusters to a supercluster with a special geometrical structure.
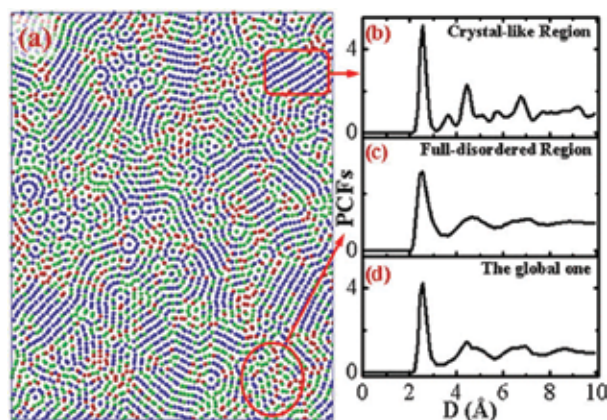

Figure 11. (a) Snapshot of the 2D copper at 300 K with the cooling rate of 250 K/ps. Crystal-like ordering regions are constituted by blue atoms, while other regions show fully disordered ordering. (b–d) PCF curves of different regions: local crystal-like regions, fully disordered regions, the global region, respectively.

In order to further clarify the origin of the splitting of the second peak, the structural config-uration of the 2D copper at 300 K at the cooling rate of $Q2 = 250$ K/ps is supplied in **Figure 11**. It is seen that the overall atomic structure consists of two types of regions: the well-organized region with crystal-like order and the fully disordered region with some packing frustration. Our theoretical results are in good agreement with the experiments by Huang and Lichtenstein [9, 10], which prove our MD simulation result is reliable. It is also worth noting that in the disordered region there are some single strings, arcs, and rings which clearly illustrate the packing frustration of the atoms in the quick cooling process. In fact, **Figure 11a** shows that the structure of the 2D amorphous Cu is the mixture of crystal-like and fully disordered structural regions with a certain percentage. The local PCFs in these two distinct regions differ from one another. As shown in **Figures 10b–d**, the local PCFs of the crystalline region have some crystal-like subpeaks, showing typical crystalline features, while the local PCFs in the fully disordered structural region show no splitting on the second peak. However, the global

PCFs averaged by the overall atomic structures of the two types of regions show a slight splitting in the second peak. It is known that the PCF is the statistical average of the structural configuration, thus, the slight splitting of the global PCF is caused by the combined average results of the crystal-like and fully disordered regions. Moreover, the very similar results are also obtained for the simulations of the 2D cobalt, which indicate the coexistence of crystal-like and fully disordered regions. The splitting of the second peak in 2D systems may not be the signature of the glass formation, but the appearance of both the crystal-like and disordered structures. The splitting second-peak can be viewed as an embryonic form of the crystal peak.

The above results arouse us to further investigate the origin of these two subpeaks in the second-peak splitting. **Figure 12** shows the respective PCF curves of the liquid, amorphous, and ideal crystalline solid Cu. It is known that in ideal FCC crystal there are four nearest coordinated shells, namely, $R1 = 2.55$ Å, $R2 = 3.61$ Å, $R3 = 4.44$ Å, and $R4 = 5.12$ Å. The positions of the first peak in both the liquid and amorphous Cu correspond to the ones in the ideal FCC crystal at $R1 = 2.55$ Å, while the second peaks correspond to three peaks of the ideal FCC crystal at the locations $R2 = 3.61$ Å, $R3 = 4.44$ Å, and $R4 = 5.12$ Å. From the correspondence of the peak positions and the evolution trend, it is concluded that the two subpeaks on the second peak are due to the appearance of a small amount of the short- or medium-range ordered structures.
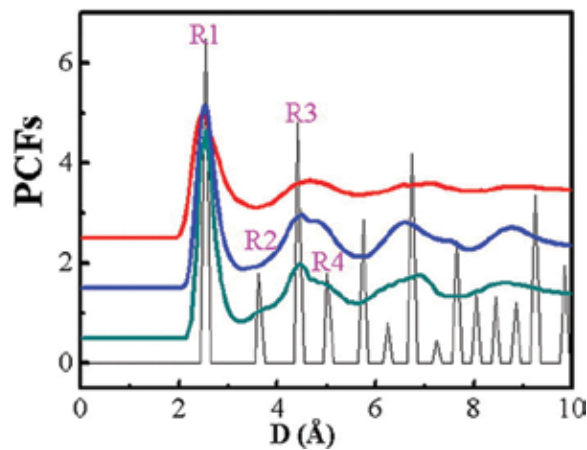
Figure 12. PCF curves of the liquid, amorphous, and ideal crystal copper. Red line: liquid at 1800 K; Blue line: amorphous solid at 300 K ($Q = 400$ K/ps); Green line: amorphous solid at 300 K ($Q = 200$ K/ps); Black line: ideal crystal. $R1$, $R2$, $R3$, and $R4$ represent the ideal FCC peaks.

Figure 13 shows the fraction of the crystal-like regions with the temperature at different cooling rates. If the splitting occurs on the right without the left subpeak, this point is labelled with a blue arrow, while if both the left and right subpeaks appear, it is labelled with a red arrow. According to this rule, **Figure 13** may be divided into three zones. When the fraction of the crystal-like region is less than 18.5%, it belongs to the non-splitting region corresponding to the fully disordered structure in the liquid state. If the fraction of crystal-like region exceeds to 50%, the left shoulder subpeak appears, which indicates it almost becomes the polycrystal-

line structure. However, if the fraction ranges from 18.5 to 50%, it is the mixture of the disordered and crystal-like structural regions, which results in the splitting second peak of the PCF. The disordered structure in 2D may be a simple mixture of crystal-like and fully disordered region, which sheds a new light on the understanding of the atomic structure of the low-dimensional materials.
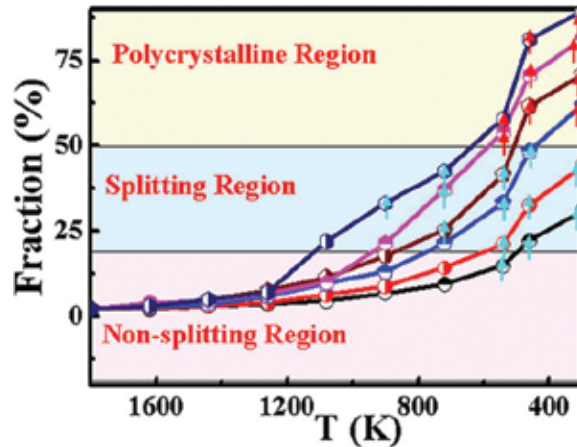
Figure 13. Relationship between the fraction of crystal-like regions and the second peak splitting at different cooling rates: 500 K/ps (blue line), 250 K/ps (red line), 100 K/ps (blue line), 50 K/ps (brown line), 25 K/ps (purple line), 10 K/ps (dark blue line).

7. Conclusion

In summary, we systematically investigate the structural evolution and dynamical properties of glassy metallic films during rapid cooling. Our results have shown several aspects as follows:

- A semi-ordered amorphous morphology with maze-like nano-patterns emerges as the temperature decreases at a high cooling rate. The growth competition between two typical dominating structures, Q2D-Is and crystalline zones, significantly affects the final solid-state structure. The FCC and HCP strutures are alternant in the crystalline zone region, acting as the precursor of CLRO structures.

- The disordered region usually has a high motion propensity distribution, whereas a lower motion propensity corresponds to the crystalline-like order region. Both the local structural distribution and the dynamical signature in metallic nano-films can be predicted by an excellent indicator $P(a, \tau, \nu)$. The region with a lower $P(a, \tau, \nu)$ can accommodate a larger crystallin-like order, and vice versa.

- The LIO has synergy and pinning effects on the freezing behavior of a monatomic liquid film. crystalline zones would gradually form through the synergy of Q2D-Is with other SRO

structures, but the pinning effect should be overcome when crystals grow in both the directions parallel and perpendicular to close-packed planes, consuming energy.

- The origin of the splitting of the second peak in PCFs is a statistical result of the disordered and crystal-like ordered structure with a certain percentage rather than the fully disordered structure. The results show that the shoulder peak on the left side of the second peak is due to the appearance of a small amount of the short-or medium- range ordered structures. The structure in 2D disordered film may be a simple mixture of the crystal-like and disordered structural regions.

Acknowledgements

Author details

Hui Li[*], Weikang Wu and Kun Zhang

*Address all correspondence to: Lihuilmy@hotmail.com

KeyLaboratory for Liquid-Solid Structural Evolution and Processing of Materials, Ministry of Education, Shandong University, Jinan, People's Republic of China

References

[1] Pfennigstorf O., Petkova A., Guenter H.L., Henzler M. Conduction mechanism in ultrathin metallic films. Physical Review B. 2002;65(4):045412.

[2] Wilkin N.K., Jensen H.J. Disorder driven destruction of a phase transition in the vortex system of a superconductor. Physical Review Letters. 1997;79(21):4254.

[3] Crauste O., Couedo F., Bergé L., Marrache C., Dumoulin L. Superconductor-insulator transition in amorphous NbxSi1-x thin films. comparison between thickness, density

of state and microscopic disorder. In: Journal of Physics: Conference Series; IOP Publishing; 2012. p. 022012.

[4] Strongin M., Thompson R.S., Kammerer O.F., Crow J.E. Destruction of superconductivity in disordered near-monolayer films. Physical Review B. 1970;1(3):1078.

[5] Ulman A. Formation and structure of self-assembled monolayers. Chemical Reviews. 1996;96(4):1533–1554.

[6] Cliffe M.J., Dove M.T., Drabold D.A., Goodwin A.L. Structure determination of disordered materials from diffraction data. Physical Review Letters. 2010;104(12): 125501.

[7] Meyer J.C., Girit C.O., Crommie M.F., Zettl A. Imaging and dynamics of light atoms and molecules on graphene. Nature. 2008;454(7202):319–322.

[8] Zheng Z., Wang F., Han Y. Glass transitions in quasi-two-dimensional suspensions of colloidal ellipsoids. Physical Review Letters. 2011;107(6):065702.

[9] Huang P.Y., Kurasch S., Srivastava A., Skakalova V., Kotakoski J., Krasheninnikov A.V., et al. Direct imaging of a two-dimensional silica glass on graphene. Nano Letters. 2012;12(2):1081–1086.

[10] Lichtenstein L., Heyde M., Freund H.-J. Crystalline-vitreous interface in two dimensional silica. Physical Review Letters. 2012;109(10):106101.

[11] Bernal J.D. A geometrical approach to the structure of liquids. Nature. 1959;183(4655): 141–147.

[12] Gaskell P.H. A new structural model for transition metal–metalloid glasses. Nature. 1978;276(5687):484–485.

[13] Levine D., Steinhardt P.J. Quasicrystals: a new class of ordered structures. Physical Review Letters. 1984;53(26):2477.

[14] Huang P.Y., Ruiz-Vargas C.S., van der Zande A.M., Whitney W.S., Levendorf M.P., Kevek J.W., et al. Grains and grain boundaries in single-layer graphene atomic patchwork quilts. Nature. 2011;469(7330):389–392.

[15] Löffler D., Uhlrich J.J., Baron M., Yang B., Yu X., Lichtenstein L., et al. Growth and structure of crystalline silica sheet on Ru (0001). Physical Review Letters. 2010;105(14): 146104.

[16] Yu X., Yang B., Boscoboinik J.A., Shaikhutdinov S., Freund H.-J. Support effects on the atomic structure of ultrathin silica films on metals. Applied Physics Letters. 2012;100(15):151608.

[17] Wu W., Zhang L., Ren H., Zhang K., Li H., He Y. Synergy and pinning effects in a monatomic liquid film in confined conditions. Physical Chemistry Chemical Physics. 2015;17(20):13380–13386.

[18] Zhang K., Jiang Y.Y., Li H., Si P.C., Li Y.F., Yu H.Q. Power-law scaling of dynamical and structural signatures in liquid metallic nano-film. Europhysics Letters. 2011;96(4): 46005.

[19] Zhang K., Li H., Li L., Bian X.F. Why does the second peak of pair correlation functions split in quasi-two-dimensional disordered films?. Applied Physics Letters. 2013;102(7): 071907.

[20] Zhou X.W., Wadley H.N.G., Johnson R.A., Larson D.J., Tabat N., Cerezo A. Atomic scale structure of sputtered metal multilayers. Acta Materialia. 2001;49(19):4005–4015.

[21] Plimpton S. Fast parallel algorithms for short-range molecular dynamics. Journal of Computational Physics. 1995;117(1):1–19.

[22] Nosé S. A unified formulation of the constant temperature molecular dynamics methods. Journal of Chemical Physics. 1984;81(1):511–519.

[23] Berardi C.R., Barros K., Douglas J.F., Losert W. Direct observation of stringlike collective motion in a two-dimensional driven granular fluid. Physical Review E. 2010;81(4):041301.

[24] Donati C., Douglas J.F., Kob W., Plimpton S.J., Poole P.H., Glotzer S.C. Stringlike cooperative motion in a supercooled liquid. Physical Review Letters. 1998;80(11):2338.

[25] Gebremichael Y., Vogel M., Glotzer S.C. Particle dynamics and the development of string-like motion in a simulated monoatomic supercooled liquid. Journal of Chemical Physics. 2004;120(9):4415–4427.

[26] Elliott S.R. Medium-range structural order in covalent amorphous solids. Nature. 1991;354(354):445–452.

[27] Morozov I.V., Kazennov A.M., Bystryi R.G., Norman G.E., Pisarev V.V., Stegailov V.V. Molecular dynamics simulations of the relaxation processes in the condensed matter on GPUs. Computer Physics Communications. 2011;182(9):1974–1978.

[28] Cleveland C.L., Luedtke W.D., Landman U. Melting of gold clusters: icosahedral precursors. Physical Review Letters. 1998;81(10):2036.

[29] Tsuzuki H., Branicio P.S., Rino J.P. Structural characterization of deformed crystals by analysis of common atomic neighborhood. Computer Physics Communications. 2007;177(6):518–523.

[30] Liu X.J., Xu Y., Hui X., Lu Z.P., Li F., Chen G.L., et al. Metallic liquids and glasses: atomic order and global packing. Physical Review Letters. 2010;105(15):155501.

[31] Truskett T.M., Torquato S., Sastry S., Debenedetti P.G., Stillinger F.H. Structural precursor to freezing in the hard-disk and hard-sphere systems. Physical Review E. 1998;58(3):3083.

[32] Faken D., Jónsson H. Systematic analysis of local atomic structure combined with 3D computer graphics. Computational Materials Science. 1994;2(2):279–286.

[33] Honeycutt J.D., Andersen H.C. Molecular dynamics study of melting and freezing of small Lennard-Jones clusters. Journal of Physical Chemistry. 1987;91(19):4950–4963.

[34] Candelier R., Dauchot O., Biroli G. Building blocks of dynamical heterogeneities in dense granular media. Physical Review Letters. 2009;102(8):088001.

[35] Garrahan J.P., Chandler D. Geometrical explanation and scaling of dynamical heterogeneities in glass forming systems. Physical Review Letters. 2002;89(3):035704.

[36] Widmer-Cooper A., Harrowell P. Predicting the long-time dynamic heterogeneity in a supercooled liquid on the basis of short-time heterogeneities. Physical Review Letters. 2006;96(18):185701.

[37] Mizuno H., Yamamoto R. Lifetime of dynamical heterogeneity in a highly supercooled liquid. Physical Review E. 2010;82(3):030501.

[38] Schöpe H.J., Bryant G., van Megen W. Two-step crystallization kinetics in colloidal hard-sphere systems. Physical Review Letters. 2006;96(17):175701.

[39] Ten Wolde P.R., Ruiz-Montero M.J., Frenkel D. Numerical evidence for bcc ordering at the surface of a critical fcc nucleus. Physical Review Letters. 1995;75(14):2714.

[40] Kelton K.F., Lee G.W., Gangopadhyay A.K., Hyers R.W., Rathz T.J., Rogers J.R., et al. First X-ray scattering studies on electrostatically levitated metallic liquids: demonstrated influence of local icosahedral order on the nucleation barrier. Physical Review Letters. 2003;90(19):195504.

[41] Kobayashi K., Salam M.U. Comparing simulated and measured values using mean squared deviation and its components. Agronomy Journal. 2000;92(2):345–352.

[42] Bennett C.H. Serially deposited amorphous aggregates of hard spheres. Journal of Applied Physics. 1972;43(6):2727–2734.

[43] Ma D., Stoica A.D., Wang X.-L. Power-law scaling and fractal nature of medium-range order in metallic glasses. Nature Materials. 2009;8(1):30–34.

Structure of the Metallic Glass and Evolution of Electronical Properties during Glass Transition in Atomic Level

HaiJun Chang

Additional information is available at the end of the chapter

Abstract

Metallic glass (MGs) has many unique properties such as low density, low Young's modulus, and so on. These unique physical and mechanical properties attract much attention on their application in manufacturing production. While, structural properties such as complete absence of the long-range order and most MGs are consist of equal or more than ternary constituent which complex factors make that the atomic level structure of metallic glass still have not well known by researchers. The limited methods and data sets obtained by experiment make the acknowledge in uncovering atomic structure of melt states of alloy, and the supercooled liquid about the alloy is absent as well. These messages are important to improve and increase the understanding of MGs, as we know that glasses are essentially frozen liquid made by quenching of their high-temperature melts. Computer simulation method is an useful tool to obtain structure messages of melt and the supercooled liquid. The static, dynamical properties as a function of temperature can also be investigated by ab initio MD simulation. The atomic level rearrangement consists of both local topological structure change and chemical reordering and evolution of electronic properties of the $Al_{87}Ni_7Nd_6$ and $Ca_{50}Mg_{20}Cu_{30}$ alloy during the glass transition process is investigated, and the discussion of the results is given in this chapter.

Keywords: supercooled liquid, glass transition, microstructure, electronic evolution, metallic glass, atomic structure, electronic properties

1. Introduction

For amorphous metals, the expanding application in manufacturing production makes metallic glass (MGs) attract much attention to uncovering their atomic structure. As a consequence of the complete absence of the long-range order, equal or more than ternary constituent elements and the varying chemical affinity between the constituent elements which complex factors known by researchers. Topological and chemical short-range order is existed in MGs and is the most pronounced structure factor in these amorphous alloys.

Atoms packing from micro-observation view and structural different together with changes by temperature decrease during the glass transition progress are important to explore these interesting properties of MGs. The electronic structure and the bond between paired atoms in amorphous alloy are still little reported.

The limited methods and data sets obtained by experiment make the acknowledge in uncovering atomic structure of melt states, and the supercooled liquid about the alloy is absent as well. These messages are important to obtain useful knowledge such as general structural models and fundamental principles of atom packing and the correlations of thermodynamic, kinetic and mechanical properties with the MG structures.

Computer simulation method is an useful method to obtain messages of melt and the supercooled liquid. The static, dynamical properties as a function of temperature can also be investigated by ab initio MD simulation from the obtain results together with the electronic structure, bond and electronic density of states evolution during the glass transition process [1, 2].

Using the first-principle computer simulation method, the atomic level structure of metallic glass was indicated, which is vital to understanding of the behaviour of these materials. The research was focussed on first-principle molecular dynamic simulation of the rapid solidification process of $Ca_{50}Mg_{20}Cu_{30}$ alloy [1] and the evolution of structural and electronic properties during the glass transition process of Al-Ni-Nd alloy [2].

Some theory means have used to propose the evolution of the structure of this alloy during the glass transition such as HA index method and bond-angle distribution function. The result indicates that the increasing pentagonal bipyramids ordering suppress the formation of the crystal structures during the rapid solidification processes.

Evidence for the existence of covalent bonds is provided by our research, the polyhedral local topological structures together with the chemical short- to medium-range order (SRO) structures play an important role in glass transition and also increase the glass-forming ability of these alloy. The charge density of the alloy was also given.

The static and dynamical properties of $Ca_{50}Mg_{20}Cu_{30}$ alloy and Al-Ni-Nd alloy during the rapid solidification process are investigated using ab initio MD simulations. The results we calculated agree well with the previous report of these MGs.

## 2. Part 1, atomic level structure of metallic glass

Since the unique physical and mechanical properties of the metallic glass, there has been increasing interest in developing and understanding this new family of materials. A number of experimental techniques, such as X-ray diffraction (XRD) and neutron diffraction, have been carried out to understand the structure of the metallic glass as well as modelling methods, which include Reverse Monte Carlo (RMC) and molecular dynamics (MD). These results given by researchers have more attraction and more attention on their application in manufacturing production.

Atomic level structure of metallic glass was investigated using ab initio MD simulations, and the local atomic structures of Ca-Mg-Cu and Al-Ni-Nd amorphous metallic glasses have been investigated by the pair distribution function (PDF) analysis of neutron diffraction data. The pair distribution function (PDF) is a pair correlation function to indicate that the probability of an atom is located at distance r from an average centre atom. PDF is used to characterize the structural properties of liquids and amorphous solids.

The α-β partial PDF is defined in Eq. (1)

$$g_{\alpha\beta}(r) = \frac{L^3}{N_\alpha N_\beta} \left\langle \sum_{i=1}^{N} \frac{n_{i\beta}(r)}{4\pi r^2 \Delta r} \right\rangle \tag{1}$$

where in the system of N atoms, N_α and N_β are the number of atoms of type α and type β, respectively. r is the interatomic distance between two atoms i (of type α) and j (of type β).
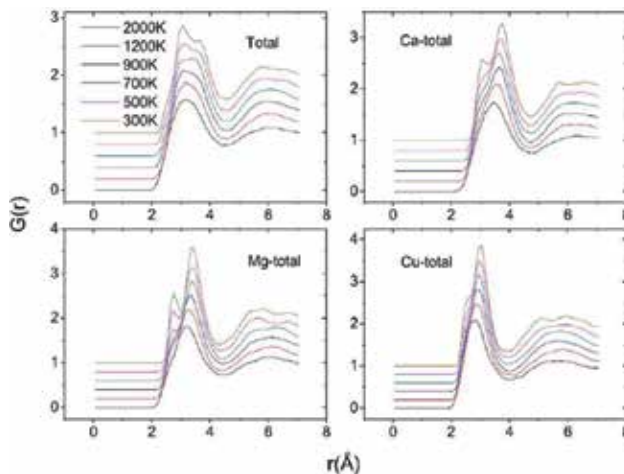
Figure 1. The total paid distribution functions and partial pair distribution functions of the $Ca_{50}Mg_{20}Cu_{30}$ alloy at different temperatures.

It can be seen that the first peak of total PDF of $Ca_{50}Mg_{20}Cu_{30}$ (**Figure 1**) gets higher as the temperature decreases, which indicates that atomic ordering in the first coordination shell increases as the temperature decreases. The first peak of total PDF starts splitting at 900 K. At the lowest temperature, 300 K, a splitting of the first peak into two peaks around 3.05A and 3.65A and a splitting of the second peak are seen. For the PDF of Ca atom, we can find a shoulder which appears at 500 K and becomes more pronounced as the temperature is decreased. This prepeak is located at 3.05A° which is equal to the interatomic distance of Ca-Cu pair and it is believed to originate from increasing interaction of the Ca-Cu atomic pairs. For Mg atom, the prepeak located at 2.75A°, which appears at 700 K, indicates that affinity of Mg and Cu atoms becomes stronger below 700 K. Besides, the shoulder of PDF of Cu atom at 300 K is due to the formation of Cu-Cu atomic pair.
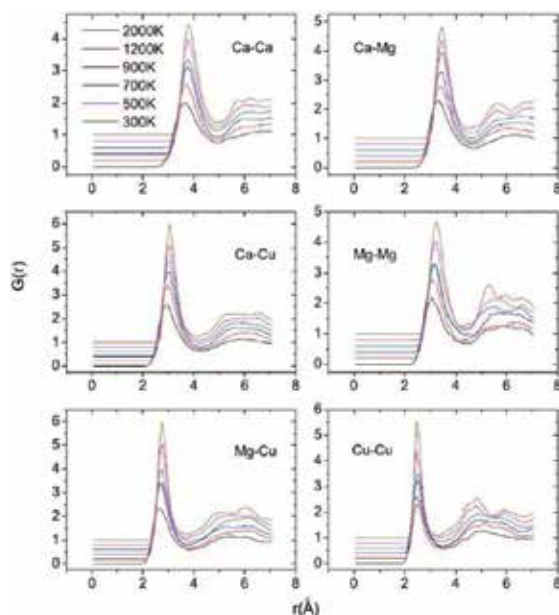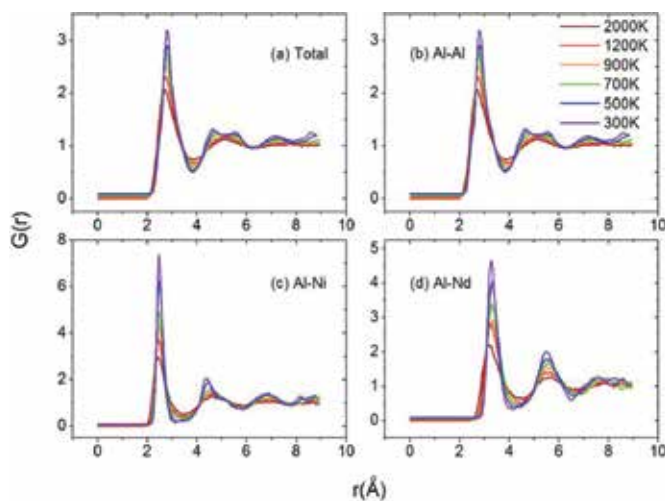

Figure 2. The partial pair distribution functions of Ca-Ca, Ca-Mg, Ca-Cu, Mg-Mg, Mg-Cu and Cu-Cu atomic pairs of the alloy at different temperatures.

The partial pair distribution functions of the different atom pairs such as Ca-Ca Mg-Mg, Mg-Cu and Cu-Cu are shown in **Figure 2**. All of these functions reveal an increase in the height of the first and second peaks with decreasing temperature, which demonstrates the increase of the short to medium range order during the solidification process, while the location of the first peak changes little at the same time. We can distinguish splittings of the second peak of all six partial pair-correlation functions. However, the splittings occur at different temperatures for these functions. For the Ca-Mg and Cu-Cu pairs, the splitting first occurs at 500 K and is well developed at 300 K. While for other pairs, the splittings occur at lower temperature than

500 K (the experimental Tg = 401 K) [3]. It demonstrates that some different substructures in prefer atom pairs have been formed before reaching the final glassy state.

Figure 3 shows the total PDF and partial PDF (Al-Al, Al-Ni and Al-Nd) of $Al_{87}Ni_7Nd_6$ alloy. The peaks about first and second of all the PDFs get higher during the glass transition process, which indicates that short to medium structure orderings of the associated atom increases as the temperature decreases. The increase of Ni atom PDF is obvious, which leads to the sharpness peak of the partial PDF (Ni atom) at 300 K eventually. It determines the compositional and geometrical order became stronger and formed during the glass transition process around Ni atom. Total PDF shows a splitting of the second peak at 500 K, and dislocation of the two well-developed new peaks is around 4.67 and 5.58 Å at 300 K.

Figure 3. The total and partial pair distribution functions of the $Al_{87}Ni_7Nd_6$ alloy at different temperatures. (a) Total, (b) Al-Al, (c) Al-Ni and (d) Al-Nd.

The splitting of the second peak with the different shapes of partial PDFs may caused by the different radii of the atoms in the atomic pairs, which indicate the complex structures of the disorder systems. The partial coordination numbers of Al-Ni and Al-Nd pairs estimated from the DRP model are 10.9 and 16.4 [4]. The CNs of the Al-Nd pair decreases with decreasing temperature, which determines that Al turns to prefer to be near Ni rather than Nd atoms during the glass transition process.

3. Part 2, the evolution of structural properties during the glass transition process

Honeycutt-Andersen (HA) bond-type index is compute to obtain detailed information [5] of the local structure of the $Al_{87}Ni_7Nd_6$ alloy. Three-dimensional image of the local configurations

is given during the solidification process. The HA bond-type index represents the number and properties of common nearest neighbours of atom pair; it can used to analysis the local environment surrounding the atomic pair, which is under consideration. Each H-A bond index is classified by the relation among their neighbours with four indices of integer.

The first integer is 1 if the pair is bonded and the considered atomic pair is closer than cut-off distance or else 2. The common neighbour of the considered atomic pair is defined as the second integer, the number of bonds among common neighbours is the third number and the fourth is used to distinguish the atomic pair if the former three integers are not sufficient.

More than 12 types of the bond pairs are found in the alloy at different temperatures with the HA bond-type index method, which indicate the complex structures of the disorder systems. The variation of seven typical bond pairs of Ca-Mg-Cu alloy is shown in **Figure 4**; whereas the other pairs of 1311, 1422, 1531, 1532 and 1651 types are not shown because they are quite rare and every type of them is <2% in the whole temperature range. It can be seen that 1551 pair has a fraction of 12.5% at 2000 K and increases rapidly with temperature decreasing (41.3% at 300 K). The 1541 does not change much in the whole temperature range; the fraction of 1541 pairs at 300 K is 18.2%. These two pairs that contain five coordinated vertices represent the pentagonal bipyramids. As the melt being quenched, a large quantity of pentagonal bipyramids structures are formed in undercooled and glassy alloy. Moreover, it can be observed that the quantity of 1431 pair, which is the most popular type at 2000 K, decreases as the temperature decreases and the 1441 pair increases about 5% in the supercooled region.
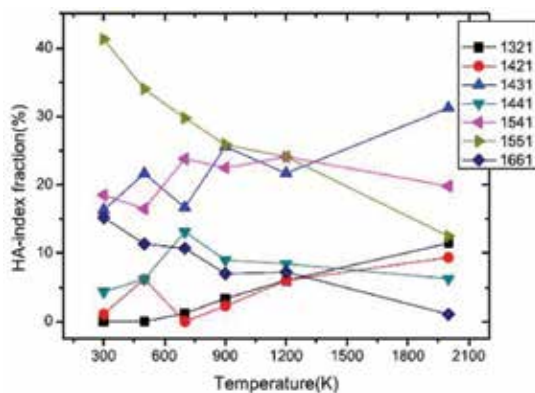

Figure 4. Evolution top seven most populated HA bond-type index in the $Ca_{50}Mg_{20}Cu_{30}$ alloy as a function of temperature.

The population of them, which indicate the fourfold bond structure, is much less than the most prevalent type of 1551 pair. In addition, the 1661 pair, which presents the sixfold bond, increases from 1.04% at 2000 K to 15.22% at 300 K. Furthermore, the 1321 pair with higher energy and larger distortion decreases obviously in the solidification process.

Much information of chemical and topological orderings of the higher order correlations can be provided by the bond-angle distribution function, which is defined about a group of three

atoms. One is defined as a central atom; the other two within a cut-off distance that is deter-
mined by the location of the minimum of PDF are denoted as the side atoms. The two side
atoms together with the central atom define the bond angle. The bond-angle distribution
function can be obtained by statistically summing the bond angles of all the groups of three
atoms.

Two peaks located at about 61.8° and 101.2° at 2000 K of total bond-angle distribution about
$Ca_{50}Mg_{20}Cu_{30}$ alloy (**Figure 5**), and the height of the of the first is higher. Peaks become higher
during the glass transition process. The total bond-angle distribution have two peaks near
60.1°and 106.7 at 300 K. Close packing of three neighbour atoms is suggested by the first peak
at around 60°, and the second peak located near 108° is consist with the pentagon configura-
tions. The shoulder appeared at 300 K at around 145° relates to threefold coordinated atoms.
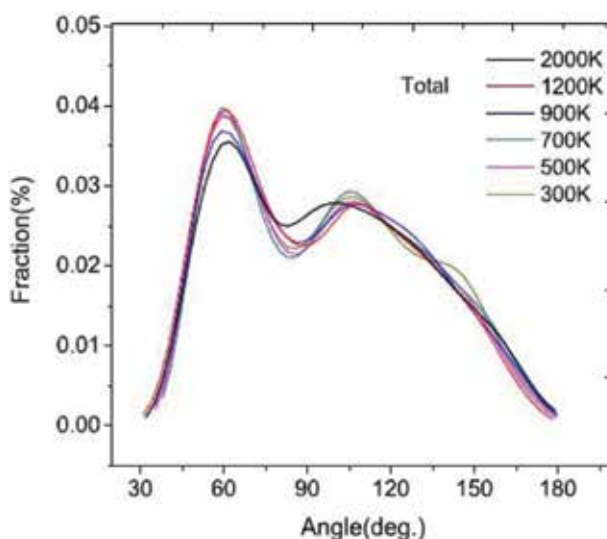
Figure 5. Calculated total bond-angle distribution functions of $Ca_{50}Mg_{20}Cu_{30}$ alloy at different temperatures.

The peaks of all the partial bond-angle distribution function of Ca-Mg-Cu alloy (**Figures 6–8**)
become more pronounced as the temperature decreases, which exhibits that the distribution
of the local structure types around the relevant atoms decreases at lower temperature. For the
bond-angle distribution around Ca atoms at 300 K, predominant angles correspond to 56°, 100°
and 145° can be seen clearly, and the flat peaks located at 58°, 95° and 95° are shown at 2000
K. The N-Mg-N bond-angle distribution functions in the amorphous phase ($T = 300$ K) have a
prominent peak at 60° and 115°, while they present two broad peaks at about 60° and 109° at
2000 K. In addition, the plot of N-Cu-N shows main peaks at 60° and 110° at 2000 K, and the
location of the peaks is at around 65°and 135° at 300 K. The second peak of N-Cu-N shifts to
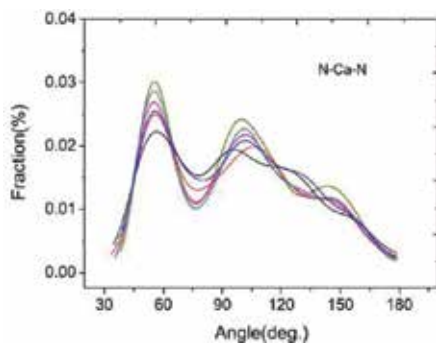large angle during the solidification process, which is more evident than the other peaks.

Figure 6. Calculated partial bond-angle distribution functions of the N-Ca-N (N = Ca, Mg, Cu) at different temperatures.
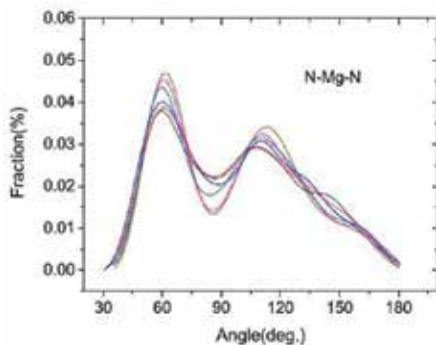

Figure 7. Calculated partial bond-angle distribution functions of the N-Mg-N (N = Ca, Mg, Cu) at different temperatures.
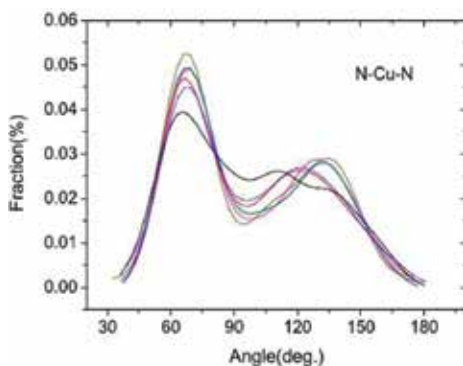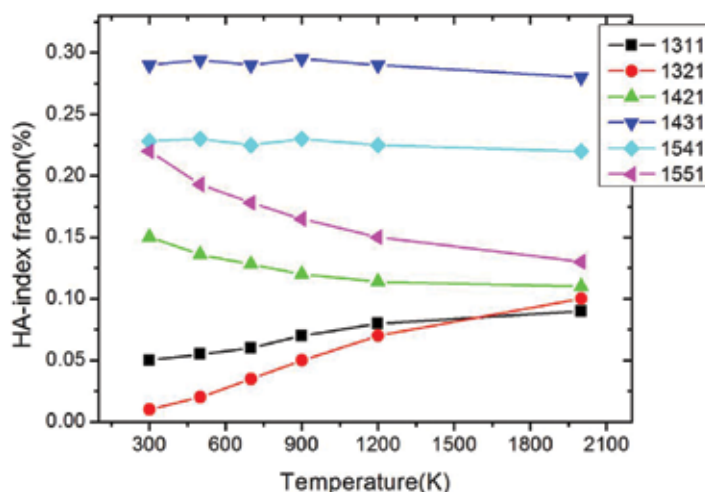

Figure 8. Calculated partial bond-angle distribution functions of the N-Cu-N (N = Ca, Mg, Cu) at different temperatures.

The detailed three-dimensional image information about the evolution of local atomic configuration of the Al-Ni-Nd alloy is obtained using the method of Honeycutt-Andersen (H-A) bond-type index during the glass transition process. The 1431 and 1541 bond pairs are the most two popular types seen from **Figure 9** in the molten alloy liquids, which fraction is 28 and 22%, respectively. The two pairs do not change very much in whole temperature range. Moreover, fraction of 1551 pair is 13% at 2000 K and increases with decreasing temperature rapidly which is 22% at 300 K. The 1541 and 1551 pairs represent the pentagonal bipyramids that contain five coordinated vertices. During the glass transition process, in the undercooled and glassy alloy, large number of pentagonal bipyramid structures are formed. The 1421 pair increases 5% during the rapid solidification process. Furthermore, 1311 and 1321 pairs decreases obviously, which consists with higher energy and larger distortion. The bond-type index around Al-Nd atomic pair is 1661 only, due to the large radius of Nd atom and fraction of this index is <2% during the whole temperature range.

Figure 9. Evolution of the top six most popular H-A indices types in the $Al_{87}Ni_7Nd_6$ alloy as a function of temperature.

Figure 10 shows the total and partial bond-angle distributions of the Al-based alloy at different temperatures. The partial bond-angle distributions have five classes: Al-Al-Al, Ni-Al-Al, Nd-Al-Al, N-Ni-Al and N-Nd-Al (N = Al, Ni, Nd). Total bond-angle distribution exhibits two peaks at 2000 K that located at 55.48° and 106.66°, but the height of the first peak is higher. The peaks become higher by the temperature decreases. Two peaks located 56.49° and 107.79° at 300 K of the total bond-angle distribution. All the partial bond-angle distribution functions have more pronounced peaks by glass transition progress, and this shows that the distribution types of the local structure around the atomic pair decreases at low temperature. The hump between two peaks decreases as the temperature decrease and becomes less distinguishable of the Al-Al-Al, Ni-Al-Al, Nd-Al-Al and N-Ni-Al (N = Al, Ni, Nd).
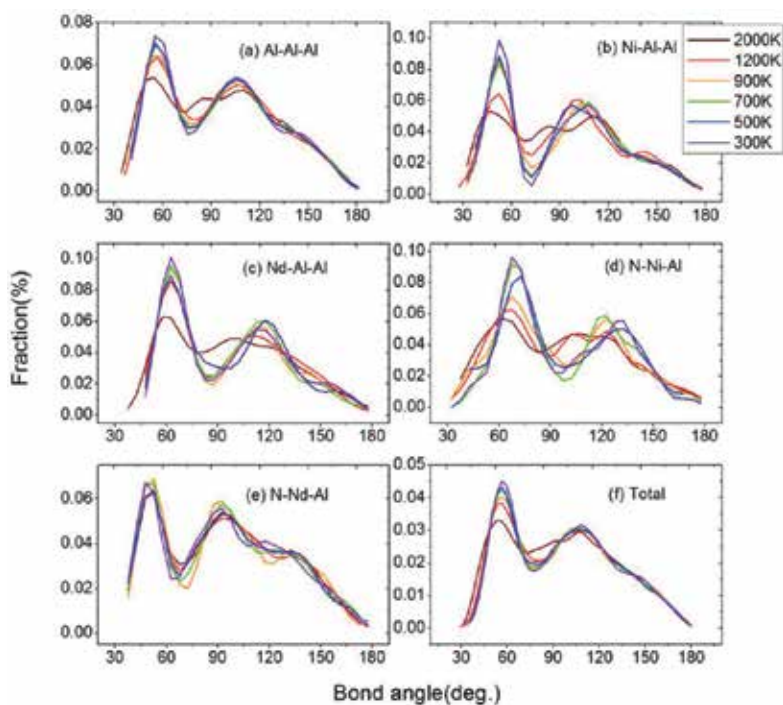
Figure 10. Calculated total and partial bond-angle distribution functions of the $Al_{87}Ni_{7}Nd_{6}$ alloy at different temperatures (N=Al, Ni, Nd). (a) Al-Al-Al, (b) Ni-Al-Al, (c) Nd-Al-Al, (d) N-Ni-Al, (e) N-Nd-Al and (f) total.

The close packing of three neighbour atoms is related to first peak at 56.49° position of the total bond angle. For Al-Al-Al, it is at around 60° shows the configuration of equilateral triangle, which is formed by the three neighbour atoms at 300 K. The second peak of the total bond angle is located near 108°, it indicates the pentagon configurations, which is agreement with the exist of the pentagonal bipyramids obtained by the HA bond-type index. The shoulder appeared at 300 K at around 145° relates to the threefold coordinated atoms. We also found that the increase in the peaks height of the bond-angle associate with the Ni is more evident than the others. The significant geometrical order around Ni is formed by the glass transition process. The shapes of the peaks for N-Nd-Al do not change very much, indicating that the neighbours' order of the elements Nd does not change much as the temperature decreases.

4. Part 3, the dynamical properties of the nucleation and glass-forming process of liquids

The dynamical properties are important for describing the nucleation and glass-forming process of liquids. The variation of mean-square displacement (MSD) as a function of temperature is also calculated through Eq. (2)

$$r^2(t) = \frac{1}{N}\left(\sum_{i=1}^{N}|r_i(t) - r_i(0)|^2\right) \tag{2}$$

$$\lim_{x \to \infty}\bar{r}^2 = c + 6Dt \tag{3}$$

These quantities of MSD [6] for Ca, Mg and Cu atoms are plotted in **Figure 11a–c**. The linear behaviour can be clearly seen and the slope decreases with temperature decreasing for all the three atoms. The self-diffusion coefficients, as the functions of temperature, are shown in **Figure 11d**. It is found that the self-diffusion coefficients of Ca atoms are less than the others at all temperatures, which is due to the larger radius of Ca atom. The relation between the self-diffusion coefficients and the temperature obeys an Arrhenius relationship.
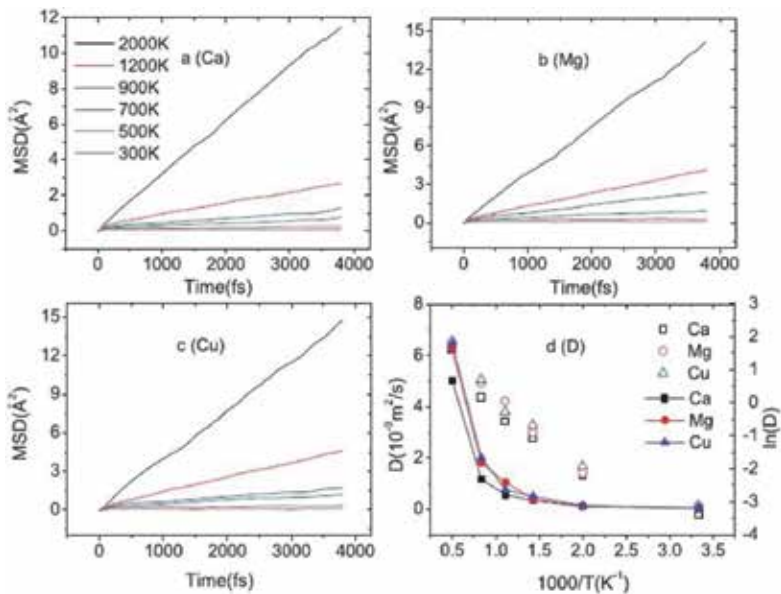

Figure 11. The MSD and self-diffusion coefficient of the alloy at different temperatures: (a)–(c) The MSD of Ca, Mg and Cu atoms; (d) variation of diffusion coefficients and the $\ln D$ of Ca, Mg and Cu atoms at different temperatures.

According to the Arrhenius relationship, there will be a linear relationship between the $\ln D$ and $1/T$, which is also plotted in **Figure 11d**, whereas, it shows non-Arrhenius in the super-cooled region in which the self-diffusion coefficients decrease more rapidly than expected. As mentioned above, the development of polyhedron local structures in the undercooled liquid delays the diffusive regime and leads to the non?Arrhenius behaviour [7], which also inhibits the crystallization and promotes the formation of the amorphous solid. The activation energy Ea is 23.01, 23.20 and 22.28 kJ/mol for the Ca, Mg and Cu self-diffusions, respectively. The pre-exponential factor D0 is 17.1210×10^{-9}, 18.9210×10^{-9} and 17.8510×10^{-9} m^2/s for Ca, Mg and Cu,

respectively. The polyhedral order and CSRO, which are enhanced in the supercooled region, decrease the self-diffusion coefficients.

5. Part 4, electronic density of states of the glass transition of the alloy

In order to investigate the electronic origin of the glass transition of the $Al_{87}Ni_7Nd_6$ alloy, we calculate the DOS for $Al_{87}Ni_7Nd_6$ alloys at different temperatures and plot in **Figure 12**. The snapshots of the configuration at 2000 and 300 K are also shown. The local DOS of N-d, Ni-d and Al-spd of **Figure 12a–c** indicates that the covalent bond is formed due to the hybridization between the electronic states of Al-p and Ni-d. Peak of DOS (Ni atom) becomes narrower and higher, the resonance between the electronic states of Ni and Al around the -2 eV is more significant during the glass transition process, shows the stronger hybridization between the electronic orbitals are formed and more ordered local structure around Ni formed. The lower peak of Nd than Ni, and the height of the peak for Nd increases slightly indicates the transition metal of Ni is more active than the rare earth of Nd during the solidification process. The chemical bonds contained in the snapshots (12 d) are calculated by the same cut-off distances of the corresponding atomic pairs at 300 and 2000 K, which presents the interaction of nearest neighbour atomic pairs are enhanced during the glass transition and the larger number of bonds are formed at the same time. It is contributing to the higher peak of DOS image (the Ni and Nd atom) at the lower temperature as well.
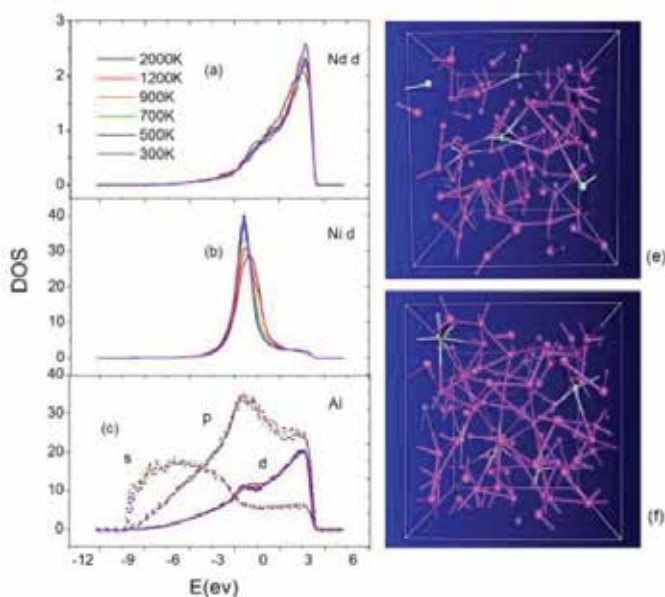
Figure 12. DOS (a)–(c) and snapshots (Al—pink, Ni—blue, Nd—green; (d) 2000 K, (e) 300 K) of the $Al_{87}Ni_7Nd_6$ alloy.
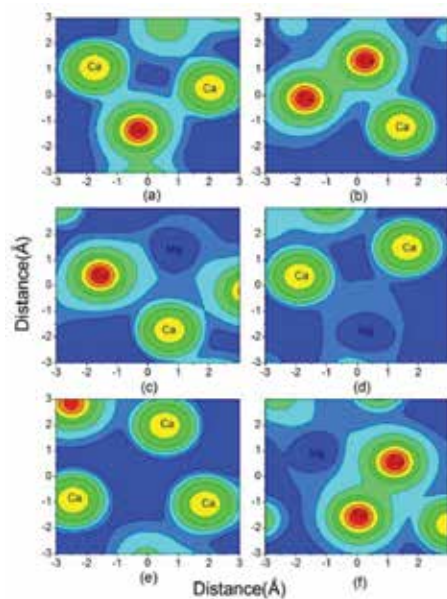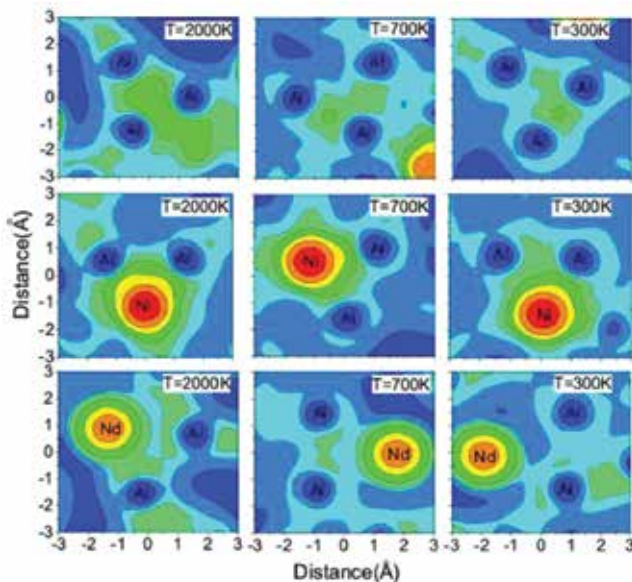
Figure 13. Contour plots of the valence electronic-charge density of amorphous solid $Ca_{50}Mg_{20}Cu_{30}$ for different atomic configurations: (a) Ca-Cu-Ca, (b) Cu-Cu-Ca, (c) Cu-Mg-Ca, (d) Ca-Mg-Ca, (e) Ca-Ca-Ca and (f) Mg-Cu-Cu.

6. Part 5, electronic charge densities of the amorphous solid

A combined neutron and x-ray diffraction study [8] have been performed for $Ca_{50}Mg_{20}Cu_{30}$ bulk metallic glass-forming system, which indicates that the average distances of Cu-Mg and Cu-Ca are consistent with the sum of covalent radii, whereas all other interatomic distances are consistent with the sum of metallic radii. Our simulation shows an accumulation of charge between Ca-Cu and Mg-Cu atomic pairs, which evidence the persistence of Ca-Cu and Mg-Cu covalent bonds (**Figure 13**). On the other hand, the covalent bonds of Cu-Cu pair are also existed as presented in the plot. The Cu-Cu interaction is not as attractive as Cu-Ca and Cu-Mg. In other words, Cu atoms prefer to cluster with Ca and Mg atoms rather than Cu itself. But this does not mean that Cu atoms repel each other. This is what the CSRO tells us. As a result, Cu-Cu covalent bonds are still found. The electrons with an sp character of the Mg atoms are transferred to the d states of Ca and Cu atoms. The accumulation of charge between Ca-Mg pairs indicates that there is Ca-Mg covalent bond in this alloy as well. While, this phenomenon is not found about Ca-Ca pair, which presents that the Ca-Ca bond is metallic bond. Our result provides string evidence for the existence of Ca-Mg, Ca-Cu, Mg-Cu and Cu-Cu covalent bonds, which is in accord with that covalent bonds between the elements dominate in the Ca-Mg-Cu alloy proposed by the former experiment. An increasing fraction of covalent bonding is benefit to increase the glass-forming ability [9], and this is in favour of the glass formation for the $Ca_{50}Mg_{20}Cu_{30}$ alloy.

7. Part 6, evolution of the electronical properties of the metallic glass

In our simulation, we also study the ground-state electronic charge densities. The charge density $\rho(r)$ in a plane defined by three neighbouring atoms at three temperatures of 2000, 700 and 300 K are plotted in **Figure 14**. The Ni ions tend to form strong interactions with Al, by the neutron diffraction data report [10], whereas the Nd bond length to Al is close to the expected sum of atomic radii about neutral ions. The accumulation of charge between Ni-Al atomic pairs at all temperatures is shown in the image 13; it indicates persistence of the Ni-Al covalent bonds. All different atomic configurations are chosen of the most nearby atomic pairs at the corresponding temperature. The interatomic distance of 2000 K is less than the others due to the broad distribution of interatomic distance at high temperature (**Figure 1**). The accumulation of charge between Al-Al atomic pair and Nd-Al atomic pair at 2000 K is more evident than the other temperature. While effect of temperature for Ni-Al atomic pair is insignificant, as a result of during the glass transition process Al atom prefer to transform near Ni atom than Al atom and Nd atom. The Al-Al and Nd-Al atomic pairs are weakly covalent bond properties in the molten liquid states, whereas Nd-Al is metallic bond properties at 300 K because of that the electronic charge density around Nd atom is a spherical distribution almost. The electrons with a sp character of the Al atom are likely transferred to the d states of Ni atoms at 300 K. The increasing fraction of covalent bond and metallic bond can increase the GFA of the alloy, and it is in favour of the glass formation during the solidification process of the multicomponent molten alloy.

Figure 14. Contour plots of the valence electronic charge density of $Al_{87}Ni_7Nd_6$ alloy for different atomic configurations at different temperatures.

8. Conclusion

Ab initio molecular dynamic simulations are used to understand the evolution of structural and electronic properties during the glass transition process of the $Al_{87}Ni_7Nd_6$ and $Ca_{50}Mg_{20}Cu_{30}$ alloy based on the density functional theory. The pair correlation function, CN, diffusion coefficient, mean square displacement, HA bond-type index and bond-angle distribution at different temperatures are observed by our simulation.

The PDF images investigates that the short to medium structure orderings are enhanced with decreasing temperature during the rapid solidification process. The interaction between different atomic pairs is strengthened, and the splitting of the second peaks occurs at different temperatures for the partial PDF, which indicates that some different substructures in prefer atom pairs have been formed before reaching the final glassy state.

The CNs we calculated agree well with the previous report of Ca-Mg-Cu MGs [11]. The CN of Ca atoms changes from 14.87 to 15.39, it is from 12.15 to 12.35 for Mg atoms and it is from 9.18 to 9.32 for Cu atoms, which are very close to the previous theoretical result. According to the ECP model [12, 13], which allows the number of structural sites to be counted, each Mg atom will be surrounded by 10 Ca atoms in the binary Ca-Mg MGs, and three additional solute sites occur at the interstices of these Mg-centred clusters. The CNs around Ca atom are about 15 while which is more than result of 13 in the Ca-Mg-Zn MGs [14], which shows that the packing around Ca atoms is more efficient in the Ca-Mg-Cu alloy. The interatomic distance we obtained and the partial coordination numbers of Al-Ni and Al-Nd pairs in our simulation are consistent with the previous experimental of the neutron diffraction and theoretical results of Al-Ni-Nd alloy [10].

The pentagon configurations and the three neighbour atoms packing are the most primary short-range order in both these two alloys, which local structural order is enhanced obviously by the decreases of temperature during the glass transition progress concluded by the bond-angle distribution methods in these two alloys, which is consist with results evaluated by the Honeycutt-Andersen (H-A) bond-type index that the amount of pentagon configurations increases during the glass transition and become the primary short-range order (SRO) as temperature decreases.

Our modelling studies of multicomponent of Al-based MGs and Ca-based MGs show that the covalent bonds of Ca-Mg, Ca-Cu, Mg-Cu and Cu-Cu pairs are existed in Ca-Mg-Cu alloy and accumulation of charge between Ni-Al atomic pairs which evidences the persistence of the Ni-Al covalent bonds in Al-Ni-Nd alloy at all the temperatures.

The evolution of structural and electronic properties during the glass transition process of Al-Ni-Nd alloy is also simulated. A result of the fact is that Al turns to prefer to be near Ni than Al and Nd during the glass transition process. In the molten liquid of 2000 K, weakly covalent properties of Al-Al and Nd-Al atomic pairs are existed, while the electronic charge density around Nd is almost a spherical distribution at 300 K.

Glass-forming ability (GFA) is also another important research issue. Inoue have provide three empirical rules for BMG formation [15, 16]: which suggested that multicomponent system of

more than three elements, difference of atomic size mismatch large than 12%, and negative heat of mixing between the components atoms tends to transform to glass easily of this multicomponent alloy system. The formation of the crystal structures is suppressed by the increasing polyhedral local structures ordering and chemical SRO of covalent bonds and metallic bonds; the increasing of the electronical interaction during the rapid solidification processes plays an important role during the glass transition and increases the glass-forming ability of the Al-Ni-Nd alloy.

We also found that the electrons with a sp character of the Al atoms are more likely to transfer to the d states of the Ni atoms. The more disordered amorphous state and the optimum bonding state seem to achieve the confused compositions and multicomponent MGs with good glass-forming ability and unique mechanical properties.

Author details

HaiJun Chang

Address all correspondence to: changhaijun01@163.com

School of Materials Science and Engineering, ShangHai JiaoTong University, Shanghai, China

References

[1] H. J. Chang, L. F. Chen and X. F. Zhu, J. Phys. D: Appl. Phys. 46, 105303 (6pp) (2013).

[2] H. J. Chang, L. F. Chen, and X. F. Zhu, J. Appl. Phys. 112, 073517 (2012). doi: 10.1063/1.4757626.

[3] O. N. Senkov, D. B. Miracle, and J. M. Scott, Intermetallics. 14, 1055 (2006).

[4] Ahn K, Louca D, Poon S J and Shiflet G J 2003 J. Phys.:Condens. Matter 15 S2357–64

[5] J. D. Honeycutt and H. C. Andersen. J. Phys. Chem. 91, 4950 (1987).

[6] J. P. Hansen and I. R. McDonald, Theory of Simple Liquids (Academic, London, 1986).

[7] A. Pasturel, E. S. Tasci, M. H. F. Sluiter, and N. Jakse, Phys. Rev. B 81, 140202 (2010).

[8] E. R. Barney, A. C. Hannon, O. N. Senkov, J. M. Scott, D. B. Miracle, and R. M. Moss, Intermetallics. 19, 860–870 (2011).

[9] R. W. Cahn, P. Haasen, and E. J. Kramer, In glasses amorphous metals, edited by Weinheim (VCH, NY, 1991).

[10] K. Ahn, D. Louca, S. J. Poon and G. J. Shiflet. J. Phys.: Condens. Matter. 15, S2357–S2364 (2003).

[11] Ahn K, Louca D, Poon S J and Shiflet G J 2003 J. Phys.:Condens. Matter 15 S2357–64

[12] D. B. Miracle, D. Louzguine-Luzgin, L. Louzguina-Luzgina, and A. Inoue, Int. Mater. Rev. 55, 218 (2010).

[13] D. B. Miracle, Acta Mater. 54, 4317 (2006).

[14] O. N. Senkov, D. B. Miracle, E. R. Barney, A. C. Hannon, Y. Q. Cheng, and E. Ma, Phys. Rev. B 82, 104206 (2010).

[15] A. Inoue, Acta Mater. 48(1), 279 (2000).

[16] A. Inoue, Mater Trans. 36(7), 866 (1995).

Corrosion Resistance and Electrocatalytic Properties of Metallic Glasses

Shanlin Wang

Abstract

Metallic glasses exhibit excellent corrosion resistance and electrocatalytic properties, and present extensive potential applications as anticorrosion, antiwearing, and catalysis materials in many industries. The effects of minor alloying element, microstructure, and service environment on the corrosion resistance, pitting corrosion, and electrocatalytic efficiency of metallic glasses are reviewed. Some scarcities in corrosion behaviors, pitting mechanism, and eletrocatalytic reactive activity for hydrogen are discussed. It is hoped that the overview is beneficial for some researcher paying attention to metallic glasses.

**Keywords:** metallic glass, corrosion resistance, pitting corrosion, electrocatalytic property

1. Introduction

Except for high compression strength, microhardness, electrical resistivity, and good soft magnetic properties, most metallic glasses exhibit excellent corrosion resistance. The excellent corrosion resistances of metallic glasses are mainly attributed to the homogeneous single glass phase, the alloy chemistry, and the presence of metalloids [1–3]. No grain boundaries, dislocations, and other defects where corrosion can occur preferentially are expected to allow the growth of a uniform protective film. The chemical homogeneity is believed for rapid cooling rates required to produce full amorphous structure since no enough time is available for solid-state diffusion, that is, it is impossible for the formation of second phases, precipitation, and segregations. The homogeneity in chemical composition and microstructure promotes amorphous oxide formation on the surface which retards ionic transport. The

improvement of corrosion resistance is also considered to link to the ability of these metastable alloys to form supersaturated solid solution in one or more alloying elements. The alloying element available in solid solution may be incorporated into the oxide film to enhance its passivity. Thus, the effect of the amorphous structure, chemical and structural homogeneity, and the possibility of forming unique chemical composition not typical of near-equilibrium crystalline alloys are mostly considered as factors that can affect the corrosion properties of metallic glass.
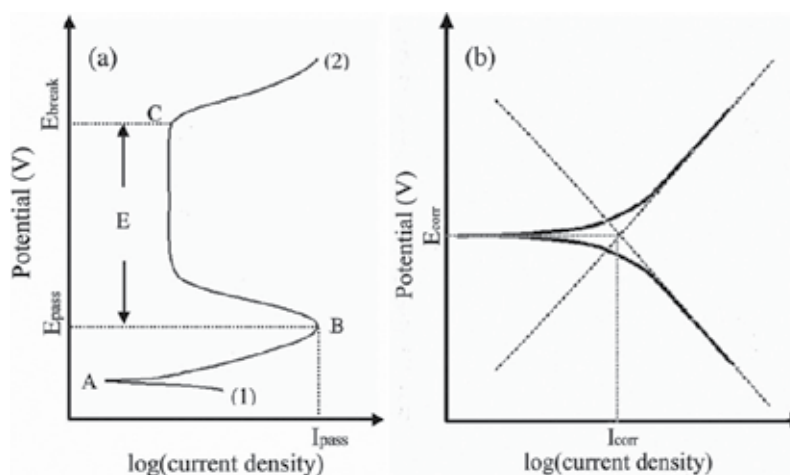
Figure 1. A schematic diagram of potentiodynamic polarization: (a) the theoretical anodic polarization curve, (b) the calculation of corrosion potential and corrosion current density.

In order to estimate the corrosion resistance, immersion test is one of method to calculate the average corrosion rate in one year, while the electronic chemistry methods such as the potentiodynamic polarization are applied in most researches, where the considerable information on the electrode processes can be attained, such as corrosion potential (E_{corr}), corrosion current density (I_{corr}), corrosion rate, pitting susceptibility, passivity, and the cathodic behavior. A schematic curve of the theoretical anodic polarization (a) and the calculation of corrosion potential and corrosion current density (b) are illustrated in **Figure 1**. As can be seen in **Figure 1(a)**, the scan start forms point (1) and progresses in the positive potential direction until termination at point (2), the open circuit potential is located at point A. At the potential, the sum of the anodic and cathodic reaction rates on the electrode surface is zero. As a result, the measured current will be closed to zero. With the increase of the potential, it moves to active region. In this region, metal oxidation is the dominant reaction taking place. Point B is known as the passivation potential, and as the applied potential increases above the value the current density is seen to decrease until a low, passive current density is achieved in passive region E. Once the potential reached a sufficiently positive value, that is located as point C, sometimes termed the breakaway potential, the applied current rapidly increases. Around the open circuit potential, a new line is fitted according to the linear regions of the polarization curve as illustrated in **Figure 1(b)**. The current density at that point is the corrosion current density
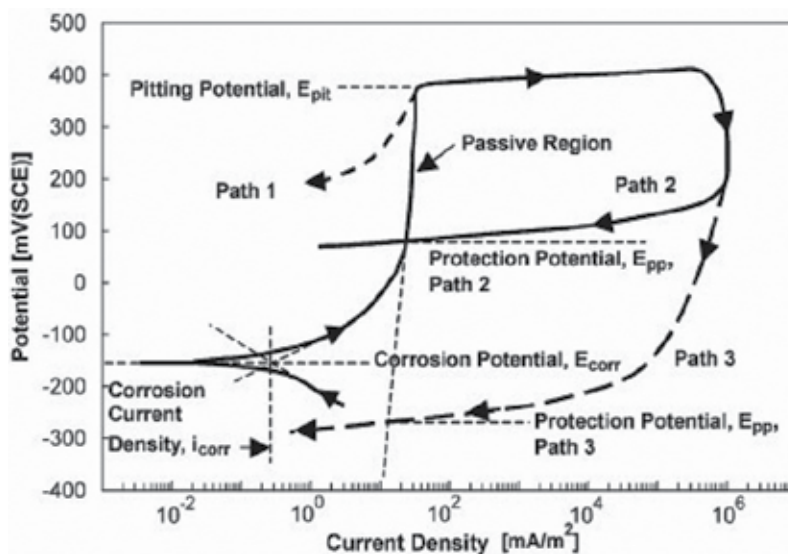
Figure 2. A schematic cyclic-anodic-polarization curve [4].

(I_{corr}) and the potential at which it falls is the corrosion potential (E_{corr}). It is generally agreed that the higher is the corrosion potential, the more difficult is the occurrence of the oxidation reaction for the metals, moreover, the larger is corrosion current density, the higher is corrosion rate, that is, the lower corrosion resistance for metallic glass.

While for the susceptibility of pitting corrosion, the cyclic-anodic-polarization is usually measured, and some parameters and typical characteristics with regard to pitting corrosion susceptibility are defined in the schematic polarization curves of **Figure 2** [4]. A potential scan is started below the corrosion potential, E_{corr}. At E_{corr}, the current density goes to zero, and then increases to a low and approximately constant anodic value in the passive range. In this range, a thin oxide/hydroxide film, a passive film, protects the material from high corrosion rates. If the current density decreases when the potential scan direction is reversed, as in path 1, the material is shown to be immune to pit corrosion. However, if on the potential up scan, the current density suddenly increases, and remains high on the down scan, until finally decreasing to the passive-region value, as in path 2, the material is shown to undergo a form of pitting corrosion. The potential at which the current density suddenly increases (pitting initiation) is known as the pit potential, E_{pit}, and the potential at which the current density returns to the passive value is known as the repassivation potential or the protection potential, E_{pp}. Between E_{pit} and E_{pp}, pits are initiating and propagating. In the case of path 2, pits will not initiate at E_{corr}, the natural corrosion potential; and, therefore, the material will not undergo pitting corrosion under natural corrosion conditions. If, on the other hand, path 3 is exhibited, where E_{pp} is below E_{corr}, the material will undergo pitting corrosion at surface flaws or after incubation time periods at E_{corr}. In terms of the overall resistance to pitting corrosion, two parameters of ($E_{pit} - E_{corr}$) and ($E_{pp} - E_{corr}$) are important. Higher values of both are desirable to reflect high values of E_{pit} and E_{pp} relative to E_{corr}.

## 2. Corrosion resistances of nonferrous metallic glasses

Metallic glass is comparatively newcomer to the amorphous material group, which is fabricated from a cooled liquid without crystallization under a rapid cooling rate. As the first metallic glass of $Au_{80}Si_{20}$ was discovered in 1960 by Duwez and coworkers [5], a series of metallic glasses such as Zr-, Ti-, Pd-, Cu-, Fe-, and Mg-based alloys are successfully fabricated by the method of melt quenching. In order to extend the industrial application of metallic glasses, the corrosion behaviors of metallic glass have been of great interest. The corrosion resistance of nonferrous metallic glass of Cu-, Ti-, Zr-, and Mg-based alloys will be discussed in the following part.

2.1. Effect of composition

Among of nonferrous metallic glasses, Zr-based metallic glass (Zr-MG) is investigated abroad in corrosion resistances. Addition of minor element such as Ag, Cu, Y, Ti, Ni, and Nb has been utilized to enhance the glass forming ability and resistance to general and local corrosion. Inoue and coworkers [6–10] have investigated the effect of Ni on the corrosion resistance of Zr-Ni-Cu-Al alloy. Zr-MG without Ni shows lowest corrosion potential and no obvious passivation region, but pitting directly can be observed as potential rises. Zr-MG with Ni is spontaneously passivated with current density around 10^{-3} A/m^2 before the occurrence of pitting corrosion in chloride solution. Since the Cu element in the Zr-MG is easily dissolved in chloride solutions, thus leads to a low corrosion resistance. The additional Ni inhibits the formation of soluble Cu-Cl films and facilitates forming the protective surface films with a high concentration of Zr cation, leading to a denser, thicker, and more pitting resistance ZrO_2 passive film. Zhang and coworkers [11, 12] reported that partial substitution of Ni and Co by Ag was effective in improving the corrosion resistance of Zr-MG, as the Ag addition increases the concentration of Zr and decreases the concentration of Al in the surface passive films, while Liu and coworkers [13] found that the addition of Ag could promote the formation of Al_2O_3 but slightly suppressed the formation of ZrO_2. The cast $Zr_{56}Al_{16}Co_{28-x}Nb_x$ (x = 1, 3, and 5 at%) metallic glass are spontaneously passivated in NaCl solution with a passive current density between 10^{-5} and 10^{-6} A/cm^2, and the pitting potentials shift to positive direction with the increasing of Nb content [14]. Though the Nb-bearing alloy's pitting potential and passive region are larger than Nb-free alloy, after pitting, however, the alloy with 4 at% Nb exhibits higher corrosion current density than Nb-free alloy, as shown in **Figure 3**, meaning that the corrosion reactions in Nb-bearing alloy are more severe at high potential [15]. Generally, the addition of Nb element in Zr-MG can facilitate the formation of highly protective Zr-, Al-, and Nb-enriched surface film, while Cu addition will deteriorate the passivation [16]. For $Zr_{55}Al_{10}Ni_5Cu_{30}$ metallic glass alloy, the mass loss and the average corrosion rate decrease with increase of Ti content in 1 M HCl solution [17], and the Ti addition improves the stability of passive film and pitting resistance, while they are susceptible to pitting corrosion [18].

Compared to Zr-MG, Cu-based metallic glasses with their superiority in price and mechanical properties possess great potential applications in the fields, such as bipolar plate materials, biomedical instruments, and microdevices. The investigations about corrosion resistance have

been carried extensively. Small addition of Nb, Cr, Ta, and Mo has proved to be effective in improving the corrosion resistance [19–21]. Asami et al. [19] investigated the effect of small addition of Nb, Mo, and Ta to $Cu_{60}Zr_{30}Ti_{10}$ at% metallic glass in 1 M HCl, HNO_3, NaOH, and 0.5 M NaCl solutions. The results demonstrate that Nb element is most effective in decreasing the corrosion rate in all of the solutions, moreover, the corrosion rate decreases with increasing the Nb content. The minor element addition can enhance the stability of passive film enriched in ZrO_2 and TiO_2. Except the minor addition Mentioned above, some rare metal element additions of In, Y, Ce, and Ln to Cu-MG are effective to improve the corrosion resistance [22–25]. The results demonstrate that the dissolution of rare element is favorable to forming continuous Zr-, Ti-rich protective oxide film and alleviates the local corrosion and propagation at the initial corrosion stage. The Ln addition can increase the nearest neighbor atomic distance affecting the topological instability, which is attributed to the improvement of corrosion resistance.
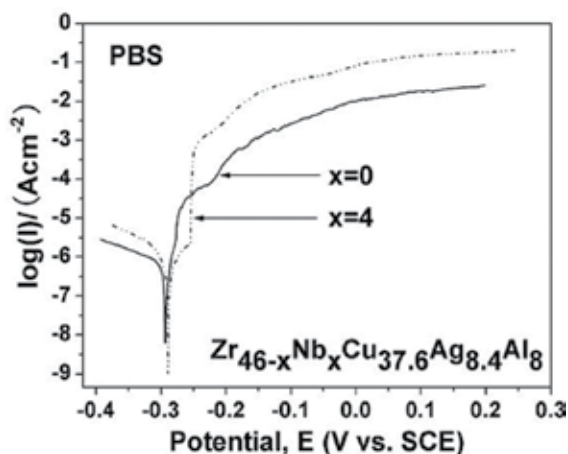
Figure 3. Potentiodynamic polarization curves for the alloy in phosphate-buffered solutions at 37°C [15].

As conventional titanium alloy, Ti-based metallic glass with high yield strength, low Young's modulus, high corrosion resistance can be applied as biomaterial [26], and mostly possesses higher corrosion resistance than Ti-6Al-4V alloy in a simulated body fluid environment. The minor element addition of Zr, Nb, and Cu will change the corrosion behavior of Ti-MG [27–29]. Nb addition can enhance the pitting resistance due to an improvement of the passive layer properties for near-homogenous alloys. Small addition of Zr promotes the corrosion potential and decreases the corrosion current density. The addition of Cu can shift the beginning of polarization reaction to a positive voltage level, while provokes severe Cu-induced selective dissolution under the higher applied voltage levels, resulting continuous pitting and the depletion of Ti and Zr in the alloy. With increase of (Ti + Zr)/Cu ratio, the pitting corrosion resistance is greatly enhanced due to the formation of surface film mainly composed of TiO_2 and ZrO_2.

As well known, magnesium alloy is also one of biomaterials. Recently, the corrosion behavior of Mg-based metallic glass is investigated. Wang et al. [30] reported that the Mn addition can promote the formation of a dense passive film, which delays the corrosion of the matrix. The Zn addition provokes the formation of $Zn(HO)_2$ and $Mg(OH)_2$, and the evolution of the corrosion process of the MgZnCa glass is schematically illustrated in **Figure 4** [31]. When Mg-MG is immersed in body fluid, the anodic dissolution of magnesium occurs and the magnesium hydroxide layer well is formed on the surface of the sample. The attack of Cl^- occurs at the weak sites of the magnesium hydroxide layer and transforms the magnesium hydroxide into soluble magnesium chloride. The fresh substrate, exposed to the medium directly, suffers further corrosion, and results in the releasing of Mg^{2+} and Zn^{2+}, as shown **Figure 4(a)**. As immersion prolonged, the Zn^{2+} concentration is increasing due to the continuous dissolution of Zn. The $Zn(OH)_2$ precipitates preferentially, compared to that of $Mg(OH)_2$ (**Figure 4(b)**), the $Zn(OH)_2$ precipitations will repair the defects in the surface layer, and then forms a continuous and uniform layer. With the corrosion proceeding, the corrosion product layer will be thickened and $Zn(OH)_2$ precipitation spreads, which are evidently depicted in **Figure 4(c)**. Meanwhile, the undissolved $Mg(OH)_2$ and $Zn(OH)_2$ precipitation can provide favorable sites for apatite nucleation. With Ti addition, the protective film of $Mg(OH)_2$ will enrich Ti, improving the stability [32].
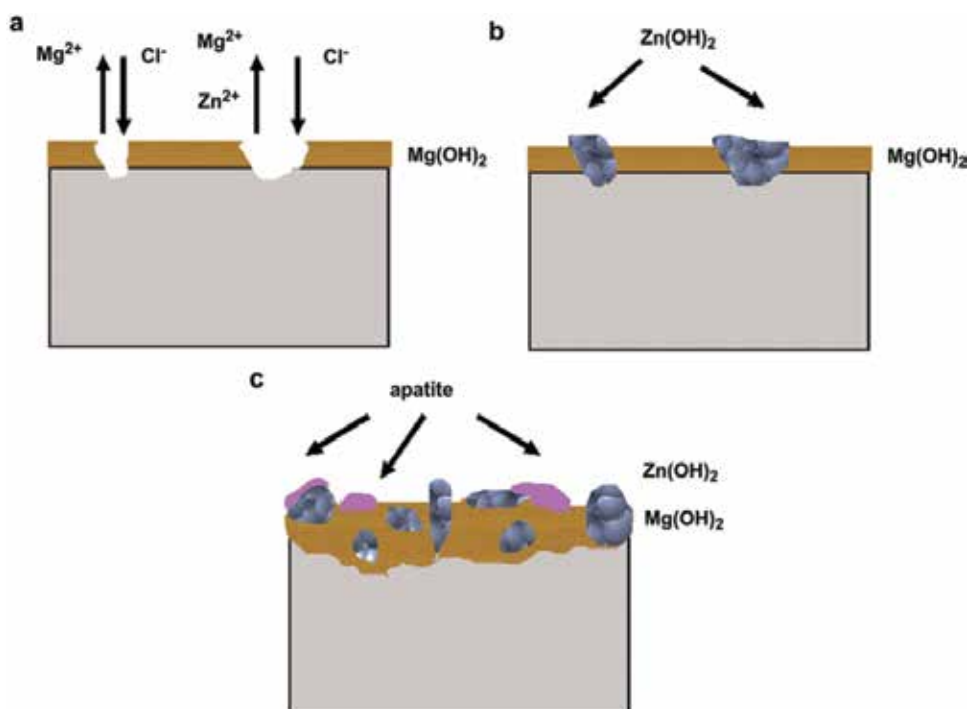
Figure 4. The sketch map for the evolution of corrosion process of Mg-Zn-Ca bulk metallic glass immersed in SBF: (a) initial stage, (b) middle stage, (c) final stage [31].

2.2. Effect of microstructure

The microstructure and composition homogeneities are destroyed with the crystallization, which is necessary to deteriorate the corrosion resistance of metallic glasses. $Zr_{56}Al_{16}Co_{28}$ metallic glass exhibits a decrease of passivation potential and an increasing of penetration rate with increasing heating temperature in Ringer's simulated body fluid at room temperature [33]. The corrosion parameters of some metallic glasses are summarized in the **Table 1** [34–39]. It can be attained that the corrosion resistance of most metallic glasses after crystallized will decrease, as shown that the corrosion potential decreases and the corrosion current density increases relatively, suggesting that the passive films formed on the surface of the glassy alloy in the anodic process are protective and denser than those on the crystal alloys. However, another metallic glasses exhibit more positive corrosion potential and low corrosion current density after crystallized, meaning that the crystalline alloy possesses excellent corrosion resistance, compared to metallic glass with same composition, since the nanocrystal phase such as a-Ti, CuZr precipitation or the reduction of the free volume in amorphous state that in turn reduces the average atomic distance.

| Composition	State	E_{corr} (mV)	I_{corr} (A/ cm^2)	E_{pit} (mV)	E_{pit}–E_{corr} (mV)	I_{pass} (A/ cm^2)	CPR (um/y)	Temp (K)	Solution
$Zr_{62.3}Cu_{22.5}Fe_{4.9}Al_{6.8}Ag_{3.5}$ [34]	Am.	−290	5.5×10^{-8}	−22	268	---	1.5	310	PBS
	Cry.	−305	7.7×10^{-8}	−45	160	---	0.9	310	PBS
$Ti_{40}Zr_{10}Cu_{38}Pd_{12}$ [35]	Am.	−31	4.6×10^{-7}	---	---	---	---	---	HBSS
	Cry.	−61	2.0×10^{-8}	---	---	---	---	---	HBSS
$Ti_{42}Zr_{40}Si_{15}Ta_3$ [36]	Am.	−455	4.9×10^{-8}	113	---	2.9×10^{-6}	---	310	SBF
	Cry.	−321	8.7×10^{-8}	176	---	4.0×10^{-6}	---	310	SBF
$Zr_{60}Cu_{20}Al_{10}Fe_5Ti_5$ [37]	Am.	−214	3.0×10^{-4}	---	---	---	---	310	SBF
	Relx	−43	8.8×10^{-6}	39	83	---	---	310	SBF
	Cry.	−22	1.4×10^{-6}	407	429	---	---	310	SBF
Zr_2Ni [38]	Am.	−354	1.3×10^{-7}	82	---	1.1×10^{-6}	---	300	0.1 M NaCl
	Cry.	−369	1.4×10^{-7}	76	---	9.3×10^{-7}	---	300	0.1 M NaCl
$Cu_{47.5}Zr_{47.5}Al_5$ [39]	Am.	−760	1.2×10^{-7}	110	870	5.2×10^{-7}	---	300	ASS
	Cry.	−460	5.0×10^{-8}	110	570	1.6×19^{-6}	---	300	ASS

Table 1. Summary of corrosion parameters for some metallic glasses and its crystalline alloys from literature reports.

Wang et al. [40, 41] reported that the corrosion resistance of Mg-MGs was slightly reduced when the in situ second phase or reinforcement phase were induced into metallic glass. It is believed, when corrosion is developing, the continuous distribution of glass matrix might be able to prevent corrosion from spreading from one a grain to another a grain directly across

the glass matrix. Then corrosion is stopped after the crystalline phases dissolves and a continuous glass matrix is exposed to solution. If the crystalline phase is nanoparticle and presents high chemical potential, the corrosion resistance of metallic glass composite will not reduce, even increase for some metallic glass alloy [39, 42].

When bulk metallic glass is fabricated into metallic glass coating, the corrosion resistance of metallic glass coating is affected not only by the composition, but also by the surface and porosity of the metallic glass coating [43]. The effect of porosity on corrosion resistance for Ti-MG evaluated with potentiodynamic polarization is shown in **Figure 5** [44]. The metastable current transition of different magnitude can be observed for the porous bulk metallic glass. Although rapid increase in anodic current due to pitting is not observed, anodic current density slightly increases, indicating that some of metastable pitting occur within the pore at the same time and afterward are stabilized by the pore wall during the anodic polarization process. Undoubtedly, the existing of pores would result in crevice corrosion, where potentiodynamic polarization curve exhibits a slow increase of current density in the anodic polarization part. Gebert et al. [45] reported that the state of surface finishing of Zr-based metallic glass remarkably influences its corrosion and passivity. It is considered that the smoothness, homogeneity, and the modification of surface chemistry such as Cu concentration on the surface of Zr-MG are modified after polished with different polishing materials.
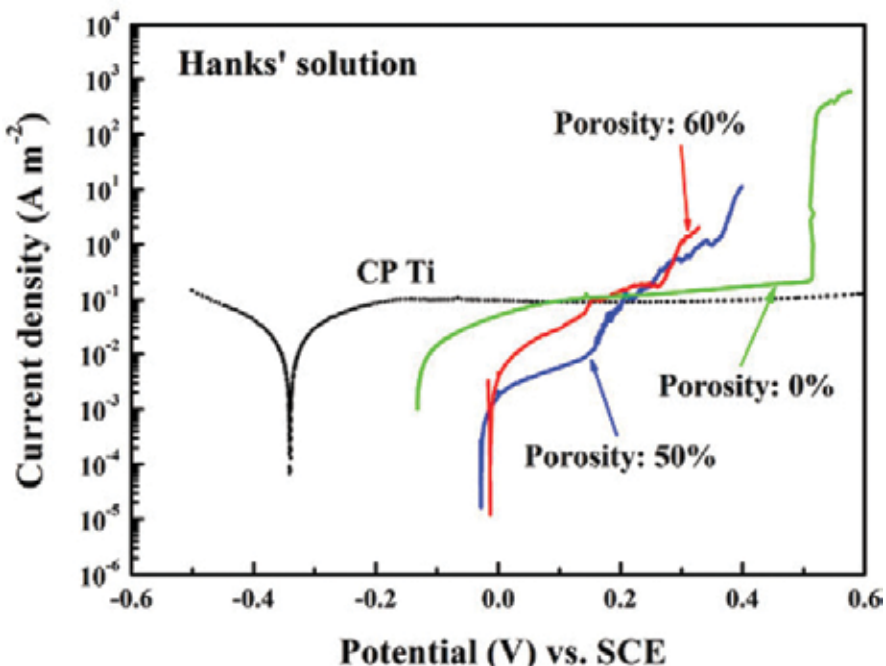
Figure 5. Potentiodynamic polarization curves of the produced porous $Ti_{45}Zr_{10}Cu_{31}Pd_{10}Sn_4$ bulk metallic glass with various porosities in Hanks' solution at 310 K compared to pure Ti alloy [44].

Besides chemical and physical defects of glassy alloy, the mechanically generated defects can enhance the corrosion susceptibility. Gebert et al. [46] reported that a slight improvement of spontaneous passivity but a decrease of resistance against chloride-induce pitting were detected when Zr-based bulk metallic glass was shot-peened with long time, and the corrosion damage evolution was governed by the nature of the mechanically generated defects, such as craters, cracks of scratches and their surrounding stress fields. The effect of shear bands breaking through a sample surface on corrosion processes in acidic environments is investigated. The preferential sites for corrosion initiation and propagation are formed along the shear bands, as shown **Figure 6** [47]. The local chemical and structural changes in the close vicinity of the shear band zone are mainly predisposing factor. An et al. [48] found that the Cu-MG after tensioned exhibited more negative corrosion potential and larger corrosion current density in chloride solution, which indicated the deterioration of corrosion resistance of Cu-MG tensioned, compared with as-cast.
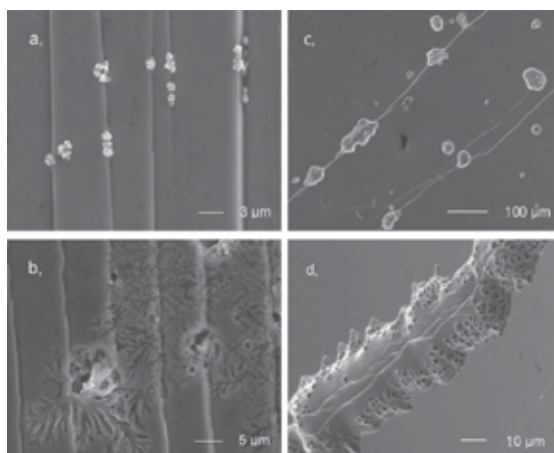
Figure 6. SEM images of corroded shear band regions at surfaces of predeformed Zr-based metallic glass after exposure to 12 M HCl: (a, b) bent ribbon; (c, d) lateral area [47].

2.3. Effect of environment

Though the microstructure and chemical composition of nonferrous affect the corrosion resistance, it is evident from **Table 2** that the environment is also a significant factor in the corrosion properties. **Table 2** provides corrosion parameters for some nonferrous metallic glass in various electrolytes. Pourgashti et al. [49] found that Zr-MG exhibited excellent corrosion resistance in 3.5% NaCl solution, and showed better corrosion resistance than 316L in HNO_3 and H_2SO_4 solutions. It can be seen from **Table 2** that the tendency of corrosion current density I_{corr} is $I_{corr/HCl} > I_{corr/HNO3} > I_{corr/NaCl} > I_{corr/H2SO4}$. The Zr-MG reveals to increase in passive current density and decrease of transpassive potential with increase in nitric acidic concentration [51]. Gebert et al. [50, 55] reported that $Zr_{55}Cu_{30}Al_{10}Ni_5$ was immune to localized corrosion in alkaline solution. However, a susceptibility to pitting corrosion was observed

during anodic polarization experiment at chloride concentration as low as 10^{-3} M. Moreover, the effect of temperature on the corrosion resistance was investigated. The Zr-MG exhibits that E_{pit} decreases as the temperature increases, indicating an increased tendency of pitting in the chloride solutions as the temperature is increasing.

Composition	E_{corr} (mV)	I_{corr} (A/ cm²)	E_{pit} (mV)	E_{pit}–E_{corr} (mV)	I_{pass} (A/cm²)	CPR (um/y)	Temp (K)	Solution
$Zr_{41.2}Ti_{13.8}Ni_{10}Cu_{12.5}Be_{22.5}$ [49]	−469	6.7×10^{-7}	97	---	---	10	298	3.5% NaCl
	−428	9.0×10^{-7}	---	---	---	80	298	1 M HNO₃
	−491	5.4×10^{-7}	---	---	---	620	298	0.5M H₁SO₄
	−322	1.4×10^{-6}	---	---	---	260	298	1 M HCl
$Zr_{55}Cu_{30}Al_{10}Ni_5$ [50]	---	---	450	---	---	---	298	0.001 M NaCl
	---	---	50	---	---	---	423	0.001 M NaCl
	---	---	−100	---	---	---	523	0.001 M NaCl
$Zr_{59}Ti_3Cu_{20}Al_{10}Ni_8$ [51]	603	2.3×10^{-8}	1450	---	1.1×10^{-7}	---	298	1 M HNO₃
	357	5.6×10^{-7}	1370	---	2.2×10^{-6}	---	298	6M HNO₃
	818	3.4×10^{-6}	1200	---	9.8×10^{-5}	---	298	11.5M HNO₃
$Cu_{55}Zr_{35}T_{10}$ [52]	18.9	2.4×10^{-4}	---	---	---	33.2	298	0.005M HCl
	−10.2	1.2×10^{-4}	---	---	---	82.5	298	0.01 M HCl
	−119.6	2.0×10^{-4}	---	---	---	342	298	0.5M HCl
	−322.9	1.2×10^{-3}	---	---	---	702	298	1 M HCl
	164.9	2.7×10^{-5}	---	---	---	2.6	298	0.005M NaCl
	−21.1	2.3×10^{-5}	---	---	---	7.7	298	0.01 M NaCl
	−58.0	1.8×10^{-4}	---	---	---	37.6	298	0.5M NaCl
	−87.6	6.4×10^{-5}	---	---	---	79.2	298	1 M NaCl
$Ti_{46}Cu_{27.5}Zr_{11.5}Co_7Sn_3Si_1Ag_4$ [53]	−270.8	2.7×10^{-4}	---	---	---	---	310	PBS
	−151.7	2.0×10^{-4}	---	---	---	---	298	0.9 wt% NaCl
	−289.8	1.6×10^{-4}	---	---	---	---	298	1 M HCl
	−345.6	1.4×10^{-3}	---	---	---	---	298	1 M NaOH
$Mg_{69}Zn_{27}Ca_4$ [54]	−1120	---	−976	144	---	---	320	SBF
	−1330	---	87	1417	---	---	320	PBS

**Table 2.** Summary of corrosion parameters for some metallic glasses in different corrosive environment.

As similar to Zr-MG, $Cu_{60}Zr_{20}T_{20}$ metallic glass during the potentiodynamic polarization exhibits the active dissolution state in the whole anodic region in different solutions [56]. The current density increases to a very high value after the E_{corr} is reached indicating high rate of metal dissolution and no sign of passivity is observed. The higher the concentration of chloride, the higher is the I_{corr} value which in turn indicates that the rate of corrosion increases with increase in concentration of Cl^-. The E_{corr} becomes more negative with the increase in concentration of solution. The tendency of I_{corr} and E_{corr} also can be seen in **Table 2** for Cu-, Ti- and Mg-based metallic glass.

3. Corrosion resistance of Fe-based metallic glass

Due to its high strength, good soft magnetic properties, excellent corrosion resistance, and low producing cost, Fe-based metallic glass is attended extensively to the researchers in material science and technology fields around the world. Besides the glass forming ability, strength, and soft magnetic properties, the investigation on corrosion resistance is interesting for the industrial application of Fe-based metallic glasses.

3.1. Enhance of minor element addition

The effects of the addition of a small amount of metallic elements such as Cr, Mo, Nb, W, Ni, Ta, Y, Al, Co, and Mn on the corrosion resistance of Fe-MGs are investigated by means of electrochemical polarization and weight loss measurements. It is well known that chromium is an effective element enhancing corrosion resistance of Fe-MGs. In Fe-Co-B-Si-Nb metallic glass [57], the corrosion rate decreases from 0.7 mm/year for Cr-free alloy to 6×10^{-2} mm/year for the alloy with 4 at% Cr in 0.5 M NaCl solution at 298 K. For the $Fe_{73.5}Si_{13.5}B_9Nb_3Cu_1$ metallic glass in marine environments, the corrosion rate is 14 times lower for the material with 2 at% Cr and 88 times lower for the material with 4 and 6 at% Cr as compared with the material in amorphous state without Cr [58]. Though increasing Cr concentration up to 8 at% Cr tends to stabilize the passive layer, the corrosion rate remains very high. The addition of 8 at% is not sufficient to the formation of a stable passive layer, and the materials are dissolved or undergo severe attack in 1, 2, and 5 M H_2SO_4 [59]. In 9.7 M H_2SO_4 solution at 70°C, the $Fe_{63.1}C_{7.1}Si_{4.4}B_{6.5}P_{8.6}Cr_{8.3}Al_{2.0}$ metallic glass exhibits high corrosion rate of 13 mm/year that is five times lower than that of AISI304L [60]. The crack width on the corrosion product layer after potentiostatic polarization measurement decreases with increase of content as shown in **Figure 7(a)** and **(b)**, the pitting morphology occurs on the surface of metallic glass with 6.3 at% Cr, as showed in **Figure 7(c)**, however, a homogenous surface without cracks or pitting is formed for the alloys with Cr content exceeding 8.3 at% as shown in **Figure 7(d)** and **(e)**, due to the formation of Cr-enrich passive film on the surface.
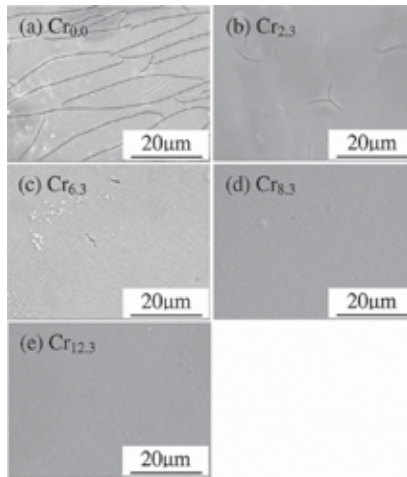
Figure 7. SEM micrographs on the surfaces in 9.7 M H$_2$SO$_4$ solution at 343 K: (a) $x = 0.0$, (b) $x = 2.3$, (c) $x = 6.3$, (d) $x = 8.3$, (e) $x = 12.3$ [60].

With minor addition of Y, not only glass forming ability, but also corrosion resistance is increasing evidently. The dependence of the electrochemical parameters upon the yttrium content is shown in **Figure 8** [61]. The corrosion current density I_{corr}, passive current density I_{pass}, corrosion potential E_{corr} from the polarization behavior and open-circuit potentials OCP of FeCrMoCBY metallic glass after immersion in 1 M HCl solution for 100 h as a function of Y content are presented, respectively. It can be seen that the passive current density is sensitive to the yttrium content. The effects of some metal element additions are summarized in **Table 3**. It is obvious that minor element addition into Fe-MG will evidently increase the corrosion resistance. The corrosion rate of FeBSiNb alloy with 0.4 at% Ni addition is about 1000 times lower than that without Ni addition in 0.5 M NaCl [62]. Generally, the minor element additions such as Mo, Y will provoke the formation of passive film, resulting in improvement of corrosion resistance [61, 65].
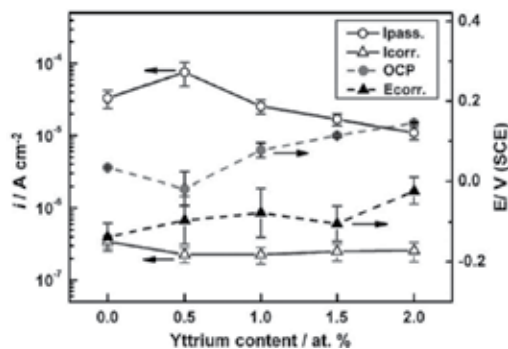
Figure 8. The statistical analysis of the various electrochemical parameters obtained from polarization behavior of immersion tests of Fe-MG with the variation of yttrium content [61].

Composition	Elem. X	Content (at%)	E_{corr} (mV)	I_{corr} (A/cm²)	E_{pit} (mV)	I_{pass} (A/cm²)	CPR (um/y)	Temp (K)	Solution
FeBSiNbX [62]	Ni	0	−626	4.5×10^{-6}	---	---	897	298	0.5M NaCl
		0.2	−426	3.2×10^{-7}	---	7.9×10^{-6}	1.8		
		0.4	−367	1.2×10^{-7}	---	4.1×10^{-6}	< 1		
		0	−936	5.9×10^{-6}	---	---	978		0.5M NaOH
		0.2	−677	9.9×10^{-7}	---	1.6×10^{-5}	56		
		0.4	−647	7.0×10^{-7}	---	1.1×10^{-5}	32		
		0	−404	7.0×10^{-5}	---	9.3×10^{-3}	2106		0.5M H$_2$SO$_4$
		0.2	−356	3.4×10^{-6}	---	1.9×10^{-3}	787		
		0.4	−334	1.1×10^{-6}	---	1.0×10^{-3}	674		
FeBCuX [63]	Nb, Zr	3.5, 3.5	---	---	−170	---	---	298	NaCl+NaOH (pH13)
	Nb, Mo	3.5, 3.5	---	---	−270	---	---		
	Zr. Mo	3.5, 3.5	---	---	−310	---	---		
	Mo	7	---	---	−340	---	---		
FeCrMoBCX [64]	Nb	0	−169	---	715	2.5×10^{-6}	---	310	RS(pH6)
		3	−45	---	876	2.0×10^{-7}	---		
		4	122	---	1299	3.8×10^{-8}	---		
FeBCrX [65]	Mo, Nb	0	---	---	---	$2.8 \times 10^{-3*}$	---	289	0.1 M H$_2$SO$_4$
	Mo,Nb	0.3, 0	---	---	---	$1.4 \times 10^{-3*}$	---		
	Mo,Nb	0, 0.3	---	---	---	$1.0 \times 10^{-3*}$	---		
	Mp,Nb	0.15, 0.15	---	---	---	$4.5 \times 10^{-4*}$	---		
FeCSiBPAlMoCoX [66]	Cr	0	−304	6.5×10^{-6}	---	1.2×10^{-2}	---	298	0.5M H$_2$SO$_4$
		2.3	−279	2.3×10^{-6}	---	1.9×10^{-4}	---		
		12.3	−235	7.0×10^{-7}	---	2.9×10^{-5}	---		
		0	−311	4.5×10^{-6}	---	7.9×10^{-3}	---		1 M HCl
		2.3	290	1.9×10^{-6}	---	2.8×10^{-4}	---		
		12.3	220	8.0×10^{-7}	---	1.7×10^{-5}	---		
FeCrNiX [67]	Si	20	−200	1.9×10^{-6}	---	---	---	298	0.01 M HCl
	P	20	−800	1.5×10^{-7}	---	---	---		
FeCrMoCX [68]	B	4	---	---	---	---	5~30	298	1 M HCl
		6	---	---	---	---	6–40		6M HCl
		8	---	---	---	---	25–70		12M HCl

Table 3. Summary of corrosion parameters affected by element addition for some metallic glasses.

Besides the metal elements, the metalloids element addition of B, Si, P, S, Ni, and C are also important to the corrosion resistance. The $Fe_{50-x}Cr_{16}Mo_{16}C_{18}B_x$ (x = 4, 6, 8 at%) glassy alloys exhibits spontaneously passivation in 1 and 6 M HCl solutions with wide passive region and low passive current density [68]. With increase of boron content in alloys, the corrosion resistance of glassy alloys is improved, even in 12 HCl solution, the glassy alloy with 8 at% B do not suffer pitting corrosion. With P addition in the $Fe_{45}C_{16}Mo_{16}C_{15}B_{10}$ glassy alloy, the kinetics of passivation and composition of passive film are improved in HCl solution. While with Si replacement of P, the corrosion resistance can be enhanced due to the formation of passive film composed of chromium oxide with some amounts of silica [67].

3.2. Effects of microstructure homogeneity

Since metallic glasses are metastable and can be transformed into stable crystalline phase by heat treatment or mechanical working, the structural change can also affect corrosion resistance for metallic glasses. A comparison of passive current density I_{pass}, corrosion/transpassivation potential E_{corr} and corrosion rate CPR for some Fe-based metallic glasses and their crystalline alloy is summarized in **Table 4** [69–71]. It can be observed from **Table 4** that the corrosion/passive current density and corrosion rate increase for the crystalline alloys compared with metallic glass, while corrosion/transpassivation potential depends on their compositions.

Composition	State	E_{corr} (mV)	I_{pass} (A/cm²)	CPR (um/y)	Temp (K)	Solution
FeCrMoCBY [69]	Amor	77	3.0×10^{-5}	---	298	1 M HCl
		200	6.0×10^{-5}	---		6M HCl
	Cryst	29	1.0×10^{-4}	---		1 M HCl
		152	---	---		6M HCl
FeSiB [70]	Amor	−735	---	---	298	0.5M NaCl
	Cryst	−765	---	---		
FeSiBNbCu [70]	Amor	−605	---	120	298	0.5M NaCl
	Cryst	−515	---	310		
FeZrB [71]	Amor	−520*	1.9×10^{-3}	---	298	0.5M H$_2$O$_4$
	Cryst	−463*	2.2×10^{-2}	---		
FeNbZrBCu [71]	Amor	−860*	1.0×10^{-3}	---	298	0.5M H$_2$O$_4$
	Cryst	−685*	1.3×10^{-2}	---		
FeNbB [71]	Amor	−1070*	7.5×10^{-4}	---	298	0.5M H$_2$O$_4$
	Cryst	−850*	1.0×10^{-2}	---		

**Table 4.** Summary of corrosion parameters affected by microstructure for some Fe-MGs.
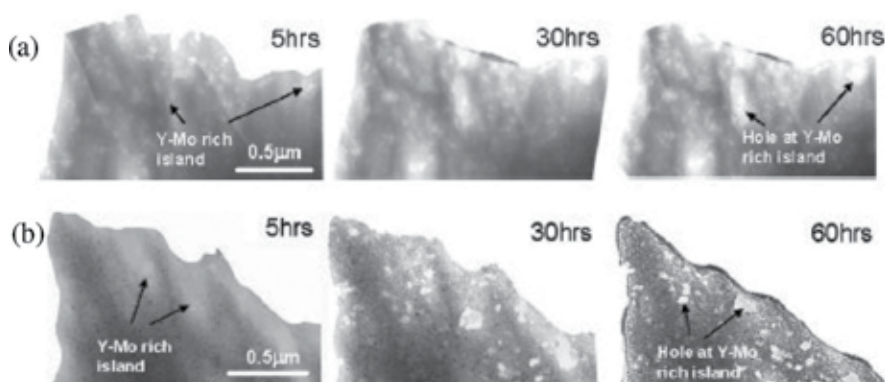
Figure 9. BF-TEM micrographs of (a) fully amorphous, (b) devitrified SAM 1651 after immersion in 6 M HCl for different periods of time [69].

The decrease of corrosion resistance in crystalline alloys obtained by the isothermal heat treatment of Fe-M-B (M = Nb, Zr) metallic glasses is explained by the formation of the α-Fe crystalline phase that has greater corrosion susceptibility in compared to that of the amorphous phase [70]. Long et al. thought the galvanic effects between adjacent phases with different composition were resulted in the deterioration of corrosion resistance for Fe-Co-B-Si-Nb metallic glass [72]. A comparison of BF-TEM morphologies for amorphous and devitrified SAM 1651 [69] is shown in **Figure 9**. It indicates that the lacier morphologies for devitrified SAM 1651 mean the degradation in the corrosion resistance. However, the abrupt increase in the corrosion potential for crystalline alloy is attributed to the decrease of the residual stress during densification, and the surface atom electrochemically active site [73]. Since atom at a glassy metal surface are in nonequilibrium configuration and may effectively sit on higher energy wells than that corresponding to atoms on an equilibrium configuration. Moreover, the faster migration of silicon ions to the surface in the crystalline structure promotes the SiO_2 film formation, which enhances the corrosion properties [74].

During the fabrication processing of bulk metallic glass and metallic glass coating, the porosity is not avoided due to rapid cooling. The effect of porosity on the corrosion resistance is investigated in some literatures [75–77].The corrosion resistance of coating 1 with the porosity of 0.04% is better than that of another two coatings with the porosity of 0.2% and 0.5%, respectively [75]. When the porosity decreases form 1.89% of low deposition rate to 1.22% of high deposition rate, the corrosion resistance of FeCrMoCBY amorphous coating increases evidently due to the elimination of through pores [76]. However, when the porosity is lower than 1.22%, the corrosion resistance seems more sensitive to the amorphous phase content. If the thickness of the coating decreases, the number of through-porosity in coating increases, which affects the corrosion resistance, as shown in **Figure 10** [77]. It indicates that through-porosity is much more detrimental to the corrosion resistance of the coated material compared with nonthrough porosity.
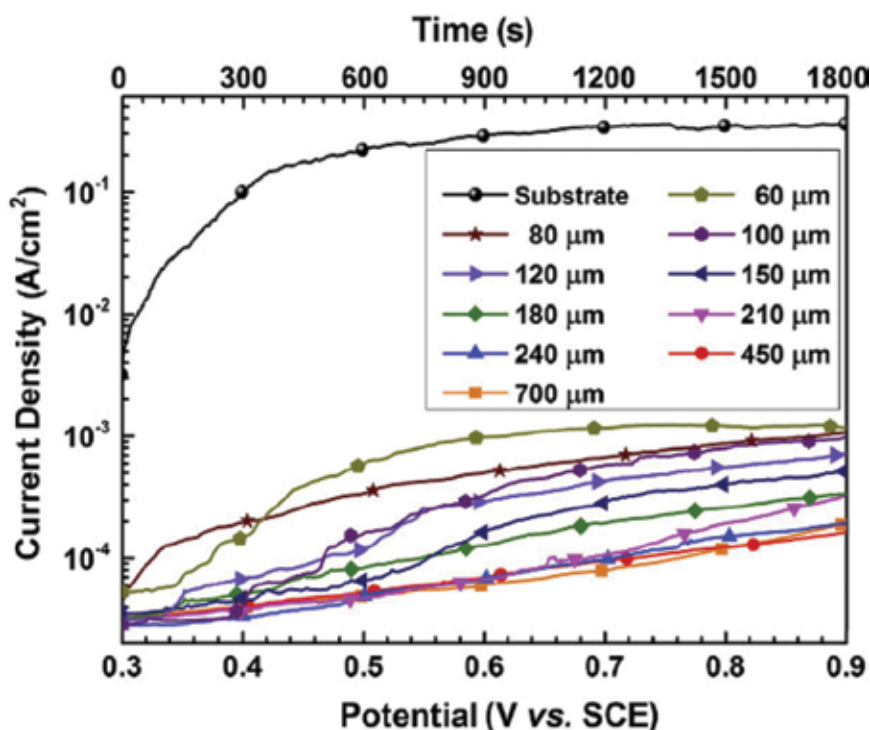
Figure 10. Anodic polarization conducted on the bare substrate and coated substrate with various thickness of Fe-MG coating in 3.5 wt% NaCl solution [77].

In some bulk metallic glass or metallic glass coating, the crystallize particles such as WC, TiN, SUS316, NbC, TiO_2, and Al_2O_3 are induced [78–83]. It is obvious that the crystallized particles are deteriorated the structural homogeneity. However, little investigations are done about the influence of crystalline particle on the corrosion resistance, which is important for the potential application of Fe-based metallic glass as anticorrosion and antiwearing materials.

3.3. Effects of service environment

The corrosion behaviors of Fe-based metallic glasses are affected by environmental factors. Intuitively, the stronger the aggressiveness of the solution is, the weaker the corrosion resistance of metallic glass exhibits. The results [68] attained in immersion experiments for $Fe_{48}Cr_{16}Mo_{16}C_8B_4$ glassy alloy in 1, 6, and 12 M HCl solutions exhibit, as expected, that the corrosion rate increases as the increase in concentration of HCl solution. The alloy occurs pitting on the surface after 168 h of immersion in the 12 M HCl solution at room temperature. FeCrMoCBP alloy is spontaneously passivated with a passive current density of about 10^{-1} A/m^2 and a wide passive region in 1 M HCl solution, however, its passive film is not stable by anodic polarization, as an anodic current density increases with increasing potential in 6 M HCl solution, and no passive film seems formed on the surface with rapid increasing of current

density in 12 M HCl solution [84]. $Fe_{54.2}Cr_{18.3}Mo_{13.7}Mn_{2.0}W_{6.0}B_{3.3}C_{1.1}Si_{1.4}$ (wt%) alloy can passivate spontaneously in the H_2SO_4 solution, and the passive current density is changed from 1×10^{-5} A/cm^2 with 0.4 M to 2×10^{-5} A/cm^2 with 0.1 M [85]. The corrosion penetration rates of $Fe_{48}Cr_{15}Mo_{14}Er_2C_{15}B_6$ metallic glass [86] are 39.9, 27.5, and 3 mm/year in 1 M HCl, 1 M NaOH, and 0.6 M NaCl with pH 7 solutions, respectively. The critical passivation potential E_{corr} and critical passivation current density I_{corr} of Fe-Ni metallic glass decrease with increase of pH value of solution, as shown in **Figure 11** [87].
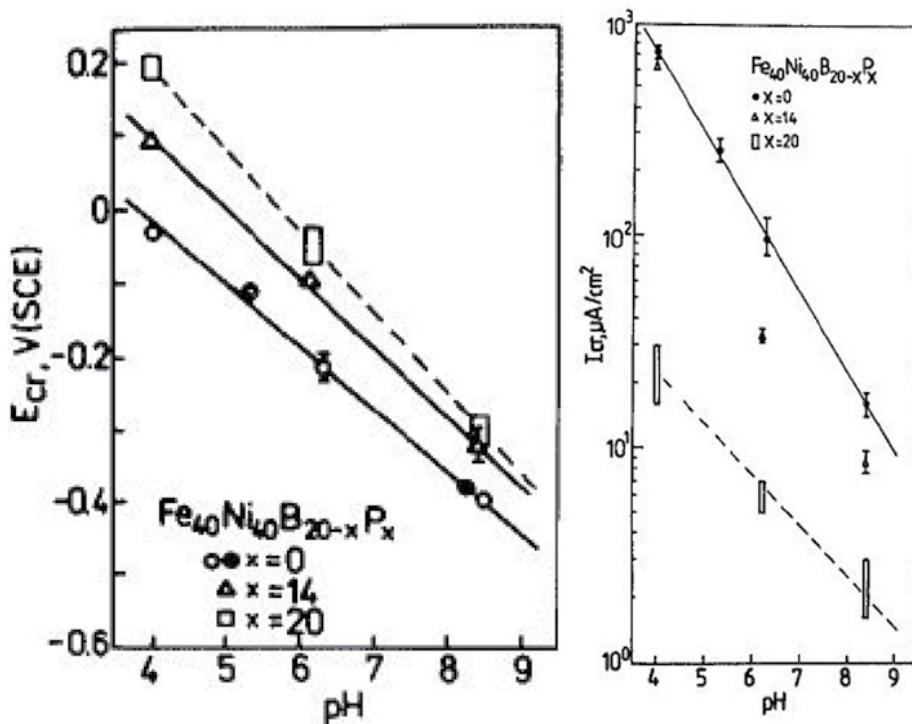
Figure 11. The effect on critical passivation potential E_{cr} and current density I_{cr} of Fe-Ni amorphous alloy at 298 K [87].

The corrosion rate of FeNiB metallic glass is only 70 µm/year in 3.5 wt% NaCl solution [73], while the corrosion rate increases to 130,000 µm/year in 1 M HNO_3 solution, near two thousand times larger than that in sodium chloride solution, as shown in **Table 5**. In **Table 5**, it is attained that more negative corrosion potential is obtained with increase of pH value, and the corrosion current density decreases. As the acidic ion or hydroxyl ion concentration increase, the corrosion potential becomes more negative and the corrosion current density increases generally. That is, the corrosion resistance decreases with increase of acidic ion concentration and hydroxyl ion content. When the concentration of hydrogen ion is same, the existence of chloride ion will deteriorate the corrosion resistance. In a word, the corrosion resistance of Fe-based metallic glass decreases as the solution aggressiveness increases.

Composition	E_{corr} (mV)	I_{corr} (A/cm²)	E_{pit} (mV)	I_{pass} (A/cm²)	CPR (um/y)	Temp (K)	Solution
FeNiB [88]	---	1.5×10^{-2}	---	---	130,000	298	1 M HNO$_3$
	---	1.5×10^{-3}	---	---	14,900	---	1 M NaOH
	---	8.0×10^{-5}	---	---	70	---	3.5 wt% NaCl
	---	1.3×10^{-4}	---	---	1140	---	1 M HCl
FeNiBAiNb [62]	−367	1.2×10^{-7}	---	1.1×10^{-6}	<1	298	0.5 M NaCl
	−647	7.0×10^{-7}	---	1.1×10^{-5}	32	298	0.5 M NaOH
	−334	1.1×10^{-6}	---	1.0×10^{-3}	674	298	0.5 M H$_2$SO$_4$
FeCSiBPCrAlMo [89]	−264	9.0×10^{-7}	---	---	---	298	0.5 M H$_2$SO$_5$
	−283	4.1×10^{-6}	---	---	---	298	1 M HCl
FeCoCrMoCBY [90]	−269	2.4×10^{-7}	1090	---	---	298	Hank's
	−315	4.8×10^{-8}	1200	---	---	298	Saliva
FeCrMoCBY [91]	−614	2.0×10^{-6}	988	$1.3 \times 10_{-3}$	---	298	3.5wt% NaCl
	−414	1.1×10^{-5}	904	1.7×10^{-3}	---	298	1 M HCl
	−377	4.6×10^{-6}	879	5.5×10^{-4}	---	298	1 M H$_2$SO$_4$
FeCoCrMoCBY [92]	---	---	---	---	0.12	298	1 M HCl
	---	---	---	---	0.12	298	1 M HNO$_3$
	---	---	---	---	0.13	298	1 M NaOH
	---	---	---	---	0.07	298	3.5 wt% NaCl
FeCrMnMoWBCSi [85]	−367	---	---	---	---	298	0.25 M H$_2$SO$_4$
	−219	---	---	---	---	298	0.25 M Na$_2$SO$_4$
	−455	---	---	---	---	298	0.5 M HCl
	49	---	---	---	---	298	0.5 M NaCl
FeCoCrMoCBY [93]	−257	4.7×10^{-8}	715	---	---	298	Acid rain
	−378	7.5×10^{-8}	1033	---	---	298	3.5 wt% NaCl
FeBNb [94]	−458	1.5×10^{-5}	---	---	---	298	NaCl+H$_2$SO$_4$pH1.0
	−700	1.5×10^{-5}	---	---	---	298	NaCl pH5.5
	−637	7.0×10^{-6}	---	---	---	298	NaCl+NaOH pH10
FeCoBSiNb [94]	−381	1.5×10^{-5}	---	---	---	298	NaCl+H$_2$SO$_4$ pH1.0
	−550	2.0×10^{-6}	---	---	---	298	NaCl pH5.5
	−509	1.5×10^{-6}	---	---	---	298	NaCl+NaOH pH10
FeCrNiB [94]	−192	6.0×10^{-8}	---	---	---	298	NaCl+H$_2$SO$_4$ pH1.0
	−128	1.5×10^{-8}	---	---	---	298	NaCl pH5.5
	−209	2.0×10^{-8}	---	---	---	298	NaCl +NaOH pH10

**Table 5.** Summary of corrosion parameters affected by environment for some Fe-MGs.

4. Pitting corrosion of metallic glasses

Though metallic glass exhibits excellent general corrosion resistance, it is also susceptible to pitting corrosion in aggressive solutions, especially containing Cl^- ion [95]. Since the surface film is not stable during the anodic polarization, many pits are observed on the surface of FeCrMoCB metallic glass with 4 at% B immersed in 12 M HCl solution for 168 h [68]. During potentiodynamic polarization in 1.7 M HCl solution, many peaks of current density occur for FeCrMB (M = Mo, Nb) metallic glass, which is attributed from pitting corrosion. Moreover, the morphologies of pits are confirmed by SEM analysis after the immersion test [65]. $Fe_{52}Mn_{10}Mo_{14}Cr_4B_6C_{14}$ metallic glass is susceptible to pitting corrosion, although presents good corrosion resistance characterized by a low passivating current in 0.6 M NaCl solution [96]. $Fe_{48}Cr_{15}Mo_{14}B_6C_{15}Y_2$ metallic glass, as known SAM1651, exhibits hysteresis loop during cyclic potentiodynamic polarization in 4 M NaCl solution at 373 K, which indicates the formation of localized corrosion [97]. Pardo et al. [58, 59] found that FeSiNbBCuCr metallic glass was immune to pitting corrosion in simulated industrial environments, since the current density decreased when the potential scan direction is reversed and it is identified that no pit formed on surface after immersion test. Though no hysteresis loop is observed and E_{corr} shifted toward more anodic values from the cyclic polarization curve, the formation of pits occurs when the anodic branch is enlarged during the forward scan [98]. The size of corrosion pit is less than 50 μm in the PBS solution [99], and the pits are distributed inhomogeneous on the surface of Zr-based metallic glass in NaCl solution [100]. The formation of pits is attributed from the broken of the passive film or irregular microstructure on the surface [101]. Jiang and coworkers [102] found that almost all pits were passed through by shear bands for as-cast sample, while the pit was distributed randomly after annealing.

Gostin et al. [103] considers that no pitting propagation is attributed from the high repassivation ability due to the high content of the beneficial Mo in its composition, although the yttrium oxide particle provides a favorable location for pit formation and local dissolution is initiated at their interface with the glassy matrix. However, Gostin et al. [104] also found that a pitting-like process occurred for the glassy alloy with high concentration of C, as the initial breakdown of passive film caused by the sudden direct exposure of the alloy surface to the electrolyte subsequent to local rupturing of the C-rich layer by growing CO_2 bubbles. Liu and coworkers [105] reported the pitting was initiated since the formation of a nanoscale Cr-depleted zone near the intersplat due to oxidation effect during thermal spraying, as shown in **Figure 12**. Paillier et al. [106] reported that Cu-rich nanocrystals of 5–10 nm were formed inside the corrosion pits during the corrosion process, as shown in **Figure 13**. The corrosion mechanisms of is feasible that elements like Zr, Ti, and Al mainly dissolve in solution whereas Cu and probably Ni is prone to form nanocrystals on the surface covered by a passive oxide layer, as in **Figure 13(a)**, the structure vanishes with the complete removing of the surface oxide by HF (**Figure 13(b)**). On the bare surface alloy without native oxide layer, the small pits develop first with the bow-like morphology, and then, because the corrosion appears to proceed quicker in the vertical direction, and goes along with the canyon-like morphology. Very deep trenches are indeed hollowed leading to a canyon aspect, as shown in **Figure 13(c)**.
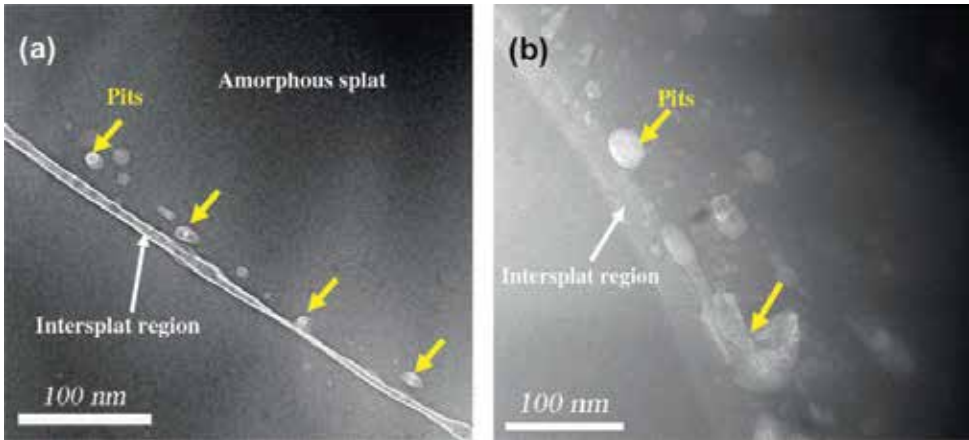
Figure 12. TEM images of the corroded morphologies of the amorphous coating after immersion in 6 M NaCl solution for 1 h (a) and 2 h (b) [105].
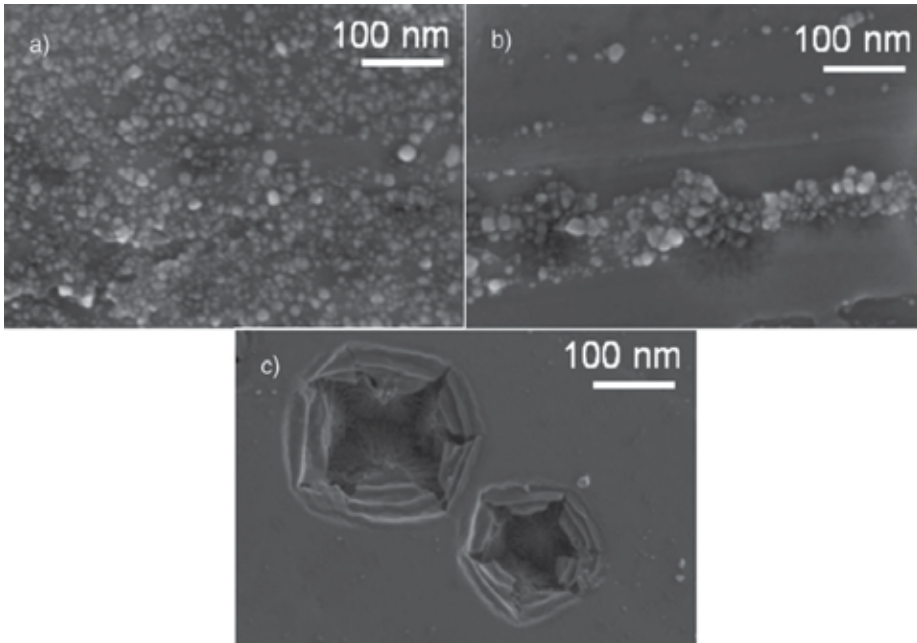
Figure 13. SEM images of $Zr_{59}Ti_3Cu_{20}Al_{10}Ni_8$ after different immersion times in HF 0.1%: (a) 60 s, (b) 120 s, and (c) 180 s [106].

5. Electrocatalytic properties of metallic glasses

Metallic glasses have gained considerable attention in catalysis research due to their unique structural and chemical properties [107], such as the unique atomic structure with a short-range ordering of the constituents, the large flexibility in their chemical composition compared to that of crystalline alloys, the structural and chemical homogeneity, the high reactivity due to their metastable structure, and the excellent conductivity for electricity and heat. Some investigations about the electrocatalytic activity of metallic glasses for the hydrogen evolution reaction or oxygen reduction reaction, such as Co- [108, 109], Zr- [110, 111], Ni- [113], Cu- [114], Pt- [115, 116], and Au-based [117] metallic glasses, are done in last few decades. However, Fe-based metallic glasses are the most attractive as catalytic material. Since the first catalytic materials of Fe-based metallic glass were reported in 1981 [118], a larger number of investigations have be done [118–123], such as the $Fe_{82.7}B_{17.8}$ amorphous ribbon used as a catalyst for the Fischer-Tropsch-type reaction of $CO + H_2$ [119], amorphous Fe-Zr precursor for ammonia synthesis [120], amorphous FeNiCrPB alloy as catalysts for acetylene hydrogenation [121] and hydrogen evolution [122,123]. The chromium effect on the catalytic activity for FeNiCrPB metallic glass is shown in **Figure 14**. It can be seen that the catalytic activity is strongly affected by Cr presence, while catalytic efficiency is independent of Cr content.
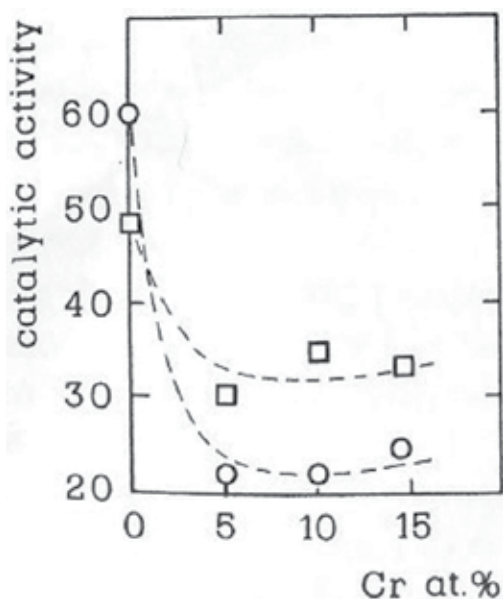
Figure 14. Catalytic activity vs. % Cr: ○, amorphous; □, crystalline [122].

The famous composition of $Fe_{60}Co_{20}Si_{10}B_{10}$ (G14) [124] is firstly reported in 1988, exhibiting good electrocatalytic activity for hydrogen evolution reaction (HER) comparable with Pt. A comparison of kinetics parameters between G14 and pure Fe, vit.7505, pure Pt is illustrated in **Table 6**. With increasing temperature the exchange current densities i_0 of G14 is significant-

ly greater than that of the polycrystalline iron. After this, the relationship between electrocatalytic activity of hydrogen evolution and crystallization [125], anodic treatment [126], and anodic dissolution [127] of amorphous G14 have been investigated in KOH solution. The results indicate amorphous G14 exhibits higher electrocatalytic activities compared with their crystalline alloys. This enhancement is not related to the electronic properties of metallic glass.

| Electrode	T (K)	i_0 (A/cm^2)	b (−mV)
Fe (poly)	298	1.0×10^{-5}	135
	323	3.3×10^{-5}	140
	348	4.0×10^{-5}	150
$Fe_{78}Si_{11}B_{11}$	298	1.0×10^{-6}	140
	323	5.0×10^{-5}	150
	348	1.6×10^{-4}	155
$Fe_{60}Co_{20}Si_{10}B_{10}$	298	1.0×10^{-6}	95
	323	4.8×10^{-5}	140
	348	2.7×10^{-4}	150
Pt (poly)	298	2.4×10^{-5}	120
	323	4.8×10^{-5}	150
	348	3.3×10^{-4}	170

Table 6. Electrocatalytic activity parameters of the cathodic hydrogen evolution for G14 and pure Fe, vit. 7505($Fe_{78}Si_{11}B_{11}$), pure Pt.

The electrocatalytic properties are affected not only by the composition of alloy, but also by the surface composition and/or surface area by chemical pretreatment. The catalytic studies [128] on the hydrogenation of carbon monoxide by Fe-based alloy indicated that the activity is augmented by a treatment in HNO_3 solution. Guczi et al. [129] thought that the surface composition and valence state determined in depth were related to the catalytic activity and selectivity revealed in $CO + H_2$ reaction. An increased number of nickel and iron sites by removing of the prevailing boron oxide, iron oxide, and iron oxide layer after HCl treatment was responsible for the enhanced catalytic activity, as shown in **Figure 15**, that is, the activity of the FeB sample in as-received state was about twice that observed for the FeNiB sample, on the other hand, comparing the HCl etched samples, the activity of the FeNiB alloy was about 30 times higher than that of the FeB ribbon.

The electrocatalytic activity of $Fe_{40}Ni_{40}P_{14}B_6$ metallic glass [130] is improved for HER by acid pretreatment with 1 M HF or HNO_3 for 10 min, since a porous structure with highly roughed and numerous small craters resulted from the selectively leachability of phosphorous from the surface of $Fe_{40}Ni_{40}P_{14}B_6$ metallic glass enhanced the electrode surface area in comparison to the as-polished surface.

The mechanism of hydrogen evolution reaction at the metal electrode in alkaline solution is based on three-step reactions as following:
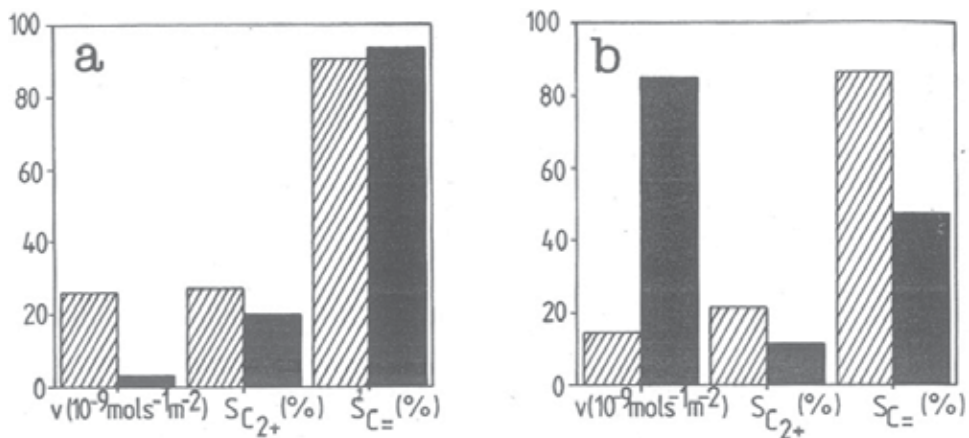
Figure 15. Catalytic activity, S_{c2+} and S_{c-} selectivities over (a) $Fe_{80}B_{20}$, (b) $Fe_{40}Ni_{20}B_{20}$. Hatched: as received. Full black: treated with HCl [129].

Electronation of water with adsorption of hydrogen—Volmer reaction is shown in Eq. (1):

$$M + H_2O + e \Leftrightarrow MH_{ads} + OH^- \tag{1}$$

Electrochemical desorption of H_2—Heyrouvsky reaction is shown in Eq. (2):

$$MH_{ads} + H_2O + e \Leftrightarrow M + H_2 + OH^- \tag{2}$$

Chemical desorption—Tafel reaction is shown in Eq. (3):

$$2MH_{ads} \Leftrightarrow 2M + H_2 \tag{3}$$

Due to involving the transfer of electron from the electrode surface, the density of electrons close to the energy level of metal surface is an important parameter governing electrocatalytic reaction activity. However, it is difficult to estimate during HER, so the efficiency is usually evaluated with overpotential η, Tafel slope b, and exchange current density i_0. The performance of cathodic electrode with respect to HER is primarily characterized by the overpotential which is given by the working electrode potential minus the reversible potential. A linear relationship exists between the overpotential and the cathodic current density as shown in Eq. (4) [131]:

$$\eta = a + b \log(i) \tag{4}$$

where a is constant, b is the Tafel slope, and the exchange current density $i_0 = 10^{-a/b}$. The Tafel slope is mainly affected by the reaction mechanism. In the case of identical Tafel slope, the exchange current density is mainly affected by the effective surface area.

Some Fe-based metallic glasses with high electrocatalytic efficiency are reported, such as a low overpotential $\eta_{300} = 318$ mV for amorphous $Fe_{71}Mo_{29}$ alloy [132] at 30% KOH solution at 303 K, a low Tafel slope $b = 95$ mV and a large exchange current density $i_0 = 1$ μm/cm^2 for amorphous $Fe_{60}Co_{20}Si_{10}B_{10}$ alloy [124] at 1 M KOH solution at 298 K, and $Fe_{59.5}C_3Si_{7.3}B_{8.5}P_{5.7}Mo_{2.5}Co_{13.5}$ alloy with $b = 110$ mV and $i_0 = 16$ μm/cm^2 [133]. It is evident that the Tafel slope as well as overpotential decrease with increase of Mo content at the same conditions [132]. However, the Tafel slope does not change with replace of Co for Fe in the amorphous FeCoB alloy [134]. The results of Tafel slope are considered that the effective transfer coefficients for the dissolution of boron and the metals are equal.

6. Summary

The investigation of corrosion resistance of metallic glass is attractive for allover researchers in materials science and engineering, since the unique structure and properties, extensive potential application. Most researches are focus on the effects of element addition and nanocrystallization on the general and local corrosion resistance in various environments. Certain elements are identified are quite effective in improving the corrosion resistance. And the crystallization of metallic glass is usually deleterious for the corrosion resistance. In general, the decreasing is the corrosion resistance of metallic glasses, the increasing is the solution aggressiveness, especial for the chloride ion concentration. Unfortunately, the mechanism of pitting corrosion of metallic glass is not clear, as that of conventional materials such as stainless steel. As practical application of the metallic glasses in industrial field, some metallic glasses such as Fe-based metallic glass are used as anticorrosion or antiwearing materials. The coating is one of effective methods. During the coating processing, some inclusion, oxidation, crystallization, and even second particle as reinforcement phase in the coat layer is inevitable. However, the effect of these particles on the general and pitting corrosion resistance is seldom reported. Therefore, further investigation about the pitting corrosion is necessary to the industrial application of metallic glass.

Acknowledgements

Author details

Shanlin Wang

Address all correspondence to: slwang70518@nchu.edu.cn

National Defense Key Discipline Laboratory of Light Alloy Processing Science and Technology, Nanchang hangkong university, Nanchang, China

References

[1] Naka M, Hashinoto K, Masumoto T. Effect of metalloidal elements on corrosion resistance of amorphous iron-chromium alloys. J. Non-Cryst. Solids. 1978; 28: 403–413.

[2] Liaw MMP. Bulk metallic glasses an overview. Springer. USA, 2008, p. 10.

[3] Scully J R, Gebert A, Payer J H. Corrosion and related mechanical properties of bulk metallic glasses. J. Mater. Res. 2007; 17(6): 302–313.

[4] Peter W H, Buchanan R A, Liu C T. Localized corrosion behavior of a zirconium-based bulk metallic glass relative to its crystalline state. Intermetallics. 2002; 10: 1157–1162.

[5] Klement W, Willens R H, Duwez P. Non-crystalline structure in solidified gold-silicon alloys. Nature. 1960; 187: 869–870.

[6] Li Y H, Zhang W, Inoue A. Effects of Ni addition on the glass-forming ability, mechanical properties and corrosion resistance of Zr–Cu–Al bulk metallic glasses. Mater. Sci. Eng. A. 2011; 528: 8551–8556.

[7] Li Y H, Zhang W, Inoue A. Glass-forming ability and corrosion resistance of Zr-based Zr–Ni–Al bulk metallic glasses. J. Alloys Compd. 2012; 536s: S117–S121.

[8] Kawashima A, Ohmura K, Inoue A. The corrosion behavior of Zr-based bulk metallic glasses in 0.5 M NaCl solution. Corr. Sci. 2011; 53: 2778–2784.

[9] Huang H H, Huang H M, Lin M C. Enhancing the bio-corrosion resistance of Ni-free ZrCuFeAl bulk metallic glass through nitrogen plasma immersion ion implantation. J. Alloys Compd. 2014; 615: s660–s665.

[10] Zhao G H, Aune R E, Mao H H. Degradation of Zr-based bulk metallic glasses used in load-bearing implants: a tribocorrosion appraisal. J. Mech. Behav. Biol. Mater. 2016; 60: 56–67.

[11] Hua N B, Huang L, Zhang T. Corrosion behavior and in vitro biocompatibility of Zr–Al–Co–Ag bulk metallic glasses: an experimental case study. 2012; 358: 1599–1640.

[12] Hua N B, Zhang T. Glass-forming ability, crystallization kinetics, mechanical property, and corrosion behavior of Zr–Al–Ni–Ag glassy alloys. J. Alloys Compd. 2014; 602: 339–345.

[13] Zhang C, Li N, Liu L. Enhancement of glass-forming ability and bio-corrosion resistance of Zr–Co–Al bulk metallic glasses by the addition of Ag. J. Alloys Compd. 2010; 504: s163–s167.

[14] Guan B R, Shi X T, Qin F X. Corrosion behavior, mechanical properties and cell cytotoxity of Zr-based bulk metallic glasses. Intermetallics. 2016; 72: 69–75.

[15] Nie X P, Xu X M, Jiang J Z. Effect of microalloying of Nb on corrosion resistance and thermal stability of ZrCu-based bulk metallic glasses. J. Non-Cryst. Solids. 2009; 355: 203–207.

[16] Li Y H, Zhang W, Qin F X. Mechanical properties and corrosion resistance of a new $Zr_{56}Ni_{20}Al_{15}Nb_4Cu_5$ bulk metallic glass with a diameter up to 25 mm. J. Alloys Compd. 2014; 615: s71–s74.

[17] Zhuang Y X, Wang S C, Wang C J. Effect of Ti on microstructure, mechanical and corrosion properties of $(Zr_{0.55}Al_{0.1}Ni_{0.05}Cu_{0.3})_{100-x}Ti_x$ bulk metallic glasses. Trans. Nonferrous Met. Soc. China. 2016; 26: 138–143.

[18] Liu Z Q, Huang L, Zhang T. Novel low Cu content and Ni-free Zr-based bulk metallic glasses for biomedical applications. J. Non-Cryst. Solids. 2013; 363: 1–5.

[19] Asami K, Qin C L, Zhang T. Effect of additional elements on the corrosion behavior of a Cu–Zr–Ti bulk metallic glass. Mater. Sci. Eng. A. 2004; 375: 235–239.

[20] Liu B, Liu L. Determination of isothermal section of Fe-Ni-Zr ternary system at 1198 K. Acta Metall. Sin. 2007; 20(6): 398–402.

[21] Qin C L, Asami K, Zhang T. The corrosion behavior of Zr-based bulk metallic glasses in 0.5 M NaCl solution. Mater. Trans. 2003; 44: 1042–1147.

[22] Pi J H, Pan Y, Wu J L. Influence of Minor Addition of In on corrosion resistance of Cu-based bulk metallic glasses in 3.5% NaCl solution. Rare Met. Mater. Eng. 2014; 43: 32–35.

[23] Chen S F, Lin S L, Chen J K. Thermal stability and corrosion behavior of Cu–Zr–Al–Y bulk metallic glass. Intermetallics. 2010; 18: 1954–1957.

[24] Zhang C Z, Wang J H, Qiu N N. Facile and large-scale syntheses of nanocrystal rare earth metal–organic frameworks at room temperature and their photoluminescence properties. J. Rare Earth. 2015; 33: 680–685.

[25] Zhang C Z, Qiu N N, Kong L L. Thermodynamic and structural basis for electrochemical response of Cu–Zr based metallic glass. J. Alloys Compd. 2015; 645: 487–490.

[26] Pang S J, Liu Y, Zhang T. New Ti-based Ti–Cu–Zr–Fe–Sn–Si–Ag bulk metallic glass for biomedical applications. J. Alloys Compd. 2015; 625: 323–327.

[27] Guo Y, Bataev I, Georgarakis K. Ni- and Cu-free Ti-based metallic glasses with potential biomedical application. Intermetallics. 2015; 63: 86–96.

[28] Fornell J, Pellicer E, Sort J. Improved plasticity and corrosion behavior in Ti–Zr–Cu–Pd metallic glass with minor additions of Nb: an alloy composition intended for biomedical applications. Mater. Sci. Eng. A. 2013; 559: 159–164.

[29] Liu N, Wu P H, Zhou P J. Rapid solidification and liquid-phase separation of undercooled CoCrCuFeNi high-entropy alloys. Intermetallics. 2016; 72: 44–52.

[30] Wang J F, Huang S, Li Y. Microstructure, mechanical and bio-corrosion properties of Mn-doped Mg–Zn–Ca bulk metallic glass composites. Mater. Sci. Eng. C. 2013; 33: 3832–3833.

[31] Gu X N, Zheng Y F, Zhong S P. Corrosion of, and cellular responses to Mg–Zn–Ca bulk metallic glasses. Biomaterials. 2010; 31: 1093–1103.

[32] Zhang X L, Chen G. The effects of microalloying on thermal stability, mechanical property and corrosion resistance of Mg-based bulk metallic glasses. J. Non-Cryst. Solids. 2012; 358: 1319–1323.

[33] Wang R R, Wang Y Y, Yang J. Influence of heat treatment on the mechanical properties, corrosion behavior, and biocompatibility of $Zr_{56}Al_{16}Co_{28}$ bulk metallic glass. J. Non-Cryst. Solids. 2015; 411: 45–52.

[34] Guo S F, Liu Z, Chan K C. A plastic Ni-free Zr-based bulk metallic glass with high specific strength and good corrosion properties in simulated body fluid. Mater. Lett. 2012; 84: 81–84.

[35] Fornell J, Steenberge N V, Varea A. Enhanced mechanical properties and in vitro corrosion behavior of amorphous and devitrified $Ti_{40}Zr_{10}Cu_{38}Pd_{12}$ metallic glass. J. Mech. Behav. Biol. Mater. 2011; 4: 1709–1717.

[36] Huang C H, Lai J J, Wei T Y. Improvement of bio-corrosion resistance for $Ti_{42}Zr_{40}Si_{15}Ta_3$ metallic glasses in simulated body fluid by annealing within supercooled liquid region. Mater. Sci. Eng. C. 2015; 52: 144–150.

[37] Gonzalez S, Pellicer E, Surinach S. Mechanical and corrosion behaviour of as-cast and annealed $Zr_{60}Cu_{20}Al_{10}Fe_5Ti_5$ bulk metallic glass. Intermetallics. 2012; 28: 149–155.

[38] Wang D P, Wang S L, Wang J Q. Relationship between amorphous structure and corrosion behaviour in a Zr–Ni metallic glass. Corr. Sci. 2012; 59: 88–95.

[39] Gu Y, Zheng Z, Niu S Z. The seawater corrosion resistance and mechanical properties of $Cu_{47.5}Zr_{47.5}Al_5$ bulk metallic glass and its composites. J. Non-Cryst. Solids. 2013; 380: 135–140.

[40] Wang J F, Huang S, Wei Y Y. Enhanced mechanical properties and corrosion resistance of a Mg–Zn–Ca bulk metallic glass composite by Fe particle addition. Mater. Lett. 2013; 91: 311–314.

[41] Zhang X L, Chen G, Bauer T. Mg-based bulk metallic glass composite with high bio-corrosion resistance and excellent mechanical properties. Intermetallics. 2012; 29: 56–60.

[42] Kai W, Kao P C, Chen W S . The oxidation behavior of a $Ti_{50}Cu_{28}Ni_{15}Sn_7$ bulk metallic glass at 400–500 °C. J. Alloys Compd. 2010; 504s: s180–s185.

[43] Subramanian B. In vitro corrosion and biocompatibility screening of sputtered $Ti_{40}Cu_{36}Pd_{14}Zr_{10}$ thin film metallic glasses on steels. Mater. Sci. Eng. C. 2014; 47: 48–56.

[44] Xie G Q, Qin F X, Zhou S L. Corrosion behaviour of porous Ni-free Ti-based bulk metallic glass produced by spark plasma sintering in Hanks' solution. Intermetallics. 2014; 44: 55–59.

[45] Gebert A, Gostin P F, Schultz L. Effect of surface finishing of a Zr-based bulk metallic glass on its corrosion behaviour. Corr. Sci. 2010; 52: 1711–1720.

[46] Gebert A, Consustell A, Greer A L. Effect of shot-peening on the corrosion resistance of a Zr-based bulk metallic glass. Scripta Mater. 2010; 62: 635–638.

[47] Gebert A, Gostin P F, Uhlemann M. Interactions between mechanically generated defects and corrosion phenomena of Zr-based bulk metallic glasses. Acta Mater. 2012; 60: 2300–2309.

[48] An W K, Cai A H, Xiong X. Effect of tension on corrosive and thermal properties of $Cu_{60}Zr_{30}Ti_{10}$ metallic glass. J. Alloys Compd. 2013; 563: 55–62.

[49] Pourgashti M H, Marzbanrad E, Ahnadi E. Corrosion behavior of $Zr_{41.2}Ti_{13.8}Ni_{10}Cu_{12.5}Be_{22.5}$ bulk metallic glass in various aqueous solutions. Mater. Des. 2010; 31: 2676–2679.

[50] Gebert A, Buchholz K, Eckert J. Hot water corrosion behaviour of Zr–Cu–Al–Ni bulk metallic glass. Mater. Sci. Eng. A. 2001; 316: 60–65.

[51] Ningshen S, Kamachi Mudali U, Krishnan R. Corrosion behavior of Zr-based metallic glass coating on type 304L stainless steel by pulsed laser deposition method. Surf. Coat. Technol. 2011; 205: 3961–3966.

[52] Cai A H, Xiong X, Liu Y. Corrosion behavior of $Cu_{55}Zr_{35}Ti_{10}$ metallic glass in the chloride media. Mater. Chem. Phys. 2012; 134: 938–944.

[53] Wang T, Wu Y D, Hui X D. Novel Ti-based bulk metallic glasses with superior plastic yielding strength and corrosion resistance. Mater. Sci. Eng. A. 2015; 642: 297–303.

[54] Guo S F, Chan K C, Jiang X Q. Atmospheric RE-free Mg-based bulk metallic glass with high bio-corrosion resistance. J. Non-Cryst. Solids. 2013; 379: 107–111.

[55] Gebert A, Mummert K, Eckert J. Electrochemical investigations on the bulk glass forming $Zr_{55}Cu_{30}Al_{10}Ni_5$ alloy. Mater. Corros. 1997; 48: 293–297.

[56] Vincent S, Khan A F, Bhatt J. Corrosion characterization on melt spun $Cu_{60}Zr_{20}Ti_{20}$ metallic glass: An experimental case study. J. Non-Cryst. Solids. 2013; 379: 48–53.

[57] Long Z L, Shao Y, Inoue A. Cr effects on magnetic and corrosion properties of Fe–Co–Si–B–Nb–Cr bulk glassy alloys with high glass-forming ability. Intermetallics. 2007; 15: 1453–1458.

[58] Pardo A, Otero E, Merino M C. The influence of Cr addition on the corrosion resistance of $Fe_{73.5}Si_{13.5}B_9Nb_3Cu_1$ metallic glass in marine environments. Corr. Sci. 2002; 44: 1193–1211.

[59] Pardo A, Merino M C, Otero E. Influence of Cr additions on corrosion resistance of Fe- and Co-based metallic glasses and nanocrystals in H_2SO_4. J. Non-Cryst. Solids. 2006; 352: 3179–3190.

[60] Wang S L, Yi S. The corrosion behaviors of Fe-based bulk metallic glasses in a sulfuric solution at 70 °C. Intermetallics. 2010; 18: 1950–1953.

[61] Wang Z M, Ma Y T, Wang J Q. Influence of yttrium as a minority alloying element on the corrosion behavior in Fe-based bulk metallic glasses. Electrochem. Acta. 2008; 54: 261–269.

[62] Long Z L, Chang C T, Inoue A. Corrosion behavior of Fe-based ferromagnetic (Fe, Ni)–B–Si–Nb bulk glassy alloys in aqueous electrolytes. J. Non-Cryst. Solids. 2008; 354: 4609–4613.

[63] Souza C A C, Mar J E, Kiminami C S. Influence of composition and partial crystallization on corrosion resistance of amorphous Fe–M–B–Cu (M = Zr, Nb, Mo) alloys. J. Non-Cryst. Solids. 2001; 284: 99–104.

[64] Zohdi H, Shahverdi H R, Hadavi S M M. Effect of Nb addition on corrosion behavior of Fe-based metallic glasses in Ringer's solution for biomedical applications. Electrochem. Commun. 2011; 13: 840–843.

[65] Kiminami C S, Souza C A C, Botta W J. Partial crystallization and corrosion resistance of amorphous Fe-Cr-M-B (M = Mo, Nb) alloys. J. Non-Cryst. Solids. 2010; 356: 2651–2657.

[66] Wang S L, Li H X, Yi S. Effects of Cr contents in Fe-based bulk metallic glasses on the glass forming ability and the corrosion resistance. Mater. Chem. Phys. 2009; 13: 878–883.

[67] Lopez M F, Escudero M L, Vida E. Corrosion behaviour of amorphous FeCrNi(Si,P) alloys. Electrochem. Acta. 1997; 42: 659–665.

[68] Pang S J, Zhang T, Inoue A. Bulk glassy Fe–Cr–Mo–C–B alloys with high corrosion resistance. Corros. Sci. 2002; 44: 1847–1856.

[69] Ha H M, Miller J R, Payer J H. Devitrification of Fe-based amorphous metal SAM 1651 and the effect of heat-treatment on corrosion behavior. Eletrochem. J. Soc. 2009; 156: 246–252.

[70] Baron A, Szewieczek D, Nawrat G. Corrosion of amorphous and nanocrystalline Fe-based alloys and its influence on their magnetic behavior. Electrochem. Acta. 2007; 52: 5690–5695.

[71] Souza C A C, May J E, Kiminami C S. Corrosion resistance of amorphous and nano-crystalline Fe–M–B (M Zr, Nb) alloys. J. Non-Cryst. Solids. 2000; 273: 282–288.

[72] Long Z L, Shen B L, Inoue A. Cr effects on magnetic and corrosion properties of Fe–Co–Si–B–N. Intermetallics. 2007; 15: 1453–1458.

[73] Marzo F F, Pierma A R, Vega M M. Effect of irreversible structural relaxation on the electrochemical behavior of $Fe_{78-x}Si_{13}B_9Cr$ (x = 3, 4, 7) amorphous alloys. J. Non-Cryst. Solids. 2003; 329: 108–114.

[74] Souza C A C, Kuri S E, Politti F S. Corrosion resistance of amorphous and polycrystal-line FeCuNbSiB alloys in sulphuric acid solution. J. Non-Cryst. Solids. 1999; 247: 69–73.

[75] Liu G, An Y L, Chen J M. Structure and corrosion behavior of iron-based metallic glass coatings prepared by LPPS. Appl. Surf. Sci. 2012; 258: 5380–5386.

[76] Zhou Z, Wang L, Wang F C. Formation and corrosion behavior of Fe-based amorphous metallic coatings by HVOF thermal spraying. Surf. Coat. Technol. 2009; 204: 563–570.

[77] Zhang S D, Zhang W L, Wang J Q. Characterisation of three-dimensional porosity in an Fe-based amorphous coating and its correlation with corrosion behaviour. Corr. Sci. 2015; 93: 211–221.

[78] Wang S L, Cheng J C, Yi S. Corrosion resistance of Fe-based amorphous metallic matrix coating fabricated by HVOF thermal spraying. Trans. Nonferrous Met. Soc. China. 2014; 24: 146–151.

[79] Cui C, Hou W. Properties of Fe-based amorphous alloy coatings with Al_2O_3–13% TiO_2 deposited by plasma spraying. Rare Met. Mater. Eng. 2014; 43: 2576–2579.

[80] Yasir M, Zhang C, Liu L. Wear behaviors of Fe-based amorphous composite coatings reinforced by Al_2O_3 particles in air and in NaCl solution. Mater. Des. 2015; 88: 207–213.

[81] Yugeswarn S, Kobayashi A. Characterization of gas tunnel type plasma sprayed TiN reinforced Fe-based metallic glass coatings. J. Alloys Compd. 2013; 551: 168–175.

[82] Zhou H, Zhang C, Wang W. Microstructure and mechanical properties of Fe-based amorphous composite coatings reinforced by stainless steel powders. J. Mater. Sci. Technol. 2014; 31: 43–47.

[83] Zhu Y Y, Li Z G, Li R F. Microstructure and property of Fe–Co–B–Si–C–Nb amorphous composite coating fabricated by laser cladding process. Appl. Surf. Sci. 2013; 280: 50–54.

[84] Pang S J, Zhang T, Inoue A. Synthesis of Fe–Cr–Mo–C–B–P bulk metallic glasses with high corrosion resistance. Acta Mater. 2002; 50: 489–497.

[85] Wang Y, Jiang S L, Wang J Q. Electrochemical behaviour of Fe-based metallic glasses in acidic and neutral solutions. Corr. Sci. 2012; 63: 159–173.

[86] Qiao D C, Green B, Morrison M. Bulk metallic glass. Rev. Adv. Mater. Sci. 2008; 18: 149–153.

[87] Czachor M J. Effect of nitrogen and sensitization on the microstructure and pitting corrosion behavior of AISI Type 316LN stainless steels. ISIJ Int. 1991; 31: 1170–1178.

[88] Patsalas P, Lekatou A, Pavlidou E. Surface properties and activity of Fe–Ni–B ternary glasses. J. Alloys Compd. 2007; 434: 229–233.

[89] Li H X, Yi S. Corrosion behaviors of bulk metallic glasses $Fe_{66.7}C_{7.0}Si_{3.3}B_{5.5}P_{8.7}Cr_{2.3}Al_{2.0}Mo_{4.5}$ having different crystal volume fractions. Mater. Chem. Phys. 2008; 112: 305–309.

[90] Wang Y B, Li H F, Zheng Y F. Corrosion performances of a nickel-free Fe-based bulk metallic glass in simulated body fluids. Electrochem. Commun. 2009; 11: 2187–2190.

[91] Zhou Z, Wang L, He D Y. Effect of feed stock particle sizes on wear resistance of plasma sprayed Fe-based amorphous coatings. Surf. Coat. Technol. 2011; 20: 495–502.

[92] Wang L, Chao Y S. Corrosion behavior of $Fe_{41}Co_7Cr_{15}Mo_{14}C_{15}B_6Y_2$ bulk metallic glass in NaCl solution. Mater. Lett. 2012; 69: 76–78 .

[93] Guo S F, Chan K C, Xie S H. Novel centimeter-sized Fe-based bulk metallic glass with high corrosion resistance in simulated acid rain and seawater. J. Non-Cryst. Solids. 2013; 369: 29–33.

[94] Botta W J, Berger J E, Kiminami C S. Corrosion resistance of Fe-based amorphous alloys. J. Alloys Compd. 2014; 586: s105–s110.

[95] Lekatou A, Marinou A, Patsalas P. Aqueous corrosion behaviour of Fe–Ni–B metal glasses. J. Alloys Compd.. 2009; 48: 514–518.

[96] Poon S J, Shiflet G. J, Guo F Q. Glass formability of ferrous- and aluminum-based structural metallic alloys. J. Non-Cryst. Solids. 2003; 317: 1–9.

[97] Shan X, Ha H, Payer J H. Comparison of crevice corrosion of Fe-based amorphous metal and crystalline Ni-Cr-Mo alloy. Metall. Mater. Trans. A. 2009; 40: 1324–1333.

[98] Fornell J, Gonzalez S, Sort J. Deformation and fracture behavior of corrosion-resistant, potentially biocompatible $Ti_{40}Zr_{10}Cu_{38}Pd_{12}$ bulk metallic glass. J. Alloys Compd. 2012; 536: s74–s77.

[99]   Hua N B, Zheng Z Q, Fang H. Dry and lubricated tribological behavior of a Ni- and Cu-free Zr-based bulk metallic glass. J. Non-Cryst. Solids. 2015; 426: 63–71.

[100] Kou H C, Li Y, Zhang T. Electrochemical corrosion properties of Zr- and Ti-based bulk metallic glasses. Trans. Nonferrous Met. Soc. China. 2011; 21: 552–557.

[101] Green B A, Steward R V, Kim I. In situ observation of pitting corrosion of the $Zr_{50}Cu_{40}Al_{10}$ bulk metallic glass. Intermetallics. 2009; 17: 568–571.

[102] Nie X P, Cao Q P, Jiang J Z. The pitting corrosion behavior of shear bands in a Zr-based bulk metallic glass. Scripta Mater. 2012; 67: 376–379.

[103] Gosin P F, Gebert A, Schultz L. Comparison of the corrosion of bulk amorphous steel with conventional steel. Corr. Sci. 2010; 52: 273–281.

[104] Gostin P F, Oswald S, Gebert A. Acid corrosion process of Fe-based bulk metallic glass. Corr. Sci. 2012; 62: 112–121.

[105] Zhang C, Chan K C, Liu L. Pitting initiation in Fe-based amorphous coatings. Acta. Mater. 2012; 60: 4152–4159.

[106] Paillier J, Mickel C, Flaviu P. Characterization of corrosion phenomena of Zr–Ti–Cu–Al–Ni metallic glass by SEM and TEM. Mater. Charact. 2010; 61: 1000–1008.

[107] Ertl G, Knozinger H, Weitkamp J. Preparation of solid catalysts. Springer, USA. 1999; p. 43.

[108] Carim A I, Saadi F H, Levis N S. Stabilization of n-cadmium telluride photoanodes for water oxidation to $O_2(g)$ in aqueous alkaline electrolytes using amorphous TiO_2 films formed by atomic-layer deposition. J. Mater. Chem. A. 2014; 2: 138–35.

[109] Jukic A, Piljac J, Hukovic M M. Electrocatalytic behavior of the $Co_{33}Zr_{67}$ metallic glass for hydrogen evolution. A: Chemical, 2001, 166: 293–302.

[110] Hukovic M M, Jukic A. Correlation of electronic structure and catalytic activity of Zr–Ni amorphous alloys for the hydrogen evolution reaction. Electrochim. Acta. 2000; 45: 4159–4170.

[111] Mihailov L, Spassov T, Bojinov M. Effect of microstructure on the electrocatalytic activity for hydrogen evolution of amorphous and nanocrystalline Zr–Ni alloys. Inter. J. Hydrogen Energy. 2012; 37: 10499–10506.

[112] Ramos-sanchez G, Pierna A R, Solorza-Feria O. Amorphous $Ni_{59}Nb_{40}Pt_xM_{1-x}$ (M = Ru, Sn) electrocatalysts for oxygen reduction reaction. J. Non-Cryst. Solids. 2008; 354: 5165–5168.

[113] Jiang J H, Zhai R S, Bao X H. Electrocatalytic properties of Cu–Zr amorphous alloy towards the electrochemical hydrogenation of nitrobenzene. J. Alloys Compd. 2003; 354: 248–258.

[114] Sun S G, Lipkowski J. Altounian Z. Electrocatalytic oxidation of formic acid and methanal at the amorphous $Pt_{66}Sb_{34}$ Electrode. J. Electrochem. Soc. 1990; 137: 2443–2451.

[115] Dan Z H, Qin F X, Wada T. Nanoporous palladium fabricated from an amorphous $Pd_{42.5}Cu_{30}Ni_{7.5}P_{20}$ precursor and its ethanol electro-oxidation performance. Electrochim. Acta. 2013; 108: 512–519.

[116] Brunelli K, Dabala M, Frattini R. Structural characterization and electrocatalytic properties of $Au_{30}Zr_{70}$ amorphous alloy obtained by rapid quenching. J. Appl. Electrochem. 2003; 33: 995–1000.

[117] Yokoyama A, Komiyama H, Inoue H. The hydrogenation of carbon monoxide by amorphous ribbons. J. Catal. 1981; 68: 355–361.

[118] Kisfaludi G, Kazar K, Schay Z. Surface characterization and catalytic $CO + H_2$ reaction on $Fe_{82.2}B_{17.8}$ amorphous alloy. Appl. Surf. Sci. 1985; 24: 225–238.

[119] Baiker A, Schlogl R, Armbruster E. New catalytic materials from amorphous metal alloys. J. Catal. 1989; 107: 329–383.

[120] Carturan G, Cocco G. Amorphous and crystalline FeNiCrPB alloys as catalysts for acetylene hydrogenation. J. Catal. 1984; 90: 178–181.

[121] Kovocs P, Ando T, Ishiwatari M. Electrochemical studies on the potentiostatic hydrogenatiaon of amorphous $Fe_{90}Zr_{10}$ and $Fe_{91}Hf_9$ alloys. J. Electrochem, Soc. 1989; 136: 1958–1961.

[122] Paseka I, Velika J. Hydrogen evolution and hydrogen sorption on amorphous smooth MeP(x) (MeNi, Co and FeNi) electrodes. Electrochem. Acta. 1997; 42: 237–242.

[123] Alemu H, Juttner K. Characterization of the electrocatalytic properties of amorphous metals for oxygen and hydrogen evolution by impedance measurements. Electrochem. Acta. 1988; 33: 1101–1109.

[124] Trudeau M L, Huot J Y, Schulz R. The crystallization of amorphous $Fe_{60}Co_{20}Si_{10}B_{10}$ and its effect on the electrocatalytic activity for H_2 evolution. J. Appl. Phys. 1990; 67: 2333–2342.

[125] Crousier J, Crousier J P, Bellucci F. Electrochemical and electrocatalytic behaviour of iron-base amorphous alloys in 1 M KOH at 25°C. Electrochem. Acta. 1993; 38: 821–825.

[126] Crousier J, Crousier J P, Bellucci F. Anodic dissolution and electrocatalytic properties of $Fe_{60}Co_{20}Si_{10}B_{10}$ amorphous alloy in 1 M KOH. Corros. Sci. 1994; 36: 995–1055.

[127] Albertos F, Harji B H, Kenney C N. Catalytic behaviour of some glassy alloys to the Fischer-Tropsch reaction at high pressures. Appl. Catal. 1990; 65: 85–100.

[128] Guczi L, Kisfaludi G, Schay Z. Surface structure and catalytic activity of rapidly quenched amorphous iron based alloys. III. Effect of surface composition. Appl. Surf. Sci. 1989; 35: 469–480.

[129] Brookes H C, Carruthers C M. The electrochemical and electrocatalytic behaviour of glassy metals. J. Appl. Electrochem. 2005, 35: 903–913.

[130] Trudeau M L, Huot J Y, Schulz R. Nanocrystalline Fe-(Co,Ni)-Si-B: The mechanical crystallization of amorphous alloys and the effects on electrocatalytic reactions. Phys. Rev. B. 1992; 45: 4626–4636.

[131] Niu Z J, Wu T H, Yang F Z. Electrocatalytic activity of electrodeposited amorphous Fe-Mo alloy for hydrogen evolution reaction in alkaline solution. Mater. Protection. 2003; 36: 9–12.

[132] Wang S L, Kim D H, Yi S. Electrocatalytic properties of Fe-based bulk metallic glasses for hydrogen evolution reaction. Korean J. Chem. Eng. 2011; 28: 1672–1676.

[133] Heusler K E, Huerta D. Kinetics and mechanisms of the anodic dissolution of metallic glasses. J. Electrochem. Soc. 1988; 136: 65–71.

Structure and Mechanical Behaviour of Cu-Zr-Ni-Al Amorphous Alloys Produced by Rapid Solidification

Celal Kursun and Musa Gogebakan

Additional information is available at the end of the chapter

Abstract

The amorphous ribbons of $Cu_{50}Zr_{40}Ni_5Al_5$ alloy were manufactured by rapid solidification. The ribbons were investigated by X-ray diffraction (XRD), scanning electron microscopy coupled with energy dispersive spectroscopy (SEM-EDX) and differential scanning calorimetry (DSC). The activation energy of the crystallisation in amorphous alloys was determined by Kissenger technique. The mechanical properties of the ribbons were characterized using Vickers microhardness (HV) tester. According to the XRD and SEM results, the $Cu_{50}Zr_{40}Ni_5Al_5$ alloys have a fully amorphous structure. The EDX analysis of the ribbons showed that compositional homogeneity of the $Cu_{50}Zr_{40}Ni_5Al_5$ alloy was fairly high. From the DSC curves of the amorphous ribbons, it was determined that glass transition temperature (T_g) is around 440–442°C and super-cooled liquid region ($\Delta T_x = T_x - T_x$) before crystallisation is around 61–64°C. The microhardness of the as-quenched ribbons was measured about 550 HV. However, this microhardness value decreased with increasing annealing temperature and it was calculated about 465 HV after annealing temperature of 800°C.

Keywords: rapid solidification, microhardness, copper-based alloy, crystallisation, Kissenger plot

1. Introduction

Amorphous alloys, with high corrosion resistant, ultrahigh strength and soft ferromagnetic and mechanical properties, have widely been the subject of intense investigation [1–4]. These excellent properties stem from their high chemical and structural homogeneous creation. Besides, it is possible to synthesise the amorphous alloys without restriction a wide chemical composition range. Amorphous alloys are used in many applications such as defence, electri-

cal, welding, automobile and aircrafts industries. Cu-based amorphous alloys are optimal materials because of their excellent mechanical properties and high electrical and thermal conductivities for these applications [5, 6]. In addition to these applications, copper alloys are also used as the rocket nozzles, high-performance switches, the heat exchangers, the condenser tubes of ships [7, 8].

Cu-based amorphous alloys can be produced by many different techniques such as rapid solidification, mechanical alloying, vapour depositions, plasma processing and solid state reactions. In the rapid solidification method, the amorphous alloys are manufactured on thin ribbons forms, which are usually ductile and bright surface. Many Cu-based binary, ternary, quaternary and quinary alloys have been manufactured by these methods [9–15]. In this work, Cu-Zr-Ni-Al quaternary amorphous alloys are produced by rapid solidification technique at wheel surface velocities of 35 and 41 ms^{-1} as ribbons forms with very flexible. The effects of the wheel surface velocities and different annealing process on mechanical and microstructural properties of produced ribbons are systematically investigated. Therefore, it has been revealed the amorphous nature of $Cu_{50}Zr_{40}Ni_5Al_5$ ribbon alloys in order to contribute the continuously improving Cu-based alloys in industry.

2. Methods and materials

An ingot of the $Cu_{50}Zr_{40}Ni_5Al_5$ (at.%) alloy was prepared by arc melting the mixtures of the pure elements, Cu (99.7%), Zr (99.9%), Ni (99.5%) and Al (99.99%) in a titanium-gettered argon atmosphere. From this alloy, ribbon materials of approximately 75 μm thickness and 5 mm in width were manufactured by a single-roller Edmund Bühler melt spinner at wheel surface velocities of 35 and 41 ms^{-1}. The structure of the ribbon samples was examined by XRD using a Philips X'Pert powder diffractometer with Cu-Kα radiation generated at 40 kV and 30 mA. The transformations temperatures and heat effects during transformations were examined by Perkin-Elmer Sapphire DSC unit under inert gas atmosphere using continuous heating mode with the heating rate of 40 K min^{-1}. Moreover, the DSC analysis was carried out for the melt-spun ribbon at wheel speed of 35 ms^{-1} using continuous heating mode with the heating rates of 5–40 K min^{-1}. The cross section of the melt-spun ribbons was studied by Zeiss Evo LS10 SEM and SEM-EDX after conventional metallographic preparation. The ribbons were annealed for 30 min at different temperatures under vacuum/inert gas atmosphere. These temperature values are 300, 580, 680 and 800°C. The annealed ribbons were investigated by XRD from surface, SEM from cross-section with the same conditions used for as-quenched ribbons. The Vickers microhardness measurements of the as-quenched and subsequently annealed ribbons were performed using a Shimadzu HMV-2 by an applied load of 0.98 N with a dwell time of 10 s at ten different locations.

3. Results and Discussion

Figure 1 shows the X-ray diffraction patterns of the rapidly solidified $Cu_{50}Zr_{40}Ni_5Al_5$ ribbons produced at wheel surface velocities of 35 and 41 ms^{-1}. As shown in **Figure 1**, the XRD patterns

exhibit the broad maxima characteristic which is feature of amorphous materials without the evidence of any crystalline peaks. This means that the surface velocities of 35 and 41 ms^{-1} are optimal to synthesize $Cu_{50}Zr_{40}Ni_5Al_5$ alloy as fully amorphous structure.
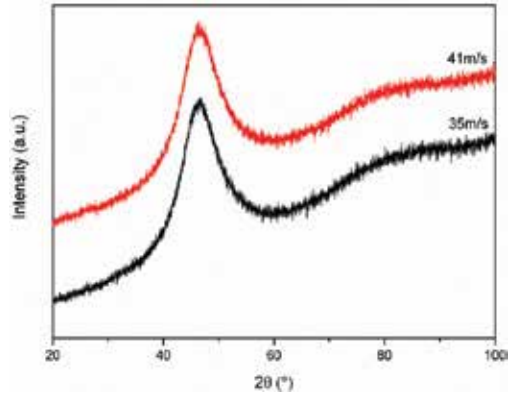
Figure 1. XRD pattern of the melt-spun $Cu_{50}Zr_{40}Ni_5Al_5$ ribbons prepared at wheel speeds of 35 and 41 ms^{-1} as-quenched.

DSC traces of amorphous $Cu_{50}Zr_{40}Ni_5Al_5$ alloys at wheel speeds of 35 and 41 ms^{-1} at a heating rate of 40 K min^{-1} display distinct and an obvious glass transition temperature, T_g, before crystallisation, as shown in **Figure 2**. From the DSC curves, it is seen a wide super-cooled liquid temperature range followed by a pronounced exothermic reaction for both ribbon alloys. **Table 1** summarises the characteristic temperatures which are glass transition temperature (T_g), crystallisation temperature (T_x), super-cooled liquid region (ΔT_x ($\Delta T_x = T_x - T_g$)), and peak temperature (T_p) of the $Cu_{50}Zr_{40}Ni_5Al_5$ alloy. According to the **Table 1**, T_x, ΔT_x and T_p increase while T_g decreases with increasing melt-spun wheel surface velocity.
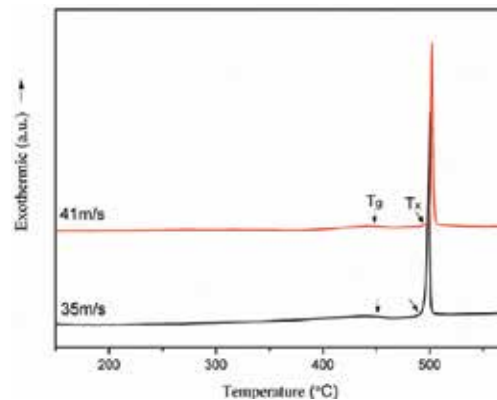
Figure 2. The DSC curves of the $Cu_{50}Zr_{40}Ni_5Al_5$ ribbon alloys at wheel speeds of 35 and 41 ms^{-1} obtained during heating at a heating rate of 40 K min^{-1}.

Wheel speed/ms^{-1}	T$_g$/°C	T$_x$/°C	ΔT$_x$/°C	T$_p$/°C
35	442	503	61	507
41	440	504	64	509

Table 1. Thermal values obtained from DSC curves for melt-spun Cu$_{50}$Zr$_{40}$Ni$_5$Al$_5$ ribbons at different wheel speed.

Figure 3 exhibits the DSC curves at 5, 10, 20 and 40 K min^{-1} of the ribbon alloy which are manufactured at wheel speeds of 35 ms^{-1}. The obtained peak temperature values, T_g, T_x, T_p and the super-cooled liquid region (ΔT_x) from **Figure 3** are presented **Table 2**. As can be seen **Table 2**, T_g, T_x, T_p and ΔT_x values are moved to higher temperatures with increasing heating rate. It is attributed the heating rate which are depended on the parameters of crystallisation and glass transition during continuous heating [7, 16]. Therefore, this case reveals the significant of the kinetic aspects of the glass transition for glassy alloys [17].
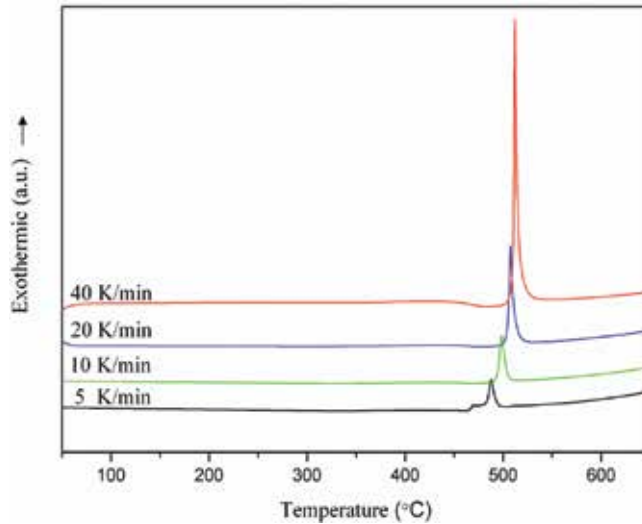
Figure 3. DSC analysis results for the melt-spun ribbon prepared at wheel speed of 35 ms^{-1} using continuous heating mode with the heating rates of 5–40 K min^{-1}.

φ (K/min)	T$_g$/K	T$_x$/K	ΔT$_x$/K	T$_p$/K
5	703	761	58	764
10	708	766	58	771
20	715	776	61	780
40	723	783	60	785

Table 2. Thermal values obtained from DSC curves for rapidly solidified Cu$_{50}$Zr$_{40}$Ni$_5$Al$_5$ amorphous ribbons manufactured at wheel speed of 35 ms^{-1} at different heating rates.

The activation energy (E) for glass transition or crystallisation is commonly estimated by the Kissinger [18] equation. The Eq. (1) is given below. To calculate activation energy of the amorphous alloys with this equation, it is necessary to use data from different heating rates of the alloy

$$\ln\left(\frac{\phi}{T^2}\right) = -\frac{E}{RT} + A \tag{1}$$

where T is the specific temperature, glass transition temperature (T_g), crystallisation temperature (T_x), or peak temperature (T_p), of crystallisation, φ is the heating rate, R is the gas constant (8.314 J/mol K), E is the activation energy, A is a constant. By plotting $\ln(\varphi/T^2)$ versus $1/(RT)$, nearly a straight line is obtained. From the slope of this straight line, the activation energies E_g, E_x or E_p are calculated using the certain peak temperatures (T_g, T_x, T_p). **Figure 4** shows the Kissenger plots of $Cu_{50}Zr_{40}Ni_5Al_5$ ribbon alloy produced at wheel speed of 35 ms^{-1}. From the Kissenger plots, the activation energies of E_g, E_x and E_p are determined 421.35 (±12), 432.26 (±9) and 403.05 (±6) kJ/mol, respectively. These values are very high compared with previous studies whose activation energies are $E_x = 393$, $E_p = 381$ kJ/mol for $Cu_{50}Zr_{40}Ni_5Al_5$ alloy [7], $E_g = 357$, $E_x = 297$, $E_p = 289$ kJ/mol for $Cu_{52.5}Zr_{11.5}Ti_{30}Ni_6$ [19] and $E_g = 377$, $E_x = 307$, $E_p = 340$ kJ/mol for $Cu_{45}Zr_{45}Ag_7Al_3$ alloy [20]. On the other hand, it is also possible to mention that the amorphous $Cu_{50}Zr_{40}Ni_5Al_5$ alloy has very high thermodynamic stability with $E_x = 432.26$ kJ/mol value compared with previous works.
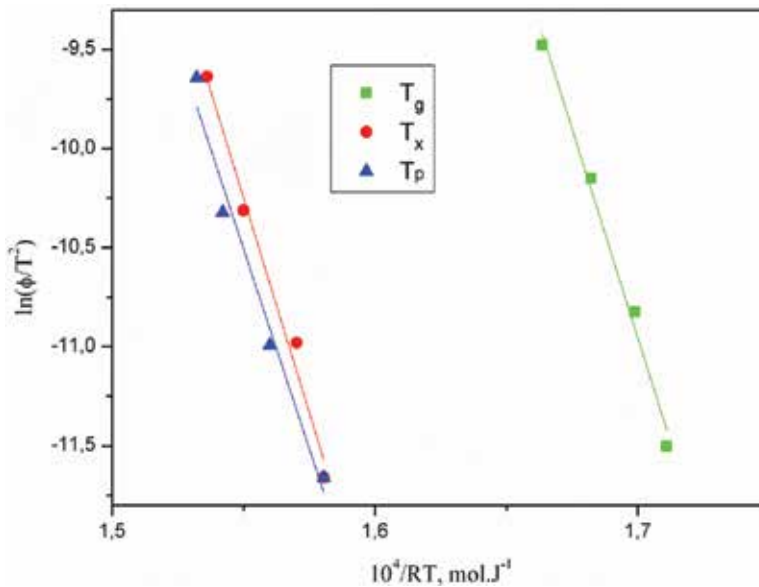
Figure 4. Kissinger plots of the amorphous $Cu_{50}Zr_{40}Ni_5Al_5$ alloy produced at wheel speed of 35 ms^{-1}.

The annealing of the amorphous alloys is a significant process to characterise their crystallisation behaviour. Thus, it might be revealed that the amorphous structure transforms into what kind of crystalline phases with increasing annealing temperature. For this purpose, the melt-spun ribbon of $Cu_{50}Zr_{40}Ni_5Al_5$ alloy synthesised at wheel speed of 35 ms^{-1} was annealed in the temperature range of 300–800°C for 30 min. **Figure 5** shows the XRD patterns of $Cu_{50}Zr_{40}Ni_5Al_5$ alloy after annealing. According to **Figure 5**, before exothermic reaction, the XRD pattern of $Cu_{50}Zr_{40}Ni_5Al_5$ alloy with annealed of 300°C exhibits fully an amorphous structure. After the annealing temperature of 580°C, intermetallic phases with sharp diffraction peaks have been obtained from the amorphous matrix and fully crystallisation of the amorphous phase. This result is in good agreement with crystallisation peak in DSC traces which is above 503°C. The obtained phases in the XRD spectrum were marked by symbols and indexed as cubic-$AlCu_2Zr$ with lattice parameters, $a = b = c = 6215$ Å, orthorhombic-$Cu_{10}Zr_7$ with lattice parameters, $a = 9347$; $b = 9322$; $c = 12,976$ Å, tetragonal-Zr_2Cu with lattice parameters, $a = 3220$; $b = 3220$; $c = 11,183$ Å and f.c.c-Cu with lattice parameters, $a = b = c = 3615$ Å. These phases were also observed in previous works after a similar annealing process for Cu-based amorphous alloys [7, 20–22]. Number of the crystalline peaks which belongs to $AlCu_2Z$, $Cu_{10}Zr_7$, Zr_2Cu and Cu phases was increased by increasing annealing temperature (800°C), as shown in **Figure 5**.
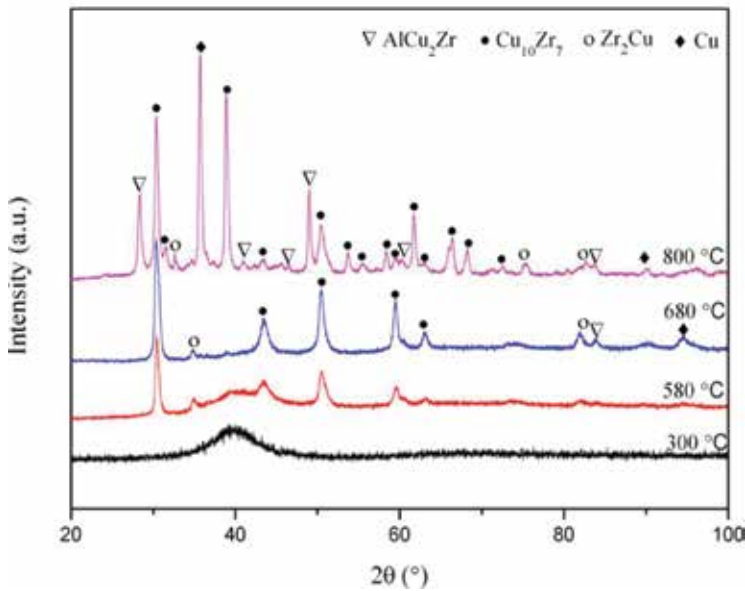
Figure 5. XRD pattern of the melt-spun ribbon of $Cu_{50}Zr_{40}Ni_5Al_5$ alloy manufactured at a wheel speed of 35 ms^{-1} and annealed in the temperature range of 200–800°C for 30 min.

In addition to XRD patterns of annealed ribbons, typical SEM micrographs from cross section of the amorphous $Cu_{50}Zr_{40}Ni_5Al_5$ alloy prepared at a wheel speed of 35 ms^{-1} as well as annealing ribbons at 300, 580, 680 and 800°C are shown in **Figure 6**. In **Figure 6a**, **b**, the microstructure

with featureless morphology of unannealed and annealed at 300°C ribbons are exhibited. This featureless morphology is a typical characteristic of the amorphous materials. In previous works, similar SEM images taken surface of amorphous structured materials were reported [7, 23, 24]. These micrographs are in accord with the XRD spectrums which exhibit fully amorphous features unannealed (**Figure 1**) and annealed at 300°C ribbons (**Figure 5**). As can be seen obviously in **Figure 6c–e**, with increasing annealing temperature (580, 680, 800°C), the microstructure of $Cu_{50}Zr_{40}Ni_5Al_5$ ribbon alloys changes and transforms into irregularly shaped features which is a characteristic of crystalline structures. These crystalline structures belong to $AlCu_2Zr$, $Cu_{10}Zr_7$, Zr_2Cu or Cu phases obtained by XRD patterns (**Figure 5**)
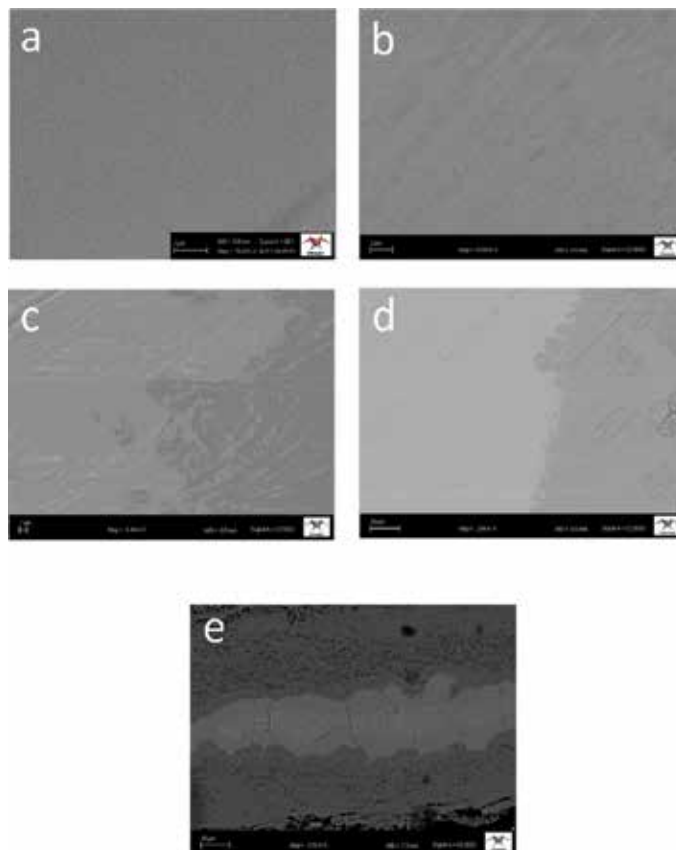
Figure 6. Typical SEM images from the cross section of the melt-spun ribbon of $Cu_{50}Zr_{40}Ni_5Al_5$ alloy prepared at a wheel speed of 35 ms^{-1}. (a) As-quenched and annealed at the temperatures, (b) 300°C, (c) 580°C, (d) 680°C, and (e) 800°C.

The compositional homogeneity of the amorphous $Cu_{50}Zr_{40}Ni_5Al_5$ ribbons was by measured EDX in order to confirm initially intended composition values. The EDX analysis illustrates mean values of element concentrations of $Cu_{50}Zr_{40}Ni_5Al_5$ alloy produced at a wheel speed of

35 ms^{-1} in **Figure 7**. As can be seen obviously from the EDX results, the peaks in the spectrum belong to Cu, Zr, Ni and Al elements. As shown in **Figure 7**, the average chemical composition of the ribbon alloy is in good agreement with the chemical composition values of $Cu_{50}Zr_{40}Ni_5Al_5$ alloy.
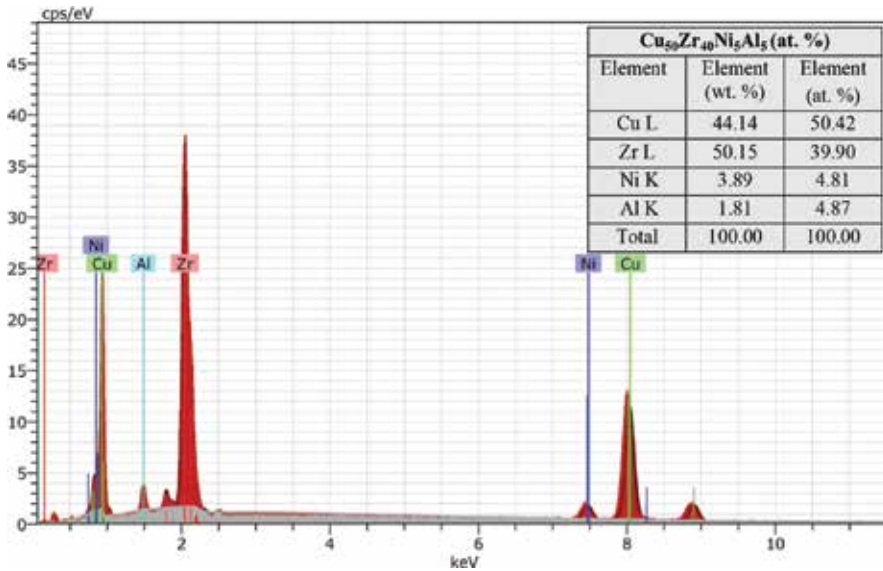

Figure 7. EDX analysis result of the melt-spun ribbon of $Cu_{50}Zr_{40}Ni_5Al_5$ alloy produced at a wheel speed of 35 ms^{-1} as-quenched.

In order to determine the influence of annealing on the microhardness of the $Cu_{50}Zr_{40}Ni_5Al_5$ ribbon alloys which are as-quenched and annealed at different temperatures such as 200, 275, 400, 500, 600 and 800°C, Vickers HV measurements were analysed. The following Eq. (2) was used for these measurements [25]

$$HV = \frac{2P\sin(\theta/2)}{d^2} = \frac{1.8544(P)}{d^2} \tag{2}$$

where P is the indentation force, d is the mean diagonal length, and 1.854 is the geometrical factor for the diamond pyramid. **Figure 8** shows the variation of microhardness values with increasing annealing temperature for $Cu_{50}Zr_{40}Ni_5Al_5$ alloy prepared at wheel speed of 35 ms^{-1}. As shown in **Figure 8**, the hardness values decrease with increasing annealing temperature. In previous works, this decline of the hardness values with the annealing temperature is generally reported for Cu-based amorphous alloys [7, 26–31]. The microhardness of as-quenched ribbon was calculated 550 HV, while it was determined 532–470 HV for annealed ribbons in the range of 200–500°C (**Figure 8**). At the temperature range of 500–800°C, the

microhardness values of the $Cu_{50}Zr_{40}Ni_5Al_5$ alloy were not changed distinctly and it was determined as approximately 465 HV. Thus, it can easily be concluded that the highest microhardness value (550 HV) of the $Cu_{50}Zr_{40}Ni_5Al_5$ alloy was measured for as-quenched ribbon alloy.
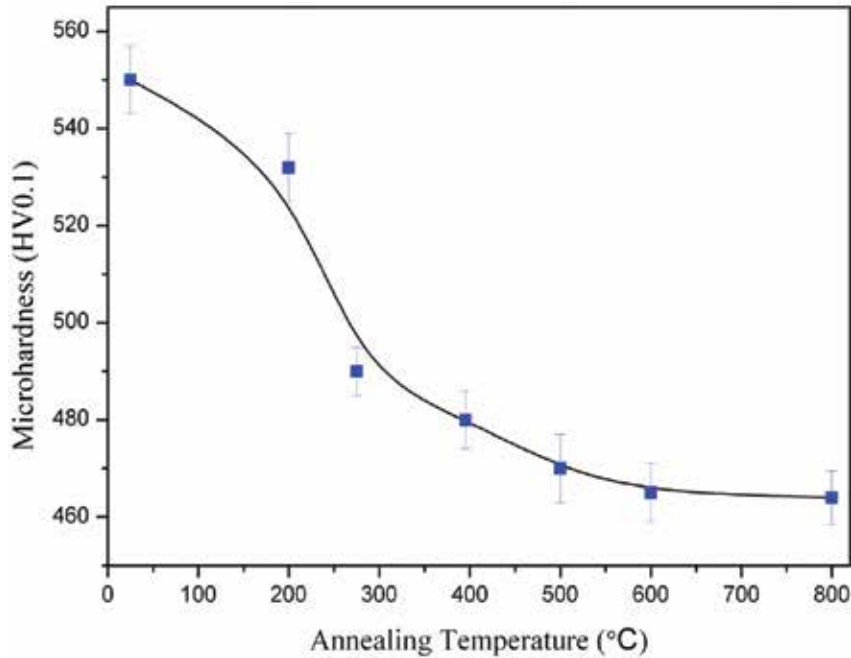
Figure 8. The change in Vickers microhardness values for $Cu_{50}Zr_{40}Ni_5Al_5$ alloy prepared by the wheel speed of 35 ms^{-1}with annealing temperatures.

4. Conclusions

1. The metallic glass $Cu_{50}Zr_{40}Ni_5Al_5$ alloys were successfully produced by rapid solidification technique at wheel speeds of 35 and 41 ms^{-1}.

2. DSC traces of the $Cu_{50}Zr_{40}Ni_5Al_5$ alloys showed similar distinct glass transition, T_g which are around 440–442°C. The ribbon alloys exhibited also wide super-cooled liquid regions, ΔT_x which are 61–64°C.

3. The activation energies of E_g, E_x and E_p for $Cu_{50}Zr_{40}Ni_5Al_5$ alloy prepared at wheel speed of 35 ms^{-1} were determined 421.35 (±12), 432.26 (±9) and 403.05 (±6) kJ/mol, respectively.

4. The intermetallic $AlCu_2Zr$, $Cu_{10}Zr_7$, Zr_2Cu and Cu phases in the microstructure of $Cu_{50}Zr_{40}Ni_5Al_5$ alloy were observed after annealing temperature of 800°C.

5. The compositional homogeneity of $Cu_{50}Zr_{40}Ni_5Al_5$ as-quenched ribbons was most correctly confirmed by EDX.

6. The microhardness value of $Cu_{50}Zr_{40}Ni_5Al_5$ alloy was calculated approximately 550 HV for unannealed ribbons. However, it decreased with increasing annealing temperatures and was measured about 465 HV after annealing temperature of 800°C.

Acknowledgements

Author details

Celal Kursun[*] and Musa Gogebakan

*Address all correspondence to: celalkursun@ksu.edu.tr

Department of Physics, Faculty of Art and Sciences, Kahramanmaras Sutcu Imam University, Kahramanmaras, Turkey

References

[1] A. Boutahara, H. Lassria, E.K. Hlilb, D. Fruchart, Critical behavior and its correlation with magnetocaloric effect in amorphous $Fe_{80-x}V_xB_{12}Si_8$ (x = 8, 10 and 13.7) alloys. Journal of Magnetism and Magnetic Materials. 2016;398:26–31.

[2] K. Tomolya, D. Janovszky, A. Sycheva, M. Sveda, T. Ferenczi, A. Roósz, Peculiarities of ball-milling induced crystalline–amorphous transformation in Cu–Zr–Al–Ni–Ti alloys. Intermetallics. 2015; 65:117–121.

[3] Y. Ying-Jun, K. Fu-Wei, X. Da-Wei, S. Jian-Fei, S. Qing-Ke, S. Jun, Formation and mechanical properties of bulk Cu–Ti–Zr–Ni metallic glasses with high glass forming ability. Transactions of Nonferrous Metals Society of China. 2007;17:16–20.

[4] C.K. Kim, H.S. Lee, S.Y. Shin, J.C. Lee, D.H. Kim, S. Lee, Microstructure and mechanical properties of Cu-based bulk amorphous alloy billets fabricated by spark plasma sintering. Materials Science and Engineering: A. 2005;406:293–299.

[5] A. Inoue, K. Hashimoto, Amorphous and nano-crystalline materials, preparation, properties and application. Berlin: Springer, 2001.

[6]   M. Gogebakan, C. Kursun, J. Eckert, Formation of new Cu-based nanocrystalline powders by mechanical alloying technique. Powder Technology. 2013;247:172–177.

[7]   C. Kursun, M. Gogebakan, Y. Gencer, Microstructural characterization of rapidly solidified $Cu_{50}Zr_{40}Ni_5Ti_5$ amorphous alloy. Journal of Alloys and Compounds. 2015;643:S33–S38.

[8]   A.M. Shams El Din, R.A. Mohammed, Contribution to the problem of vapour-side corrosion of copper–nickel tubes in MSF distillers. Desalination. 1998;115:135–144.

[9]   M. Weifang, L. Shuling, W. Jingtang, Isothermal crystallization kinetics of an amorphous CuTi alloy. Chinese Journal of Metal Science and Technology. 1992;8:197–203.

[10] M. Gogebakan, C. Kursun, J. Eckert, Formation of new Cu-based nanocrystalline powders by mechanical alloying technique. Powder Technology. 2013;247:172–177.

[11] J. Eckert, J. Das, K.B. Kim, F. Baier, M.B. Tang, W.T. Wang, Z.F. Zhang, High strength ductile Cu-based metallic glass. Intermetallics. 2006;14:876–881.

[12] Y.J. Yang, R. Zhou, S.D. Wei, D.Y. Liu, H.L. Xu, S.L. Li, Microstructural evolution of slowly solidified Cu–Ti–Zr–Ni amorphous alloy. Journal of Non-Crystalline Solids. 2011;357:1516–1521.

[13] S. Venkataraman, W. Loser, J. Eckert, T. Gemming, C. Mickel, P. Schulbert-Bischoff, N. Wanderka, L. Schultz, D.J. Sordelet, Nanocrystal development in $Cu_{47}Ti_{33}Zr_{11}Ni_8Si_1$ metallic glass powders. Journal of Alloys and Compounds. 2006;415:162–169.

[14] C.J. Hu, P.Y. Lee, Formation of Cu–Zr–Ni amorphous powders with significant supercooled liquid region by mechanical alloying technique. Materials Chemistry and Physics. 2002;74:13–18.

[15] E.S. Park, H.K. Lim, W.T. Kim, et al. The effect of Sn on the glass-forming ability of Cu–Ti–Zr–Ni–Si metallic glass alloys. Journal of Non-Crystalline Solids. 2002;298:15–22.

[16] J. Wu, Y. Pan, J. Huang, J. Pia, Non-isothermal crystallization kinetics and glass-forming ability of Cu–Zr–Ti–In bulk metallic glasses. Thermochimica Acta. 2013;552:15–22.

[17] L. Liu, Z.F. Wu, J. Zhang, Crystallization kinetics of $Zr_{55}Cu_{30}Al_{10}Ni_5$ bulk amorphous alloy. Journal of Alloys and Compounds. 2002;339:90–95.

[18] H.E. Kissinger, Reaction kinetics in differential thermal analysis. Analytical Chemistry. 1957;29:1702.

[19] Y.J. Yang, D.W. Xing, J. Shen, J.F. Sun, S.D. Wei, H.J. He, D.G. McCartney, Crystallization kinetics of a bulk amorphous Cu–Ti–Zr–Ni alloy investigated by differential scanning calorimetry. Journal of Alloys and Compounds. 2006;415:106–110.

[20] L. Zhang, Z. HuaChen, Q. Zheng, D. Chen, Isochronal and isothermal phase transformation of $Cu_{45}Zr_{45}Ag_7Al_3$ bulk metallic glass. Physica B. 2013;411:149–153.

[21] D. Janovszky, A. Sycheva, K. Tomolya, J. Geiger, J. Solyom, A. Roosz, Solidification processes in Cu–Zr–Ag amorphisable alloy system. Journal of Alloys and Compounds. 2014;584:600–606.

[22] F.A. Javid, N. Mattern, S. Pauly, J. Eckert, Effect of cobalt on phase formation, microstructure, and mechanical properties of $Cu_{50-x}Co_xZr_{50}$ (x = 2, 5, 10, 20 at. pct) alloys. Metallurgical and Materials Transactions A: Physical Metallurgy and Materials Science. 2012;43:2631–2636.

[23] C. Hu, P. Lee, Formation of Cu–Zr–Ni amorphous powders with significant supercooled liquid region by mechanical alloying technique. Materials Chemistry and Physics. 2002;74:13–18.

[24] H. Yang, J.Q. Wang, Y. Li, Glass formation and microstructure evolution in Al–Ni–RE (RE^La, Ce, Pr, Nd and misch metal) ternary systems. Philosophical Magazine. 2007;87:4211–4228.

[25] M. Gogebakan, O. Uzun, T. Karaaslan, M. Keskin, Rapidly solidified Al–6.5 wt% Ni alloy. Journal of Materials Processing Technology. 2003;142:87–92.

[26] X. Mao, F. Fang, F. Yang, J. Jiang, R. Tan, Effect of annealing on microstructure and properties of Cu–30Ni alloy tube. Journal of Materials Processing Technology. 2009;209:2145–2151.

[27] M.O. Prado, A. Tolley, Hardness of Cu–Mn–Al alloys as a function of the annealing temperature in the β phase. Materials Science and Engineering A. 1999;273–275:590–594.

[28] Z. Wang, Y. Zhong, G. Cao, C. Wang, J. Wang, W. Ren, Z. Lei, Z. Ren, Influence of dc electric current on the hardness of thermally aged Cu–Cr–Zr alloy. Journal of Alloys and Compounds. 2009;479:303–306.

[29] L. Huaqing, X. Shuisheng, M. Xujun, L. Yong, C. Lei, Influence of cerium and yttrium on Cu–Cr–Zr alloys. Journal of Rare Earths. 2006;24:367.

[30] S. Suzuki, N. Shibutani, K. Mimura, M. Isshiki, Y. Waseda, Improvement in strength and electrical conductivity of Cu–Ni–Si alloys by aging and cold rolling. Journal of Alloys and Compounds. 2006;417:116–120.

[31] Q. Lei, Z. Li, T. Xiao, Y. Pang, Z.Q. Xiang, W.T. Qiu, Z. Xiao, A new ultrahigh strength Cu–Ni–Si alloy. Intermetallics. 2013;42:77–84.

Mechanical Behavior of Zr-Based Metallic Glasses and Their Nanocomposites

Devinder Singh, R.K. Mandal, R.S. Tiwari and
O.N. Srivastava

Additional information is available at the end of the chapter

Abstract

In the present chapter, results of our recent investigations on the role of gallium (Ga) on the aluminum (Al) site in $Zr_{69.5}Al_{7.5-x}Ga_xCu_{12}Ni_{11}$ metallic glass (MG) composition have been discussed. The material tailoring and cooling rate effects on the mechanical behavior of Zr-based metallic glasses and their nanocomposites have been studied. The substitution of Ga on the Al site in Zr–Al–Cu–Ni alloy affects the nucleation and growth characteristics of quasicrystals (QCs) and consequently changes the morphology of nanoquasicrystals. The $Zr_{69.5}Al_{7.5-x}Ga_xCu_{12}Ni_{11}$ system displayed metallic glass formation in the range of $x = 0$–7.5. In this process, we have come out with a new glass composition; Zr-Ga-Cu-Ni with glass transition temperature (T_g)—614 K. The effect of cooling rate on the glass forming ability (GFA) and mechanical properties for this new metallic glass composition has been discussed and compared with some other Zr-based metallic glasses. The various indentation parameters such as microhardness, yield strength, strain hardening constant, nature of shear band formation, and so on for the alloys have been analyzed. The study is focused on investigations of these materials to understand the structure (microstructure) property correlations.

Keywords: metallic glasses, quasicrystal, composites, mechanical properties, cooling rate

1. Introduction

Metallic materials are traditionally considered as crystalline in nature, possessing translational as well as orientation symmetry, i.e., their constituent atoms are arranged in a regular and periodic manner in three dimensions. However, a revolution in the concept of metals was

brought, when metallic glasses (MGs) and quasicrystals (QCs) have been discovered. MGs are amorphous in nature possessing short-range ordering while QCs possess aperiodic long-range order associated with crystallographically forbidden rotational symmetries. Both quasicrystal-forming alloys and MGs giving rise to nanoquasicrystalline phase on annealing have attracted attention owing to their promise to qualify for many potential applications.

1.1. Metallic glasses

Ever since the formation of first metallic glass in the Au–Si system by rapid solidification, numerous investigations have been carried out over the past 15 years due to their attractive properties and technological potential. In initial period of metallic glass study, high cooling rates of the order of 10^5 to 10^6 K/s were the usual requirement for the formation of glassy phase. However, in the recent years, a new class of metallic glass known as bulk metallic glass (BMG) has been synthesized using very slow cooling rates. These newly developed BMGs have generated immense research activity driven by both a fundamental interest in the structure and properties of disordered materials and their unique promise for structural and functional applications. MGs have very high-yield strength and very high elastic limit compared to crystalline steel and Ti alloys (**Figure 1(a)**). They have very high fracture strength coupled with 2–3% of elastic strain. Conventional aluminum, titanium alloys and steels can sustain 1–2% of elastic strain. The glasses have tensile yield strength ($\sigma \sim$ 1.9 GPa), i.e., a high strength-to-weight ratio, making them a possible replacement for Al, but with a much greater resistance to permanent, plastic deformation (i.e., fracture toughness). A large domain of high fracture strength and elastic strain can be achieved by nanocrystallization into the amorphous matrix. **Figure 1(b)** represents the highest strength, specific strength and specific Young's modulus of any bulk amorphous or crystalline metal.
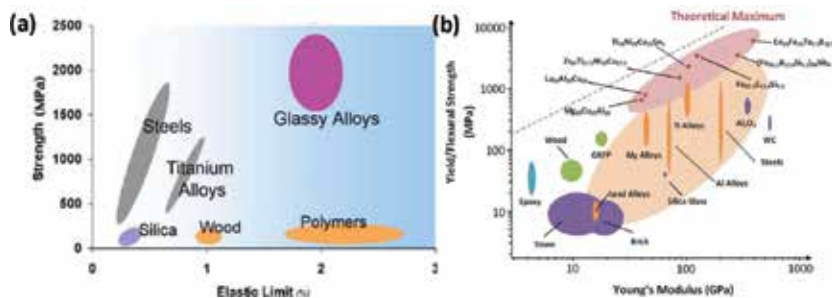
Figure 1. (a) Amorphous metallic alloys combine higher strength than crystalline metal alloys with the elasticity of polymers [1]. (b) Schematic representation of room temperature yield (metals, composites, and polymers) or flexural strength (ceramics) as a function of modulus. Note the increased strength of amorphous metals over conventional crystalline metals [2].

MGs possess a number of very attractive properties, and in many cases, these properties are enhanced by suitable heat treatment. The ability to store a high amount of elastic energy has made this material to use as a potential spring material. This has led to its first and most visible use in the heads of golf clubs. The addition of ceramic second-phase particles into the material

improves its ductility. This composite can be used in aircraft frames and automobiles as armor penetrator material and medical implants. Due to large super-cooled liquid regions, the workability of these materials is very high. This property has been applied in friction welding of Pd-based bulk MGs [3]. The high strength, hardness, fracture toughness, and fatigue strength of MGs make them ideal for the use as optical, die, tool, and cutting materials [4, 5].

Among the large number of multicomponent glassy alloy systems, Zr-based MGs have outstanding glass forming ability (GFA). The exceptionally high-yield strength, close to the theoretical limit, high hardness, and elastic modulus of these MGs offer them potential for structural applications. However, plastic deformation at room temperature occurs in a highly localized manner by the formation of shear bands. In these MGs, the definitive correlations between mechanical behavior and atomic structures have not been clearly understood.

1.2. Quasicrystals

Another important class of material is QCs. The breakthrough experiments by Shechtman et al. on rapidly solidified Al-14% Mn alloys have created a new concept of nonperiodic atomic arrangements with only orientational order, which exhibit sharp diffraction peaks with five-fold symmetry [6]. This new form of ordered structures having orientational order and lacking strict translational periodicity was designated as "quasicrystal" by Levine and Steinhardt [7]. It may be noted that in contrast to both crystal and QCs, amorphous solids possess neither orientational nor translational order. Most familiar quasicrystalline systems are Al-, Ti-, and Mg-based binary and ternary alloys, though there have been a few reports in other systems such as Cd-Mg-Yb, Ag-In(Cd), Al-Zn-Ce, and Cu-Ga-Mg-Sc, etc. The discovery of the quasi-crystalline phases has also generated a great deal of interest in regard to complex crystalline structures known as approximant phases, which have remarkable similarities with their parent quasicrystalline structures. These often coexist with QCs and have similar chemical composi-tions and similar electron diffraction patterns (**Figure 2**). Quasicrystal approximants have similar local atomic structures to QCs [8–12]. Because of these structural similarities, the search for other possible phases as well as intensive investigations of their phase transformation has
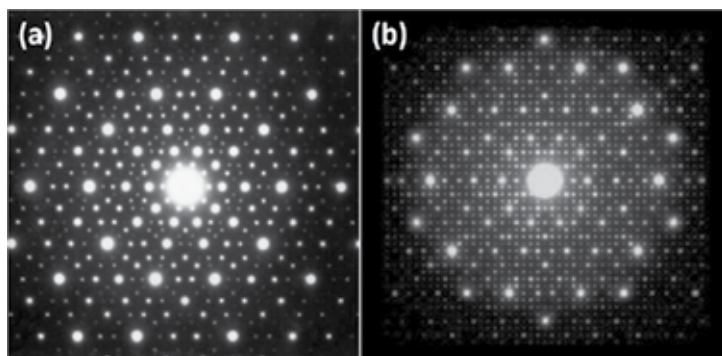
Figure 2. Selected area diffraction patterns of (a) icosahedral quasicrystal showing five-fold symmetry in Al-Mn and (b) pseudodecagonal quasicrystal approximant in Al-Co-Ni alloy [6, 12].

become quite pertinent in connection with the determination of the phase stability of quasi-crystalline system.

The successful applications of QCs are very limited. QCs are corrosion resistant and have low coefficients of friction, and thus, they can be used as a surface coating for frying pans. They can also be used in wear resistant coatings. Al-based quasicrystalline alloys, e.g., Al-Mn-Ce containing nanoicosahedral particles may be used in surgical blades. Ti- and Zr-based QCs could be incorporated into hydrogen storage materials.

1.3. Nanocomposites

Quasicrystal forming alloys and MGs promise to qualify for many potential applications. However, bulk QCs are mostly brittle and this problem can be surmounted by producing glass-nanocrystal (nc)/nanoquasicrystal (nqc) composites ($Zr_{69.5}Al_{7.5}Cu_{12}Ni_{11}$) through controlled crystallization of MGs. Quasicrystal evolution from metallic glass systems may provide a way to produce nanostructured quasicrystalline alloys with attractive mechanical properties. The advantage of formation of quasicrystalline phase through devitrification of MGs is also due to the fact that the microstructure can be precisely controlled. The control of microstructure is very important as the optimum property design is related to the microstructure. It has been pointed out that Ti- and Zr-rich alloys have significantly higher hardness in the nanoquasi-crystalline state (755 and 610 VHN, respectively) compared to the amorphous state in melt-spun condition. The hardness values of Ti- and Zr-rich alloys increase further by nanoquasicrystallization of the amorphous phase to 810 and 620 VHN, respectively. Misra et al. [13] have studied the plastic deformation in nanostructured bulk glass composites during nanoindentation. The structural changes are accompanied by decrease in specific volume, bulk modulus and Poisson's ratio. Small specific changes upon primary devitrification suggest a close relationship between the glassy structure and the icosahedral structure.

2. Effect of material tailoring on the mechanical properties

Elemental substitution is widely used to find new MGs and QCs with improved properties. In this section, the role of Ga on the Al site in $Zr_{69.5}Al_{7.5-x}Ga_xCu_{12}Ni_{11}$ metallic glass composition has been discussed. The alloy design principle adopted in arriving at Ga-substituted glass compositions pertains to retaining the valence electron ratio (e/a) constant. In this respect, Ga substitution on the Al site seems to be ideal. The substitution of Ga in $Zr_{69.5}Al_{7.5-x}Ga_xCu_{12}Ni_{11}$ alloys results in a change from a two-step crystallization ($x = 0$) to a single-step one ($x = 7.5$) [14, 15]. For $x = 0$, we have the well investigated Zr-based alloy; and for $x = 7.5$, we have come out with a new composition of glass with $T_g = 614$ K [16–20]. The effect of the said material tailoring on the mechanical properties of these alloys has also been studied. The recent emphasis on nanostructured materials and synthesis of MGs has added a new dimension to the study of their indentation behavior. Indentation studies offer opportunities to investigate the fundamental nature of deformation in glasses and their composites from a relatively small volume

of material. The indentation size effect (ISE) and shear band formation under compression are able to throw light on the mechanical behavior of materials.

2.1. Microstructural and structural features

The $Zr_{69.5}Al_{7.5-x}Ga_xCu_{12}Ni_{11}$ (x = 0, 1.5, and 7.5) MGs with a thickness of ~40–50 µm and lengths of ~1–2 m have been synthesized using melt spinning technique [19, 21]. **Figure 3(a)** shows the macroscopic image of the melt-spun ribbons synthesized at 40 m/s. **Figure 3(b)** and the inset therein show the transmission electron microscopy (TEM) image and corresponding selected area diffraction pattern (SADP) displaying diffuse halos for $Zr_{69.5}Al_{7.5-x}Ga_xCu_{12}Ni_{11}$($x$ = 7.5) alloy. We note that the TEM bright-field micrograph displayed no discernible contrast. This clearly indicates the formation of glassy phase in the system and similar features were observed for x = 0 and 1.5. The glass-nc/nqc composites are produced after controlled crystallization of melt-spun ribbons corresponding to compositions x = 0, 1.5, and 7.5 [19–21]. The TEM micrograph of these composites is shown in **Figure 4**. Inset in them demonstrates the presence of crystalline/quasicrystalline particles embedded in the glassy matrix. The composition of the alloys with x > 1.5 consists of icosahedral and Zr_2Cu phases embedded in the glassy matrix. The finer grains of both these phases have been observed in the Ga-bearing glass composition (x = 7.5) [19]. The grain refinement of quasicrystals with respect to Ga substitution may be understood by recalling expression [22, 23] of the steady-state nucleation rate (I^s) and is reproduced below

$$I^s = Aexp[(-16\Pi\sigma^3)/(3KT(\Delta G_v)^2)] \tag{1}$$

where 'A' is known as dynamical prefactor and is a function of the atomic mobility at the nuclei-liquid/glass interface. ΔG_v = driving free energy per unit volume for the phase transformation. According to classical theory of nucleation, the nucleation barrier is controlled by interfacial free energy (σ) between the nuclei and the liquid/glass [22]. The decrease in σ between the icosahedral quasicrystalline nuclei and the liquid with increasing Ga content leads to the
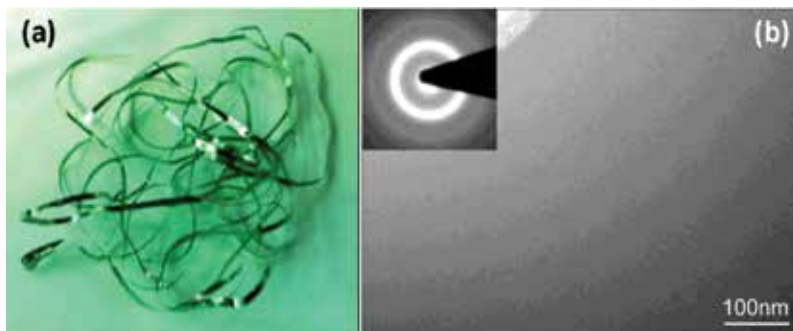
Figure 3. (a) Optical image showing the formation of long melt-spun ribbons synthesized at 40 m/s. (b) TEM image and the corresponding diffraction pattern of as-synthesized $Zr_{69.5}Ga_{7.5}Cu_{12}Ni_{11}$ alloy. (Reprinted with kind permission from references [15, 19], Copyright 2015 and 2011, Elsevier.)

increase in the nucleation rate. The reported interfacial energy per unit area of Ga ($\sim$0.6 J/m^2) is less than that of Al ($\sim$1.2 J/m^2) [24–26]. Thus, it can be said that the substitution of Ga reduces the interfacial energy between quasicrystal and remaining amorphous phase, thereby increasing the nucleation rate of the crystalline/quasicrystalline phases. The formation of icosahedral phase has been observed for all the annealed glasses. Thus, the icosahedral order presents predominantly in the supercooled liquid for all the samples ($x = 0$–7.5).
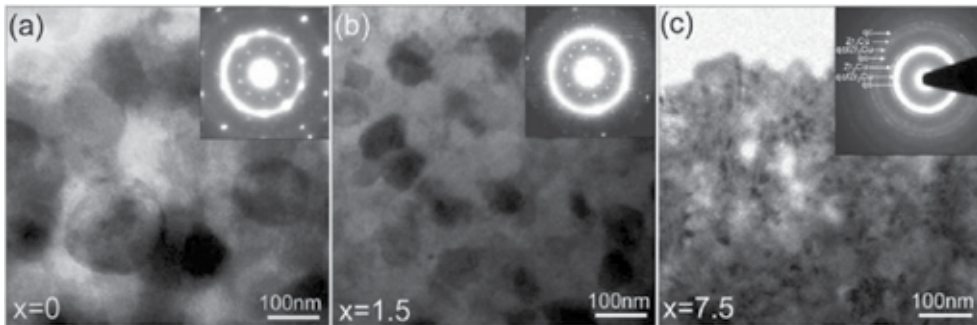

Figure 4. TEM microstructures and the corresponding diffraction patterns of $Zr_{69.5}Al_{7.5-x}Ga_xCu_{12}Ni_{11}$ alloy with $x = 0$ (a), $x = 1.5$ (b), and $x = 7.5$ (c) formed after heat treatment. (Reprinted with kind permission from reference [19], Copyright 2011, Elsevier.)

The composition of the alloys (in at.%) based on electron probe microanalysis (EPMA) has been found to be $Zr_{69.6}Al_{7.6}Cu_{12.5}Ni_{10.3}$ (for $x = 0$), $Zr_{69.2}Al_{6.2}Ga_{1.6}Cu_{12.8}Ni_{10.2}$ (for $x = 1.5$), and $Zr_{69.4}Ga_{7.7}Cu_{12.5}Ni_{10.4}$ (for $x = 7.5$). The presence of oxygen within the detectable limit of EPMA was not found.

2.2. Mechanical properties

In this section, we present the results of micro-/nanoindentation behavior of the three glassy compositions and their respective composites. **Figure 5** depicts the images of microindent for the as-synthesized and annealed ribbons of $x = 7.5$. It has been observed that a number of shear
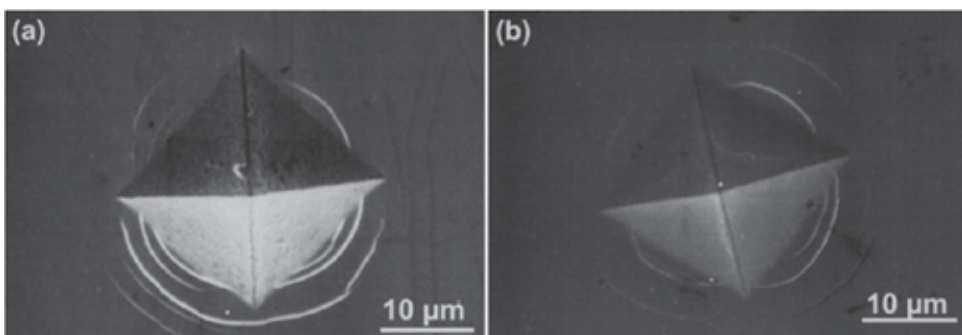

Figure 5. SEM micrographs for the as-synthesized (a) and annealed ribbons (b) of $x = 7.5$ displaying shear bands. (Reprinted with kind permission from reference [19], Copyright 2011, Elsevier.)

bands decrease gradually in the annealed condition as compared to that of glassy state. At this stage, the indentation behavior is governed by the volume fraction of nanocrystalline/ nanoquasicrystalline phases. Thus, the glass-nc/nqc composite possesses different indentation characteristics as is seen in the case of x=7.5 that Zr_2Cu intermetallic phase exists along with the nqc phase, which inhibits the propagation of shear bands in the glassy matrix during indentation. We note from **Table 1** that annealed ribbons for x = 7.5 display the highest microhardness value (~10 GPa). The microhardness values for x = 1.5 at 300 g load are ~4.81 and ~5.89 GPa for as-synthesized and annealed samples, respectively. These are quite close to that of Zr-Al-Ni-Cu-Ag and Zr-Al-Ni-Cu-Nb MGs and their nqc composites [27].

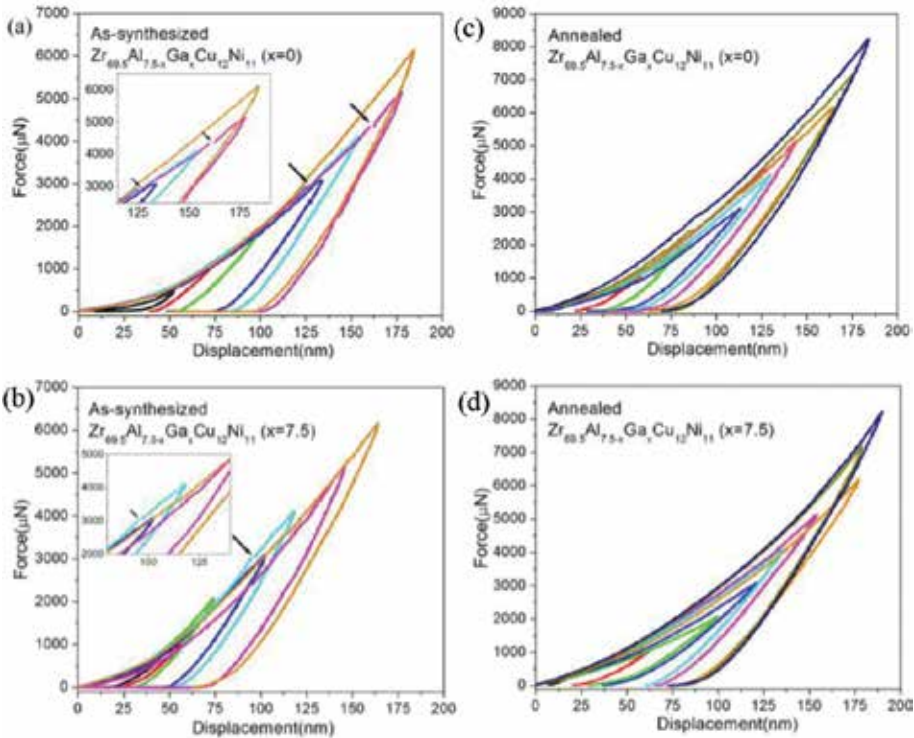| x	As-synthesized ribbons			Annealed ribbons		
(at.%)	Microhardness (GPa) at 100 g load ($\pm$0.1)	Nanohardness (GPa) at 5000 μN ($\pm$0.2)	Reduced Modulus (GPa) at 5000 μN ($\pm$5.0)	Microhardness (GPa) at 100 g load ($\pm$0.1)	Nanohardness (GPa) at 8000 μN ($\pm$0.2)	Reduced Modulus (GPa) at 8000 μN ($\pm$5.0)
0	4.7	8.7	98	6.7	11.5	115
1.5	6.1	9.5	112	7.5	12.8	136
7.5	6.6	11.8	140	10.1	14.4	151

Table 1. Mechanical properties of as-synthesized and annealed ribbons of $Zr_{69.5}Al_{7.5-x}Ga_xCu_{12}Ni_{11}$ (x = 0, 1.5, and 7.5) alloys. (Reprinted with kind permission from reference [19], Copyright 2011, Elsevier).
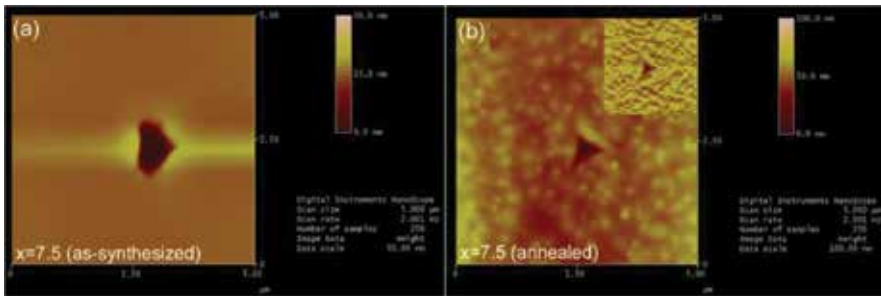
Figure 6. AFM observation of the nanoindentation imprints from the as-synthesized (a) and annealed ribbon (b) of x = 7.5 at 5000 μN. The inset of (b) showing the tip image of nanoindenter [19].

To study the nature of indentation at submicroscopic scale as well as the plastic deformation of composites containing nc/nqc phases, we now present the results of nanoindentation. The indentation impressions of Berkovich indenter at 5000 μN for x = 7.5 are shown in **Figures 6(a)** and **(b)**. These are to compare the indentation impressions of the glassy phase with that of their nanocomposite. The inset in **Figure 6(b)** shows the tip image of the nanoindenter. We note clearly the presence of fine grains in **Figure 6(b)** that are absent in **Figure 6(a)**. The size of the indentation impression changes with partial crystallization and no cracking occurred. The height contrast around the indents is due to pileup. The contrast of the pileup

in glassy sample is much more prominent as compared to that of annealed ribbons. The formation of pileups around the indents must be related to shear banding operations and are extensively observed in amorphous alloys [28–32].


Figure 7. Plot of the indentation force (P) versus indenter displacement (h) obtained from nanoindentation tests for the as-synthesized (a and b) and annealed (c and d) ribbons of $x = 0$ and 7.5 respectively [19].

Figures 7(a) and **(b)** depict the load (P) versus depth (h) behavior of melt-spun ribbons, whereas **Figures 7(c)** and **(d)** display the P versus h characteristics of their respective composites. The values of nanohardness and reduced modulus for $x = 0$, 1.5, and 7.5 are given in **Table 1**. The values of nanohardness for the glassy alloys ($x = 0$–7.5) are in the range of ∼9–12 GPa. Reduced modulus is sensitive to compositions of the alloy as well as atomic arrangements. The reduced modulii for the glassy alloys ($x = 0$–7.5) lies in the range of ∼98–140 GPa. These values of nanohardness and reduced modulus are comparable to those of the Zr-based alloys [33–35]. It can be seen from **Table 1** that composites have higher micro- /nanohardness values than those of glassy alloys. Ramamurty et al. [36] reported that the presence of nanocrystalline particles in the glassy matrix significantly improves the stiffness and strength values. The nanohardness value (mean contact pressure) is higher than that of Vickers hardness value [37]. The difference in the values is primarily due to two reasons: (i) indentation size effect and (ii) actual and projected area of contacts, respectively, for nano- and microhardness measurements.

We have observed pop-ins during loading (marked by the arrow in **Figures 7(a)** and **(b))** for the melt-spun ribbons. These pop-ins indicate displacement bursts that signify the formation of shear bands [38]. The pop-ins are prominent in amorphous alloys while the presence of these is either less prominent or even completely suppressed in case of annealed alloys. Our observation is in agreement with the results reported by others [29, 38, 39]. The pop-ins are absent in composites and this may be attributed to the presence of nc/nqc grains in the glassy matrix. The nature of deformation can be influenced by structural features while the chemistry affects such behavior in a quantitative way. This is the reason why we observe similar kind of P versus h curves corresponding to x = 0 and 7.5 after crystallization of the glasses. The observation of pop-ins during loading cannot be attributed to the process of nanocrystallization as noted in reference [40]. The break in the P versus h curves for such a case should appear while unloading. To settle this issue experimentally, the TEM investigations of the indented portion of these samples have been done. The bright-field images of the thinned specimens for the glassy alloys with x = 0 and 7.5 are shown in **Figures 8(a)** and **(b)**. The preparation of these samples was done by masking the indented side and thinning was done from the opposite side. The bright-field images resemble analogous to those shown in **Figure 3(b)** and do not show any regions of residual contrast. The curvilinear line (marked by arrows) has given evidence of layer wise displacement separated by boundary. These lines must be related to the shear banding operations, and thus, the possibility of nanocrystallization has been ruled out.
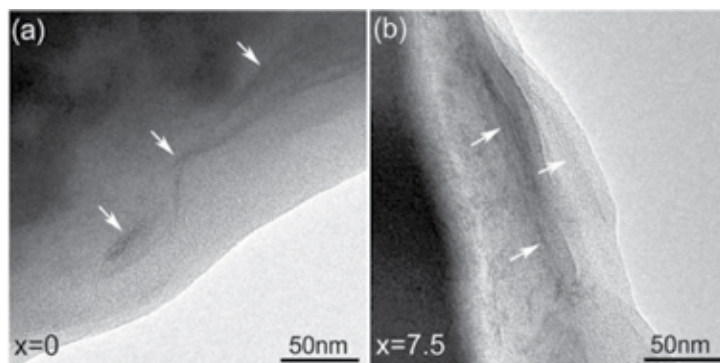
Figure 8. Bright-field TEM images of the indented portion of as-synthesized thinned specimens for x = 0 and 7.5. (Reprinted with kind permission from reference [19], Copyright 2011, Elsevier.)

The change in the mechanical behavior of MGs and their composites can be understood on the basis of free volume model. In the present case, the variation of free volume with Ga substitution may increase the hardness of the MGs. The atomic radius of Ga (0.141 nm) is intermediate between the atomic radius of Al (0.143 nm) and Ni (0.125 nm) and the atomic radius of Zr (0.160 nm) and Cu (0.128 nm). Thus, the substitution of Ga may increase the packing density of the alloy and this would lead to the decrease in the free volume [41]. The high resistance to plastic deformation under applied stress may be attributed to a low free volume [42]. The increase in the hardness of MGs with alloying addition has been reported recently [41]. The shear transformation zones (STZs) are the primary carriers of plasticity in amorphous

materials [43, 44]. The formation of STZs depends upon the availability of free volume. The precipitation of nc/nqc phases in the case of composites decreases the free volume and this causes densification of the metallic glass [45]. This results in an increased resistance to plastic deformation and therefore enhancement of hardness of the metallic glass upon structural relaxation and nanocrystallization. This observation is consistent with the results reported earlier [46, 47]. In the case of glass-nc/nqc composites, the hardness increases with increase in Ga addition. This may be due to the grain refinement of nanocrystals/nanoquasicrystals that produces many interfaces leading to the strengthening phenomenon.

## 3. Effect of cooling rate on the mechanical properties

The absence of grain boundaries and dislocations in MGs contributes to its exceptional properties [48–53]. MGs lack long-range order and thus, they can be considered as solids with frozen-liquid structures composed of tightly bonded atomic clusters and free volume zones [54–56]. The frozen-in excess volume is often interpreted as an increase of free volume content in the MGs [57, 58]. The functional and mechanical properties of a metallic glass are determined by its internal atomic configuration [59, 60]. The different variables such as the cooling rate and composition affect the structure of MGs [14, 61, 62]. Among these, the critical cooling rate is a very important factor that plays a crucial role in determining the atomic structure and hence deformation behavior of MGs [63–65]. The limited macroscopic plastic strain before fracture of MGs constrains their applications [43]. Plastic deformation of MGs is localized within relatively thin regions called shear bands, resulting in a very low macroscopic plastic flow limit [13, 43, 66]. Recent investigations show that the plastic strain of some monolithic MGs can be improved by enhancing the homogeneity in microstructure through the high cooling rate [67]. The high cooling rate may result in the configurationally looser atomic packing and thus more free volume zones, which therefore contribute to larger plasticity. Chen et al. [68] suggested that the plasticity for MGs can be tailored by applying different cooling rates during solidification. Jiang et al. [69] found that the Cu-based bulk metallic glass (BMG) is having higher hardness as compared to its ribbon counterpart of the same composition but synthesized at a much higher cooling rate. It has been observed that decreasing the cooling rate of glass forming promoted the formation of denser atomic configuration in the resultant alloy [57]. The study of cooling rate effect on the nanomechanical response for a Ti-based BMG reveals that the hardness increases while the plastic deformation gradually decreases from the edge to the center of the sample [70]. Recently, Huang et al. [71] reported the effect of cooling rate on the local atomic ordering and the wear behavior of Zr-Cu-Al-Ag BMG. These results indicate that the cooling rate used during glass formation is a processing parameter that may be tuned to change the mechanical properties of MGs.

The effect of cooling rate on the mechanical behavior of $Zr_{69.5}Ga_{7.5}Cu_{12}Ni_{11}$ metallic glass has been studied using microindentation technique. The ribbons of alloy have been synthesized at three cooling rates, corresponding to wheel speeds of 30, 40, and 50 m/s. The different properties such as glass forming indicators, structural relaxation heat, microhardness, yield strength, strain-hardening constant, material constant related to the resistance of the metal to

penetration and pileup parameter pertaining to nature of shear band are expected to throw light on the internal structure of glass. They are compared and discussed with respect to the rate of cooling. This study provides some insights to understand the correlation between the cooling rate and the mechanical behavior of Zr-Ga-Cu-Ni metallic glass.

3.1. Microstructural and structural features

Figure 9 shows the X-ray diffraction (XRD) patterns of as-synthesized $Zr_{69.5}Ga_{7.5}Cu_{12}Ni_{11}$ melt-spun ribbons synthesized at different wheel speeds. It has been observed that all the patterns of the alloys consist of only broad diffraction maxima (at the position 2θ ≈ 36°) without a detectable sharp Bragg peak. This shows formation of a glassy phase. The XRD pattern of the ribbon synthesized at 40 m/s revealing the presence of a glassy phase exhibits greater peak broadening and lower XRD intensity as compared to the ribbons synthesized at 30 m/s. These effects are more pronounced by further increasing the wheel speed to 50 m/s. The full width at half maximum (FWHM) was found to be 5.5°, 4.7°, and 3.9° for the ribbons synthesized at 50, 40, and 30 m/s, respectively. These results indicate that the ribbon synthesized at 30 m/s has higher degree of short-range ordering. The formation of a glassy phase in these samples
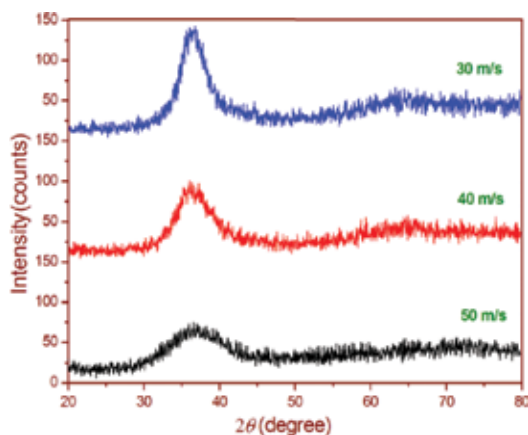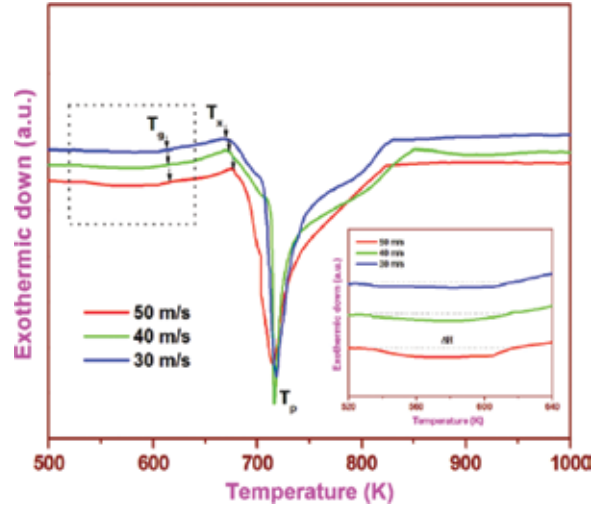

Figure 9. XRD patterns of as-synthesized ribbons of $Zr_{69.5}Ga_{7.5}Cu_{12}Ni_{11}$ metallic glass at wheel speed of 30, 40, and 50 m/s. (Reprinted with kind permission from reference [15], Copyright 2015, Elsevier.)
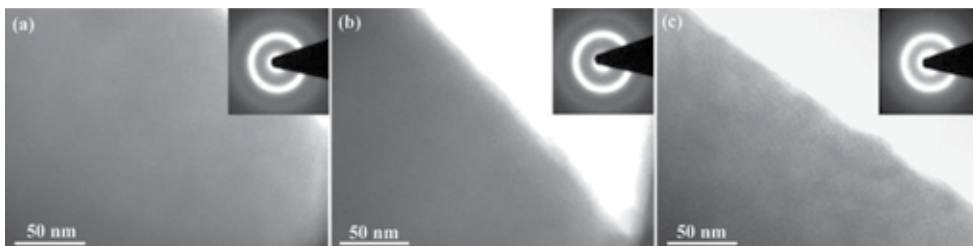
Figure 10. TEM micrographs with inset showing the selected area electron diffraction patterns of as-synthesized $Zr_{69.5}Ga_{7.5}Cu_{12}Ni_{11}$ alloys synthesized at wheel speeds (a) 50, (b) 40, and (c) 30 m/s. (Reprinted with kind permission from reference [15], Copyright 2015, Elsevier.)

was further investigated by TEM. **Figure 10** and the insets therein show the TEM micrographs and the corresponding selected area electron diffraction (SAED) patterns for $Zr_{69.5}Ga_{7.5}Cu_{12}Ni_{11}$ melt-spun alloys synthesized at 50, 40, and 30 m/s, respectively. We note that all TEM micrographs depict no discernible contrast and the corresponding SAED patterns displaying diffuse halos. This confirms to the XRD results presented above.

Figure 11. DSC curves of the as-synthesized $Zr_{69.5}Ga_{7.5}Cu_{12}Ni_{11}$ metallic glass samples synthesized under different cooling conditions. Inset highlights the enlarged section of the DSC curves below the glass transition temperature. (Reprinted with kind permission from reference [15], Copyright 2015, Elsevier.)

Figure 11 shows differential scanning calorimeter (DSC) scans taken at a heating rate of 20 K/min for the glassy alloys prepared under different cooling conditions. All DSC curves exhibited one clear endothermic heat event, characteristic of the glass transition to a supercooled liquid state, followed by only one single exothermic peak between about 670 and 820 K. It can be seen that the DSC curves of all the samples are very similar with glass transition temperature (T_g) in the range of 612–616 K and onset crystallization temperature (T_x) in the range of 670–676 K. This indicates the comparable thermal stability (ΔT_x) among the samples. **Table 2** summarizes the thermal stability data for all the investigated samples. The crystallization enthalpies can be obtained by integrating the area covered by the crystallization peak in the DSC curve and are found to be 61.1, 60.3, and 58.9 J/g for the ribbons synthesized at 50, 40, and 30 m/s, respectively. The crystallization enthalpy decreases with the decreasing cooling rate and thus confirming that the sample synthesized at 30 m/s contains a larger degree of short-range ordering or medium-range ordering. The degree of ordering can also be estimated by evaluating the crystallization fraction (V_f) of the sample from the DSC curves and is given by [72]:

$$V_f = \frac{\Delta H_{max} - \Delta H}{\Delta H_{max}} \tag{2}$$

where $\Delta H_{\max}$ is the total enthalpy change when the fully amorphous alloy transforms into a completely crystallized one and ΔH is the crystallization enthalpy of the examining sample. Considering the sample synthesized at 50 m/s to be fully amorphous with zero crystallization fraction, the crystallization fraction for the samples synthesized at 40 and 30 m/s was found to be 1.3% and 3.6%, respectively, suggesting a negligible crystalline content in the samples. The small increase in the crystallization fraction results from the enhanced short-range ordering.

Cooling rate (m/s)	T_g (K)	T_x (K)	T_p (K)	ΔT_x (K)
30	612	670	718	58
40	614	673	716	59
50	616	676	714	60

T_g: glass transition temperature; T_x: onset crystallization temperature; ΔT_x: supercooled liquid region; T_p: exothermic peak.

Table 2. Thermal analysis of the melt-spun $Zr_{69.5}Ga_{7.5}Cu_{12}Ni_{11}$ ribbons synthesized at different cooling rate.(Reprinted with kind permission from reference [15], Copyright 2015, Elsevier.)

As evident from **Figure 11** and **Table 2**, there is a slight increase in the value of T_g, T_x, and ΔT_x with the increasing cooling rate. However, careful analysis reveals some differences around the glass transition regions, as more clearly seen in the inset of **Figure 11**. The inset of **Figure 11** is a local magnified region of the DSC curves below T_g, illustrating the heat release events due to structural relaxation. The structural relaxation enthalpy associated with the exothermic peak below T_g can be calculated by integrating the heat flow near the glass transition range (the area between the dotted lines and the curves shown in the inset of **Figure 11**). The relaxation enthalpy has been found to be 2.69, 3.98, and 5.84 J/g for the glassy ribbons synthesized at 30, 40, and 50 m/s, respectively, as provided in **Table 3**. A higher cooling rate has resulted in a larger relaxation enthalpy. Slipenyuk et al. [73] have shown that the exothermic heat release is directly related to the structural relaxation, i.e., the change of free volume in metallic glasses, and can be calculated by

$$(\Delta H)_{fv} = \beta \Delta_{vf} \tag{3}$$

where β is a constant, $(\Delta H)_{fv}$ is the change in enthalpy due to per unit free volume, and Δv_f is the change of free volume per atomic volume. Thus, the change in free volume of the glassy ribbons synthesized at different wheel speeds may be obtained by Eq. (3). Assuming that the free volume per atomic volume for the ribbon synthesized at 50 m/s to be ρ_o, the substitution of values of ΔH (cf. **Table 3** and the inset in **Figure 11**) into Eq. (3), the values of free volume per atomic volume for the ribbons synthesized at 40 and 30 m/s were found to be 0.68 ρ_o and 0.46 ρ_o, respectively. Such a computation suggests that the glassy ribbons synthesized at lower wheel speed have less free volume per atomic volume than the ribbons synthesized at higher wheel speed. The ribbons synthesized at 50 m/s are, therefore, believed to possess the highest

free volume. According to Turnbull and Cohen [74], the amount of free volume in a metallic glass is determined by the cooling rate. A slower cooling rate gives sufficient time to the atoms to attain their local ordered equilibrium positions, thereby, a more ordered atomic structure forms during cooling from the melt and thus, the obtained glassy sample has a smaller amount of free volume [69]. The amount of free volume in a metallic glass corresponds to the atomic packing density and one of the important parameters exerts a strong influence on the mechanical properties of the metallic glass.

Cooling rate (m/s)	Hardness (VHN) (GPa) (±0.10)	n	Log K	σ_0 (GPa) (100 g load) (±0.05)	$\alpha = A/A_s$	Crystallization enthalpy (ΔH) (J/g)	Structural relaxation enthalpy (J/g)
30	6.81	1.82	2.23	3.43	1.45	58.9	2.69
40	6.63	1.83	2.24	3.26	1.50	60.3	3.98
50	6.43	1.84	2.25	3.09	1.57	61.1	5.84

Table 3. Summary of hardness (VHN), Meyer's exponent (n), material constant (K), yield strength (σ_0), pileup parameter (α), crystallization enthalpy (ΔH) and structural relaxation heat of the Zr-based metallic glass samples with different cooling rate. (Reprinted with kind permission from reference [15], Copyright 2015, Elsevier.)

3.2. Mechanical properties

In this section, we present the results of cooling rate effect on the mechanical behavior of $Zr_{69.5}Ga_{7.5}Cu_{12}Ni_{11}$ MGs synthesized at different wheel speeds. The microhardness measurements were carried out by Vickers microhardness tester. The mean hardness reported here is
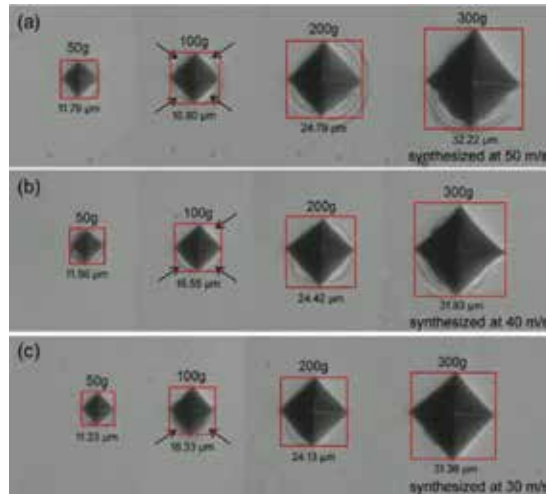
Figure 12. Indentation imprints at different loads for the as-synthesized ribbons of $Zr_{69.5}Ga_{7.5}Cu_{12}Ni_{11}$ metallic glass at wheel speed of (a) 50, (b) 40, and (c) 30 m/s showing the formation of shear bands around the indents. Four indentation impressions from various regions of the sample are superimposed. (Reprinted with kind permission from reference [15], Copyright 2015, Elsevier.)

the average of at least five points on each sample. **Figure 12** shows the representative optical micrographs of indents at different loads in $Zr_{69.5}Ga_{7.5}Cu_{12}Ni_{11}$ MGs synthesized at 50, 40, and 30 m/s, respectively. These micrographs reveal that the indents are crack free up to the load of 300 g for all the samples. The wavy patterns around the indent reveal the generation and formation of shear bands (marked by arrows in **Figure 12**). It can be clearly seen that the number of visible shear bands for the ribbons synthesized at 50 m/s is higher than those observed for the ribbons synthesized at 40 and 30 m/s. To further confirm this, we have calculated the pileup parameter. The characteristic spiral pattern around indents constitutes pileup and is related to the formation of shear bands. Pileups at which shear band reaches the surface are extensively observed around indents in amorphous alloys [19, 20]. The pileup parameter (α) can be calculated by employing the following relationship [75]:
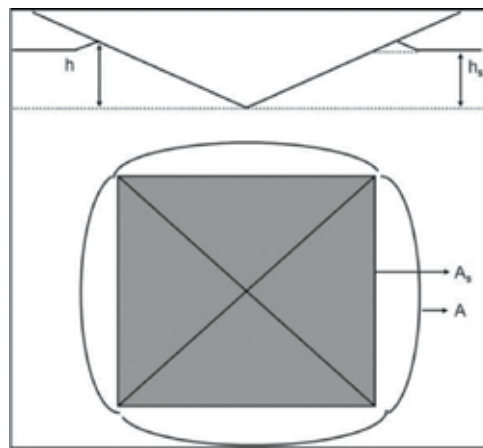
Figure 13. Schematic representation of various quantities used for calculation of pileup parameter (α) [75]; A_s and A are the area of impression before and after pileup, whereas h_s and h are the depth of impression before and after pileup.

$$\alpha = A/A_s \tag{4}$$

where $A_s = f h_s^2$ with f as a constant and is equal to 24.5 for Vickers pyramid indenter. The values of A_s and A are the area of impression before and after pileup, whereas h_s and h are the depth of impression before and after pileup. Various quantities utilized for the determination of α are displayed through a schematic diagram in **Figure 13**. The pileup area calculation was done by graphical methods. The values of α for the ribbons synthesized under different cooling conditions are reported in **Table 3**. The pileup parameter has been found to be maximum for the ribbons synthesized at 50 m/s. In contrast to this, the ribbons synthesized at 40 and 30 m/s are having relatively lower value of α indicates that few shear bands are generated during indentation. Among the three types of specimens, the ribbons synthesized at 50 m/s contain the large free volume and have the highest shear band density. The high free volume content not only favors the nucleation of shear bands but also helps to enhance the atomic mobility

that can alleviate the stress concentration and therefore prevent the metallic glass from cracking. Thus, it can be inferred that for the glassy alloy of fixed composition gives rise to the larger number of shear bands with higher cooling rate. Furthermore, higher free volume at enhanced cooling rates not only facilitates permanent flow of materials under compressive stresses but also contributes to enhancement in the fracture strength.

The hardness (H) was calculated in GPa units by employing the following relationship [76]:

$$H = 1.854 \times 9.8 \times \frac{P}{d^2} \tag{5}$$

where P is the load (g) and d is the diagonal length in μm. **Figure 14(a)** shows hardness (VHN) versus load (g) characteristic curves for the ribbons synthesized at 30, 40, and 50 m/s, respectively. It can be seen from the load-dependent hardness curves (**Figure 14(a)**) that the hardness decreases with increase in the load due to indentation size effect (ISE) [77, 78]. **Table 3** compares the values of microhardness and other indentation parameters of the ribbons synthesized at different cooling rates. The hardness values of the ribbons synthesized at 30, 40, and 50 m/s at 100 g load are ∼6.81, ∼6.63, and ∼6.43 GPa, respectively, clearly suggesting that faster the cooling rate during solidification, the lower the microhardness. The glass forming ability parameters and hardness values of $Zr_{69.5}Ga_{7.5}Cu_{12}Ni_{11}$ alloy synthesized at 50 m/s have been compared with some other known Zr-based alloys (cf. **Table 4**). Compared with the other typical MGs, $Zr_{69.5}Ga_{7.5}Cu_{12}Ni_{11}$ alloy has higher hardness but lower T_g and ΔT_x values. The hardness for $Zr_{69.5}Ga_{7.5}Cu_{12}Ni_{11}$ alloy is 6.43 GPa that is higher in comparison to the majority of the metallic glass alloy systems listed in **Table 4**.
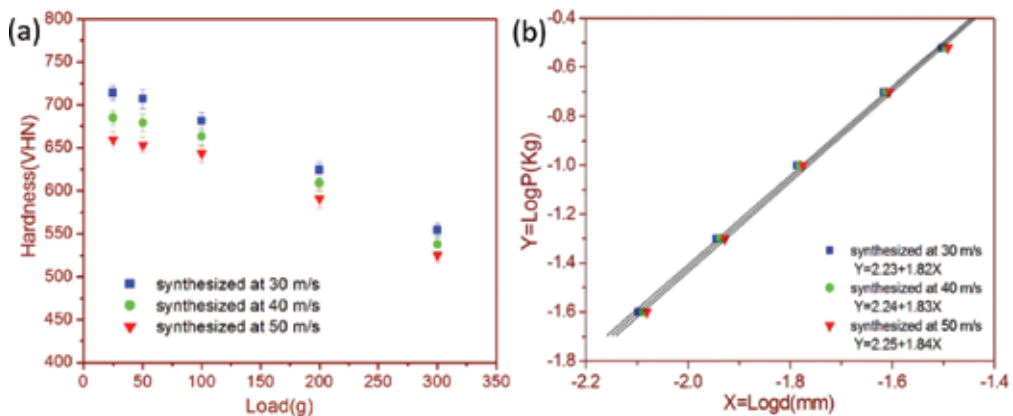
Figure 14. (a) Variation of hardness (VHN) with respect to load (g) for the as-synthesized ribbons of $Zr_{69.5}Ga_{7.5}Cu_{12}Ni_{11}$ metallic glass synthesized at different cooling rates. (b) Log P versus Log d plots for the as-synthesized ribbons of $Zr_{69.5}Ga_{7.5}Cu_{12}Ni_{11}$ metallic glass at wheel speed of 30, 40, and 50 m/s. (Reprinted with kind permission from reference [15], Copyright 2015, Elsevier.)

Alloys	T_g (K)	T_x (K)	ΔT_x (K)	Hardness (GPa)	Reference
$Zr_{41.2}Ti_{13.8}Cu_{12.5}Ni_{10}Be_{22.5}$	623	705	82	5.34	Raghavan etal. [50]
$Zr_{55}Pd_{10}Cu_{20}Ni_5Al_{10}$	696	775	79	5.28	Liu et al. [62]
$Zr_{55}Cu_{17.5}Al_{7.5}Ni_{10}Si_{10}$	700	748	48	7.20	Jang et al. [51]
$(Zr_{69.5}Al_{7.5}Cu_{12}Ni_{11})_{88}Ti_{12}$	628	686	58	6.00	Singh et al. [53]
$Zr_{51.9}Cu_{23.3}Ni_{10.5}Al_{4.3}$	705	801	96	5.50	Sun et al. [83]
$Zr_{51}Ti_5Ni_{10}Cu_{25}Al_9$	675	729	54	5.42	Sun et al. [83]
$Zr_{46}Cu_{37.6}Ag_{8.4}Al_8$	706	796	90	5.54	Sun et al. [83]
$Zr_{57}Cu_{27}Al_{11}Ni_5$	682	745	63	5.85	Jana et al. [67]
$Zr_{69.5}Al_{7.5}Cu_{12}Ni_{11}$	624	702	78	4.70	Singh et al. [20]
$Zr_{65}Al_{7.5}Cu_{17.5}Ni_{10}$	656	735	79	5.50	Jang et al. [51]
$Zr_{69.5}Ga_{7.5}Cu_{12}Ni_{11}$	616	676	60	6.43	Singh et al. [15]

Table 4. Comparison of T_g, T_x, ΔT_x and hardness values of $Zr_{69.5}Ga_{7.5}Cu_{12}Ni_{11}$ melt-spun alloy synthesized at 50 m/s with some other Zr-based metallic glasses.

The load independent hardness values permits us to compute the 0.2% offset yield strength (σ_0) by using the following relationship [79]:

$$\sigma_0 = (VHN/3)0.1^{n-2} \tag{6}$$

where n = Meyer's exponent. This is determined by the slope log P (in Kg) versus log d (in mm) curve. The intercept of this curve K is the material constant related to the resistance of the metal to penetration. **Figure 14(b)** shows log P versus log d curves for the ribbons synthesized at different wheel speeds. The values of n and K are reported in **Table 3**. There is no significant variation observed in the values of n and K for the samples. The values of exponent are less than 2 as observed for intermetallics [80]. The yield strength lies in the range of ~3.09–3.43 GPa for the samples and is found to be maximum for the ribbon synthesized at 30 m/s. In the present case, both hardness and yield strength increase with decrease in the cooling rate and this may be attributed to the variation of free volume with the cooling rate. As the cooling rate decreases, the free volume decreases and thus causes densification of the metallic glass that results in an increased resistance to plastic deformation and therefore enhancement of hardness of the metallic glass upon structural relaxation [81–87].

4. Conclusion

In this chapter, the recent progress in the development of metallic glasses, quasicrystals and their nanocomposites are discussed. The $Zr_{69.5}Al_{7.5-x}Ga_xCu_{12}Ni_{11}$ system displayed metallic glass formation in the range of x = 0–7.5. In this process, we have come out with a new composition of glass without Al corresponding to x = 7.5. The nanohardness and reduced

elastic modulus values of the metallic glasses have been compared to their nanocomposites. The indentation characteristics of the glass composition with $x = 7.5$ have shown significant improvement in regard to hardness and elastic modulus. Based on transmission electron microscopic studies of the indented glassy specimen, the possibility of deformation-induced nanocrystallization has been ruled out.

In addition to, the cooling rate effect on the glass forming ability, crystallization and mechanical behavior of $Zr_{69.5}Ga_{7.5}Cu_{12}Ni_{11}$ metallic glass composition is presented. A slower cooling rate leads to higher degree of structural relaxation, less free volume content and therefore better short-range ordering. Such relatively ordered atomic configuration and less free volume content result in a higher hardness and yield strength for the samples synthesized at slower cooling rate than those synthesized at faster cooling rate. The ribbons synthesized at faster cooling rate contain the large free volume and have the highest shear band density. The glass forming ability parameters and hardness values of $Zr_{69.5}Ga_{7.5}Cu_{12}Ni_{11}$ alloy have shown significant improvement in comparison to some other known Zr-based alloys.

Acknowledgements

Author details

Devinder Singh[1*], R.K. Mandal[2], R.S. Tiwari[3] and O.N. Srivastava[3]

*Address all correspondence to: devinderbhu@yahoo.com

1 Department of Physics, Panjab University, Chandigarh, India

2 Department of Metallurgical Engineering, Indian Institute of Technology (Banaras Hindu University), Varanasi, India

3 Department of Physics, Nano-Science Unit, Banaras Hindu University, Varanasi, India

References

[1]   Telford M. The case for bulk metallic glasses. Mater Today. 2004;7:36.

[2] Ashby MF, Greer AL. Metallic glasses as structural materials. Scripta Mater. 2006;54:321.

[3] Kawamura Y, Ohno Y. Superplastic bonding of bulk metallic glasses using friction. Scripta Mater. 2001;45:279.

[4] Li M, Eckert J, Kecskes L, Lewandowski J. Mechanical properties of metallic glasses and applications. J Mater Res. 2007;22:255.

[5] Inoue A, Fan C, Saida J, Zhang T. High strength Zr-based bulk amorphous alloys containing nanocrystalline and nanoquasicrystalline particles. Sci TechnolAdv Mater. 2000;1:73.

[6] Shechtman D, Blech I, Gratias D, Cahn JW. Metallic phase with long-range orientational order and no translational symmetry. Phys Rev Lett. 1984;53:1951.

[7] Levine D, Steinhardt PJ. Quasicrystals. I. Definition and structure. Phys Rev B. 1986;34:596.

[8] Singh D, Yadav TP, Tiwari RS, Srivastava ON. Phase formation in rapidly quenched Cu-based alloys. J Mater Sci. 2009;44:3883.

[9] Zou XD, Fung KK, Kuo KH. Orientation relationship of decagonal quasicrystal and tenfold twins in rapidly cooled Al-Fe alloy. Phys Rev B. 1987;35:4526.

[10] Goldman AI, Kelton KF. Quasicrystals and crystalline approximants. Rev Mod Phys. 1993;65:213.

[11] Singh D, Yun Y, Wan W, Grushko B, Hovmöller S, Zou XD. A complex pseudo-decagonal quasicrystal approximant $Al_{37}(Co,Ni)_{15.5}$ solved by the rotation electron diffraction (RED) method. J Appl Crystallography. 2014;47:215.

[12] Singh D, Yun Y, Wan W, Grushko B, Hovmöller S, Zou XD. Structure determination of a pseudo-decagonal quasicrystal approximant by the strong-reflections approach and rotation electron diffraction. J Appl Crystallography. 2016;49:433-441. doi:10.1107/S1600576716000042.

[13] Misra DK, Sohn SW, Kim WT, Kim DH. Plastic deformation in nanostructured bulk glass composites during nanoindentation. Intermetallics. 2009;17:1.

[14] Singh D, Yadav TP, Mandal RK, Tiwari RS, Srivastava ON. Effect of Ga substitution on the crystallization behaviour and glass forming ability of Zr-Al-Cu-Ni alloy. Mater Sci Eng A. 2010;527:469.

[15] Singh D, Mandal RK, Tiwari RS, Srivastava ON. Effect of cooling rate on the crystallization and mechanical behaviour of Zr-Ga-Cu-Ni metallic glass composition. J Alloys & Compds. 2015;648:456.

[16] Koster U, Meinhardt J, Roos S, Liebertz H. Formation of quasicrystals in bulk glass forming Zr-Cu-Ni-Al alloys. Appl Phys Lett. 1996;69:179.

[17] Inoue A. Stabilization of metallic supercooled liquid and bulk amorphous alloys. Acta Mater. 2000;48:279.

[18] Wang WH, Dong C, Shek CH. Bulk metallic glasses. Mater Sci Eng R. 2004;44:45.

[19] Singh D, Mandal RK, Tiwari RS, Srivastava ON. Nanoindentation characteristics of $Zr_{69.5}Al_{7.5-x}Ga_xCu_{12}Ni_{11}$ glasses and their nanocomposites. J Alloys & Compds. 2011;509:8657.

[20] Singh D, Yadav TP, Mandal RK, Tiwari RS, Srivastava ON. Indentation characteristics of metallic glass and nanoquasicrystal-glass composite in Zr-Al(Ga)-Cu-Ni alloys. Intermetallics. 2010;18:2445.

[21] Singh D, Singh M, Yadav TP, Mandal RK, Tiwari RS, Srivastava ON. Nanoindentation studies of metallic glasses and nanoquasicrystal-glass composites in Zr-Al (Ga)-Cu-Ni alloys. Int J Nanosci. 2011;10:929.

[22] Kelton KF. Crystallization of liquids and glasses to quasicrystals. J Non-Cryst Solids. 2004;334 & 335:253.

[23] Mei JN, Li JS, Kon HC, Fu HZ, Zhou L. Effects of Nb on the formation of icosahedral quasicrystalline phase in Ti-rich Ti-Zr-Ni-Cu-Be glassy forming alloys. J Non-Cryst Solids. 2008;354:3332.

[24] Heinzig M, Jenks CJ, Hove MV, Fisher I, Canfield P, Thiel PA. Surface preparation and characterization of the icosahedral Al-Ga-Pd-Mn quasicrystal. J Alloys & Compds. 2002;338:248.

[25] Yadav TP, Singh D, Shahi RR, Shaz MA, Tiwari RS, Srivastava ON. Formation of quasicrystalline phase in $Al_{70-x}Ga_xPd_{17}Mn_{13}$ alloys. Phil Mag. 2011;91:2474.

[26] Yadav TP, Singh D, Shaz MA, Tiwari RS, Srivastava ON. Synthesis of quasicrystalline film of Al-Ga-Pd-Mn alloy. Thin Solid Films. 2013;534:265.

[27] Qiang JB, Zhang W, Xie G, Kimura H, Dong C, Inoue A. An in situ bulk $Zr_{58}Al_9Ni_9Cu_{14}Nb_{10}$ quasicrystal-glass composite with superior room temperature mechanical properties. Intermetallics. 2007;15:1197.

[28] Vaidyanathan R, Dao M, Ravichandran G, Suresh S. Study of mechanical deformation in bulk metallic glass through instrumented indentation. Acta Mater. 2001;49:3781.

[29] Kim JJ, Cho Y, Suresh SA, Argon S. Nanocrystallization during nanoindentation of a bulk amorphous metal alloy at room temperature. Science. 2002;295:654.

[30] Singh D, Tiwari RS, Srivastava ON, Mandal RK., R.C. Sobti, Anupama Kaushik, Bhupinder Singh and S.K. Tripathi Synthesis and mechanical properties of $Zr_{69.5}Ga_{7.5}Cu_{12}Ni_{11}$ metallic glass and nanoquasicrystal-glass composites. *Emerging Paradigms in Nanotechnology*. Pearson Education. Chennai, India. 2013;81. ISBN: 978-81-317-8991-9.

[31] Singh D, Mandal RK, Tiwari RS, Srivastava ON. Role of nano-quasicrystals in the formation of shear bands in Zr-based glassy alloys. *Nanotechnology: Novel Perspectives and Prospects*. McGraw-Hill, USA. 2015. ISBN: 978-93-392-2109-6.

[32] Singh D, Tiwari RS, Srivastava ON. *Metallic Glasses, Quasicrystals and Their Nanocomposites*. Lap Lambert Academic Publishing, Germany. 2014;111156:165. ISBN: 978-3-659-62088-1.

[33] Trexler MM, Thadhani NN. Mechanical properties of bulk metallic glasses. ProgMater Sci. 2010;55:759.

[34] Wang JG, Choi BW, Nieh TG, Liu CT. Crystallization and nanoindentation behavior of a bulk Zr-Al-Ti-Cu-Ni amorphous alloy. J Mater Res. 2000;15:798.

[35] Tariq NH, Hasan BA, Akhter JI, Ali F. Mechanical and tribological properties of Zr-Al Ni-Cu bulk metallic glasses. J Alloys & Compds. 2009;469:179.

[36] Ramamurty U, Nagendra N, Li Y. Variation in mechanical properties with crystallinity of a La-based bulk metallic glass. J Metastruct Mater. 2001;10:61.

[37] Qian L, Li M, Zhou Z, Yang H, Shi X. Comparison of nano-indentation hardness to microhardness. Surf Coat Technol. 2005;195:264.

[38] Drozdz D, Kulik T, Fecht HJ. Nanoindentation studies of Zr-based bulk metallic glasses. J Alloys Compds. 2007;441:62.

[39] Azad S, Mandal A, Mandal RK. On the parameters of glass formation in metallic systems. Mater Sci Eng. A 2007;458:348.

[40] Anthony Fischer-Cripps C. *Nano-Indentation, Mechanical Engineering Series*. Frederick F. Ling (Series ed.), Springer-Verlag, New York. 2004.

[41] Jang JSC, Jian SR, Chang CF, Chang LJ, Huang YC, Li TH, Huang JC, Liu CT. Thermal and mechanical properties of the $Zr_{53}Cu_{30}Ni_9Al_8$ based bulk metallic glass microalloyed with silicon. J Alloys & Compds. 2009;478:215.

[42] Jiang WH, Pinkerton FE, Atzmon M. Mechanical behavior of shear bands and the effect of their relaxation in a rolled amorphous Al-based alloy. Acta Mater. 2005;53:3469.

[43] Schuh CA, Hufnagel TC, Ramamurty U. Mechanical behavior of amorphous alloys. Acta Mater. 2007;55:4067.

[44] Dubach A, Dalla Torre FH, Loffler JF. Constitutive model for inhomogeneous flow in bulk metallic glasses. Acta Mater. 2009;57:881.

[45] Uhhenhaut DI, Dalla Torre FH, Castellero A, Gomez CAP, Djowrelon N, Krauss G, Schmitt B, Patterson B, Loffler JF. Structural analysis of rapidly solidified Mg-Cu-Y glasses during room-temperature embrittlement. Phil Mag. 2009;89:233.

[46] Xie S, George EP. Hardness and shear band evolution in bulk metallic glasses after plastic deformation and annealing. Acta Mater. 2008;56:5202.

[47] Yoo BG, Park KW, Lee JC, Ramamurty U, Jang JI. Role of free volume in strain softening of as-cast and annealed bulk metallic glass. J Mater Res. 2009;24:1405.

[48] Mandal RK, Tiwari RS, Singh D, Singh D. Influence of Ga substitution on the mechanical behavior of $Zr_{69.5}Al_{7.5-x}Ga_xCu_{12}Ni_{11}$ and $Ce_{75}Al_{25-x}Ga_x$ metallic glass compositions. MRS Proceeding. 2015;1757. doi:10.1557/opl.2015.45.

[49] Singh D, Shahi RR, Yadav TP, Mandal RK, Tiwari RS, Srivastava ON. Hydrogenation of $(Zr_{69.5}Al_{7.5}Cu_{12}Ni_{11})_{100-x}Ti_x$ quasicrystalline alloys and its effect on their structural and microhardness behaviour. J Non-Cryst Solids. 2013;380:11.

[50] Raghavan R, Murali P, Ramamurty U. Ductile to brittle transition in the $Zr_{41.2}Ti_{13.75}Cu_{12.5}Ni_{10}Be_{22.5}$ bulk metallic glass. Intermetallics. 2006;14:1051.

[51] Jang JSC, Chen YW, Chang LJ, Cheng HZ, Huang CC, Tsau CY. Crystallization and fracture behavior of the $Zr_{65-x}Al_{7.5}Cu_{17.5}Ni_{10}Si_x$ bulk amorphous alloys. Mater Chem Phys. 2005;89:122.

[52] Huang YJ, Shen J, Sun JF. Bulk metallic glass: smaller is softer. Appl Phys Lett. 2007;90:081919.

[53] Singh D, Yadav TP, Mandal RK, Tiwari RS, Srivastava ON. Effect of Ti addition on the quasicrystalline phase formation and indentation characteristics of $Zr_{69.5}Al_{7.5}Cu_{12}Ni_{11}$ alloy. Phil Mag. 2011;91:2837.

[54] Dubach A, Prasad KE, Raghavan R, Löffler JF, Michler J, Ramamurty U. Free-volume dependent pressure sensitivity of Zr-based bulk metallic glass. J Mater Res. 2009;24:2697.

[55] Ye JC, Lu J, Liu CT, Wang Q, Yang Y. Atomistic free volume zones and inelastic deformation of metallic glasses. Nat Mater. 2010;9:619.

[56] Xu Y, Shi B, Ma Z, Li J. Evolution of shear bands, free volume and structure in room temperature rolled $Pd_{40}Ni_{40}P_{20}$ bulk metallic glass. Mater Sci & Eng A. 2015;623:145.

[57] Zhu ZD, Ma E, Xu J. Elevating the fracture toughness of $Cu_{49}Hf_{42}Al_9$ bulk metallic glass: effects of cooling rate and frozen-in excess volume. Intermetallics. 2014;46:164.

[58] Evenson Z, Koschire T, Wei S, Gross O, Bednarcik J, Gallino I, Kruzic JJ, Rätzke K, Faupel F, Busch R. The effect of low-temperature structural relaxation on free volume and chemical short-range ordering in a $Al_{49}Cu_{26.9}Si_{16.3}Ag_{5.5}Pd_{2.3}$ bulk metallic glass. Scripta Mater. 2015;103:14.

[59] Tan J, Wang G, Liu ZY, Bednarclk J, Gao YL, Zhai QJ, Mattern N, Eckert J. Correlation between atomic structure evolution and strength in a bulk metallic glass at cryogenic temperature. Sci Reports. 2014;4. doi:10.1038/srep03897.

[60] Cheng YQ, Cao AJ, Sheng HW, Ma E. Local order influences initiation of plastic flow in metallic glass effects of alloy composition and sample cooling history. Acta Mater. 2008;56:5263.

[61] Chen M. A brief overview of bulk metallic glasses. NPG Asia Mater. 2011;3:82.

[62] Liu ZY, Yang Y, Guo S, Liu XJ, Lu J, Liu YH, Liu CT. Cooling rate effect on Young's modulus and hardness of a Zr-based metallic glass. J Alloys & Compds. 2011;509:3269.

[63] Hu Y, Yan HH, Lin T, Li JF, Zhou YH. Effect of cooling rate on the bending plasticity of $Zr_{55}Al_{10}Ni_5Cu_{30}$ bulk metallic glass. J Alloys & Compds. 2012;527:36.

[64] Liu Y, Bei H, Liu CT, George EP. Cooling-rate induced softening in a $Zr_{50}Cu_{50}$ bulk metallic glass. Appl Phys Lett. 2007;90:071909.

[65] Shen J, Huang YJ, Sun JF. Plasticity of a TiCu-based bulk metallic glass: effect of cooling rate. J Mater Res. 2007;22:3067.

[66] Misra DK, Sohn SW, Kim WT, Kim DH. Rate-dependent serrated flow and plastic deformation in $Ti_{45}Zr_{16}Be_{20}Cu_{10}Ni_9$ bulk amorphous alloy during nanoindentation. Sci Technol Adv Mater. 2008;9:045004.

[67] Jana S, Bhowmick R, Kawamura Y, Chattopadhyay K, Ramamurty U. Deformation morphology underneath the Vickers indent in a Zr-based bulk metallic glass. Intermetallics. 2004;12:1097.

[68] Chen LY, Setyawan AD, Kato H, Inoue A, Zhang GQ, Saida J, Wang XD, Cao QP, Jiang JZ. Free-volume-induced enhancement of plasticity in a monolithic bulk metallic glass at room temperature. Scripta Mater. 2008;59:75.

[69] Jiang WH, Liu FX, Wang YD, Zhang HF, Choo H, Liaw PK. Comparison of mechanical behavior between bulk and ribbon Cu-based metallic glasses. Mater Sci Eng A. 2006;430:350.

[70] Huang Y, Chiu YL, Shen J, Chen JJ, Sun J. Cooling rate effect of nanomechanical response for a Ti-based bulk metallic glass. J Non-Cryst Solids. 2010;356:966.

[71] Huang Y, Fan H, Wang D, Sun Y, Liu F, Shen J, Sun J, Mi J. The effect of cooling rate on the wear performance of a ZrCuAlAg bulk metallic glass. Materials & Design. 2014;58:284.

[72] Zhang LC, Jiang F, Zhang DH, He L, Sun J, Fan JT, Zhang ZF. In-situ precipitated nanocrystals beneficial to enhanced plasticity of Cu-Zr based bulk metallic glasses. Adv Eng Mater. 2008;10:943.

[73] Slipenyuk A, Eckert J. Correlationbetween enthalpy change and free volume reduction during structural relaxation of $Zr_{55}Cu_{30}Al_{10}Ni_5$ metallic glass. Scripta Mater. 2004;50:39.

[74] Turnbull D, Cohen MH. On the free-volume model of the liquid-glass transition. J Chem Phys. 1970;52:3038.

[75] Casals O, Alcala J. The duality in mechanical property extractions from Vickers and Berkovich instrumented indentation experiments. Acta Mater. 2005;53:3545.

[76] Mukhopadhyay NK, Weatherly GC, Embury JD. An analysis of microhardness of single-quasicrystals in the Al-Cu-Co-Si system. Mater Sci Eng A. 2001;315:202.

[77] Mukhopadhyay NK, Paufler P. Micro and nanoindentation techniques for mechanical characterization of materials. Int Mater Rev. 2006;51:209.

[78] Singh D, Singh D, Yadav TP, Mandal RK, Tiwari RS, Srivastava ON. Synthesis and indentation behaviour of amorphous and nanocrystalline phases in rapidly quenched Cu-Ga-Mg-Ti and Cu-Al-Mg-Ti alloys. Metallogr Microstruct Anal. 2013;2:321.

[79] Cahoon JR, Broughton WH, Kutzak AR. The determination of yield strength from hardness measurements. Metall Trans. 1971;2:1979.

[80] Mukhopadhyay NK, Bhatt J, Pramanik AK, Murty BS, Paufler P. Synthesis of nano-crystalline/nanoquasicrystalline $Mg_{32}(AlZn)_{49}$ by melt spinningand mechanical alloying. J Mater Sci. 2004;39:5155.

[81] Uhlenhaut DI, Dalla Torre FH, Castellero A, Gomez CAP, Djourelov N, Krauss G, Schmitt B, Patterson B, Löffler JF. Structural analysis of rapidly solidified Mg-Cu-Y glasses during room-temperature embrittlement. Phil Mag. 2009;89:233.

[82] Singh D, Singh D, Mandal RK, Srivastava ON, Tiwari RS. Glass forming ability, thermal stability and indentation characteristics in $Ce_{75}Al_{25-x}Ga_x$ metallic glasses. J. Alloys & Compds. 2014;590:15.

[83] Sun Y, Huang Y, Fan H, Liu F, Shen J, Sun J, Chen JJJ. Comparison of mechanical behaviours of several bulk metallic glasses for biomedical application. J Non-Cryst Solids. 2014;406:144.

[84] Singh D, Mandal RK, Srivastava ON, Tiwari RS. Glass forming ability, thermal stability and indentation characteristics of $Ce_{60}Cu_{25}Al_{15-x}Ga_x$ ($0 \leq x \leq 4$) metallic glasses. J Non-Cryst Solids. 2015;427:98.

[85] Singh D, Basu S, Mandal RK, Srivastava ON, Tiwari RS. Formation of nano-amorphous domains in $Ce_{75}Al_{25-x}Ga_x$ alloys with delocalization of cerium 4f electrons. Intermetallics. 2015;67:87.

[86] Singh D, Singh D, Srivastava ON, Tiwari RS. Microstructural effect on the low temperature transport properties of Ce-Al (Ga) metallic glasses. Scripta Mater. 2016;118:24.

[87] Yadav TP, Singh D, Tiwari RS, Srivastava ON. Enhanced microhardness of mechanically activated carbon-quasicrystal composite. Mater Lett. 2012;80:5.

Applications

On the Prospects of Using Metallic Glasses for In-vessel Mirrors for Plasma Diagnostics in ITER

Vladimir S. Voitsenya, Alexandra F. Bardamid,
Martin Balden, Flaviu Gostin, Sergey V. Khovrich,
Vladimir G. Konovalov, Konstantin V. Kovtun,
Petro M. Lytvyn, Sergey V. Ketov,
Dmitri V. Luzguine-Luzgin, Sergei I. Solodovchenko,
Anatoly N. Shapoval, Anatoly F. Shtan',
Vladislav N. Bondarenko, Ivan V. Ruzhkov,
Ol'ga O. Skoryk and Andrei A. Vasil'ev

Additional information is available at the end of the chapter

Abstract

This chapter reviews main results obtained on mirror-like samples made of several grades of bulk metallic glasses (BMG). Experiments were carried out under simulated conditions typical for the operation of plasma facing in-vessel mirrors of optical plasma diagnostics in fusion reactor ITER. Bombardment with D^0 and T^0 atoms radiated from burning plasma was predicted to be the main reason for the degradation of optical properties of such mirrors. Therefore, to simulate the behavior of mirrors in ITER, mirror-like samples were subjected to bombardment by ions of deuterium plasma with fixed or wide energy distribution. The effects of ion bombardment on optical properties, development of roughness, uptake of deuterium, appearance of blisters, and manifestation of some chemical processes are presented and discussed.

Keywords: amorphous mirrors, sputtering effects, deuterium uptake, chemical processes, blister-like features

1. Introduction

In the experimental fusion reactor ITER, many different methods of plasma diagnostics are envisaged to be used [1]. A big portion of methods are intended for optical measurements, and these have to be based on reflective optics, because of the high level of deeply penetrating radiations, gammas, and neutrons, which may degenerate the refractive optics components. The mirrors facing the burning plasma (first mirrors, FM) will be additionally subjected to fluxes of charge-exchange atoms (CXA, mainly D^0 and T^0 atoms) with a wide energy distribution, up to several hundred eV [2]. To overcome negative effects of CXA sputtering on mirror characteristics (due development of surface roughness), it was decided to fabricate first mirrors for ITER from single crystal (SC) metal, and molybdenum is the first candidate as a FM material.

At present, it is not known which effect the simultaneous irradiation of the FM surface with neutrons and CXA will have. However, there is a probability that a single crystal will lose its ideal SC structure what would result in gradual development of roughness (under CXA bombardment) and degradation of optical properties.

A real alternative to SC mirrors can be mirrors fabricated from amorphous metal alloys (bulk metallic glasses, BMGs). They do not have any arranged structure larger than a few nanometer and therefore may be more resistive under irradiation with neutrons in comparison with crystallized metals. Recent results on simulating the neutron irradiation effects by exposing BMG samples with 3 MeV Ni^+ ions did not lead to big degradation of hardness and Young's modulus in the dose range of 0.1–10 dpa [3,4]. It is important to note that the structure of samples has continued to be amorphous, without indication of appearance of crystallization.

Additionally, due to the lack of crystallized structure, under long-term sputtering, a polished BMG mirror has to resemble a liquid under evaporation: its surface has to be smooth regardless of sputtering time. Such assumption was mentioned in [5] and has found support later, after appearance of technology to produce BMG casts with size (≥10 mm) sufficient for the fabrication of mirror samples to provide corresponding experiments. Zr-based BMGs reveal relatively high crystallization temperature compared with other BMGs. From a practical standpoint, the glass forming ability of Zr-based BMGs is very good enabling the manufacturing of fully glassy components with thickness values in excess of 10 mm.

This chapter is a short review of main results obtained with BMG mirror samples in experiments that partly simulate the conditions for FM operation in ITER, that is, long-term sputtering by ions of deuterium plasma (in some cases by ions of argon plasma) with energy from 60 eV up to 1350 eV. Mirror samples were fabricated from five BMG grades (**Table 1**). The program of experiments with each BMG grade was not identical, and thus, new information was obtained, and some new properties of BMGs were found for both amorphous and crystallized BMG specimens. This chapter presents results on the following: (1) effects of long-term ion sputtering on optical properties of mirror-like BMG samples, (3) effects of deuterium adsorption, (4) the role of chemical processes on BMG surface when the deuterium plasma is contaminated with oxygen, and (5) observation of blister-like features due to deuterium exposure.

In Section 2, the specimens and the experimental details regarding the plasma exposures and characterization are described. Section 3 contains the main results on changes due to plasma exposure, in particular deuterium adsorption, reflectance, and erosion rate and the differences due to the state, amorphous or crystallized by annealing. In Section 4, some concluding remarks are provided. Appendix A contains details on BMG sample preparation in NSC KIPT (Kharkov, Ukraine), and in Appendix B, the results of processing of an image of laser beam after reflection from amorphous and crystallized mirrors are shown.

2. Experimental and precharacterization

2.1. Descriptions of specimens

A list of all grades of samples with their composition, shape, and size is presented in **Table 1**.

Grade #	Composition	Size, mm
1 (Vit1-LM)	Zr41.2Ti13.8Cu12.5Ni10Be22.5	Ø22 × 3
2 (Vit1-NSC)	Zr41.2Ti13.8Cu12.5Ni10Be22.5	Ø22 × 3
3 (Vit4)	Zr46.75Ti8.25Cu7.5Ni10Be27.5	Ø5 × 3
4	Zr48Cu36Al8Ag8	Ø(16–22) × 2
5 (Vit106)	Zr57Cu15.4Al10Ni12.6Nb5	20 × 22

Table 1. List of grades with composition given in at.%.
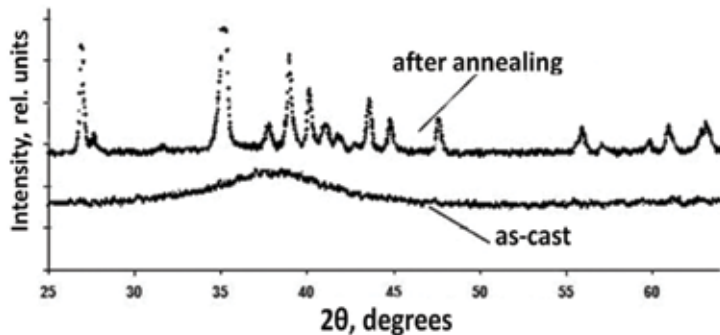
Figure 1. Results of X-ray diffraction measurements obtained with the half of the amorphous sample of grade #2 (lower curve) and the half annealed at 773°K during 1 hour.

Three BMG samples of **grade #1** produced by Liquidmetal Co (USA) and three billets of **grade #2** have the same nominal composition.

The billets of grade #2 were casted as discs with diameter ~26 and ~8 mm in thickness (the details of their fabrication in NSC KIPT are described in Appendix A). They were cut into

approximately equal halves (final size Ø22 × 3 mm): one half of every billet was left amorphous and the second half was annealed (1 hour at 773°K) to have a fine-crystalline material. Thus, for this grade, there was a possibility to compare the behavior of mirrors from the identical material but with different structures, amorphous and fine-crystalline. The X-ray data on the structure of such a pair are shown in **Figure 1**.

The position of the peaks in a diffractogram indicated the existence of the following nano-crystals: Zr_2Ni, Ti_2Ni, Zr_2Cu, and Zr_xCu_y with x and y exceeding two. By measuring the half-width of the peaks, the size of crystallites was roughly estimated to 50 nm using the following formula [6]:

$$D = \frac{0.9\,\lambda}{\beta\,\cos\theta} \qquad (1)$$

where λ is the X-ray wavelength, θ is the Bragg angle, and β is the full width at half maximum of the diffraction peak.

After crystallization of three halves, all three pairs of grade #2 were polished simultaneously.

The mirror specimens of **grade #3** (more than 10 pieces) were cut from a 5-mm-diameter rod to discs of 3 mm thickness. Because of the small surface area, they were not used for some experiments, namely for measuring the absorptivity of deuterium.

The cast of **grade #4** had a complicated shape; therefore, the mirror samples (five pieces) had different diameter from Ø16 to Ø22 mm with thickness of 2 mm each.

The cast of **grade #5** was of rectangular shape; after cutting it into two samples the size of mirror specimens became 20 × 22 × 3 mm.

XRD (X-ray diffraction) analysis confirmed the glassy state of all samples (diffraction patterns not shown here).

All prepared billets were polished to a high optical quality.

2.2. Pretreatment and initial reflectance

Prior to exposure experiments, all mirror samples were initially cleaned for ≥20 min with low-energy deuterium plasma ions, $E_i \sim 60$ eV or sometimes with low-energy Ar plasma ions, to remove the organic film appeared due to rinsing of samples in acetone and alcohol after the polishing. The reflectance of mirror samples after this exposure was taken as their initial spectral reflectance.

The comparison of initial reflectance, $R_0(\lambda)$, for one BMG mirror specimens of each grade is presented in **Figure 2** together with W and Mo reflectivity data from [7]. The measurements were done in the wavelength range 220–650 nm at normal incidence of the light by the use of a two-channel method described in [8] with a homemade attachment to a standard mono-chromator.
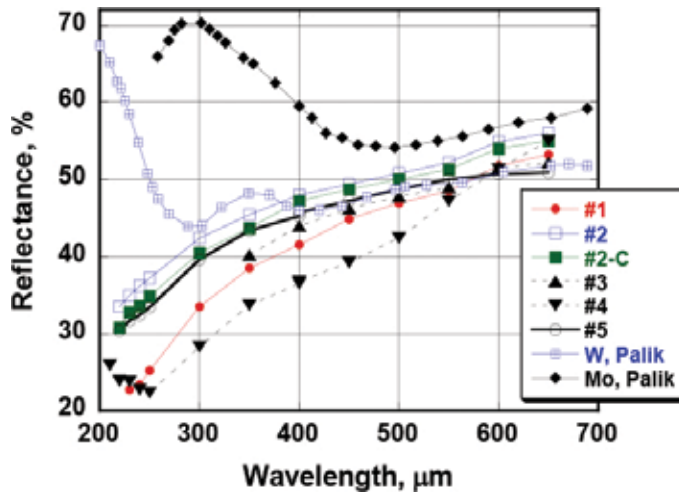
Figure 2. Initial reflectance $R_0(\lambda)$ measured just after cleaning by low-energy ions of deuterium or argon plasma of samples of the five grades together with the data for W and Mo from literature [7].

The $R_0(\lambda)$ values of some BMG mirror samples are close to $R_0(\lambda)$ values of tungsten for the wavelengths range ~400–700 nm and is approaching to the reflectance of Mo mirror at $\lambda > 600$ nm. Crystallization does not lead to any significant change of initial optical properties of samples in the wavelength interval of measurements (220–650 nm), as can be concluded from comparing the data for grades #2 and #2-C (crystallized).

2.3. Heterogeneities observed in the body of BMG samples

After the last polishing procedure, some local peculiarities were discovered on smooth sample surfaces of the grade #1. Such peculiarities were not observed on the other grades.

Their level was a little below the main surface, appear usually as a group, are roughly of oval shape, distributed over the main surface of mirror sample more or less uniformly, and are observable in both, optical microscope and scanning electron microscope (SEM). The total relative area of these inhomogeneities was estimated to be at the level of ~1%, so they did not have any essential influence on measurement of reflectance, that is, the performance of the mirror. The fact of their elevation below the matrix supposed that the composition of these features differs from that of the main volume of material and that their hardness again mechanical treatment is inferior to the hardness of the bulk.

Figure 3 shows two SEM images of the same region obtained by different detectors of SEM, detecting (a) mainly secondary electrons and (b) backscattered electrons. In the first case, the contrast of the image is mainly determined by the surface topography, but in the second regime, the contrast occurs due to differences in the atomic number of the surface elements. In this second case, the domains with predominance of light elements appear darker than the surrounding; therefore, we may state that the recessed domains are enriched by the lighter component of the material (the average atomic number here is below that of the matrix).
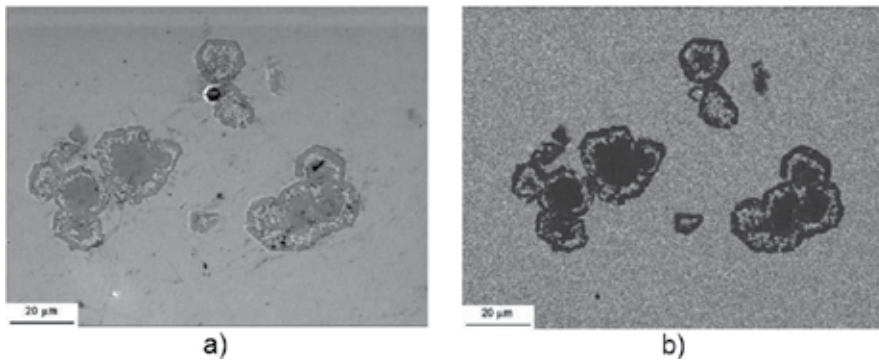
Figure 3. SEM images from secondary (a) and backscattered electrons (b) of inhomogeneities on the sample surface of grade #1 [9].

Under ion bombardment, as a result of the sputtering process, initially lower parts of the surface descended deeper below the main level and turned into shallow holes with a rather nonplanar bottom shown in **Figure 4**. The depth of holes increased with increase in ion fluence, which indicates (i) a lower resistance of these inclusions to ion sputtering and (ii) their volumetric character.
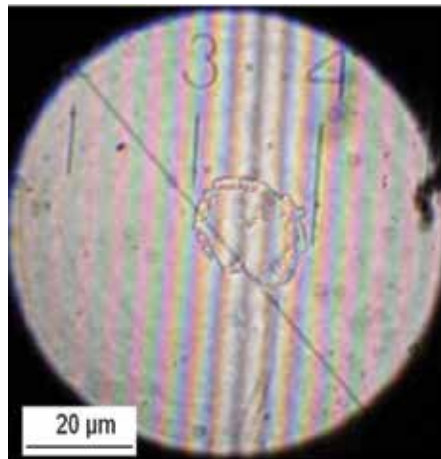
Figure 4. Photograph of interferometer microscope after the layer of ~2 µm was sputtered with deuterium plasma ions [10]. The interference fringes indicate a depth of ~150 nm fort the central feature.

The difference in composition of the material inside the inhomogeneities and the surrounding matrix was confirmed by the following two methods: an electron microprobe analysis (**Table 2**) and scanning electron microscope (SEM) with energy-dispersive X-ray spectroscopy (EDX), **Figure 5**. The data of microprobe analysis demonstrate that the material in the holes is depleted in zirconium (Zr) and titanium (Ti), and enriched with the other elements such as copper and nickel. From this result, it is not surprising that the rate of sputtering of the inhomogeneities

is higher than of the matrix. Taking into account, the sputtering yields, Y, of components of the mirror material [11] one can find for deuterium ions at energy 1000 eV, $Y(Zr)=5.5\times10^{-3}$ at/ion, is about one order of magnitude lower than $Y(Be)$, $Y(Cu)$, $Y(Ni)$, and two times lower than $Y(Ti)$. At lower ion energy, the difference in sputtering yields is much greater. The microprobe data show that after long-term sputtering the composition of Zr in holes continues to be below that in the matrix.

Element	Nominal composition (at.%)	Matrix composition (at.%)	Inhomogeneity composition (at.%)
Zr	41.2 (100%)	52.8 (100%)	43.0 (100%)
Ti	13.8 (33.2%)	17.4 (33%)	12.0 (28%)
Cu	12.5 (30%)	15.2 (28.8%)	24.3 (56.5%)
Ni	10 (24%)	14.6 (27.7%)	20.7 (43%)
Be	22.5 (54.9%)		

Table 2. Elemental composition of the mirror material from grade #1: nominal (second column) and measured by means of microprobe method in the matrix and in the inhomogeneity (without taking into account Be). Ratio to the Zr content is given in brackets [10].
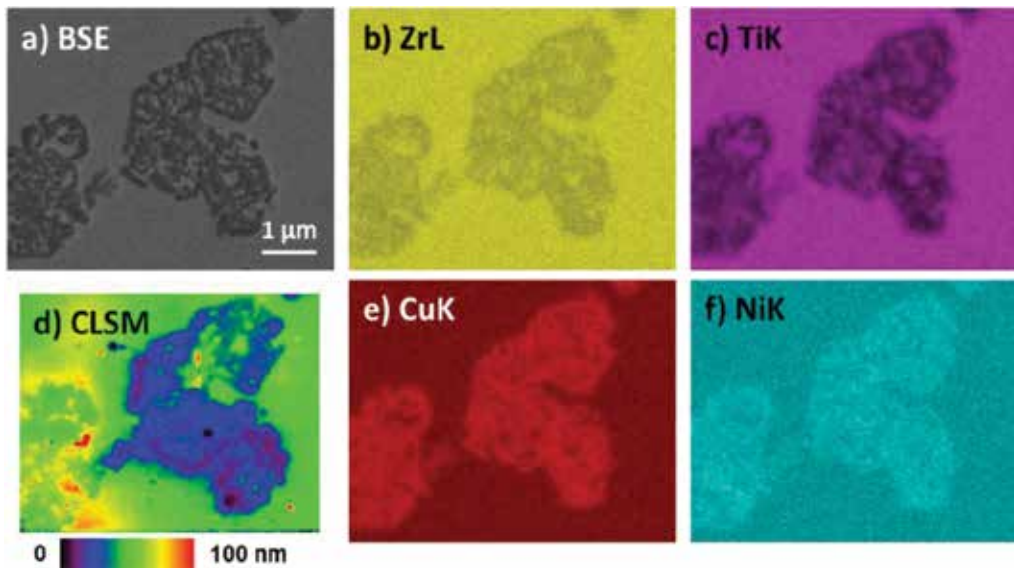

Figure 5. (a) SEM image from backscattered electrons and (b, c, e, f) the corresponding elemental maps obtained by EDX of the polished mirror surface of a sample of grade #1. (d) Height plot obtained by confocal laser scanning microscopy.

Comparing the EDX maps for zirconium, nickel, copper, and titanium (**Figure 5**), one could see that for inhomogeneities of the hole type, the intensities of ZrL and TiK lines are in anticorrelation with intensities of CuL and NiL lines what is in agreement with the results of

microprobe analysis. The data obtained by confocal laser scanning microscopy, **Figure 5d**, indicate that inhomogeneity is below the matrix level.

As **Figure 6** shows, the alloys grades #3 and #4 also contain heterogeneities, however of another kind. The majority of the heterogeneities have a dendritic appearance. On one occasion, a rather full structure of such an inhomogeneity was revealed after bombardment of one of grade #3 samples with argon ions, **Figure 6a**. Its shape is quite similar to the shape of crystals described by the authors of this alloy [12] (see also references ibidem). Important, the surface between these features is continuing to be smooth.
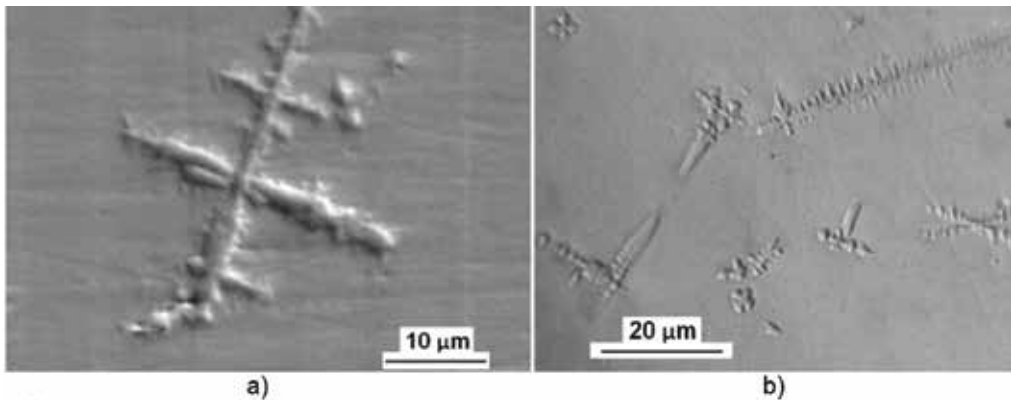
Figure 6. SEM images of the mirror surface: (a) sample of grade #3 after sputtering with argon ions of the layer of ~5 μm, (b) sample of grade #4 after sputtering with deuterium plasma ions of the layer of ~1 μm.

No heterogeneities of this kind were found in the other two alloys: grade #2 and #5.

2.4. Plasma exposure and methods of surface analysis

To simulate the impact of charge-exchange atoms (CXA) flux on BMG mirror samples in ITER, ions of deuterium or argon plasma were used. The detail description of the experimental stand DSM-2 used for performing the ion bombardment can be found in [13,14]. The BMG mirror samples were exposed to electron cyclotron resonance plasma (ECR, frequency of generator 2.45 GHz) produced in a double-mirror magnetic configuration. Mirror specimens were fixed on a water-cooled holder just outside of magnetic mirror. During the exposure, the temperature did not exceed 40°C. The electron density of plasma was ~10^{16} m^{-3} and electron temperature ~5 eV. A fixed negative voltage (in the range 50–1350 V) was supplied to the mirror holder for the acceleration of ions to the mirror surface. In some cases, when using deuterium plasma, the ion flux was energy distributed between 50 eV and 1350 eV by the combination of fixed negative potential and a time-varying (frequency 50 Hz) half-wave positive potential for ion acceleration [13,14]. The latter was done to be closer to real energy distribution of CXA flux, calculated for ITER [2]. The mean ion current density to the sample was of the order of 1 mA/cm^2, that is, ~10^{20} ions/m^2.

In the low-energy ECR deuterium discharge, there are usually not only monoatomic ions (D^+) but also molecular ions (D_2^+ and D_3^+) [15]. In proximity to the mirror surface, such polyatomic ions fall apart into atoms and monoatomic ions in such a way that their energy, acquired during passing the accelerating voltage, is divided equally between fragments. Thus, the surface of mirror is bombarded by particles of equal mass but different energies: E, $E/2$, and $E/3$, where E is the ion energy due to application of an accelerating voltage. With this peculiarity of plasma composition and sinusoidal time variation of accelerating voltage, the character of calculated energy distribution of projectiles bombarding the mirror surface is in a qualitative accordance with the CXA energy distributions measured at tokamaks ([16, 17]) and calculated for ITER conditions [2].

All samples were exposed in several steps in DSM-2 to nonmass-separated plasma ions in order to study the evolution of investigated properties with fluence. After each exposure step, the mass change and the reflectance at normal incidence of light (range 220–650 nm) were measured. The state of sample surface was analyzed by various microscopes (in addition to mentioned SEM with EDX): optical microscope, interferometer microscope, confocal laser scanning microscopy (CLSM), atomic force microscopy (AFM); for some BMG samples, the state of surface was studied by secondary ion mass spectrometry (SIMS), electron microprobe method, and laser ablation method.

3. Properties after plasma exposure

3.1. Absorption of deuterium

3.1.1. Amorphous specimens

It was found that mirror samples of all grades absorb large amounts of deuterium after the mirror specimens were bombarded with ions of the deuterium plasma. Because of deuterium absorption, a weight gain was observed for all tested BMG grades, even if sometime clearly sputter erosion takes place. This is expected due to the high fraction of hydride forming elements (Zr, Ti, Be). In **Table 3**, the weight gain after each plasma exposure step for a sample of grade #1 is shown. For low enough energies, that is, up to 100 eV, one may suppose that ion sputter erosion is negligible. Therefore, the ratio of retained deuterium to the impacting ions can be calculated up to 100 eV, and is shown in **Figure 7**. Because the ECR discharge does not only produce D^+, but also D_2^+ and D_3^+ ions, the total flux of deuterium projectiles has to be somewhat larger than the ion flux measured, and, correspondingly, the portion of retained deuterium to impacting D atoms has to be noticeably lower, assumed within a factor of ~2.

The set of data for deuterium trapping by different samples is shown in **Figure 8**. The ion energy was fixed at 60 eV for the samples of grades #1 and #2, and at 100 eV for both sides of sample of grade #5, while it was increased from 30 to 600 eV for the sample of grade #4. Obviously, for fixed ion energy the deuterium uptake increases linearly with ion fluence.

No of exposure step	Accelerating voltage, V	Ion fluence, 10^{23} ions/m²	Current density, mA/cm²	Weight change, µg/cm²	Absorption, D/ion, %
1	−30	8.1	1.2	+21	7.7
2	−30	8.1	1.2	+18.4	6.8
3	−1000	2.0	2.6	0	?
4	−20	8.1	1.2	+26.3	9.7
5	−100	9.2	1.37	+69.7	22.6
6	−60	9.2	1.36	+48.7	15.8
7	−60	9.8	1.54	+35.5	11.7

Table 3. Results of sequential exposures of one sample of grade #1 in deuterium plasma.
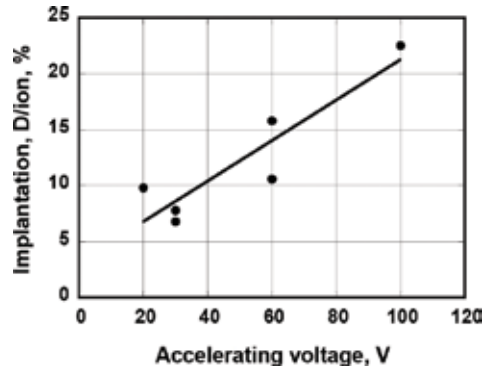
Figure 7. Dependence on ion energy of the portion of deuterium (in comparison to deuterium ion fluence) retained in the amorphous mirror sample of grade #1 [10].
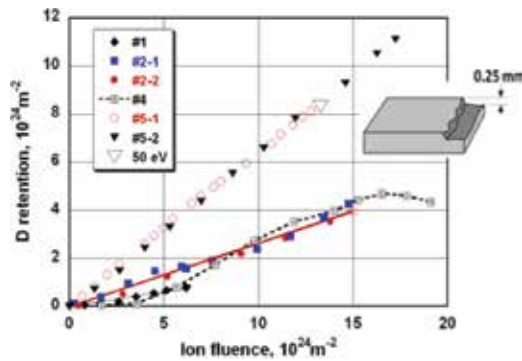

Figure 8. Dependence of deuterium retention for BMG samples on ion fluence found by measuring weight gain. The details are in the text. Inserted is the sketch of the sample of grade #5 after finishing its exposure in deuterium plasma on both sides. The chipped side was exposed secondly (triangles, #5-2) to the fluence 1.7×10^{25} ions/m².

A very low level of absorbed deuterium for the sample of grade #4 at the lowest fluences (30 and 60 eV) is most likely explained by insufficient cleaning of this particular sample. A clear linear dependence takes place from 60 eV up to 150 eV (fluence range from $(3.6–12)\times10^{24}$ ions/m^2), then sputtering starts to play more and more important role with increasing ion energy: at ion accelerating voltage of 400 V, sputtering and absorption are about equal, but with further rise of ion energy the weight started to decrease showing that sputtering prevails over deuterium absorption. An abrupt transition from linear dependence to saturation gives chance to estimate the thickness of sputtered layer, as it is described below (Section 3.2).

After last exposure in deuterium plasma (ion fluence~1.9×10^{25} ions/m^2) the #4 grade sample became curved with radius of curvature ~24 cm in such a way that the side exposed to D plasma ions became convex.

The experiment with exposing front side of sample of grade #5 (data #5-1) was also stopped (at ion fluence 12.8×10^{24} ions/m^2) after its bending was discovered, again with exposed side to be convex (curvature radius ~28 cm).

This fact indicates appearance of tension due to an increase in the specific volume of the near-surface layer exposed with deuterium plasma ions. The fact of bending means that deuterium does not penetrate through the whole thickness of samples, and only near-surface layer, of thickness less than the total thickness of sample, is increasing in volume.
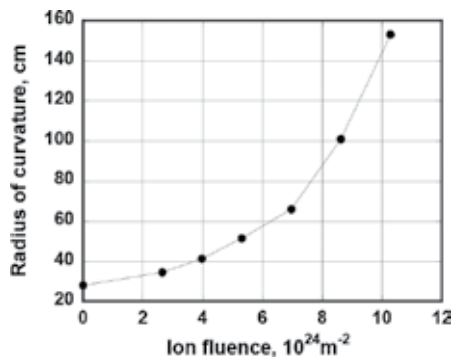
Figure 9. Straightening of the sample of grade #5 by exposing to the backside (#5-2 in **Figure 8**).

It was decided to continue the experiments by exposing the back side of the #5 sample in similar conditions (data #5-2 in **Figure 8**). During sequential exposures, the sample started to straighten gradually (**Figure 9**) and became plane at ion fluence ~12.0×10^{24} ions/m^2, that is, after approximately the same fluence to the front side caused bending of the sample. Three further exposures resulted in beginning to bend the sample in opposite direction (radius of curvature ~100 cm) and its partial destruction. Schematically, the shape of the sample after full cessation of experiment is shown as insert in **Figure 8**. The thickness of the chipped off part is ~0.25 mm. Assuming the formation of zirconium hydride in δ-phase ($ZrD_{-1.5}$) by all retained deuterium, the thickness of hydride layer would be 0.22 mm. This is excellent agreement with the observed thickness of the chipped fragment.

In **Table 4**, the efficiency of deuterium absorption is shown as the ratio of retained D atoms to the whole fluence of ions, found as the product of measured ion saturation current and the total exposure time, because the real proportion between one-, two-, and tree-atomic ions is not known (see comments in Section 2.3). It follows from **Table 4** that the efficiency of uptake depends strongly on ion energy and composition, but even with identical composition difference is significant (for grades #1 and #2).

Samples	#1	#2	#4	#5
Ion energy, eV	60	60	60–150	100
Ion fluence, 10^{24}ions/m^{-2}(F_i)	6.26	15	15	12.8
Mass gain, mg/cm^2	0.27	1.33	1.5	2.71
N_D absorbed, 1024 D atoms/m^{-2}	0.8	4	5	8.1
Efficiency of absorption (N_D/F_i)	0.13	0.27	0.33	0.63
Portion of Zr in composition	41.2	41.2	48	57

**Table 4.** Comparison of deuterium uptake by different BMG samples.

Comparing data of the table, it looks like there is a tendency for efficiency of uptake to increase with increasing the portion of zirconium.

A laser ablation technique was applied as an attempt to see the depth distribution of trapped deuterium. The diameter of laser spot was ~0.3 μm, and the step in depth for every laser shot was ~1.5 μm. As shown in **Figure 10**, deuterium is confidently registered even after the laser crater depth reached ~28 μm, However, in this method, the effect of side walls of the laser crater cannot be fully excluded, and therefore, any quantitative conclusion on the real depth distribution of implanted deuterium can only be done with a definite precaution.
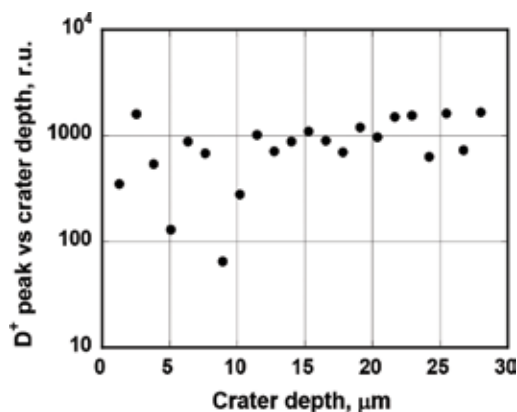
Figure 10. The amplitude of D$^+$ peak in ablated material as function of laser crater depth for a specimen of grade #1 exposed to deuterium plasma ions (60 eV/ion) up to a fluence of $5.9×10^{24}$ ions/m^2.

Samples that were not exposed to deuterium plasma did not reveal a deuterium peak in their mass spectra, as can be seen in **Figure 11**. The hydrogen peak was registered in every spectrum; however, it is well known that such peak can be an artifact appearing due to not perfect vacuum conditions in the mass spectrometer chamber.
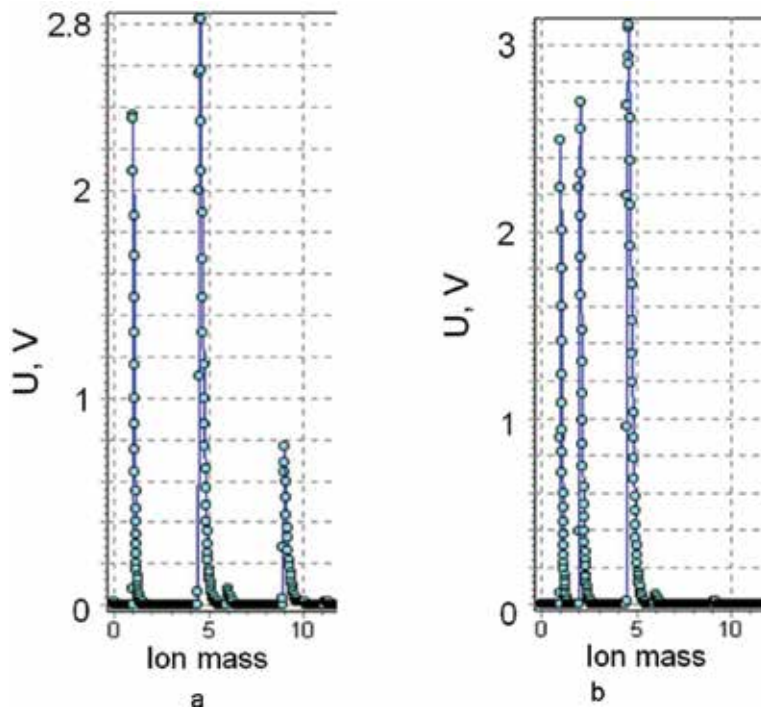
Figure 11. Mass spectra of the lighter masses of ablated material for samples of grade #1: (a) not exposed in plasma and (b) after exposure to deuterium plasma up to ion fluence 1.4×10^{25} ions/m^2 with different ion energy. Peaks of ions H$^+$, D$^+$, Be^{2+}, C^{2+}, and Be$^+$ can be clearly distinguished [9].

For another sample of grade #1 exposed to a total ion fluence of ~6×10^{24} m^{-2}, a second laser ablation test was carried out 26 days after the exposure. During that time, the sample was stored at ambient atmospheric conditions. This sample showed a very different depth distribution, namely deuterium was not registered during first five shots, and then D$^+$ peak appeared in the sixth shot, reached maximal amplitude in the 7th shot and gradually decayed to zero in the 11th laser shot. However, the weight of the sample did not change, and thus, it may be assumed that the retained deuterium was redistributed inside the sample or that some of the retained deuterium was released, but the associated weight loss was balanced out by oxidation.

3.1.2. Crystallized specimens

Two samples of grade #2, one amorphous (BMG) and one crystallized (BMG-C), were exposed in similar conditions for a long term to low-energy (60 eV) ions of deuterium plasma with a

current density of 2.1 mA/cm^2. Other important details of the experiment are presented in **Table 5**. During the fourth exposure (total ion fluence 7.5×10^{24} ions/m^2), the BMG-C was fragmented, as shown in **Figure 12a**. On the contrary, its amorphous counterpart maintained its integrity and continued to gain weight during the following three exposure steps (total ion fluence 1.4×10^{25} ions/m^2). The reflectance did not appear to be affected noticeably (not shown).

No of exposure	Ion fluence, 10^{25} ions/m^2	Weight gain for BMG, µg	Weight gain for BMG-C, µg
1	0.47	30	40
2	2.4	620	0
3	2.4	920	640
4	2.4	820	Destroyed
5	1.6	375	
6	2.4	825	
7	2.4	870	

Table 5. The history of weight change during exposure of samples of grade #2 to ions of deuterium plasma of 60 eV/ion, ion current density 2.1 mA/cm^2.
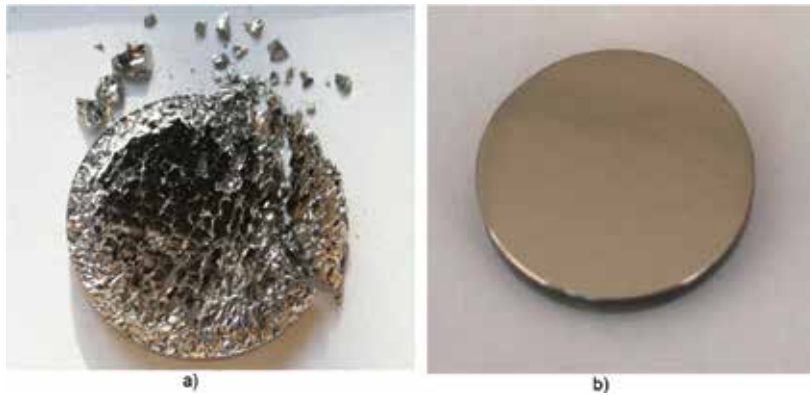
Figure 12. Photographs of (a) the BMG-C crystallized sample of grade #2 after the fourth exposure to 60 eV ions of deuterium plasma and (b) its amorphous counterpart (BMG) after the seventh exposure to 60 eV ions of deuterium plasma [18].

Not catastrophic for the sample, but detrimental for the optical characteristics was the modification of the surface of another crystallized mirror samples of grade #2, exposed to deuterium plasma ions in different regimes, **Table 6**. After the last exposure on the surface of this sample, there appeared defects in the form of chips and cracks of different sizes and significant weight loss was measured due to the loss of some fragments inside the vacuum chamber. The SEM images of chip surface at two magnifications, presented in **Figure 13**, exhibit the characteristic for a brittle rupture. The amorphous counterpart was unaltered.

Such difference in behavior of BMG and BMG-C samples is in a good qualitative agreement with the results published by Suh and Asoka Kumar on amorphous and crystallized samples of similar composition that were subjected to cathodic charging [19]. After a critical charging time, both amorphous and crystalline samples disintegrated. However, the maximum hydrogen content before total disintegration was up to 30 times greater for the amorphous phase compared to the crystalline counterpart.

No of exposure	Working gas	Ion energy	Current density, mA/cm^2	Ion fluence, 10^{23} ions/m^2	Mass loss, μg
1	Ar	200 eV	1.4	3.2	1970
2	Ar	500 eV	1.3	0.73	1195
3	Ar	1000 eV	1.9	0 .36	980
4	D$_2$	1000 eV	2.1	1.6	0
5	D$_2$	1000 eV	2.1	2.4	20
6	D$_2$	1000 eV	2.1	2.4	130
7	D$_2$	1000 eV	2.1	2.4	560
8	D$_2$	1000 eV	2.1	3.2	265
9	D$_2$	60 eV	2.1	14.1	2900

Table 6. The history of exposure of one of the BMG-C crystallized samples of grade #2 to ions of argon and deuterium plasma.
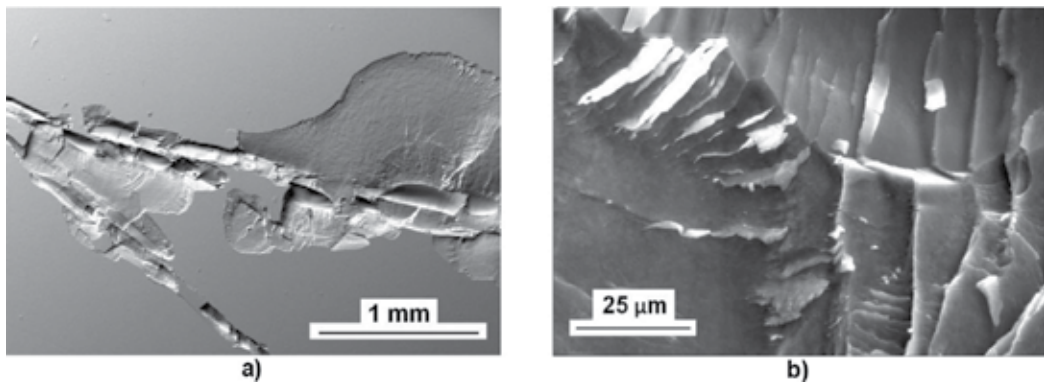
Figure 13. SEM images of the crystallized sample of grade #2 after the last exposure (no 9) shown in **Table 6** [18].

3.2. Sputtering rate

The adsorption of deuterium makes difficulties when trying to obtain data on sputtering yield by measuring the weight loss. Therefore, a stainless steel diaphragm (diameter 8 mm) which hid the rest part of BMG sample surface of grade #1 (diameter 22 mm) was used for determi-

nation of the rate of sputtering by deuterium plasma ions. The depth of the erosion hole measured for ion energies 300, 650, 1000, and 1350 eV are presented in **Table 7**. The corresponding values of sputtering yield were estimated with taking into account the depth of the hole, ion current density, and exposure time. The results are presented in **Figure 14**.

No. of experiment	Ion energy, eV	Depth of erosion, nm	Microhardness, kg/mm²	Mass change, μg	k	n
1	1350	709	639 ± 23	-210	2.65	2.05
2	1000	660	621 ± 21		2.69	1.91
3	650	505	668 ± 10	+40	2.7	1.96
4	300	188	682 ± 18	+80	2.68	1.93
5	Not sputter eroded surface		540 ± 18		2.61	1.77

Table 7. Results of exposure through a diaphragm (8 mm in diameter) of the sample of grade #1 for four ion accelerating voltage.
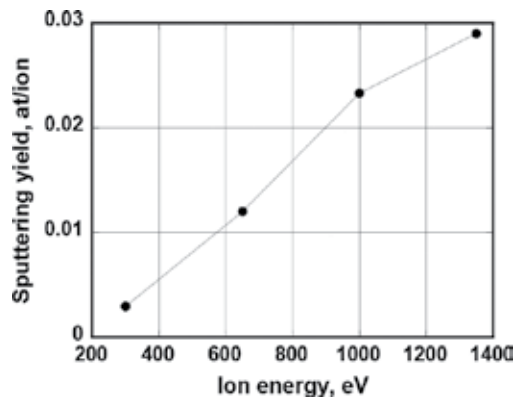

Figure 14. Sputtering yield found from the depths of holes appeared on the surface of sample of grade #1 exposed to D^+ plasma ions through an 8 mm diaphragm.

In addition to the erosion depth, the microhardness and the optical constants of surface inside each exposure spot were determined. It is seen from the **Table 7** that D^+ ion bombardment modifies the hardness of the near surface layer. The limited information on this subject, like the amount of trapped deuterium, its depth distribution, etc., does not allow to make a definite conclusion on the reason of this phenomenon, for example, on its link with volumetric density of trapped deuterium, as was found by the authors of [19].

After finishing the exposure to ions of energies indicated in the **Table 7**, optical indices n and k were measured with ellipsometry. **Table 7** shows that both optical indices do not depend strongly on the chosen D^+ ion energies and fluences; however, they differ a little from the indices measured for the initial surface, that is, not eroded by ions of deuterium plasma due to protection by diaphragm.

Because of the small size (Ø5 mm in diameter) of grade #3 samples the deuterium adsorption was not measured quantitatively for these samples (too low mass gain). Aiming to obtain data on sputtering, one sample of grade #3 was exposed to ions through a Ni gauze with wire diameter of 20 μm and mesh window width of 80 × 80 μm. The data obtained are shown in **Figures 15** and **16**. **Figure 15a** shows a typical photograph made with an interference micro-scope of the sample of grade #3 after it was bombarded with deuterium plasma ions (E_i=1000 eV, total ion fluence ~6×10^{24} ions/m^2) through the gauze, and **Figure 15b** shows the result of processing of the interference picture along several windows between wires of the gauze. As one can see, the sputter depth is about 1 μm. This depth corresponds to the sputtering yield (for not mass separated deuterium ion flux) Y≈0.05 atom/ion, which is about a factor two of the value found for grade #2 (**Figure 14**).
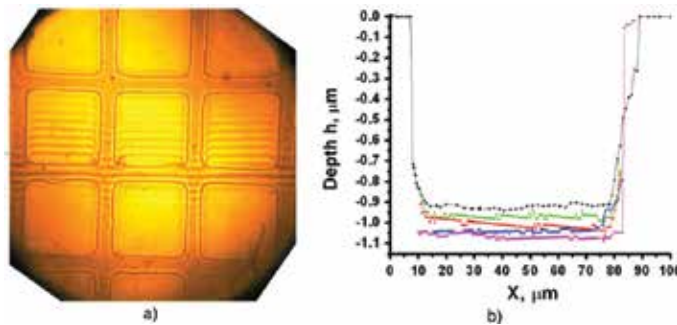
Figure 15. Interference fringes on the surface of the sample of grade #3 after long-term bombardment through the mesh (a), and the structure of the relief found by processing of the interference fringes (b) [20].

The optical and AFM data presented in **Figure 15** and **Figure 16** demonstrate similar depth of erosion in different windows. Also, they do clearly indicate that sputtering of the wire itself occurs because the edges of each wire are bombarded by ions at small angle to the surface, for which the sputtering yield exceed considerable the yield at normal incidence [21].
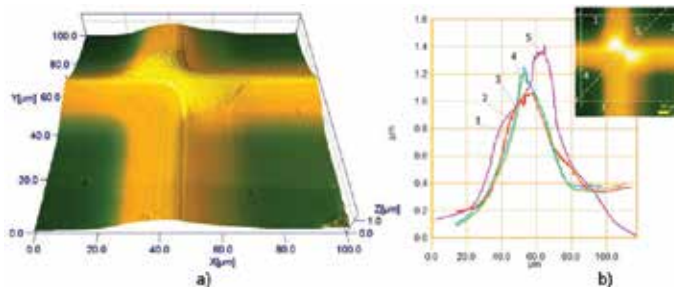
Figure 16. AFM data for the same sample of grade #3 exposed to plasma through Ni gauze as in **Figure 15**: (a) 3-D picture near crossing of Ni wires, (b) 2D picture of same data and height distributions along the lines shown in picture.

Important to note that saturation seen for the grade #4 sample in **Figure 8** is not because cessation of D absorption but due to faster mass loss caused by ion sputtering in comparison with the mass gain due to deuterium implantation. Taking this into account and comparing the linear fit of deuterium absorption with the saturation level of mass rise measured, one can find for this sample that thickness of sputtered layer after last exposure shown in **Figure 8** is ~1 μm, mainly due to sputtering by ions in the range 300–600 eV.

With the use of Ar plasma ions, there was not any problem to measure the weight loss even after short exposure. The results of these measurements for amorphous and crystallized specimens of grade #2, depending on the ion energy, are presented in **Figure 17** in comparison with data (solid line) for the bombardment of zirconium with Ar$^+$ ions from [11]. As seen, there is no measurable dependence in the sputter rate for samples in different state. Besides, there is a trend for lower sputter erosion rate of both samples in comparison to zirconium. This is in qualitative agreement with data for stainless steel in [21], sputtering yield of which was less than sputtering yields of each component (Fe, Ni, Cr).
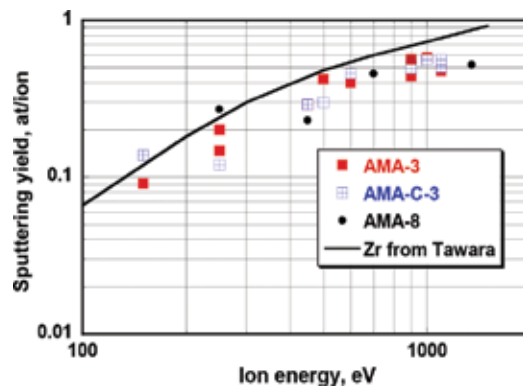
Figure 17. Sputtering yield depending on the Ar$^+$ ion energy for amorphous (BMG) and crystalline (BMG-C) mirror samples of grade #2. For comparison sputtering yield for pure Zr by Ar from Yamamura and Tawara [11] are shown. Amorphous sample BMG-3 and crystallized sample BMG-C-3 were made from same ingot.

When performing this experiment, not only mass loss but also the reflectance at normal incidence was measured after each sputtering procedure. Thus, the behavior of reflectance under long-term sputtering for samples (BMG and BMG-C) made from the same ingot of grade #2 but with different structure was determined (see next section).

3.3. Modification of optical properties of amorphous mirrors

3.3.1. Impact of deuterium plasma ions

When exposing BMG specimens of grades #1 and #2 in deuterium plasma, it was found that even rather short-time bombardment with ions of keV energy range, when sputter erosion

could be neglected, leads to a measurable decrease of reflectance in the whole spectral interval of measurement, both for amorphous (BMG) and for crystallized (BMG-C) mirror samples. The decrement of reflectance change depends on the wavelength: the shorter the wavelength the deeper the drop. The reflectance may be restored by long-time exposure to low energy (~50 eV) ions of deuterium plasma; the restoration is full or partial, depending on the exposure time to low-energy ions. This means that the reflectance decrease due to keV ion energy impact is not connected with modification of the surface microrelief but with some chemical processes on the surface, like it was established earlier for Be and Al mirror samples [22, 23]. We shall discuss this fact below in a special section.

As an example, **Figure 18** demonstrates the results obtained on one of BMG-C samples of grade #2. Initially, it was sputtered with ions of Ar plasma, what resulted in the development of some surface roughness and corresponding reflectance decrease (solid circles ⇒ squares). Then, the sample was bombarded with 1.0 keV ions of deuterium plasma, what caused further reflectance drop (rhombuses); however, not due to increase of the surface roughness, because this drop was fully restored by subsequent (much longer) exposure to low-energy (60 eV) ions of the same deuterium plasma (open circles). In contrast, the drop of reflectance caused by Ar ion sputtering could not be restored in similar way, that is, by exposing sample to low energy D^+ ions, as it occurred due to development of surface roughness.
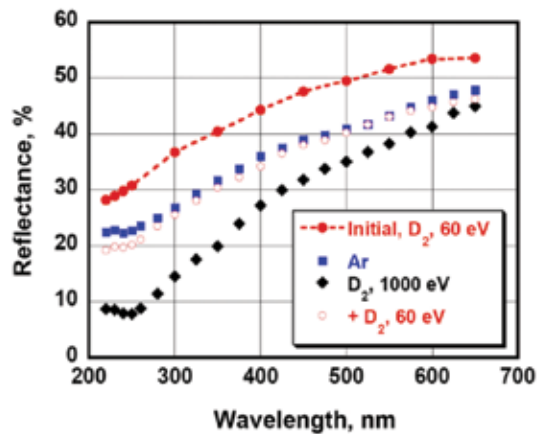
Figure 18. Spectral dependence of reflectance for BMG-C mirror sample of grade #2 after short exposure (ion fluence of the order 10^{22} ions/m²) to ions of deuterium plasma with energy 1 keV (◆) and following much longer exposure to 60 eV deuterium plasma ions (o).

The correlation of drop and restoration of reflectance for Be-containing BMG samples of grade #2 is in qualitative agreement with the results of experiments when specimen of grade #1 was exposed by turns to high (1.0 keV) and low (60 eV) energy ions of deuterium plasma [10].

For BMG specimens of grade #3, qualitatively similar effect was observed; however, detail investigation was not provided because of small size (diameter 5 mm).

### 3.3.2. Impact of argon plasma ions

To avoid the effects connected with chemistry, the consequence of long-term erosion was studied by the use of Ar plasma ions. In comparison with deuterium, the use of argon as a working gas is characterized by the following three principle moments: (1) argon is inert under most conditions and does not form confirmed stable compounds at room temperature; (2) argon uptake and the creation of a contaminating layer on the metal surface may be neglected; and (3) the time of experiments can be much shortened because of the sputtering rate of BMGs with Ar^+ ions is significantly higher as compared with D^+ ions.

The evolution of the microrelief and the reflectance of BMG mirror sample of grade #2 was determined up to erosion depth of 13.4 μm by sequential exposures to Ar^+ ions of different energy (0.1–1.35 keV). **Figure 19** shows the reflectance at three wavelengths versus the thickness of eroded layer. The data demonstrate that the amorphous mirror maintains the reflectance at about initial value even after strong sputter erosion. The constancy of reflectance means that the surface of amorphous mirror does not change during all sputtering procedures. This fact confirms the supposition made by Voitsenya et al. [5].
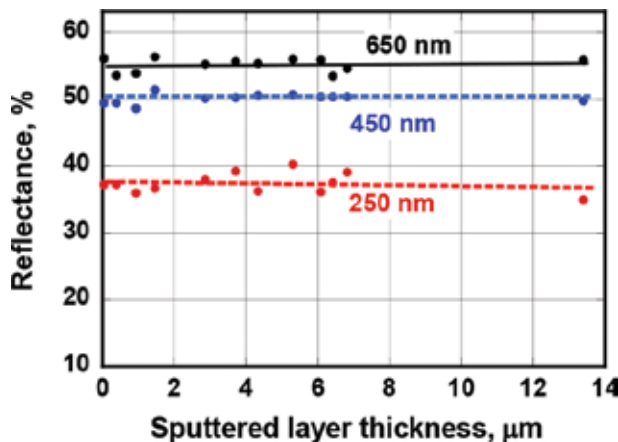

Figure 19. Dependence of reflectance of one of BMG sample mirrors of grade #2 on thickness of layer eroded due to manifold exposures to ions of Ar plasma with different energy [20].

At the same time, the surface of BMG-C sample (grade #2) made from same ingot but crystallized, became quite rough after sputtering to much lower erosion depth. In **Figure 20**, the comparison of SEM images of both samples are shown at the same magnification. One can observe that the relief appeared on the surface of the crystallized sample of grade #2 has approximately the lateral size of ~1 μm, while the amorphous sample of grade #2 stays very smooth.
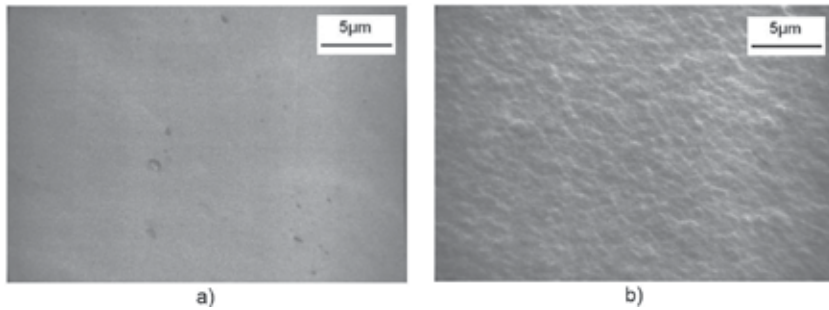
Figure 20. SEM photos of (a) BMG and (b) BMG-C specimens of grade #2 (made from the same ingot) after sputtering by Ar plasma ions to the depth 13.4 μm and 8.9 μm, respectively [10].

We have to emphasize a very significant difference in behavior of optical characteristics of mirror samples of grade #2 with amorphous (BMG) and crystalline (BMG-C) structures. The development of roughness on the surface of BMG-C (**Figure 20**) resulted in degradation of its ability to transmit an image. **Figure 21** shows the images of He-Ne laser beam spot after reflection: (a) from etalon mirror (Al film on quartz, that is, "ideal mirror"); (b) from amorphous mirror of grade #2 after long-term bombarded with Ar$^+$ ions (13.4 μm sputtered); and (c) from crystallized BMG-C sample of same grade after Ar bombardment (8.9 μm sputtered). The reflection of the crystallized BMG-C is strongly distorted, while the image of the eroded BMG has about the same quality as that from the "ideal mirror". The results of comparative analysis obtained when processing these images are presented in Appendix B.
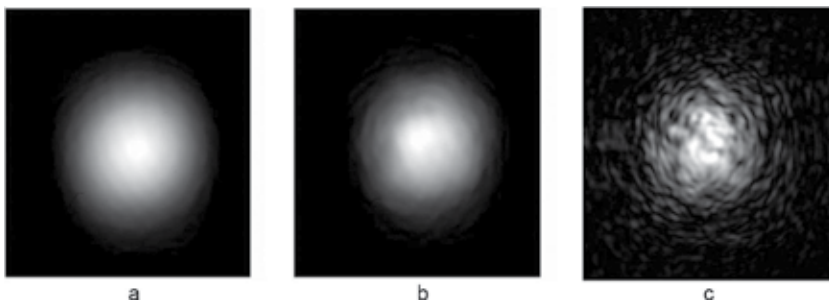

Figure 21. Image of the Ne–He laser beam spot after the beam was reflected from (a) "ideal mirror", (b) from sample of grade #2 after sputtering 13.4 μm, and (c) from crystallized sample of grade #2 after sputtering 8.9 μm [24].

3.4. Role of chemical processes

The qualitative similarity between behavior of reflectance of Be-containing BMG mirrors and Be mirrors exposed in similar manner suggests that in all cases similar processes are realized on the surface for mirror after impact of deuterium plasma ions with high (~1.0 keV) and low (~50 eV) energies. From the study of Bardamid et al [22], the reason of this transformation of BeO into Be(OD)$_2$ and gradual rise of hydroxide film thickness after the sample is subjected to

keV-energy ions of the plasma that contains also some amount of oxygen. An inverse process, namely restoration of initial state with thin BeO coating, on the Be surface occurs when ion energy is low.

To check this explanation, six BMG samples of grade #3 were sputter eroded by ions of Ar plasma to the depth of ~2 μm—for taking off the consequences of previous work with them. Then, four of them were bombarded by D plasma ions with energy of 1.35 keV. After that two of them were additionally long-term exposed to 60 eV ions of D plasma. SIMS analysis (with Cs+ ions as projectiles) was provided in two different points of the surface of the three pairs of samples. In connection with good equivalence of four data sets for each procedure (exposure to Ar ions, plus exposure to 1 keV D ions, plus exposure to 60 eV D ions), only results obtained from one point of one sample are shown in **Figure 22** for simplicity.
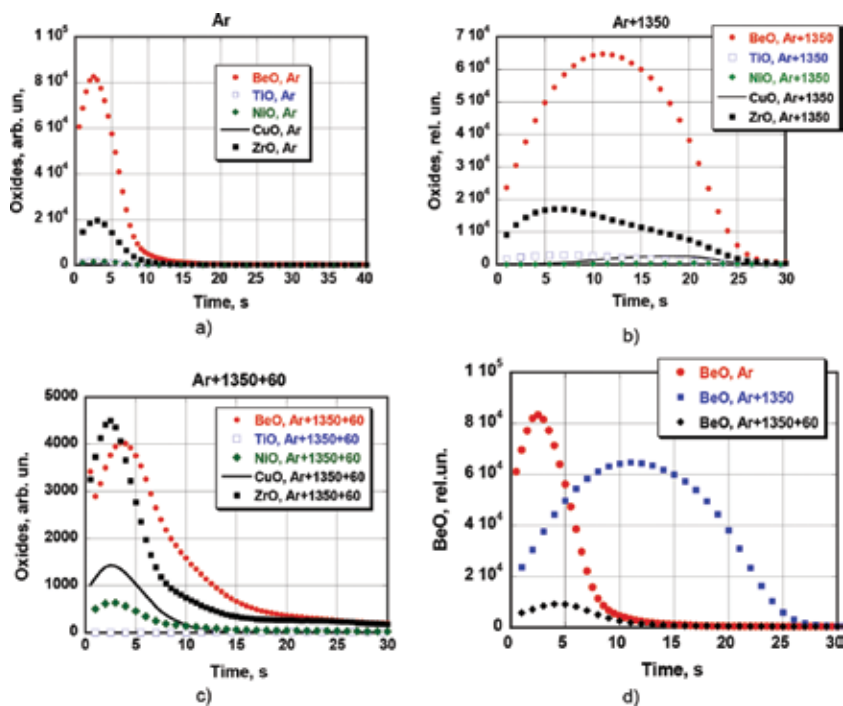
Figure 22. SIMS data for release of oxide ions for all components composed of BMG specimens of grade #3 after: (a) sputtering with Ar ions, (b) sputtering by Ar ions plus bombardment with 1.35 keV ions of deuterium plasma, (c) same as (b) plus long-term exposure to 60 eV ions of deuterium plasma; (d) comparison of the data for BeO ions only [18].

Evidently, the bombardment with keV-range D plasma ions leads to increasing the thickness of uppermost oxidized layer, but the following exposure to low-energy ions of similar D plasma results in thinning this layer and restoration of the initial depth distributions of all oxides.

These SIMS measurements were carried out with specimens having only 27.5 at.% of beryllium. At the same time, the release of BeO+ ions significantly exceeds the release of all other oxides

together. However, because the relative sensitivities of the various oxides in the SIMS meas‐ urements are unknown, no conclusion about depth distribution of different oxides in the near‐ surface layer can be obtained. It is worth to add that SIMS results are in qualitative agreement with data of XPS (X-ray photoelectron spectroscopy) measurements on specimens with a similar composition [25]. The authors of that paper have found that the uppermost oxide film is mainly composed of BeO in spite of a quite complicated chemical composition of the material.

Similar chemical processes are probably responsible for different ratios of Be^+ and Be^{2+} peaks shown in **Figure 11** when comparing the output at laser ablation of different ions from BMG samples of grade #1 exposed and not exposed to ions of deuterium plasma.

It is worth to note that qualitatively similar effects on the reflectance (drop for keV ion energy range and restoration for low-energy ions) were observed also for BMG samples of Al-containing grades #4 and #5, although not so strong.
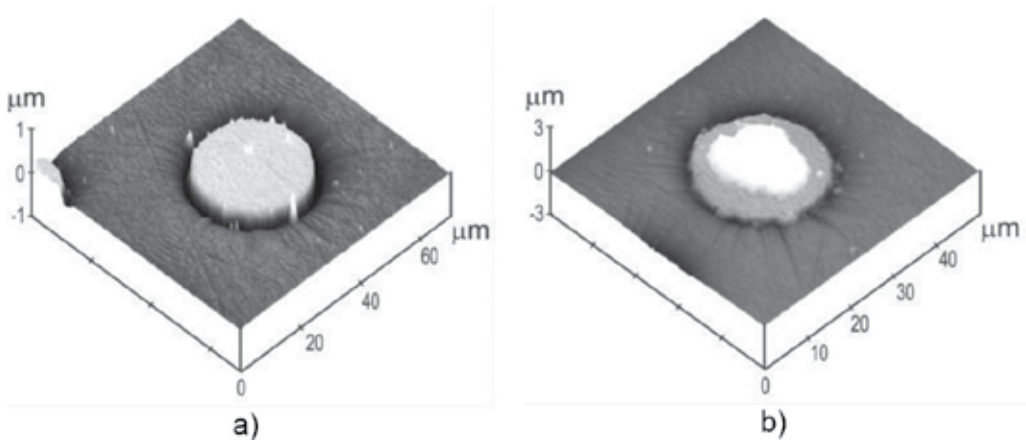
3.5. Blisters

After the determination of sputtering rate by D plasma ions (Section 3.2), many small surface features were found in that part of one BMG mirror specimens (22 mm in diameter) of grade #1 which was exposed to ions with energy 300 eV (diameter of diaphragm 8 mm, ion fluence 2.4×10^{24} ions/m^2). These "blister-like" features covered approximately 15% of the irradiated surface and generally had a round shape **Figure 23a**. Their size distribution (diameter) was obtained by measuring the dimensions of 617 such subjects observed in the view field of the microscope, ~0.4 mm^2. The mean diameter was ~10.5 μm with sizes ranging from ~3 up to 60 μm (one subject). The size distribution of these subjects is shown in **Figure 23b**. In the following sections, we use the word "blisters" for these subjects, in spite they do not look like a "classical" blisters, described by Behrisch [27].
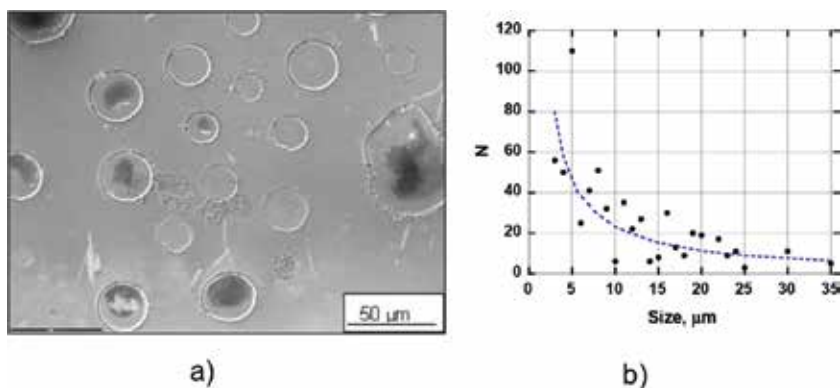

Figure 23. (a) SEM photo of the BMG mirror surface of grade #1 from secondary electrons with characteristic surface features [26]. The rough parts seen a little below the center are the structure defects described in the part 2.2 (see **Figures 3** and **4**); (b) size distribution of blister.

Figure 24 shows atomic force microscope (AFM) images of the two different types of blisters and **Figure 25** – the corresponding cross-section profiles. The height of the flat-top blister (**Figure 24a**) is ~0.2 μm and it is surrounded by an annular groove of approximately similar depth. The blister of similar size, but with a black central area (**Figure 23**) can be seen in **Figures 24b** and **25b**). This time, there is an irregular-shaped dome on a flat lid base; the dome is seen as black color in **Figure 23a**.

Figure 24. The AFM images of two different kinds of blisters: (a) with flat lid and (b) with a dome-like lid [26].
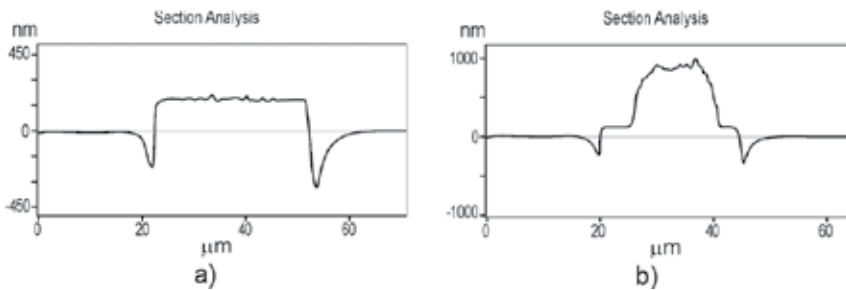

Figure 25. Cross-sectional profiles of the blisters shown in **Figure 24** [26].

A small part of the blisters is not round, and some of them have a dark part localized closer to their edge. Elemental maps obtained by EDX suggest that the elemental composition of the dome differs from that of the main BMG matrix.

The elemental composition of blister surfaces was obtained by two methods: microprobe analysis and EDX. On blisters with a uniform contrast and smooth lid, there was not found any noticeable deviation of composition in comparison with the matrix. At the same time those blister lids without contrast uniformity, seen with BSE, showed presence of impurities. As an example, in **Figure 26**, EDX-maps are shown for one of such blisters on the sample of grade

#1. It is seen that in darkest part of the surface (BSE) there are elements that are not a part of BMG composition: for example, carbon, oxygen, and iron.
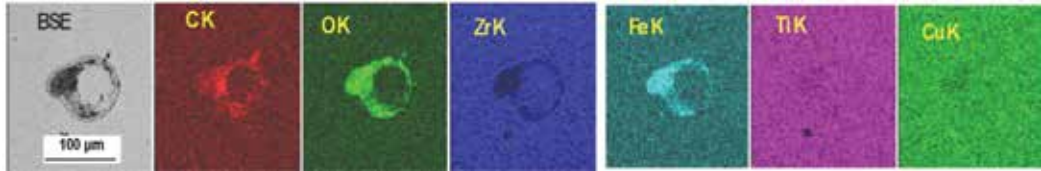
**Figure 26.** EDX-maps for a part of #1 sample surface with a large blister (~Ø65 µm).
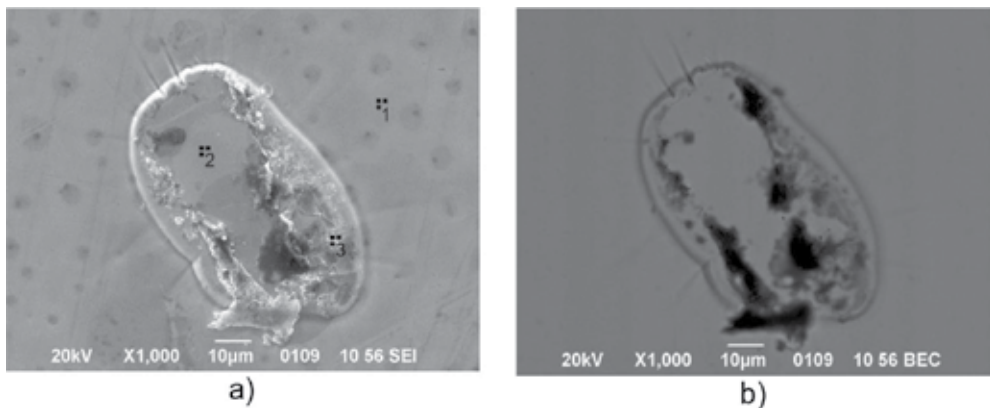
Figure 27. Image of a large blister with indication of points, P1 to P3, where measurements of composition were done: (a) SE and (b) compo (BSE).

In **Figure 27**, SE and BSE images of a blister on another sample of grade #1 are shown; the blister lid is not smooth partly. Numbers 1–3 indicate the points where a microprobe analysis was done (note that Be, C, and O cannot be registered by used setup). The results of measurements in those points are presented in the **Table 8**. Again, a small amount of impurity at the lid, this time, chromium, was registered. Based on results of EDX data for other blisters, one may assume that in the dark parts of the lid there are C and O also.

Several peculiarities of the blisters can be noted from presented data: (i) the blister location on the surface does not depend on the presence of defects in the grade #1 BMG described in the Section 2.3 (this is clearly demonstrated by **Figure 23a**); (ii) it looks like there is a probability that large blisters are localized in those parts where there are some concentration of contaminants, like iron, chromium, which can appear to be random; (iii) the parts of blister lids that look darker in BSE images are contaminated with carbon and oxygen; (iv) around practically every blister, there is evidence of stress-induced ductile deformation leading to a depression; (v) the inspection of several hundred features did not result in the observation of any cavity such as might be found following the bursting of blisters.

Element	Passport data, at%	Matrix (P1), at.%	Smooth part of the blister surface (P2), at.%	Coarse part of the blister surface (P3), at.%
Zr	41.2	56.6	57.7	49.7
Ti	13.8	16.9	17.3	15.4
Cu	12.5	13.9	13.1	12.4
Ni	10.0	12.1	12.0	11.7
Hf		0.6		0.6
Fe				8.3
Cr				1.9

Table 8. Results of microprobe analyses in points indicated in **Figure 27**.
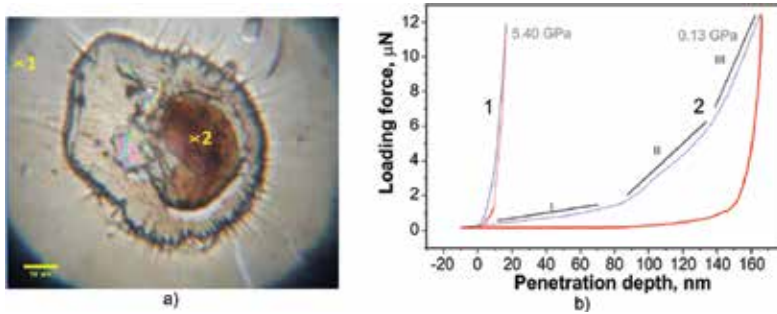
Figure 28. (a) Location of pricks by a nano-pin (yellow crosses) at the surface of a large dome-like blister, seen in **Figure 23a**. (b) The load and unloading curves of indenter measured at locations indicated in (a).

To clear up the reason of difference between both kinds of blisters, the nanoindentation procedures [28] were provided in matrix, in plane, and dome-like lids. The location of measurements is shown in **Figures 28a** and **29a**. The results are presented in **Figures 28b** and **29b**.

It is seen that the dark part of blister lid is soft and ductile. Three zones can be distinguished on the load curve: soft near-surface layer with ~80 nm in thickness (I), transition layer (II), and more solid material (comparable with hardness of matrix) at the depth starting from 140 nm (III).

These measurements demonstrate that the structure of the uppermost layer is very different for this pair of blisters: the dome-like one has a very soft uppermost layer (up to about 80 nm); the hardness of the material here became to be comparable with that measured for the plane-roof feature only at the depth ≥140 nm. At the same time, for plane roof feature, the hardness is much higher, composing ~60% of the matrix hardness.

Blisters were previously observed on metallic glasses of several kinds and on their crystal analogues after bombardment with H^+ and He^+ ions of energies up to 100 keV [29–31]. As was found, on amorphous materials blisters appear at ion fluences approximately three times greater than on the same materials in crystalline state. The blisters had dome-shaped lids with diameters in the range 0.5–2.5 μm (mean value 1.25 μm) for H^+ ions [29]. Such dimensions correlate well with the implantation range of the H^+ ions, thus suggesting the formation of "classical" blisters [27] due to accumulation of hydrogen in the near-surface region.

In conclusion, we would again state that difference in size, along with the atypical shape (like flat lids, annular grooves, the lack of broken lids, etc.), indicate that the observed features are not blisters in common understanding of this word [27].
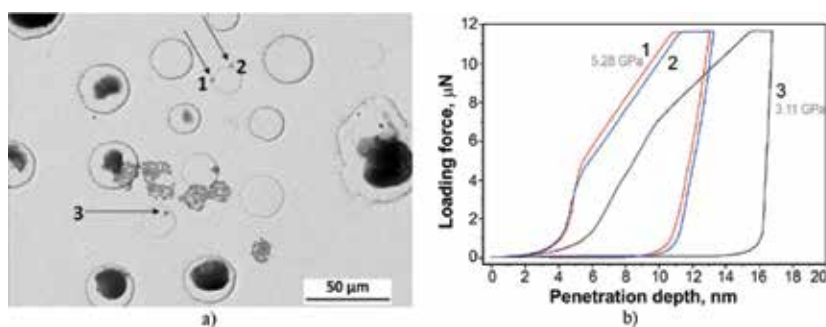
Figure 29. (a) SEM photo from backscattered electrons of the part of the surface shown in **Figure 23a**. (scale is 50 μm). Locations of pricks by a nano-pin at the surface of a plain lid blister and nearby matrix are shown by lower arrow and upper arrows, correspondingly. (b) The load and unloading curves of indenter measured at locations indicated in (a).

4. Summary

BMG mirror samples of different elemental composition were investigated in experiments simulating the behavior of first mirrors under impact of charge exchange atoms in the fusion reactor ITER. As projectiles the ions of deuterium and argon plasmas were used. Behavior of optical properties and surface topography, uptake of deuterium, effects of sputtering on optical reflectance in the visible spectrum, and chemical processes in a near-surface layer were studied. It was found that some of the studied properties have weak dependence on material composition whereas the others show noticeable differences. The following statements can be made:

1. Initial reflectance of BMG mirror samples under study is close to reflectance of W mirror for wavelengths exceeding 300-500 nm. The highest reflectance was measured for samples of grade #2 independently on the state: amorphous or crystallized.

2. In the body of three kinds of samples, structural inhomogeneities were described, which are connected with deviation of local composition from the composition of matrix, as was studied in detail for BMG samples of grade #1. The composition of inhomogeneities, that

occupied small part of the sample volume, was depleted with zirconium in comparison with amount of Zr on average. The ion-sputtering rate of material in these parts was higher than that of the main matrix, which leads to shallow depressions appearing on the sample surface with a rather planar bottom of 10–30 μm in size and the depth depended on sputtering time.

On the samples of grades #3 and #4 inhomogeneities of relief became clearly visible after eroding a layer exceeding 1 μm, either with ions of argon (grade #3) or deuterium plasma (grade #4).

3. Under long-term ion bombardment (thickness of sputter eroded layer was 13.4 μm in the case of #2 grade) no noticeable change of surface topography and reflectance for matrix of all BMG mirror samples was observed, excluding grade #4, where inhomogeneities occupied a rather big portion of the surface. In contrast, significant degradation of the mirror surface quality was found for the crystallized BMG sample of grade #2 sputtered to much less depth than its amorphous counterpart in similar conditions.

4. Under bombardment by deuterium plasma ions some amount of deuterium is absorbed, with the tendency to increase of absorbed portion when increasing the portion of zirconium. The highest value of deuterium was absorbed by BMG sample of grade #5: 1.1×10^{25} D atoms/m^2.

    The absorbed deuterium, most likely, does not penetrate through the whole thickness of the sample but is accumulated in the layer with a thickness of a few tenths of millimeter (note, thickness of samples is 2–3 mm). At ion fluence exceeding 1×10^{25} ions/m^2 samples become bent in such a way that the front side (exposed to ions of deuterium plasma) became convex with radius of curvature ~24 cm for grade #4 and ~28 cm for grade #5. Following exposures in similar conditions of the back side of grade #5 resulted in gradual straightening of the sample, and even bending it in opposite direction with further increase in ion fluence.

5. For samples of grade #2 in amorphous state, the deuterium ion fluence (15×10^{24} D ions/m^2) much exceeded the value for their crystallized counterparts when they started to the destroy: ~5×10^{24} D ions/m^2.

6. After implantation of deuterium (up to 1.1×10^{25} D atoms/m^2 for grade #5 sample), there was not observed any indication on appearance of crystallized phase in amorphous samples.

7. There was not found any measurable effect of deuterium implantation on optical properties of mirror sample, either in amorphous or crystallized states.

8. On a small part of the surface of BMG mirror sample of grade #1, exposed to ions of deuterium plasma accelerated to the energy 300 eV, the blister-like features appeared with the shape different from what can be found in literature.

9. When BMG mirrors with beryllium or aluminum in their composition are exposed to deuterium plasma, chemical processes on the surface play a definite role in behavior of their optical properties.

In conclusion, we noted that because of the high absorptivity of hydrogen isotopes, existing Zr-based BMG cannot be a prospect material for in-vessel mirrors in ITER. However, in view of rather rapid progress in the development of amorphous materials, there is a hope that BMG materials with a low absorptive capacity (for hydrogen isotopes) will be designed in the future, what will permit their use for fabrication of in-vessel mirrors operating in the conditions with high fluxes of charge exchange atoms, neutrons, and gamma radiation.

Acknowledgements

Appendix A: Fabrication of amorphous alloys containing beryllium

The main peculiarity of bulk amorphous metal alloys is that they have a multicomponent mixture; as the rule, 4–5 components are used for their preparation. Among the most perspective is Zr-based bulk amorphous metal alloy that demonstrate a high mechanical strength and fracture toughness with good corrosive resistance. For the system Zr-Ti-Cu-Ni-Be, the maximal critical thickness known from literature amounts to 30 mm at the critical cooling rate 1–5 K/s. This opens the way for preparation of mirror samples with a standard size (diameter 22 mm and thickness 3–4 mm) for experimental modeling the behavior of mirrors in ITER.

For smelting of ingots of bulk metallic glasses in Kharkov (grade #2, **Table 1**), an electric arc-smelting device with the nonconsumable electrode was used. The melting operation was realized in water-cooled copper mold, inside its cavity of reference shape and dimensions.

The alloy has the following composition: $Zr_{41}Ti_{14}Cu_{12,5}Ni_{10}Be_{22.5}$. The purity of all metal components was not less than 99.9 weight percent. As the starting materials the iodide Zr and Ti, cathodic Ni, electrical copper, and distilled Be were used.

All components were mixed in the necessary proportion and placed in a mold cavity of the water-cooled copper mold of the melting facility. After that the melting facility was pumped for degassing the furnace charge and filled with pure argon to the pressure that ensures a stable arc burning. Then, arc was initiated and the metal got fused. The form and the size of ingots are specified by the mold cavity shape and amount of the furnace charge. For obtaining a homogeneous composition of an amorphous material it was molten many times with opening the melting facility and with flip over of the ingot for 180°. The initial sizes of ingots (diameter 25–28 mm and thickness 10–14 mm) were defined by the requirements to have the standard size of mirror samples (22 mm in diameter).

The billets for fabrication of mirror samples and specimens for providing different investigations of the properties of the amorphous material were prepared by means of electric discharge sawing. **Figure A1** shows the photos of one of ingots from which the upper and lower "caps" were cut off (left), before it was cut further into two halves (right) which served as billets for fabrication of mirror samples. One half of every ingot was annealed at 773°K during one hour.

The crystallization was checked by using the X-ray diffractometer DRON-4-07, and the results are shown in **Figure 1**.

Figure A1. The photos of the ingot with cut off upper and lower "caps" before (left) and after (right) cutting into two halves which served as billets for the fabrication of mirror samples.

Appendix B: Processing of images of laser spots reflected from test mirrors

To study the structure of a laser spot image after laser beam reflection from a given surface, the sampling of brightness of pixels B(x) for every image in **Figure 21** was carried out along its diameter following a horizontal line or lines inclined at 45°, 90°, and 135° to this line. The spot is 440 pixels in diameter that corresponds to 4 mm. We removed a sampling component corresponding to a radial decrease in the spot brightness ("a bell shape") using a Fourier transform. The sequential combination of samplings extends the sampling path and improves the statistics.
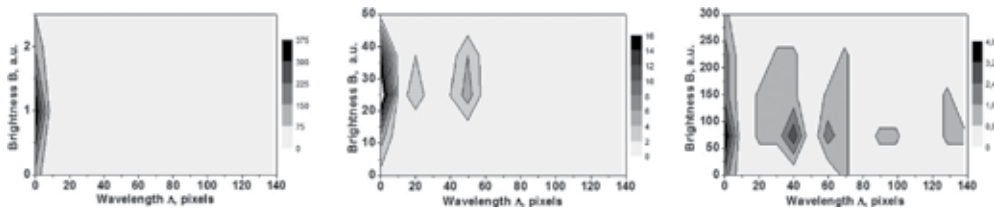
Figure B1. The contour diagrams of the distributions $\Delta N/(\Delta\Lambda \cdot \Delta B)$. The designations correspond to the laser spot images a–c of **Figure 21**.

A comparison of the samplings "by eye" shows that $B_a(x)$ is characterized by very short wavelengths and very low variations of the brightness. These parameters are higher for $B_b(x)$ and much higher for $B_c(x)$ by the reason of increasing the surface roughness.

The procedure described in [32] is intended to compute the one-dimensional distribution function $\Delta N(\Lambda)/\Delta\Lambda$ or, in other words, the number of waves N in a spectral interval $\Delta\Lambda$ where the wavelength Λ is along the image. We extended this function to two-dimensional one $\Delta N(\Lambda,B)/(\Delta\Lambda \cdot \Delta B)$. The functions a–c are marked with constant-level lines in the contour diagram of **Figure B1**. The upper limits of the wavelength axis Λ are the same for all the spots, and those of the brightness axis B are different.

We observed one group with the very short wavelengths and the very low oscillations of the brightness for the laser spot *"a"* (the "ideal mirror"). The spot *"b"* (BMG mirror) has three groups of the short and medium wavelengths, and the medium variations of the brightness. And the spot *"c"* (BMG-C mirror) has five groups of the short, medium, and long wavelengths, and the medium and high variations of the brightness. The results of an analysis are shown in **Table B1**.

	B_{av}, a. u.	B_s, a. u.	B_{max}, a. u.	S_m, pixels	Λ_{max}, pixels
a	1.2	0.5	2.5	3	7
b	27	10	50	24	59
c	78	27	300	53	138

Table B1. The parameters of distributions: B_{av}—the average brightness, B_s—the standard deviation of B, B_{max}—the highest B, S_m—the average wavelength, Λ_{max}—the longest wavelength.

The obtained distributions are in good agreement with the photos a–c of the laser spots. All the parameters in **Table B1** are growing from *"a"* to *"c"*. Especially, five groups related to the spot *"c"* confirm the existence of very long irregularities and, eventually, indicate a surface fracture.

Author details

Vladimir S. Voitsenya[1*], Alexandra F. Bardamid[2], Martin Balden[3], Flaviu Gostin[4],
Sergey V. Khovrich[1], Vladimir G. Konovalov[1], Konstantin V. Kovtun[1], Petro M. Lytvyn[5],
Sergey V. Ketov[6], Dmitri V. Luzguine-Luzgin[6], Sergei I. Solodovchenko[1],
Anatoly N. Shapoval[1], Anatoly F. Shtan'[1], Vladislav N. Bondarenko[1], Ivan V. Ruzhkov[1],
Ol'ga O. Skoryk[1] and Andrei A. Vasil'ev[1]

*Address all correspondence to: voitseny@ipp.kharkov.ua

1 National Science Center "Kharkov Institute of Physics and Technology", Kharkov, Ukraine

2 Taras Shevchenko National University of Kyiv, Kyiv, Ukraine

3 Max-Planck-Institut für Plasmaphysik, Garching, Germany

4 Leibniz-Institute for Solid State and Materials Research IFW Dresden, Dresden, Germany

5 Institute of Semiconductor Physics of NASU, Kyiv, Ukraine

6 WPI Advanced Institute for Materials Research, Tohoku University, Sendai, Japan

References

[1] Donn´e AJH, Costley AE, Barnsley R, Bindslev H, Boivin R, Conway G, Fisher R., Giannella R, Hartfuss H, von Hellermann MG, Hodgson E, Ingesson LC, Itami K, Johnson D, Kawano Y, Kondoh T, Krasilnikov A, Kusama Y, Litnovsky A, Lotte P, Nielsen P, Nishitani T, Orsitto F, Peterson BJ, Razdobarin G, Sanchez J, Sasao M, Sugie T, Vayakis G, Voitsenya V, Vukolov K, Walker C, Young K, and the ITPA Topical Group on Diagnostics. Mint: Chapter 7: Diagnostics. Nucl. Fusion. 2007;47:337–384.

[2] Behrisch R, Federichi G, Kukushkin A, Reiter D. Mint: J. Nucl. Mater . 2003;388;313–316.

[3] Perez-Bergquist AG, Bei H, Zhang Y, Zinkle SJ. Mint: Fusion Reactor Materials Program, June 30, 2013;54 :154–161. DOE/ER-0313/54.

[4] Perez-Bergquist AG, Bei H, Brechtl J, Zinkle SJ. Mint: ORNL Fusion Mater. FY. 2014 ; 9–11. ORNL/TM-2014/447.

[5] Voitsenya VS, Konovalov VG, Shtan' AF, Solodovchenko SI, Becker MF, Bardamid AF, Yakimov KI, Gritsyna VT, Orlinskij DV. Mint: Rev. Sci. Instr. 1999;70:790–793.

[6] Brindley GW, Brown G, editors. Crystal Structures of Clay Minerals and their X-ray Identification. Mineralogical Society, 41 Queen's Gate, London: SW7 5HR; 1980. 495 p.

[7] Palik ED, editor. Handbook of Optical Constants of Solids. Academic Press, San Diego; 1985. 804 p.

[8] Tolansky S. High Resolution Spectroscopy (in Russian). Moscow, IL; 1955 . 380 p.

[9] Bardamid AF, Belyaeva AI, Bondarenko VN, Galuza AA, Kolesnyk OG, Konovalov VG, Naidenkova DI, Ryzhkov IV, Shapoval AN, Skinner CH, Shtan AF, Solodovchenko SI, Voitsenya VS, Yakimov KI. Mint: Phys. Scr. 2006;73:1–5.

[10] Voitsenya VS, Bakai AS, Bardamid AF, Konovalov VG, Kovtun KV, Naidenkova DI, Ryzhkov IV, Shtan' AF, Solodovchenko SI, Trembach OV, Vasil'ev AA. Mint: J. Plasma Fusion Res. SERIES. 2009;8:1379–1384.

[11] Yamamura Y, Tawara H. Mint: Atomic Data Nucl. Data Tables. 1996;62:149–253.

[12] Wanderka N, Wei Q, Sieber I, Czubayko U, Macht MP. Mint: Mater. J. Metast. Nano-cryst. Mater. 1999;2-4:369–374, and references there.

[13] Bardamid A, Bryk V, Konovalov V, Orlinskij DV, Shtan' A, Shapoval A, Solodovchenko S, Voitsenya V, Yakimov K, Zakharenko N. Mint: Vacuum. 2000;58:10–15.

[14] Orlinski D, Voitsenya V, Vukolov K. Mint: Plasma Device Operations, 2007;15:33–75.

[15] Golovanivsky KS, Dugar-Jhabon VD, Schepilov VD, Safonov SA. Mint: Sov. J. Plasma Phys. 1981;7:324–333.

[16] Verbeek DH, Poschenrieder W, Carlson A, Fu J-K, McCormick K, Tsois N, Soldner FX, and the ASDEX Team. Mint: Plasma Phys. Control. Fusion. 1990;32:651–658.

[17] Miura FY and the JFT-2M team. Mint: Nucl. Fusion. 1997;37:175–188.

[18] Bardamid AF, Voitsenya VS, Davis JW, Konovalov VG, Kovtun KV, Ryzhkov IV, Shtan' AF, Solodovchenko SI, Trembach OV, Vasil'ev AA, Breuer U, Litnovsky A. Mint: J. Alloys & Compounds. 2012;514:189–194.

[19] Suh D, Asoka-Kumar P. Mint: Acta Materialia 2002; 50:537–551.

[20] Voitsenya VS, Bardamid AF, Belyaeva AI, Bondarenko VN, Galuza AA, Konovalov VG, Ryzhkov IV, Savchenko AA, Shapoval AN, Shtan' AF, Solodovchenko SI, Yakimov KI. Mint: Plasma Devices Operations. 2009;17:144–154.

[21] Eckstein W, Garcia-Rosales C, Roth J., Ottenberger W. Technical Report IPP 9/82, Max-Planck-Institut für Plasmaphysik, Garching, Germany, 1993. 342 p.

[22] Bardamid AF, Bondarenko VN, Davis JW, Konovalov VG, Lytvyn O, Ryzhkov IV, Shapoval AN, Shtan' AF, Solodovchenko SI, Voitsenya VS. Mint: J. Nucl. Mater. 2010;405:109–117.

[23] Bardamid AF, Belyaeva AI, Davis JW, Dobrovorskaya MV, Galuza AA, Kapitonchuk LM, Konovalov VG, Ryzhkov IV, Shtan' AF, Slatin KA, Solodovchenko SI, Voitsenya VS. Mint: J. Nucl. Mater. 2009;393:473–480.

[24] Konovalov VG, Makhov MN, Shapoval AN, Ryzhkov IV, Shtan' AF, Solodovchenko SI, Voitsenya VS. Mint: Probl. Atomic Sci. Technol. Ser. Plasma Phys. 2009;15:1;13–15.

[25] Kiene M, Strunskus T, Hasse G, Faupel F. Oxide formation on the bulk metallic glass $Zr_{46.75}Ti_{8.25}Cu_{7.5}Ni_{10}Be_{27.5}$. Mater. Res. Soc. Symp. Proc. 1999;554:167–172.

[26] Bardamid AF, Voitsenya VS, Lytvyn OS, Lytvyn PM, Konovalov VG, Shapoval AN, Solodovchenko SI, Yakimov KI. Mint: J. Nucl. Mater. 2008;376:125–127.

[27] Behrisch R. (Ed.), Sputtering by Particle Bombardment II, Springer-Verlag, Berlin–Heidelberg–New York–Tokyo, 1983 (Chapter 7, p. 360 in the Russian version, published by Moscow branch of Mir,1986).

[28] Atanassova E, Lytvyn P, Dub SN, Konakova RV, Mitin VF, Spassov D. Mint: J. Phys. D: Appl. Phys. 2012;45:475304 (13 pp).

[29] Tyagi AK, Nandedkar RV, Krishan K. Mint: J. Nucl. Mater. 1983;114:181–189.

[30] Tyagi AK, Nandedkar RV, Krishan K. Mint: J. Nucl. Mater. 1983;116:29–39.

[31] Tyagi AK, Nandedkar RV. Mint: J. Nucl. Mater. 1987;148:72–75.

[32] Voitsenya VS, Balden M, Bardamid AF, Bondarenko VN, Davis JW, Konovalov VG, Ryzhkov IV, Skoryk OO, Solodovchenko SI, Zhou Z-J. Mint: Nucl. Instrum. Methods Phys. Res. 2013;B302:32–39. [http://dx.doi.org/10.1016/j.nimb.2013.03.005]

Edited by Behrooz Movahedi

Metallic glasses and amorphous materials have attracted much more attention in the last two decades. A noncrystalline solid produced by continuous cooling from the liquid state is known as a glass. From the other point of view, a noncrystalline material, obtained by any other process, for example, vapor deposition or solid-state processing methods such as mechanical alloying, but not directly from the liquid state, is referred to as an amorphous material. At this moment, bulk metallic glasses (BMG) are appearing as a new class of metallic materials with unique physical and mechanical properties for structural and functional usage. Extreme values of strength, fracture toughness, magnetic properties, corrosion resistance, and other properties have been registered in BMG materials.

Photo by eugenesergeev / iStock

IntechOpen